Application of Johnson's approximation in finite element modeling for electric field-dependent materials for use in multi-layer ceramic capacitor applications.

By

Rassell Carl D'Silva Green

A thesis submitted in partial fulfilment of the requirements for the degree of

Doctor of Philosophy

Thesis Supervisors

Dr. Julian S. Dean

&

Prof. Derek C. Sinclair

The University of Sheffield

Faculty of Engineering

Department of Materials Science and Engineering

January 2025

List of Figures

List of Tables

Abstract

This thesis investigates the complex relationships between material properties and their response to electric fields, with a particular focus on voltage-dependent capacitance. A key objective was to develop and validate a simulation code based on Johnson's equation to model the voltage dependency of dielectric materials. The code successfully captures the nonlinear behaviour of relative permittivity under varying electric fields, with simulation results closely aligned with established models and experimental data. This verification process demonstrates the reliability of the code for predicting dielectric behaviour.

The thesis further explores the impact of parameters such as Johnson's parameter, applied electric field strength, material thickness, and intrinsic permittivity on the dielectric response. Results reveal that effective permittivity is highly sensitive to Johnson's parameter and field strength, particularly in high-permittivity materials like barium titanate, where a decline in dielectric response is observed at higher values of these parameters. A saturation effect is also noted at higher Johnson's parameter and field strengths. Additionally, material thickness plays a critical role in the final temperature coefficient of capacitance (TCC), with thickness having a stronger influence than other factors like volume fraction and conductivity ratio.

The thesis also compares analytical and simulated models, demonstrating that the simulations provide accurate results with minimal deviations from analytical solutions (less than 2%). A finite element modeling approach is developed to study multilayer ceramic capacitors (MLCCs), revealing how the core-shell structure of $BaTiO_3$ influences voltage-capacitance characteristics. The findings offer new insights into the design of MLCCs with improved performance, tailored voltage dependence, and enhanced breakdown strength. Overall, this research contributes significantly to understanding dielectric material behaviour.

Acknowledgements

I would like to express my deepest gratitude to my supervisor, Julian Dean, for his invaluable guidance, support, patience, and insightful feedback throughout my PhD journey. His expertise and dedication to my growth as a researcher have been crucial in shaping this work. I have learned so much under his supervision.

I am also profoundly grateful to my parents and sister for their love, support, and constant encouragement. Their belief in me has been a source of strength, and their unwavering support during the most challenging times has kept me grounded. I am forever thankful for their sacrifices, care, and the unwavering confidence they have always had in me.

Finally, I want to extend my heartfelt thanks to my partner for their love, patience, and constant support throughout this journey. Their understanding, encouragement, and willingness to share the highs and lows of this experience have meant the world to me. I am so grateful for her presence by my side and for her belief in me, which has made all the difference.

1 Introduction

1.1 Background

Multilayer Ceramic Capacitors (MLCCs) play a critical role in a wide range of electronic applications, from smartphones to automotive systems[1,2], with global production reaching over 3.5 trillion units annually[3]. These components are expected to evolve in response to growing demands for higher frequencies, voltages, breakdown strengths, and temperature stability, especially with the advent of technologies such as 5G and electric vehicles[4].

One of the most significant challenges in the design of MLCCs is improving their capacitance while maintaining a small size and thermally stable performance. This can be achieved through optimisation of the dielectric materials, with ferroelectric barium titanate ($BaTiO_3$) commonly used as a base due to its high relative permittivity at room temperature. However, the temperature dependence of the relative permittivity must be controlled to ensure reliable performance across a wide range of operating conditions. Techniques such as chemical doping, grain size adjustments, and core-shell microstructure designs have been developed to extend the operating temperature range and improve the temperature coefficient of capacitance (TCC). Furthermore, reducing the distance between the electrodes in MLCCs can increase capacitance but also heighten the risk of dielectric breakdown, especially in high-voltage applications.

While significant progress has been made in optimising TCC, the voltage coefficient of capacitance (VCC) remains an important consideration, as high electric fields can reduce relative permittivity and shift the Curie temperature. To better understand these phenomena, models such as Johnson’s approximation are employed to predict the macroscopic tunability of $BaTiO_3$-based materials under varying electric fields. Despite some limitations, Johnson’s equation has proven useful in explaining the voltage dependence and aiding in the design of more efficient dielectric materials for MLCCs. However, as the material size decreases, the local electric field within the material experiences increased inhomogeneity. This inhomogeneity makes Johnson's approximation, which applies a global field to the system, insufficient for accurately capturing the system's behaviour. This happens as reducing the dielectric layer thickness increases the local electric field strength under a fixed applied voltage, as the field scales inversely with thickness ($E = V/d$). This intensified local field can lead to nonlinear dielectric behaviour, enhanced leakage currents, and accelerated ageing in thinner layers compared to thicker MLCCs, where the field is distributed more uniformly. Consequently, thickness variations across MLCCs introduce performance disparities—thinner layers exhibit higher field-driven permittivity changes and greater susceptibility to breakdown. To address this, the local field values generated should be used to determine the corresponding local changes in relative permittivity.

1.2 Aim

This thesis aims to develop a computational framework for analysing the field-dependent dielectric response of three-dimensional core-shell microstructures using Johnson's equation. The primary goal is to develop a numerical code capable of resolving local electric field distributions in both core and shell materials, addressing the limitations of conventional global field approximations. By incorporating finite element analysis (FEA), the model will be validated against spatially resolved field effects, ensuring accuracy in predicting dielectric behaviour. A key focus will be investigating how microstructural parameters, such as core-shell geometry, and changes in relative permittivity and conductivity, impact the overall dielectric performance. Furthermore, the study will extend the analysis to evaluate the temperature coefficient of capacitance (TCC), establishing a link between field-dependent permittivity and thermal stability. Ultimately, this work seeks to provide a comprehensive understanding of structure-property relationships in core-shell dielectrics, offering practical insights for optimising high-performance materials in Multi-layer ceramic capacitors under varying electric fields and temperature conditions.

1.3 Thesis overview

The structure of the thesis and the content of each chapter are as follows.

Chapter 2 provides a comprehensive review of the literature relevant to this thesis, covering the basics of MLCC devices and dielectric ceramic materials. It also includes a summary of prior research on the specific systems explored in this study, specifically focusing on other approaches to modeling Johnson's equation.

Chapter 3 demonstrates an analytical model utilising Johnson's equation is developed first in the form of a simple cube and then a layered model in two configurations: series and parallel. This will be used to get a broader understanding of the field dependence of relative permittivity.

Chapter 4 presents a comprehensive exploration of finite element modeling (FEM). It begins with an introduction to the fundamental principles of FEM, explaining how it operates at a basic level. The chapter then delves into the role of software in implementing these principles, highlighting the process of model creation, with particular emphasis on the accurate representation of geometries within the problem domain. The section on boundary conditions examines how external factors, such as applied forces and constraints, are incorporated into the models to replicate real-world scenarios effectively.

The methodology section outlines a step-by-step approach to building a simple layered model, including the assignment of material properties to each layer and the definition of their interactions. The simulation segment explains how computational analyses predict the behaviour of each layer under various conditions. Furthermore, the chapter discusses series and parallel models, which represent two different configurations of layered systems. By comparing the results from these models with their corresponding analytical models, the accuracy of the simulations and the potential for more complex future models are tested.

Chapter 5 begins with the following publication:

Application of Johnson's approximation in finite element modeling for electric field-dependent materials

Rassell C. D'Silva Green, Graham Dale, Garry McLaughlin, Maureen Strawhorne, Derek C. Sinclair, Julian S. Dean

https://doi.org/10.1111/ijac.14824

This paper demonstrates how the code developed in Chapter 4 is utilised to analyse different configurations of core-shell systems, highlighting how variations in microstructure and the differences in core and shell conductivities impact the local fields generated. It also examines how these variations influence the voltage dependence of the effective relative permittivity. In addition to this, the chapter explores an alternative configuration that investigates the effect of lower initial relative permittivity. Finally, the chapter provides an overview of the overall impact on the core-shell microstructure and addresses potential sources of error in the modeling process.

Chapter 6 initially analyses experimental VCC material data provided by AVX, offering insights into how temperature changes can influence the voltage dependence of dielectrics. This data will then be used to generate TCC plots, providing a deeper understanding of how temperature stability evolves with increasing applied voltages. Following this, the method for extracting Johnson's parameter will be outlined, using the experimental data. Finally, the utility of the code described in Chapters 4 and 5 will be demonstrated by using it to generate TCC data based on the experimental material data presented in Chapter 3, focusing on two different configurations.

Finally, conclusions and future work are discussed in Chapter 7.

1.4 References

1. Sun Y, Wu S, Zhang J, Hwang C, Yang Z. Measurement Methodologies for Acoustic Noise Induced by Multilayer Ceramic Capacitors of Power Distribution Network in Mobile Systems. *IEEE Trans Electromagn Compat*. 2020;62(4):1515-1523. doi:10.1109/TEMC.2020.2993850

2. Abebe R, Vakil G, Calzo G Lo, Cox T, Lambert S, Johnson M, Gerada C, Mecrow B. Integrated motor drives: State of the art and future trends. *IET Electr Power Appl*. 2016;10(8):757-771. doi:10.1049/iet-epa.2015.0506

3. Analysis of Global Multi-Layer Ceramic Capacitor (MLCC) Markets, 2019-2024. ResearchAndMarkets.com. Published 2019. Accessed July 18, 2023. https://www.businesswire.com/news/home/20191209005389/en/Analysis-of-Global-Multi-Layer-Ceramic-Capacitor-MLCC-Markets-2019-2024---ResearchAndMarkets.com

4. Kerridge G, Sinclair DC, Dean JS. Resource-efficient exploration of ternary phase space to develop multi-layer ceramic capacitors. *Acta Mater*. 2021;207:116690. doi:10.1016/j.actamat.2021.116690

2 Theory and literature review

2.1 Overview

This chapter discusses the theoretical aspects of capacitors and dielectric materials. It begins with an introduction to capacitors and their properties. It then moves on to dielectric materials, focusing on ceramics and ferroelectric materials. The following section explores the Perovskite Structure, a common structure in dielectric materials, and its Goldschmidt Tolerance Factor, which is a key parameter in determining the stability of the structure. Next, Multi-Layer Ceramic Capacitors (MLCCs) are introduced, discussing their classification and fabrication process, thereby providing a comprehensive understanding of how MLCCs are made and their different types. Next, the temperature coefficient of capacitance or TCC, is then discussed, followed by a discussion on the voltage coefficient of capacitance or VCC.

Subsequently, Barium titanate and some methods by which ferroelectrics can be modified to tune the TCC, specifically focusing on the effects of doping, grain size, and particle size and the use of multi-layered dielectrics are discussed. Finally, we end with a brief description of some common modeling methods used to model ferroelectrics and end with talking about Johnson's equations and their utilisation in modeling dielectrics.

This chapter provides a solid foundation for understanding the theory behind capacitors and dielectric materials, which are crucial components in many electronic devices.

2.2 Capacitors

A capacitor is a key component of modern electronics. It is a passive device that can store electric charge and release it when needed. They can have different shapes and sizes, but they all have a common structure: two conductors (such as metal plates, films, or electrolytes) separated by a dielectric material (such as air, paper, or ceramics) [1] as seen in Figure 2.1. The dielectric will be explained in more detail in the following section. Due to the conductors usually being very thin and having a large surface area, they are often referred to as plates or electrodes.

Capacitors have a wide range of applications in various fields. In power electronics, capacitors are essential components in systems such as inverters. Shimizu et al.[2] discuss the use of capacitors in a utility-interactive inverter for a photovoltaic system to reduce power pulsations and generate sinusoidal voltage. Capacitors also play a crucial role in distribution systems for improving voltage profiles and reducing power loss[3,4]. Moreover, capacitors are significant in electronic engineering, where capacitor multipliers are utilised for on-chip compensation and soft-start functions[5]. Additionally, in Si analog circuit applications[6] shows the suitability of HfO_2 metal-insulator-metal capacitors. The use of fractional-order capacitors is essential for accurately modeling supercapacitors, batteries, and fuel cells[7].

Another use of capacitors is energy storage and supply, which means they can store electric charge and deliver it quickly when needed. For example, a camera flash uses a capacitor to release a burst of energy to produce bright light[8]. A third function of capacitors is signal filtering, which means they can block low-frequency signals and allow high-frequency signals to pass through. This is useful in telecommunications, where capacitors can filter out unwanted noise and improve the quality of the signal[9]. Capacitors can also be used in timing circuits, where their ability to charge and discharge at a predictable rate is leveraged to create oscillating signals or control timing in various electronic devices[10]. In commercial capacitors, two conductive components are positioned near each other without making contact. Typically, a dielectric material is utilised to separate these two plates, as displayed in Figure 2.1.

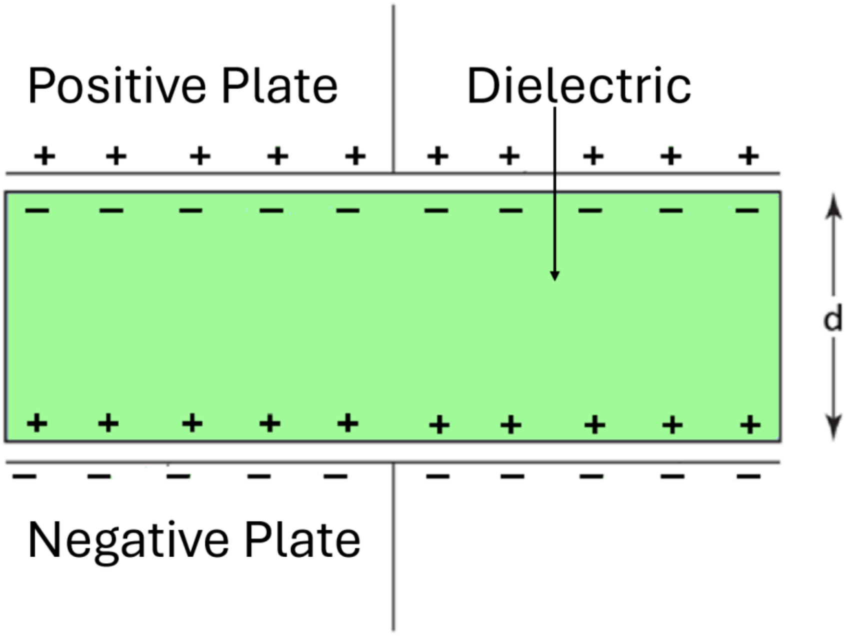

Figure 2.1: Schematic diagram of a parallel plate capacitor showing the two conductive plates separated by a distance d, filled with a dielectric having permittivity ε.

Capacitance is the maximum amount of charge a capacitor can hold due to the applied voltage across the plates

$$C = \frac{Q}{V}$$

Equation 2.1

Where C is the capacitance in farads, Q is the charge in coulombs, and V is the voltage in volts. A capacitance of 1 farad is the capacitance of a capacitor when a charge of 1 coulomb is stored when 1V of potential difference is applied across the device.

There are several types of capacitors, such as parallel plate, spherical, and cylindrical capacitors.

A spherical capacitor consists of a solid or hollow spherical conductor of radius R_1, encased by another hollow concentric spherical conductor of a different radius R_2. Similarly, a cylindrical capacitor consists of a solid or hollow cylindrical conductor of radius R_1, encased by another hollow concentric cylindrical conductor of a different radius R_2. When considering the uses of parallel plate and cylindrical capacitors, it is essential to understand the differences in their applications and characteristics. Cylindrical capacitors have higher power density and lower electromagnetic interference than parallel plate capacitors[11]. In practical applications, parallel plate capacitors are often used to achieve a balance between stability and low output ripple voltage[12]. In this thesis, we will be focusing on parallel plate capacitors

Parallel plate capacitors have two identical parallel plates with a distance d between them. The plates are filled with a dielectric material that has a permittivity ε, as shown in Figure 2.1. The plates have a surface area A, and they store a charge Q when a voltage V is applied across them. The electric field E between the plates is constant (ignoring the edge effects) due to its parallel arrangement. Using this, we can calculate V as

$$V = E \times d$$

Equation 2.2

The surface charge density σ can be defined as:

$$\sigma = \frac{Q}{A}$$

Equation 2.3

The relative permittivity ε_r can be defined as:

$$\varepsilon_r = \frac{\varepsilon}{\varepsilon_0}$$

Equation 2.4

Where ε_0 is the permittivity of free space and has a value of 8.85 x 10^{-12} F/m, and ε is the permittivity of the material. Additionally, from Gauss' law, which states that the total electric flux through any closed surface is proportional to the total electric charge inside the surface, we know that:

$$E = \frac{\sigma}{\varepsilon}$$

Equation 2.5

Substituting equations 2.2, 2.3, 2.4 and 2.5 in equation 2.1, we get

$$C = \frac{\varepsilon_r \varepsilon_0 A}{d}$$

Equation 2.6

From equation 2.6, we have seen that enhancing the capacitance of a Multilayer Ceramic Capacitor (MLCC) involves several strategies. These include:

Increasing Relative Permittivity (ε_r): Relative permittivity can be increased by using materials with higher relative permittivity. This approach, however, has its limitations. During the manufacturing process, precise control over sintering temperatures is crucial. Temperatures exceeding 1200°C can lead to metal diffusion into the dielectric material. Additionally, accurate management of the sintering atmosphere is essential to prevent electrode oxidation and minimise the likelihood of impurities being introduced into the dielectric[13]. Improper sintering may result in elevated residual stress and mechanical cracking, ultimately affecting the performance and reliability of the multilayer ceramic capacitor (MLCC). Additionally, this approach must balance with other factors like operating voltage and dielectric thickness.

Reducing Plate Distance (d): Decreasing the separation between the capacitor plates enhances capacitance. Achieving thinner dielectric layers requires smaller grain sizes (often less than 1 µm) [14]. However, this alteration significantly impacts the dielectric properties of the ceramic. This will be discussed in detail below.

Increasing Plate Area (A): Expanding the electrode surface area causes an increase in capacitance. Yet, practical limitations arise as the trend for miniaturisation of technologies limits the final size of the application.

Balancing these factors is crucial for optimising MLCC performance in various applications.

The ultimate characteristics of the multilayer ceramic capacitor (MLCC) are influenced by a diverse set of factors. These include the volume fraction of the core and shell materials, the grain size, the thickness, and the distribution of dopants. Precise control over these parameters is essential during the manufacturing process, which relies on various processing techniques[15].

2.3 Dielectric materials

A dielectric is an electric insulator that can be polarised in the presence of an external electric field. Unlike conductors, dielectrics do not possess any free electrons to move. Instead, the presence of the electric field causes their negative and positive charges to align with the direction of the applied field, creating what is known as a dipole moment[16] as seen in Figure 2.2. The degree to which a material can be polarised determines the magnitude of its relative permittivity. For instance, the relative permittivity of air is 1. On the other hand, ionic solids such as table salt (NaCl) exhibit relative permittivity values ranging from 5 to 20[17], while ferroelectric ceramics like barium titanate can demonstrate relative permittivity values from 1000 to 14000[18]. The properties of the dielectric between the plates determine the permittivity of the capacitor.

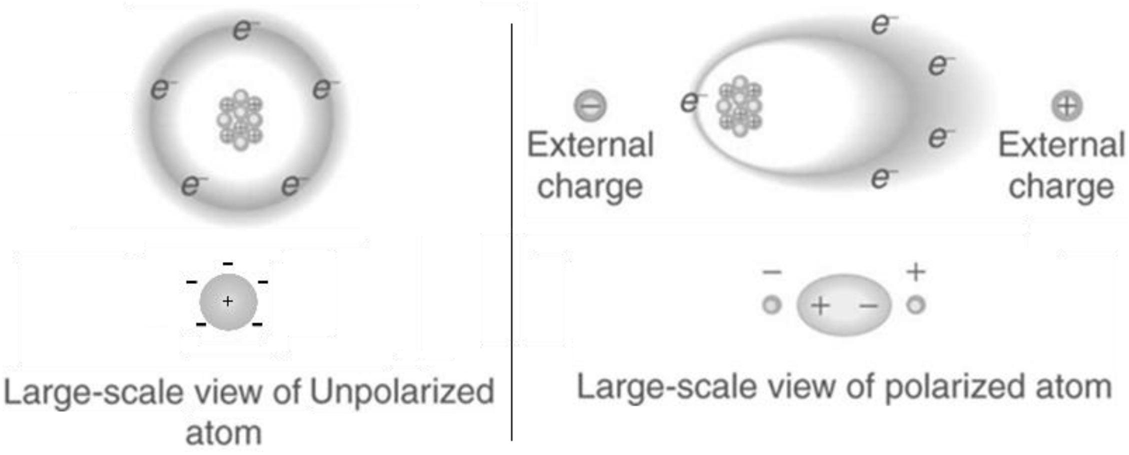

Figure 2.2: Schematic showing the polarisation of an atom in the presence of an electric field. In the presence of an electric field (right), the electron field aligns itself with the external charge, creating a dipole as seen in the polarised image above.

Polarisation in the presence of an electric field arises from four distinct charge displacement mechanisms: electronic, ionic, dipolar (orientational), and space charge polarisation, as illustrated in Figure 2.3. A material may exhibit one or a combination of these mechanisms depending on its structure and the applied field conditions. Electronic polarisation occurs in all materials and involves the shift of an atom's electron cloud, which carries a negative charge when an electric field is applied. This causes the atom to act like a dipole. Ionic polarisation, on the other hand, is the relative movement of positive and negative ions in an ionic material when an electric field is applied. This can be observed up to frequencies of approximately 10^{13} Hz. Both atomic and ionic polarisation significantly contribute to polarisation in dielectrics. Dipolar polarisation happens in materials that already have polarisation, like the water molecule. In the absence of an electric field, the dipoles are randomly oriented, resulting in a net polarisation of zero. However, when an electric field is applied, the dipoles align in the direction of the field, leading to a net polarisation. This can be observed up to frequencies of approximately 10^{6} to 10^{12}. Finally, space charge polarisation occurs when charge carriers move due to the application of an electric field and are halted at the boundaries of the material grains, creating a dipole moment.

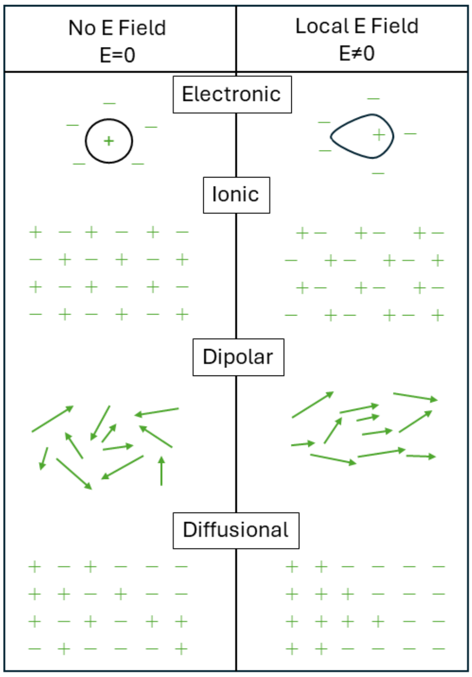

Figure 2.3: Different mechanisms for the polarisation of a dielectric under the effect of an electric field [19]

2.3.1 Ceramics

Ceramics can be broadly divided into two categories: Traditional and technical ceramics. Traditional ceramics generally include ceramic materials, which are hard or strong materials[16]. These are produced in large quantities and typically comprise silicates and include clay and its products. Ceramics that fall in this category are generally known for their high hardness, low thermal properties, high wear resistance, low ductility, and good electrical insulators.

The second group of ceramics are known as technical or advanced ceramics and are manufactured from materials such as carbides, nitrides, and oxides. They are known for their exceptional mechanical, electrical, or optical properties and can display electrical properties such as ferroelectricity, paraelectricity, and even magnetic properties. Their properties can be well controlled through intensive manufacturing processes[20]. They are used in a wide range of applications, such as battery technologies for their electrical properties, such as Yttria-stabilised zirconia, which is used in Solid oxide fuel cells, to solid state lasers for their optical and thermal properties (Doped Yttrium aluminium garnet) [21,22]. They are even used in cutting tool applications for their abrasive properties and as armours for their mechanical properties. Additionally, they often have longer lifespans compared to other materials[20] which has been attributed to their low corrosive properties. However, ceramics are quite brittle primarily because their limited slip systems (due to ionic/covalent bonding and complex crystal structures) prevent dislocation motion, forcing cracks to propagate without energy absorption.[23].

2.3.2 Perovskite Structure

Named after the Russian mineralogist Lev Perovski, Perovskites refer to a class of compounds which have the same type of crystal structure as Calcium titanate. The general chemical formula of this structure is ABO_3.

As depicted in Figure 2.4(a), the ideal perovskite structure possesses a cubic unit cell. The repeating unit cell positions the A-sites at the corners and oxygen atoms at the centre of each face, forming an oxygen octahedron. The B-site is located at the cube’s centre, enclosed by the oxygen octahedron. A-site ions are usually an alkaline earth or rare-earth element, while B-site ions are usually 3d,4d, and 5d transition metal elements.

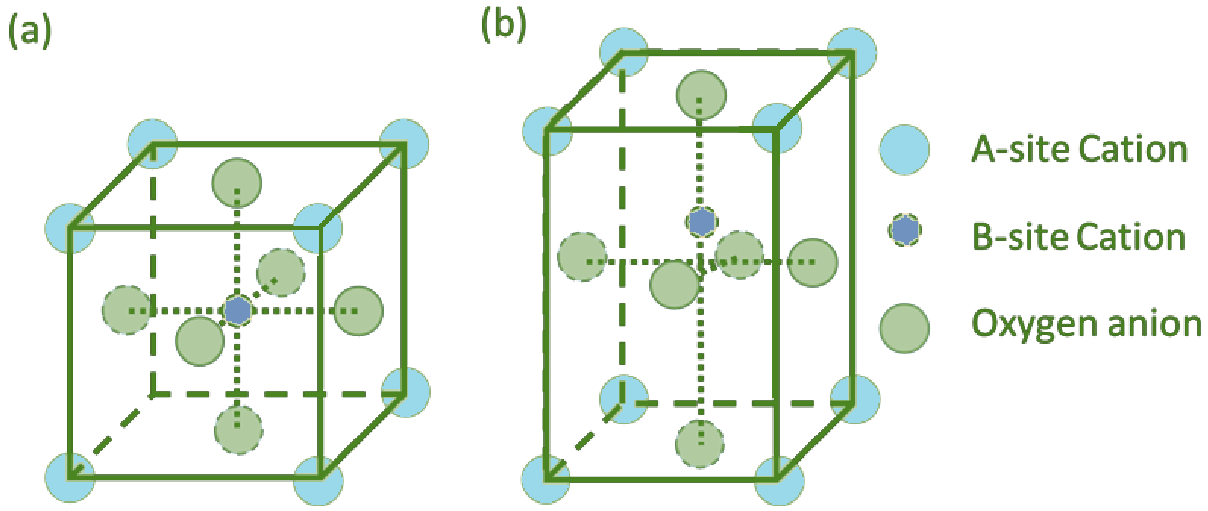

Figure 2.4: Schematic of the perovskite structure showing the A and B site cations and the Oxygen anions. a) Ideal cubic perovskite structure b) An elongation along the c-axis with the B site off-centre.

2.3.3 Goldschmidt's Tolerance Factor

As seen in Figure 2.5(a) The face-diagonal distance is √2 times the face-length value. Similarly, from (b) and (c) we can see that the atomic radii must satisfy both $x = 2(r_A + r_O)$ and $\sqrt{2}x = 2(r_B + r_O)$, for the same value of x to achieve an ideal cubic perovskite structure. From this, we can see that stability is highly dependent on the radius of the ions.

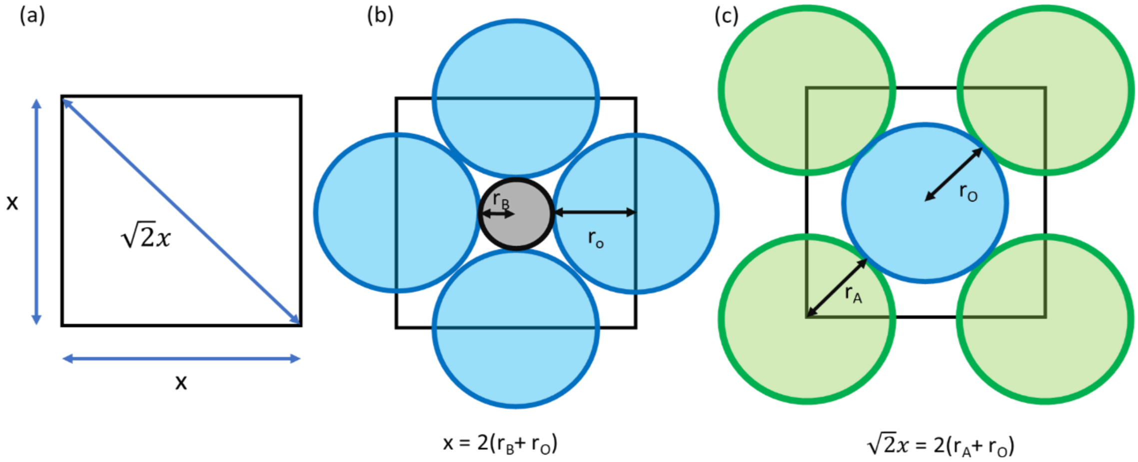

Figure 2.5: a) The relation between dimensions of the face of an ideal cube. b) The (200) cutting plane showing the small B cation in the centre surrounded by 4 of the face centre oxygen atoms. c)The (100) plane cutting through the oxygen at the centre surrounded by 4 of the corner cations.

Using the relationships mentioned above, we can quantify the degree of distortion that occurs in the perovskite structure by the equation:

$$t = \frac{R_A + R_O}{\sqrt{2}(R_B + R_O)}$$

Equation 2.7

Where t is the Goldschmidt tolerance factor, R_A is the radius of the A cation, R_B is the radius of the B cation, and R_O is the radius of oxygen, with an ideal perovskite occurring when t=1. If t is greater than one, the structure is likely to be hexagonal or tetragonal. If it is between 0.9 and 1, the structure is likely to be cubic. If it is between 0.71 and 0.9, the structure is likely to be orthorhombic or rhombohedral. If it is less than 0.71, the structure is likely to be different[24]. Quite commonly, ferroelectric materials with high permittivity values have a $t>1$[25].

2.3.4 Ferroelectric Materials

As mentioned previously, ferroelectric ceramics can display high permittivity and are often used as the dielectric in capacitors. Therefore, we need to understand what ferroelectric materials are in a little detail. Ferroelectrics have 3 defining features that distinguish them from ordinary dielectrics: (a) extremely high permittivities (several thousand[26], can be greater than 20000[27]), (b) possibility of retention of polarisation once the field has been removed, and (c) application of an applied reverse voltage reverses the polarisation[28].

As mentioned previously, a dielectric is a material that can undergo polarisation in the presence of an electric field. However, some dielectrics can undergo polarisation even in the absence of an external electric field. This is known as spontaneous polarisation and occurs mainly due to the atomic structure of the dielectric. To minimise the total energy of the system, the polar axes of individual unit cells can align in some directions. When several groups of unit cells align in the same direction, they form ferroelectric domains[29] as seen in Figure 2.6. The orientation of these domains depends upon the crystal structure of the material. Tetragonal structures possess 6 possible directions (parallel to the cube edge). Rhombohedral possesses 8 (parallel to body diagonal), and orthorhombic possesses 12 (parallel to face edge)[30]. Ferroelectrics are those materials which contain at least two orientations of spontaneous polarisation[31].

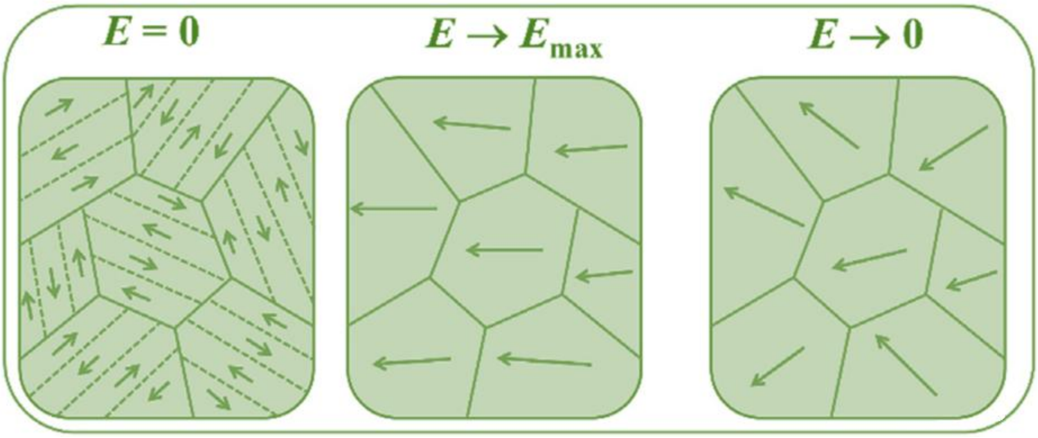

Figure 2.6: Schematic diagram showing the domain structure present in ferroelectrics, showing how the domains behave in the presence of a field ($E \to E_{max}$) and the configuration after the electric field is removed. The solid lines represent grain boundaries, and the dotted lines represent ferroelectric domain walls[32]*(reproduced with permission).*

As seen in Figure 2.7 in the presence of an electric field, ferroelectrics experience a sharp increase in polarisation as the field is increased. However, as this field is removed, they do not experience an instantaneous loss in polarisation. As the electric field is gradually amplified from zero, the total polarisation within the crystal also increases. This happens as the polarisations within various dipolar regions become aligned. Eventually, a saturation point is reached where any further increase in polarisation (P) is only due to the material's relative permittivity. The slope of the $P = E$ curve for a linear dielectric equals its permittivity. If you extrapolate this line back to the y-axis, you get the saturation value of the Spontaneous Polarisation (P_S).

When the field is reduced to zero, a remanent polarisation (P_R) remains, which is typically slightly less than P_S. Applying a negative field decreases the polarisation until it reaches zero at the coercive field (E_c). Further increasing the negative field eventually leads to a reverse saturation polarisation (P_S). When the field returns to zero, the crystal has a negative remnant polarisation (P r). Increasing the field again raises the polarisation from P_R to zero at E_C, and then to P_S, completing the ferroelectric hysteresis loop.

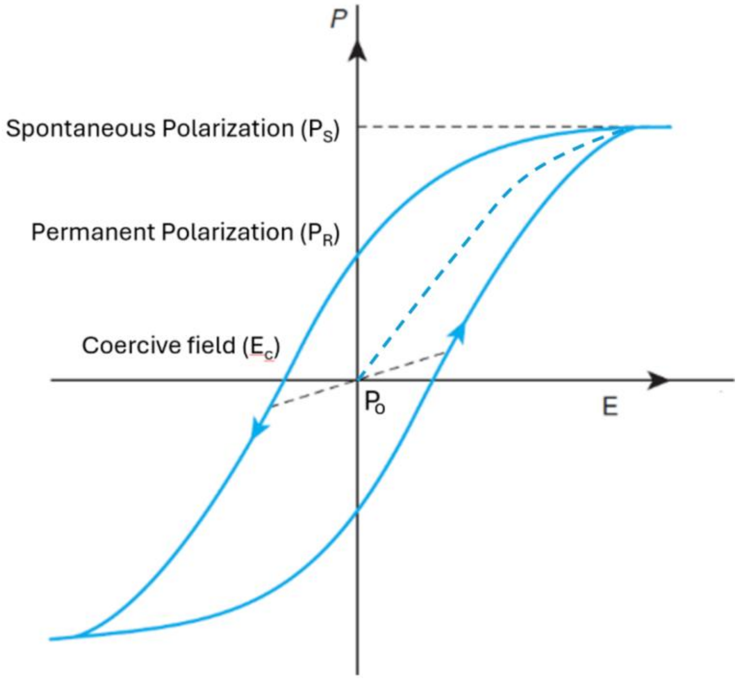

Figure 2.7: Hysteresis loop as seen in ferroelectric materials, where the dashed line passing through the origin represents the behaviour of standard dielectrics.

Ferroelectric capacitors operate in two primary modes, each exhibiting distinct field-dependent behaviours that are intrinsically linked to their hysteresis characteristics. In charge storage applications, the capacitor is cycled between zero and high electric fields without a DC bias, which is typical for energy storage scenarios. During the first cycle of a virgin material, the polarisation undergoes significant irreversible domain switching, resulting in a large initial permittivity due to extensive domain wall motion. This first cycle follows the major hysteresis loop, characterised by high remanent polarisation (P_r) and coercive field (E_C). However, subsequent cycles exhibit a stabilised domain configuration, leading to a narrower hysteresis loop with reduced permittivity and lower energy loss. At high fields, the permittivity becomes dominated by nonlinear saturation effects, where further domain switching is limited.

In contrast, signal conditioning applications involve the use of a small oscillating AC field, often superimposed on a DC bias, as seen in tunable filters or passive components. Here, the DC bias shifts the operating point along the hysteresis curve, suppressing domain switching and linearising the response to small AC perturbations. The effective permittivity (ε_{eff}) decreases with increasing DC bias, as fewer domains contribute to polarisation changes under these stabilised conditions. Unlike the charge storage mode, AC cycling under bias does not significantly alter the domain structure, resulting in a stable permittivity over time. The small AC fields induce reversible polarisation changes along minor loops, avoiding the major domain reorientation seen in charge storage.

The behaviour of the material differs markedly between the first cycle and subsequent cycles. The virgin material, during its first cycle, exhibits a large permittivity and a wide hysteresis loop due to irreversible domain switching, accompanied by high losses. After repeated cycling, the material becomes "trained," with domains settling into lower-energy configurations. This leads to a reduction and stabilisation of permittivity, along with a narrower hysteresis loop and diminished losses. However, this trained state also reduces the material's tunability, which is a critical consideration for applications requiring dynamic response.

These operational differences have important practical implications. For charge storage, the evolution of permittivity and losses during the first cycles must be accounted for in lifetime and performance predictions. In signal conditioning, the DC bias stabilises the permittivity but at the cost of reduced tunability, necessitating careful control of AC field amplitudes to avoid re-entering the nonlinear hysteresis regime. Understanding these modes is essential for optimising ferroelectric materials for specific applications, whether in energy storage, where high permittivity and controlled losses are desired, or in signal processing, where stability and linearity under bias are paramount.

2.4 Multi-Layer Ceramic Capacitors (MLCCs)

After understanding some of the basics behind capacitors, we can now finally start the discussion about MLCCs. MLCCs are like parallel plate capacitors, however, instead of consisting of just two plates with a dielectric, they are comprised of several alternating layers of a dielectric ceramic (like BT) and electrodes, as seen in Figure 2.8. The capacitance of an MLCC is calculated as follows:

$$C = \frac{\epsilon_r \epsilon_0 A}{d} \times (n - 1)$$

Equation 2.8

Where C is the Capacitance (typically measured in pF or µF in MLCCs), ϵ_r is its relative permittivity, ϵ_0 is 8.8542×10^{-12} F/m, which is the permittivity of free space, A is the area of the plates, d is the plate separation and n is the number of layers (which can be several hundred in MLCCs).

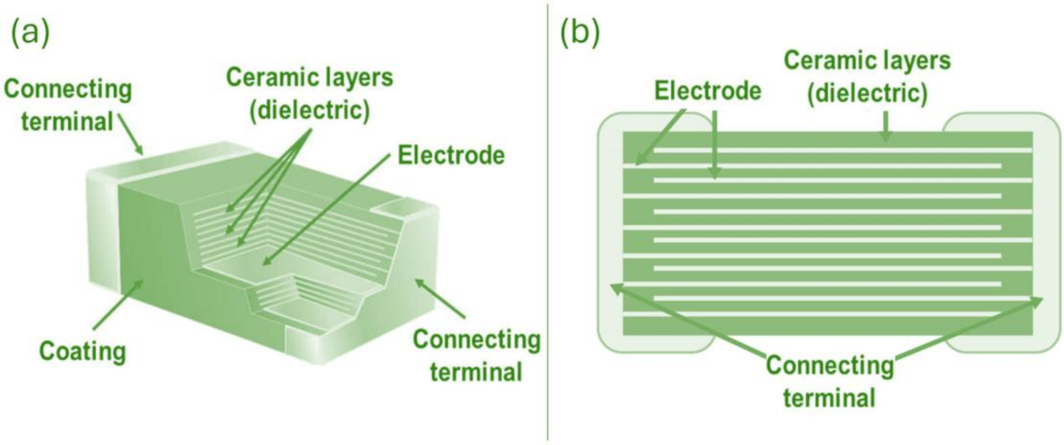

Figure 2.8: Schematic of an MLCC showing the multiple parallel ceramic layers separating the conductive electrodes and capped with the connecting terminal [33]

2.4.1 Classification

MLCCs are typically classified into three categories, class 1, 2 or 3. Class 1 capacitors exhibit high stability across a wide range of conditions. They are typically made of Paraelectrics like Calcium Zirconate and have lower capacitance (6-200) than class 2 capacitors[27]. They come with the benefit of minimum drift in capacitance for voltage, temperature, and frequency[34]. Some examples of materials that belong to this class are porcelain and mica[14].

Compared to class 1 capacitors, class 2 capacitors are significantly more compact at equal rated voltages. Additionally, class 2 capacitors have significantly higher permittivity in the range of 200-20000[27,35]. However, this high permittivity comes with a drawback of variation in capacitance over temperature and voltage. Table 1 shows the naming convention for typical class two capacitors. The first letter represents the lower end of the temperature range for the capacitor, the second represents the upper end of the temperature range, and the final letter represents the capacitance change over this temperature range. MLCCs can be subjected to harsh conditions such as working temperatures over 130 °C when used in the Engine control unit or the anti-lock brake system[36]. These would require the use of X8R class capacitors, which will have a variance of the capacitance of ±15% (as compared to its room temperature value) for a temperature range of between -30°C and 150°C.

Table 2.1: Naming convention for class 2 and 3 capacitors.

First letter	**Lower temperature use rating (°C)**	**Middle digit**	**Upper temperature use rating (°C)**	**Last letter**	**Maximum Capacitance shift from 25 °C value (%)**
X	-55	**2**	+45	**A**	+/- 1
Y	-30	**4**	+65	**B**	+/- 1.5
Z	10	**5**	+85	**C**	+/- 2.2
		6	+105	**D**	+/- 3.3
		7	+125	**E**	+/- 4.7
		8	+150	**F**	+/- 7.5
		9	+200	**P**	+/- 10.0
				R	+/- 15.0
				S	+/- 22.0
				T	+22/-33
				U	+22/-56
				V	+22/-82

2.4.2 Fabrication

Pan and Randall[14] outline a general fabrication process for capacitors. Their method involves the use of a homogenous solution of a dielectric powder mixed with solvents, dispersant, binder, and plasticisers. This is then cast into a thin sheet and subsequently dried to form a tape. Screen printing is then used to apply an electrode paste to the tape, which is then stacked in layers. Nickel is typically the principal metal used for the internal electrodes[37]. These are then cut/diced and undergo binder burnout to remove the organics. The dimensions of the dielectric blocks in the stack can be cut to specific sizes such as 1.0 mm × 0.5 mm, 1.6 mm × 0.8 mm, or any other designated chip size[37]. This is then sintered at a temperature of 1000- 1300°C into a dense body of fused dielectric tape and electrodes, after which metal terminations are added to the exposed electrodes to allow for electrical connections. If nickel is used for the electrodes, the paste used will be made of copper, and the chips are then baked at a temperature of about 800°C. Finally, a layer of nickel and a layer of tin are plated onto their surfaces by electrolytic plating. The tin helps facilitate solder mounting, while the nickel assists with improving the reliability. The schematic for this process is seen in Figure 2.9.

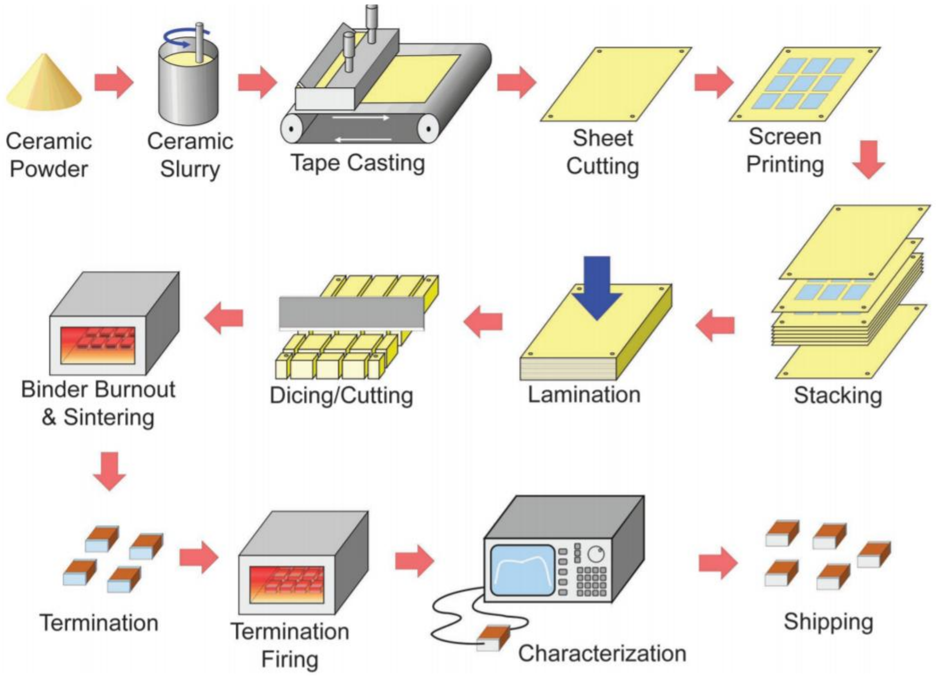

Figure 2.9: A schematic illustrating the process of transforming ceramic powder into MLCCs, ready for shipping, detailing stages from slurry preparation to final characterisation and packaging.[14]*(reproduced with permission)*

2.5 Temperature coefficient of capacitance (TCC)

Ferroelectrics such as barium titanate have high permittivity but low-temperature stability for their capacitance. This temperature variation is measured by the TCC%, which is calculated as

$$TCC\% = \frac{\epsilon_T - \epsilon_{25}}{\epsilon_{25}} \times 100$$

Equation 2.9

ϵ_{25} = Permittivity at room temperature

ϵ_T = Permittivity at reference temperature

For barium titanate, close to its Curie temperature T_c (approximately 120°C), there is a sharp increase in its relative permittivity from 1700 to about 10000 (as seen in Figure 2.10). This leads to a massive increase in the capacitance of over 450 % over the working temperature range. Industry standards typically tolerate a maximum change in capacitance of ~80% for class 3 capacitors, so this increase is unacceptable. To improve its TCC, barium titanate is usually doped with rare earth materials, which will be discussed in detail in a later section.

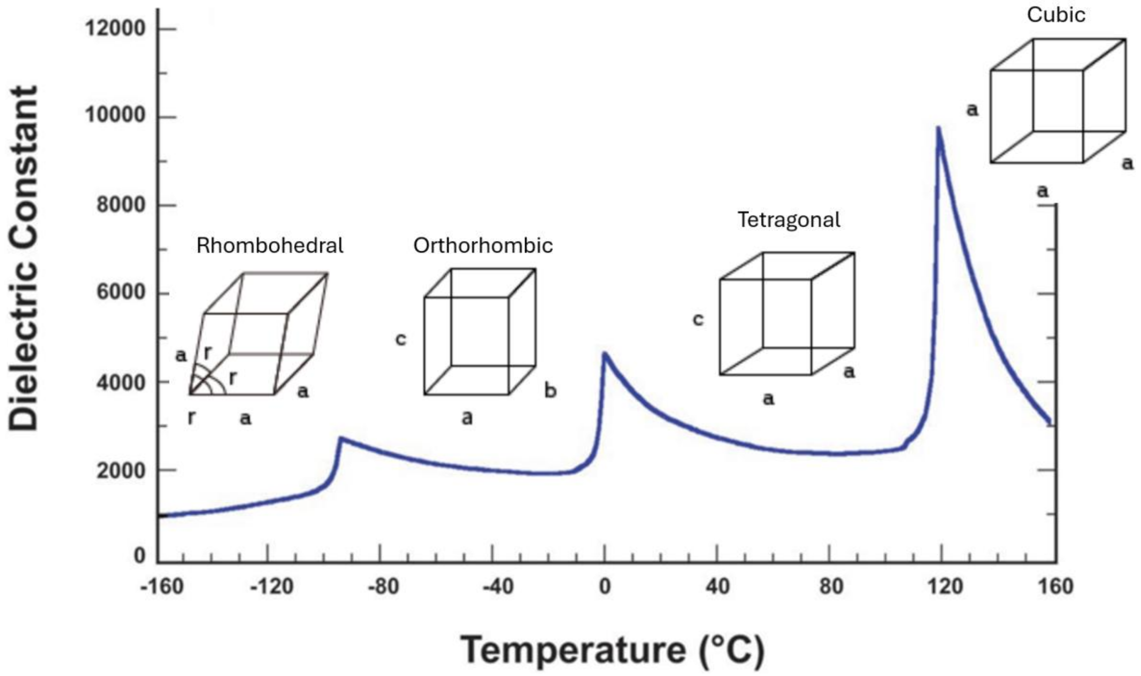

Figure 2.10: Change in relative permittivity of Barium titanate as temperature is increased. Inset images show the change in structure from rhombohedral to cubic as temperature is increased.

2.5.1 Voltage coefficient of capacitance (VCC)

Extensive research has focused on enhancing the dielectric properties of barium titanate and doped barium titanate by modifying their physical characteristics and composition. However, one often overlooked aspect is the impact of the Voltage Coefficient of Capacitance (VCC). Although not mandated by standards, considering VCC is crucial when evaluating capacitors.

VCC is typically observed in class 2 (as seen in Figure 2.11) and class 3 Multilayer Ceramic Capacitors (MLCCs). When an applied voltage is present, it leads to a reduction in capacitance. This reduction, which can be as high as 90%, is influenced by the MLCC's design and material properties. Additionally, as the applied voltage increases, the reduction intensifies, and the Curie peak shifts toward higher temperatures[38]. The primary cause of this reduction lies in the structure of barium titanate. To mitigate this effect, one must either select a material with low drift or carefully control the voltage to compensate for changes in capacitance [25,39].

The change in VCC can occur due to various factors, such as polarisation reorientation, where the polarisation vectors can reorient under the influence of an external electric field. This reorientation alters the material's overall polarisation and, consequently, its dielectric properties. The extent of this change depends on the energy barriers that must be overcome for the reorientation to occur. Similarly, the movement of domain walls—the boundaries between differently polarised regions—contributes significantly to the field dependence of ferroelectrics. Applying an electric field can facilitate the motion of these walls, thus enhancing the overall polarisation and relative permittivity.

Another factor that can affect the VCC of ferroelectrics is the introduction of dopants. These can modify the lattice structure of ferroelectric materials, which in turn influences their tunability. Doping can create additional charge carriers, alter phase transition temperatures, and modify the domain wall mobility, all of which contribute to its field dependence[40] . Mechanical strain can also be employed to modify the properties of ferroelectric materials. Applying strain can alter the lattice parameters and symmetry of the crystal structure, which in turn affects the polarisation and dielectric response. This method has been widely studied in thin films and heterostructures, where the application of uniaxial or biaxial strain can lead to significant changes in the material's properties[41].

Finally, the dielectric properties of ferroelectric materials are temperature-dependent. As the temperature approaches the phase transition point, the VCC can be modified due to the softening of the lattice and changes in domain dynamics. Understanding the temperature dependence of VCC is crucial for designing materials that operate effectively across varying thermal conditions.

Voltage Coefficient of Capacitance (VCC) is calculated as:

$$VCC(\%) = \frac{\varepsilon_r(\mathrm{V}) - \varepsilon_r(0)}{\varepsilon_r(0)} \times 100$$

Equation 2.10

where ε_r (0) is the relative permittivity at zero DC bias and ε_r(V) is the relative permittivity at applied DC voltage V. To induce domain wall motion thereby generating a net polarization in class 2 MLCCs, an AC voltage between 0.5 V to 1 V is typically applied when measuring the capacitance of a device. Many MLCC applications occur in electrical systems with a DC bias. Sufficiently high DC bias can cause some domains to lock in place, and therefore, the negative voltage will be unable to completely reverse the polarisation direction of the ferroelectric material. Increasing the DC bias can lead to more domains becoming locked as well. Since not all domains are responding to the current, this leads to an overall reduction in the capacitance of the material and is quite commonly observed in class 2 MLCCs.

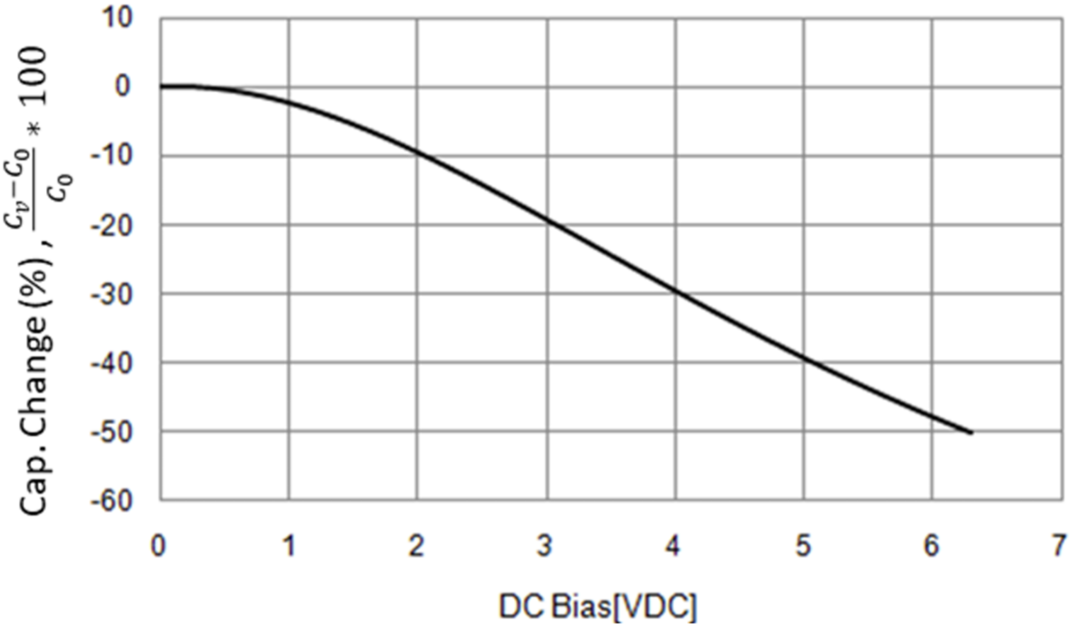

Figure 2.11: The VCC response of a standard class 2 MLCC material shows a reduction in capacitance as the applied DC bias increases. It is common to provide VCC values for MLCCs at a temperature of 25°C.

Phase Field Modeling, Mean Field Modeling, and Johnson's Equation are different approaches used in the study of VCC in Multilayer Ceramic Capacitors (MLCCs). Phase Field Modeling involves a computational approach that considers the evolution of microstructures within materials. This method has been applied to study the internal stress distribution and electrocaloric performance of MLCCs, providing insights into their behaviour under different conditions[42]. On the other hand, Mean Field Modeling focuses on understanding the average behaviour of a system rather than individual interactions. This approach has been utilised to analyse the dielectric behaviours of MLCCs under various operating conditions, shedding light on their overall performance[43,44]. Finally, Johnson's equation, based on the Landau–Ginzburg–Devonshire theory[45] is a widely used mathematical model that describes the dielectric behaviour of MLCCs, while its limitations include the need for experimental data to determine certain material-specific parameters. It remains a valuable tool in the field of MLCC development, which is why it will form the basis for the modeling used in this work. This will be described in more detail in the following chapter.

2.5.1.1 Tunability

The change in dielectric properties of a Ferroelectric in the presence of an electric field is also referred to as tunability. Tunability of ferroelectric can be broadly categorised into two main types, intrinsic and extrinsic. Intrinsic tunability arises from the material's fundamental properties, while extrinsic tunability involves modifications to the material, such as doping, strain engineering, or changing the microstructure. Tunability is often discussed in applications such as microwave voltage tunable devices like varactors or phase shifters[46,47]. Such devices require the use of Paraelectrics, due to their lack of hysteresis, high tunability and a moderate relative permittivity, to name a few factors. Due to their lower permittivities than those required by MLCCs, these will not be explored in more detail within this paper.

2.6 Barium Titanate

In Table 1, it is evident that class 2 capacitors require consistent capacitance across a wide temperature spectrum. Figure 2.12 illustrates various options for high-permittivity materials. However, some of these materials have a Curie temperature (T_c) significantly higher than the standard operating temperatures of a multilayer ceramic capacitor (MLCC), leading to their exclusion. Within the MLCC's standard operating range, PMN-PT ($Pb\ (Mg_1/3Nb_{2/3})\ O_3$–$PbTiO_3$) and barium titanate exhibit the highest permittivity. Barium titanate is preferred over PMN-PT due to its ease of manufacturing and reduced environmental impact[13].

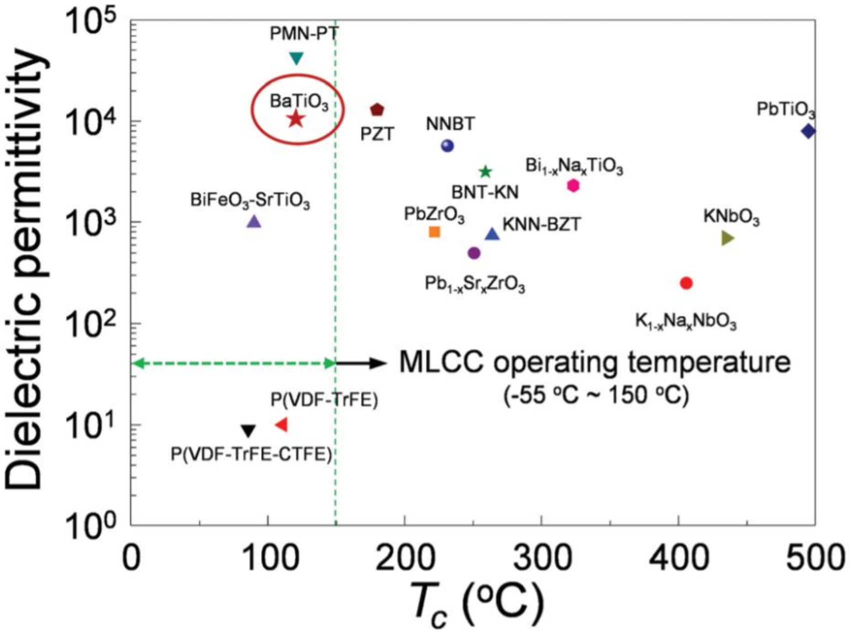

Figure 2.12: Dielectric permittivity vs Curie temperature for several ferroelectric materials 17. *(reproduced with permission)*

Barium Titanate (BT) is a ferroelectric ceramic that is one of the most well-known and widely used ceramics in capacitors. It is among the first commercially used ceramics[48] and is used extensively in the manufacture of MLCCs.

BT possesses a perovskite structure. As seen in Figure 2.13, the B cations, which are generally smaller, are in an octahedral coordination surrounded by 6 X anions, while the larger A cation is in a cubooctahedral formation with the twelve X anions.

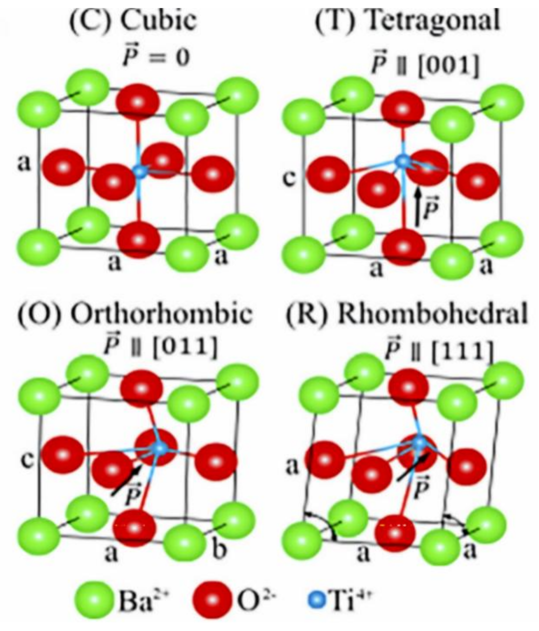

Figure 2.13: The crystal structures and the relative atomic displacements in the $BaTiO_3$ single crystal due to the phase transition.

The crystal structure of BT varies with temperature. At a temperature of 130°, BT is cubic. The symmetry of the cubic structure leads to a lack of a dipole moment, and therefore, cubic BT is paraelectric. Paraelectric materials can undergo polarisation even with the lack of a dipole moment, however, they do not undergo hysteresis loops. Most ferroelectrics turn paraelectric when heated to a certain temperature, which differs based on the material. This temperature is known as the Curie temperature T_c.

In BT, the A-site cation is larger than the ideal case, with t=1.06. At temperatures greater than 120 °C, the B-site cation (Ti4+) is positioned at the centre of the BO_6 octahedron, which results in BT having a cubic and paraelectric structure. Around 120°C, BT shifts from a cubic to a tetragonal structure, extending along the [001] direction. This distortion leads to the B-site cation (Ti^{4+}) moving away from the centre of the unit cell, creating a dipole moment, and making BT ferroelectric.

The direction of the spontaneous polarisation, Ps, is [001], which aligns with the elongated c-axis of the unit cell. The tetragonal structure remains stable until about 5°C, after which BT transforms into an orthorhombic structure ($T_{O\text{-}T}$ = 5°C). Finally, at -90°C it transitions to a rhombohedral structure ($T_{R\text{-}O}$ = -90°C). Each phase transition results in an increase in relative permittivity due to the internal distortions that occur during the phase transition. However, the responses at $T_{R\text{-}O}$ and $T_{O\text{-}C}$ are minor compared to the peak relative permittivity at Tc, with ε_{max} often surpassing 10,000. This rise in relative permittivity leads to a TCC > 450%, which greatly exceeds the requirements for MLCC applications. Therefore, undoped BT is not suitable for Class 2 MLCC applications, and there is a need to reduce the TCC. As the relative permittivity value is affected by grain size, and the temperature value is affected by the degree of chemical heterogeneity, creating a temperature-stable BT material would require controlling both factors simultaneously[49].

The tetragonal, orthorhombic, and rhombohedral phases are all ferroelectric[50] unlike the cubic phase, due to the displacement of the Ti^{4+} ions from their centrosymmetric position. The presence of this net dipole moment is why BT undergoes spontaneous polarisation[31].

BT, in its standard state, possesses zero overall polarisation due to the random configuration of its domains. However, in the presence of an electric field, the domain walls may switch either reversibly or irreversibly. Thus, not all domain walls switch back upon reduction of the field, which leads to the formation of a hysteresis loop.

In order to effectively modify BT to fit the required TCC profiles, several factors such as the Grain size, dopant concentrations, applied electric field, volume fraction of the core and shell materials, and dielectric layer thicknesses[51–60] need to be controlled. By carefully modifying these factors through an intensive trial and error process, TCC can be controlled over a wide temperature range to meet industrial requirements[61–63].

2.6.1 Doping

As seen in Figure 2.10, as temperature increases, there is a large increase in TCC of greater than 450%. Due to this, only BT in its pure form cannot be used in the fabrication of MLCCs. To solve this issue, BT is often doped with additives in order to improve its TCC.

Doping involves introducing ions into the crystal lattice of barium titanate. These elements alter the material's properties by creating defects in the crystal structure. The other factor that is taken into consideration for doping is the size of the ion. Size compatibility is crucial for maintaining a similar atomic structure. Two common types of doping are aliovalent and isovalent. Aliovalent Doping involves using ions with a different charge than the parent ions (Ba^{2+} and Ti^{4+}), while Isovalent Doping uses ions with the same charge as the parent ions.

During the addition of solute elements in BT, an inhomogeneous microstructure is formed during sintering, characterised as a core-shell structure. The core consists of pure barium titanate, while the shell surrounds the core and is made of doped barium titanate. Doped barium titanate typically has a lower TCC than pure barium titanate[36,64]. As TCC measures how capacitance changes with temperature by carefully controlling the core-shell structure, the dielectric behaviour can be stabilised over the working temperature range.

Barium titanate, as mentioned previously, exhibits interesting properties due to its ability to switch polarisation under an applied electric field. However, its capacitance can be influenced by temperature changes. To stabilise its capacitance over a working temperature range, a heterogenous microstructure of doped barium titanate is employed, leading to the production of a lower TCC over the working range of temperatures. Due to the doping process, a core-shell microstructure is formed. In this structure, pure barium titanate is coated with doped barium titanate. This is often done by first producing undoped BT grains and then milling them within a liquid which contains the chemical dopants[65,66].

Doping in barium titanate was initially fueled by the change in MLCC electrodes from noble metals like platinum (Pt) or palladium (Pd) to base metals like nickel (Ni), iron (Fe) and cobalt

(Co). This shift was brought about due to the need to develop cheaper MLCCs as their usage increased. Noble metals were able to be fired in an oxidative atmosphere, unlike the base metals. Therefore, the use of base metals as electrodes added the need for maintaining a reducing atmosphere during sintering to prevent their oxidation. This reducing atmosphere led to the generation of defects in the form of ionised oxygen vacancies in the barium titanate layer [13,67], which in turn leads to the generation of a free conduction electron, which causes high electronic conductivity in the dielectric layer. To solve this issue, several strategies were considered, out of which doping was found to be the most efficient solution. Doping with acceptors forms point defects which can trap the free electrons, thereby leading to the formation of highly insulating dielectric materials in a reducing environment. Rare earth elements like yttrium (Y) and dysprosium (Dy) are commonly used as dopants. They improve TCC and enhance ceramic stability[68–70].

The incorporation of dopants significantly influences various material characteristics, including microstructure, Curie temperature (Tc), tetragonality, and defect generation. When skilfully controlled, dopants can broaden the temperature-permittivity profile beyond what is achievable with undoped barium titanate. By adjusting properties and the volume ratios of the core-shell structure through specialised processing techniques, the temperature coefficient of capacitance (TCC) can be efficiently tailored to meet industry standards and specific requirements. However, the current approach for determining optimal formulations relies on an iterative experimental method, which is both time-consuming and labour-intensive.

2.6.2 Multi-layered dielectrics

An alternative method of improving the TCC is by using bi-layer or multi-layer materials, as opposed to single-layer parallel configurations, i.e. instead of using several layers of a single dielectric, they use more than one dielectric in the MLCC. This is done to combine their electrical properties. It has been shown that by combining undoped $BaTiO_3$ and $BaTi_{1-x}Zr_xO_3$, where x is increased from a value of 0.05 to 0.15, when the difference in Zr-content was increased between adjacent layers, the relative permittivity profiles no longer followed the expected permittivity-temperature profiles of the two individual materials[71]. This was attributed to the diffusion of Zr at the interface between layers. This demonstrated that a multi-layered stack can be used to modify the TCC properties of the MLCC.

As the selection process for the materials, as mentioned previously, can be very labour and time intensive, to expand the range of material options and enhance the efficiency of the selection process, it becomes essential to devise a method for swiftly generating formulations based on desired properties. In response to this need, Kerridge et al.[1] introduced an innovative analytical approach. Their method utilises experimental electric field data from bulk ceramics to identify optimal formulations for multilayer ceramic capacitors (MLCCs). By collecting data on nine different barium titanate compositions, they constructed contour maps related to the temperature coefficient of capacitance (TCC). An algorithm was then employed to determine favourable combinations of single, binary, or ternary systems that meet the specific formulation requirements for MLCCs.

However, while this method offers a quicker initial assessment and is not constrained by the number of materials it can compare, it overlooks certain factors influencing dielectric properties. Notably, the impact of electric field and voltage effects at the considered layer thicknesses remains unaccounted for. Developing an analytical approach to address these effects would enhance the reliability and quality of the results.

2.6.3 Grain size

The dielectric properties exhibit significant variation with decreasing grain size, depending on the atomic structure. While the change is negligible in the cubic phase, it becomes more pronounced in the tetragonal state. Hoshina et al[72] fabricated high-density ceramics with µm and nanometre sized grains by using a two-step sintering method as well as an aerosol deposition method (AD), respectively. The two-step method involved using BT powder of an average particle size of 100nm, which was then isostatically compressed at 200MPa at 20 °C. The green compacts were heated to T1 = 1320-1380°C at 5-25°C/min and then immediately cooled to various lower temperatures (T2 = 1100-1380°C) at 30°C/min. The ceramics were isothermally sintered for 10 hours. This method resulted in the generation of BT ceramics with grain sizes in the 0.6-0.13 µm range. The AD method, on the other hand, utilised BT having an average particle size of 500 nm to prepare AD thick films. These were then heated to 600 °C at 300°C/h, which resulted in the generation of BT thick films, which were then reannealed at 800-1250°C for 1h to control their grain size. This resulted in the generation of BT having grain sizes from 20 to 830nm. Using these, they were able to show that as the grain size decreases, the relative permittivity increases up to a size of 1 µm. Beyond this threshold, there is a notable decrease, as depicted in Figure 2.14. This increase in relative permittivity is attributed to a superposition effect between grain boundary and domain wall effects[18]. Interestingly, the relative permittivity of the remaining phases (Orthorhombic and rhombohedral) shows a stronger dependence on temperature rather than grain size[73].

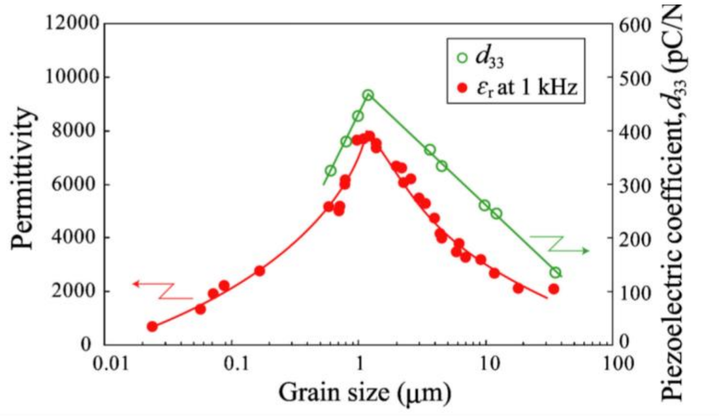

Figure 2.14: Change in relative permittivity and piezoelectric coefficient of barium titanate with grain size [72]

Additionally, the dielectric properties exhibit voltage dependence, which becomes a concern due to the presence of a sufficiently high electric field resulting from reduced size. Padurariu et al. manufactured several BT dielectrics having grain sizes ranging from 100 to 5000 nm from ultrafine powders having a particle size of about 15nm by sintering by spark plasma sintering at temperatures varying from 1050-1250°C for 3 min. After sintering, the ceramics were annealed in air at 800°C for 2 h to release the stresses and reduce the oxygen vacancies caused by the reducing atmosphere of the SPS processing. The DC-field dependence of relative permittivity ε(E) at room temperature was then determined. It was noted that as the grain size of barium titanate decreases, there is a pronounced reduction in its relative permittivity, as seen in Figure 2.15. Furthermore, the relative permittivity versus field dependence tends to linearise with decreasing grain size[74]. Interestingly, an observable sharp decrease in relative permittivity occurs as the applied voltage increases.

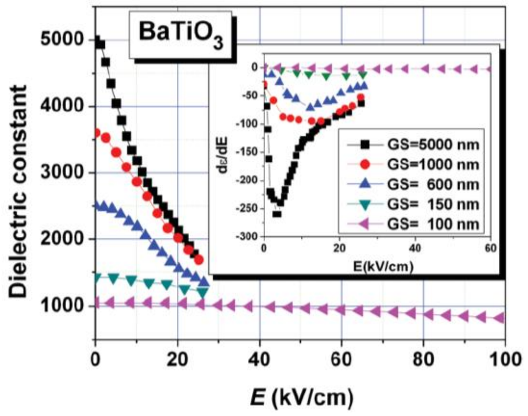

Figure 2.15: Field dependence of the relative permittivity with varying grain sizes in barium titanate[74] (reproduced with permission).

2.6.4 Particle Size

With the miniaturisation of electronics, MLCCs have been losing area on the circuit board. To keep capacitance at the same levels with this reduction in area, the thickness of a layer of dielectric has been reduced to 1 µm and is still decreasing. To create dielectric layers thinner than a µm, it is necessary to use fine powders with particle sizes below 300 nm[75]. High quality BT single crystal particles were generated by using a two-step decomposition method of barium titanyl oxalate[72]. Figure 2.16 illustrates that the permittivity of barium titanate is influenced by particle size. A particle size of 140 nm exhibits the highest permittivity. This variation in permittivity based on particle size can be understood by examining the structure of a barium titanate particle.

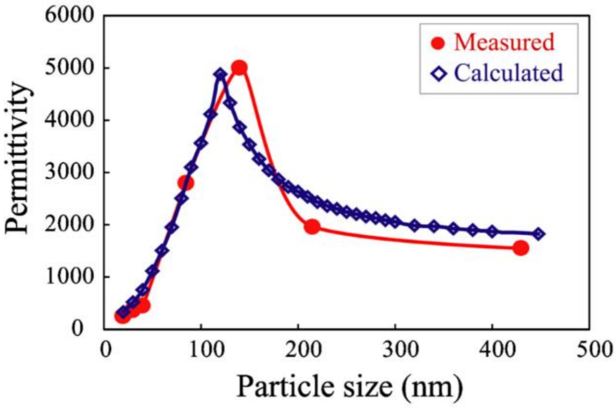

Figure 2.16: Permittivity change of barium titanate based on particle size [76]

According to Hoshina[72], a particle of barium titanate typically consists of three distinct parts, as depicted in Figure 2.17. These components include:

1. Inner Core: This region possesses a tetragonal crystal structure.
2. Surface Layer: Comprising a cubic crystal structure.
3. Gradient Lattice Strain Layer (GLSL): Located between the inner core and surface layer.

Unlike the ferroelectric tetragonal inner layer, the GLSL structure exhibits only minor ferroelectric properties. The particle's dielectric behaviour strongly depends on the volume fractions of each of these layers. As particle size increases, the thickness of the inner core and the GLSL also grow. Interestingly, the surface layer maintains a nearly constant thickness of 15-20 nanometres. For larger particle sizes, the inner layers contribute significantly to the particle's dielectric properties. However, beyond 140 nanometres, the GLSL layer grows faster than the core, resulting in a dominant effect on permittivity reduction. Conversely, when particle size decreases, the paraelectric surface layer's contribution becomes more pronounced, leading to lower permittivity values.

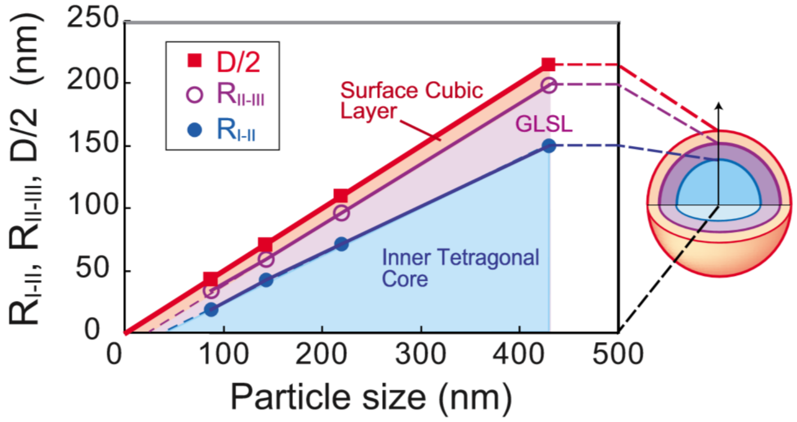

Figure 2.17: Change in thicknesses of layers with particle size [72]

2.7 Modeling Approaches

As mentioned previously, Phase Field Modeling, Mean Field Modeling, and Johnson's Equation are different approaches utilised in the study of VCC in Multilayer Ceramic Capacitors (MLCCs).

2.7.1 Phase field modeling

Phase field modeling is a popular computational technique rooted in the principles of minimising the total free energy of a system, allowing for the simulation of phase transformations, defect interactions, and microstructure development utilised to predict the evolution of the microstructure[77]. Unlike traditional mean field models, phase field modeling captures the details of interfacial dynamics and spatio-temporal patterns, providing invaluable insights into the fabrication processes and performance of MLCCs. By accurately modeling the nucleation, growth, and coarsening of various phases, this technique offers significant advantages over conventional methods, enabling researchers to optimise processing parameters, predict material behaviour, and design novel MLCC compositions with enhanced dielectric properties and reliability.

In ferroelectric systems, phase field models are derived from the Landau-Ginzburg-Devonshire theory. By numerically solving these equations, the evolving microstructure of the material can be determined. For example, Wang et al. applied a phase-field framework to investigate polarization reversal in ferroelectrics under external electric or stress fields, replicating key macroscopic behaviours such as polarization-strain hysteresis under varying electric fields[78]. In a related advancement[79], they also introduced a computational technique optimised for high-accuracy electrostatic field analysis in 3D microstructural configurations. Phase-field models have been widely used to study domain structures in ferroelectric materials and polarisation switching under an electric field[80–82].

Despite their numerous uses in the field of ferroelectrics, they haven't been used for the modeling of the VCC effect in dielectrics. This could be for a variety of reasons. Phase field models often use a sharp interface approximation, which models interfaces as two-dimensional surfaces, which may not capture the complexity of the real-world system[83]. It can also be computationally intensive. They also assume homogeneity, which would not work to accurately model VCC.

2.7.2 Mean field modeling

Mean field modeling utilises the principles of statistical mechanics, enabling researchers to explore the collective dynamics of vast numbers of interacting entities by approximating their behaviour through a single, averaged quantity referred to as the mean field. This works by replacing interactions between individual components with an average or molecular field interaction. The inherent advantages of mean field modeling lie in its ability to capture the essence of complex systems while significantly reducing computational demands, making it an invaluable tool for research. By strategically integrating mean field approximations, the intricacies of ferroelectric domains, grain boundaries, and defect structures within MLCCs and the underlying mechanisms that govern their electrical performance and reliability can be studied.

In a mean field model, the dielectric coefficient is treated as an average value that represents the collective response of the constituents of the material. This method would be feasible for meso and macro-scale dielectrics. However, in micro-scale dielectrics, as we have seen previously, the material can no longer be treated as a whole and would have to be modelled as individual parts to get an accurate representation of VCC.

2.8 Johnson's Equation

For barium titanate and other ferroelectrics, relative permittivity variation in the presence of an electric field results from a combination of paraelectric and ferroelectric effects arising from the core-shell microstructure. This behaviour is typically described by Johnson's equation—an approximation of the Landau–Ginzburg–Devonshire theory[84] as an approximation for the paraelectric phase, which successfully fits the tunability data of barium titanate[85,86].

In Johnson's approximation, only the perovskite-type structure in the paraelectric state is considered, where there are no hysteresis losses. In Devonshire's approach, the initial assumption was that this structure could be interpreted as a distorted cubic crystal. Assuming zero stress, Gibbs' free energy can be expressed as an expansion in even powers of polarisation, where the coefficients are solely dependent on temperature. He then showed that in the tetragonal and cubic regions, where polarisation is along a fixed axis, the Helmholtz free energy F simplifies to

$$F(P,T)=F(O,T)+A(T-\theta)P^2+BP^4+CP^6$$

Equation 2.11

where T is the temperature, P is the polarisation, and θ is the Curie temperature. Above the Curie temperature in the paraelectric state, where the relative permittivity k follows a Curie-Weiss law $4\pi/2A(T-\theta)$, we may compute the relative permittivity as a function of P as follows:

Since k>>1, we may write

$$\frac{E}{P}=\frac{4\pi}{k-1}\approx\frac{4\pi}{k},$$

Equation 2.12

$$\frac{\partial F}{\partial P}=E,$$

Equation 2.13

$$\frac{4\pi}{k}=2A(T-\theta)+4BP^3+6CP^5+\ldots.$$

Equation 2.14

the incremental permittivity ϵ' is given by:

$$\epsilon'=\frac{\partial D}{\partial E}=\frac{\partial(kE)}{\partial E}$$

Equation 2.15

Which reduces equation 2.14 to:

$$\frac{4\pi}{\epsilon'}=2A(T-\theta)+12BP^2+\ldots.$$

Equation 2.16

In the case of small fields, terms of P^4 or higher can be ignored. Substituting equation 2.11 in the above, we get:

$$\frac{4\pi}{k} = 2A(T - \theta) + [\frac{4Bk^2E^2}{(4\pi)^2}]$$

Equation 2.17

Holding k constant and varying only E and T, we have

$$\Delta T = \frac{(2BE^2k^2)}{A(4\pi)^2}$$

Equation 2.18

Similarly, since holding k constant is equivalent to holding ϵ' constant, we get:

$$\Delta T = \frac{(6B\epsilon'^2k^2)}{A(4\pi)^2}$$

Equation 2.19

This equation was verified over a large temperature and frequency range using incremental permittivity. Therefore, equation 2.16 becomes:

$$\frac{4\pi}{\epsilon'} = 2A(T - \theta) + [\frac{12B\epsilon'^2E^2}{(4\pi)^2}]$$

Equation 2.20

Assuming constant temperature, we get:

$$\frac{1}{\epsilon'} = \frac{1}{\epsilon_0} + [\frac{12B\epsilon'^2E^2}{(4\pi)^3m}]$$

Where $\epsilon_0 = \frac{1}{2A(T-\theta)}$.

Equation 2.21

This can be expressed in a more convenient form as:

$$\frac{\epsilon'}{\epsilon_0} = \frac{[1 - \frac{\epsilon'}{\epsilon_0} + \frac{\epsilon'^3}{\epsilon_0^3}]^{\frac{1}{3}}}{[1 + \alpha\epsilon_0^3E^2]^{\frac{1}{3}}}$$

Equation 2.22

Where α= $\frac{12B}{(4\pi)^3}$

For all values of $\frac{\epsilon'}{\epsilon_0}$ it deviates from one by only 15% at $\frac{\epsilon'}{\epsilon_0} = 0.5$. Therefore, we can assume the numerator to be zero, which gives us:

$$\frac{\epsilon'}{\epsilon_0} = \frac{1}{[1+\alpha\epsilon_0^3 E^2]^{\frac{1}{3}}}$$

Equation 2.23

This can finally be written as:

$$\epsilon(E) = \frac{\epsilon(0)}{(1+\beta(\epsilon_0\epsilon_r)^3 E^2)^{\frac{1}{3}}}$$

Equation 2.24

Where ϵ(E)is the relative permittivity at a field E, ϵ(0) is the relative permittivity at zero field, ϵ_0 is the vacuum permittivity, and β is an anharmonic coefficient also known as Johnson's parameter. The β coefficient of a ceramic sample is determined through fitting to the experimental measurements. The simulated reaction to the empirical data is depicted in Figure 2.18 as documented by Johnson et al. for the $Ba_{0.6}Sr_{0.4}TiO_3$ substance.

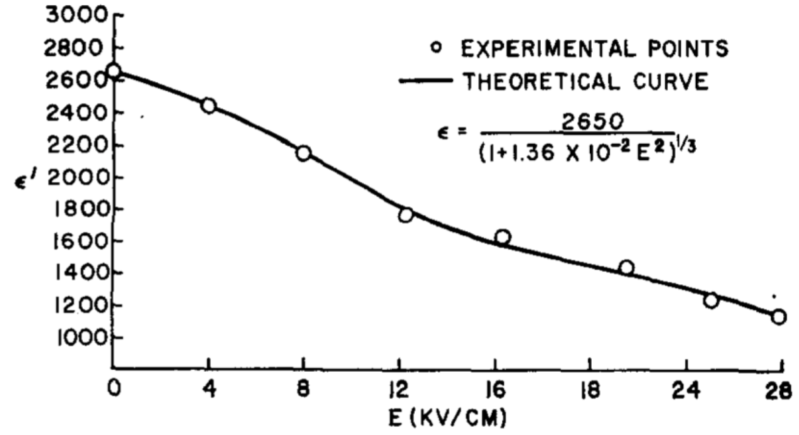

Figure 2.18: The theoretical curve for the change in permittivity response versus field, which closely matches experimental data for $Ba_{0.60}Sr_{0.40}TiO_3$ at a frequency of 3kMc, and T = 26°C, redrawn from Johnson et al.[87]. (reproduced with permission)

However, Johnson's approximation has a few limitations: firstly, it cannot accurately describe the hysteretic behaviour of the dielectric below the Curie temperature, as seen in Figure 2.19. In addition to this, its accuracy diminishes for ultrafine grain sizes[74]. Therefore, when selecting a model, it becomes crucial to account for the material’s inhomogeneous nature and grain boundaries. Additionally, the relative permittivity of barium titanate is directly influenced by its grain size, as previously observed.

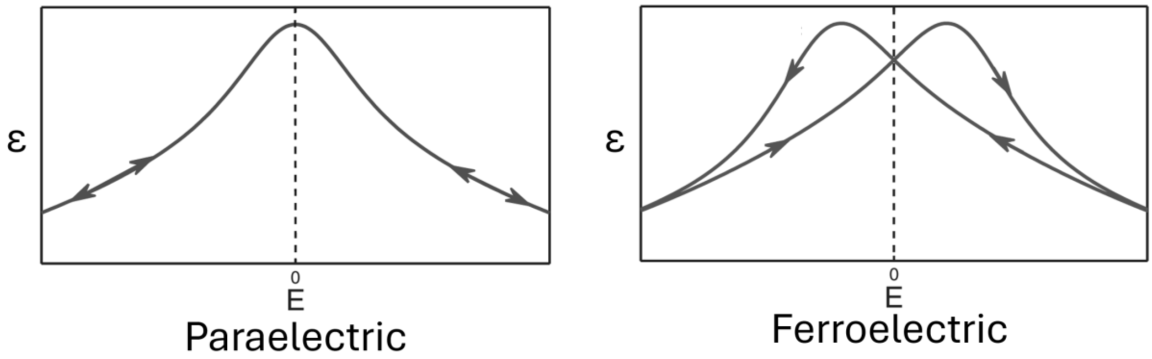

Figure 2.19: Dependence of relative permittivity on the electric field for the paraelectric and the ferroelectric state.

2.8.1 Approaches to study field effects using Johnson’s Equation

To address the challenges within the framework of Johnson’s equation, researchers have explored various strategies. Two strategies employed are through the use of analytical approaches or by modeling approaches. These approaches include incorporating a material-dependent exponent[88] or utilising a coefficient linked to the microstructure[89]. Notably, when barium titanate particles are reduced to a nano size, both relative permittivity and tunability decrease. This reduction is attributed to the growing electrical inhomogeneity as grain size diminishes[74]. In order to choose a method to study field effects, we will first take a look at some of the ways these methods have been employed.

2.8.1.1 Analytical Approaches

Liou et al.[88] studied the field dependence for $Ba_{0:65}Sr_{0:35}TiO_3$ (BST) with various grain sizes in order to determine a correlation between these two. They introduced a bias exponent α and modified Johnson’s equation to

$$\epsilon(E) = \frac{\epsilon(0)}{(1 + BE^2)^{\frac{1-\alpha}{3}}}$$

Equation 2.25

The bias exponent, ranging from values of 0 to 1, was used to represent the order of suppression of the field effect, and B represents the strength of the DC field effect and was assumed to be field independent, as they found no apparent field dependence for these parameters. These values were acquired by fitting via a two parameter least mean square fit. By utilising this method, they were able to obtain an improved fit for the bias equation in the high field and low field regions for fields up to 5000 V/cm, as seen in Figure 2.20.

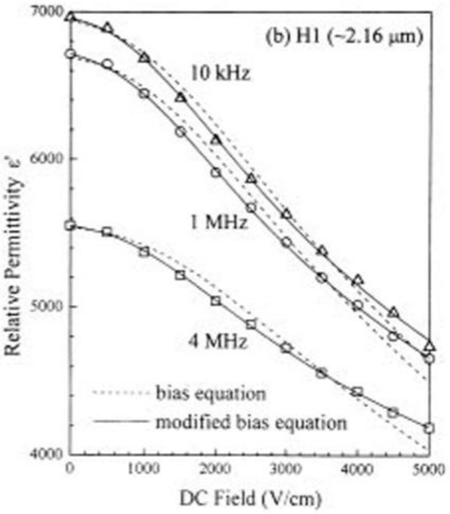

Figure 2.20: The relative permittivity ε’’ as a function of DC field for BST with a grain size of 2.16 μm. The data has been fit to both the original bias equation and a modified version, with the modified equation yielding a more precise fit compared to the original[88].

Ang et al.[90] employed a multi-polarisation mechanism model to analyse the field dependence of $Pb(Zr_{0.52}Ti_{0.48})O_3$ (PZT(52/48)) thin films, spanning from cryogenic temperatures to room temperature and explored both intrinsic and extrinsic contributions to the dielectric response. To account for the extrinsic contribution, they incorporated a Langevin-type polar cluster term into Johnson’s model. However, this Langevin term, which also exhibits a decreasing trend with increasing electric field, fails to fully capture the ferroelectric response. Specifically, it does not account for the initial rise in the relative permittivity associated with domain wall motion occurring below the coercive field and works for a relatively small temperature and electric field range.

Narayanan et al.[91] designed a model which took into account a wider electric field and temperature range by using a microstructure-dependent coefficient instead to try to describe the butterfly-shaped field dependence of the ferroelectric state. They fit the hysteresis behaviour by integrating the coercive electric field E_c as a parameter in Johnson’s formula, as seen in Equation 2.26 to describe the hysteretic behaviour of the relative permittivity.

$$\epsilon(E) = \frac{\epsilon(0)}{(1 + \beta(\epsilon_0\epsilon_r)^3(E \pm E_C)^2)^{\frac{1}{3}}}$$

Equation 2.26

Where $+E_c$ and $-E_c$ correspond to the left and right branches in the ferroelectric state seen in Figure 2.19. They validated their model by fitting model data of $BaTiO_3$, PZT (53/47), and PZT (52/48) and received very good fits (R>0.97) with the reported data for these materials, as seen in Figure 2.21. They additionally note that this data fits irrespective of the residual stress state of the films. Though this method is effective for matching the ε(E) curve theoretically, it does not link to domain structure, domain dynamics, or other nonlinear dielectric measurements.

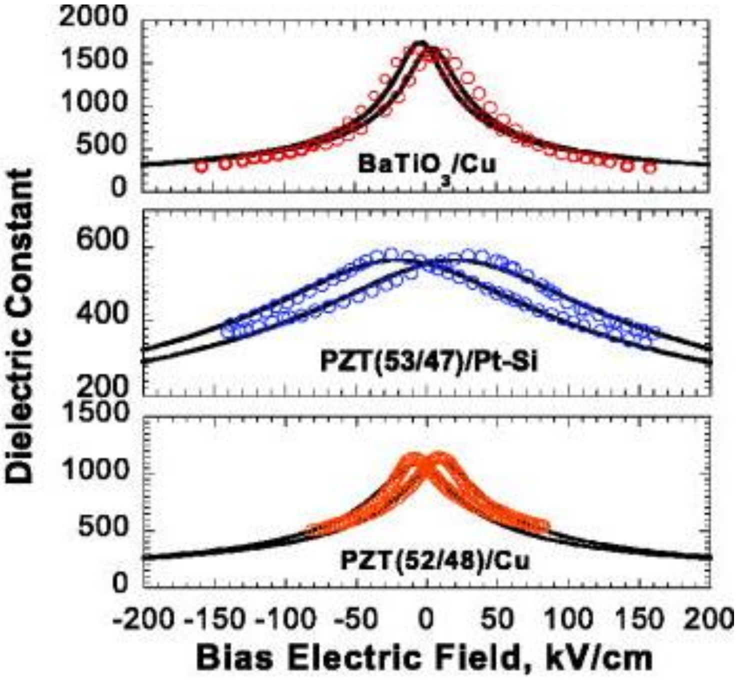

Figure 2.21 Electric Field dependence of dielectric constant for BT, PZT (53/47), and PZT(52/48) thin films on different substrates and fitted using modified-Johnson model by Narayanan et al.[91] (reproduced with permission)

Placeres-Jiménez et al.[92] utilised an alternate approach to describe the field effects on permittivity. They started by assuming that it can be described by the relationship in the equation below for the paraelectric state.

$$\varepsilon(E) = \varepsilon_{00} + \frac{\varepsilon(0)}{\alpha + \beta {E_{eff}}^2}$$

Equation 2.27

Where ε_{00}, α and β are characteristic constants of each material, and E_{eff} represent the effective localised electric field assuming the local field is homogeneous. This method involves breaking down the material into smaller domains and assuming the field across those smaller domains to be homogenous. Applying this method allowed them to isolate the intrinsic and extrinsic contributions to the dielectric response in the presence of high electric fields. Although this model was also effective for modeling field effects, it does not account for changes occurring due to the microstructure of the material.

It is worth noting that VCC data is typically not measured for nanostructured ceramics due to the requirement for permittivity measurements under high electric fields with low thickness[74,93]. Consequently, developing an analytical method to determine this information remains essential.

2.8.1.2 Modeling approaches

A few analytical approaches to further improve Johnson's have been discussed above, however, alternate approaches have also been considered, such as utilising finite element modeling. Using the Finite Element Method (FEM) to determine the field dependence of dielectrics presents several advantages over traditional analytical approaches. One of the primary benefits of FEM is its ability to handle complex geometries and material boundaries that are often encountered in real-world applications. This flexibility allows for a more accurate representation of actual structures, which can be challenging to capture using analytical methods that often assume simpler geometries.

Additionally, many dielectric materials exhibit nonlinear behaviour under varying electric fields. FEM excels in modeling these non-linear responses, as it can easily incorporate complex constitutive relations. In contrast, analytical methods may struggle to account for such intricacies, potentially leading to oversimplified or inaccurate predictions.

FEM also allows for the analysis of localized effects, such as electric field distributions that can vary significantly across a material. This is particularly important in heterogeneous materials or composites, where the interaction between different phases can have a substantial impact on overall behaviour. The capability to visualise electric field distributions and potential contours enhances the understanding of the underlying physical processes, providing insights that might be missed with analytical approaches.

Moreover, FEM can simulate dynamic, time-dependent behaviours, enabling the study of transient responses under changing electric fields. This temporal aspect is often difficult to capture in analytical models, which may focus on steady-state solutions.

By enabling systematic variation of parameters, FEM facilitates sensitivity analysis and optimization, allowing researchers to explore how different factors influence dielectric responses comprehensively. This is particularly useful for validating and refining analytical models, as FEM results can confirm or challenge theoretical predictions.

Finally, computational models can simulate conditions that may be difficult or impossible to achieve experimentally, such as extreme electric fields or temperatures, providing insights into potential material performance. Knowing this, let us take a look at some models that look at the field dependence of dielectrics.

Zhou et al.[94] simulate a model consisting of paraelectric $Ba_{0.60}Sr_{0.40}TiO_3$ (BST 60/40) particles randomly distributed within a linear low-loss dielectric matrix. The polarisation and dielectric response of the inclusions are characterised using a nonlinear thermodynamic model, which is then integrated into a two-dimensional finite element analysis. Their system was composed of a composite thin film of dimensions L and L' consisting of randomly distributed PE BST 60/40 circular particles of diameter D embedded in a linear dielectric matrix with a relative dielectric permittivity of 25, sandwiched between metallic electrodes. This system was analysed for particles having particle sizes of 20, 50, and 80 nm and utilised the Landau-Devonshire seen in equation 1 to describe the phase characteristics. They found that all three composites display a linear dielectric response when the volume fraction is below the percolation threshold. However, once the volume fraction exceeds the percolation threshold, the response increases sharply and nonlinearly in each instance, as seen in Figure 2.22.

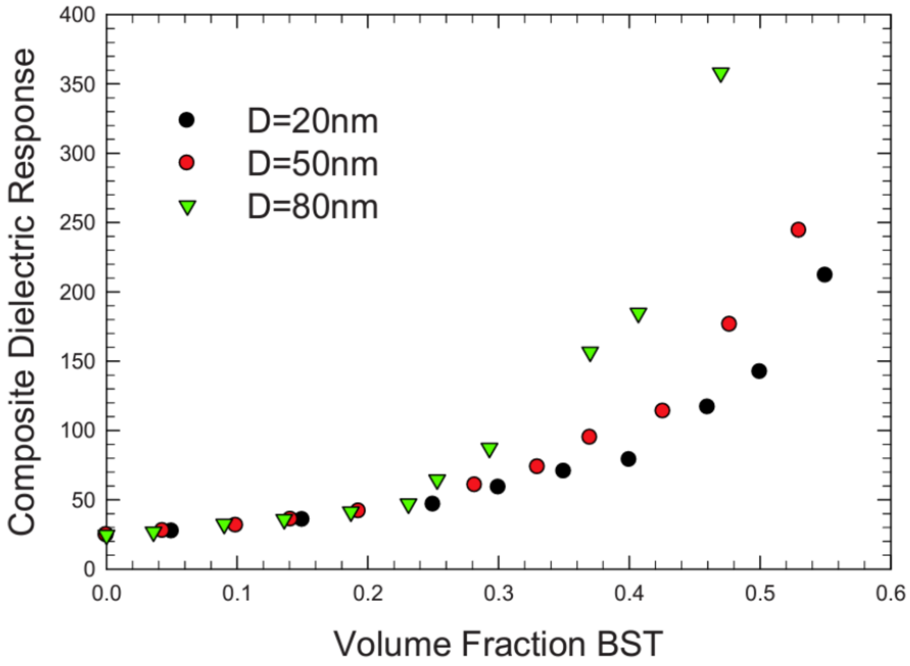

Figure 2.22 Change of the composite small-signal dielectric response as a function of BST volume fraction for different BST having particle sizes of 20nm, 50nm and 80nm. (reproduced with permission)

Similarly, Myroshnychenko et al.[95] also chose to approach the modeling of field dependence by utilising a composite two-phase medium consisting of particles randomly dispersed in a medium. However, in their model, the disks were assigned an impenetrability λ varying from 0 to 1 and were allowed to overlap. Each disk of diameter D is composed of an impenetrable core of diameter λD, and a penetrable shell. As seen in Figure 2.23. This model was selected in order to characterise Johnson's equation for an inhomogeneous microstructure commonly found in composite materials. The effective local permittivity was once again calculated using Johnson's equation, using an iterative process by utilising local fields.

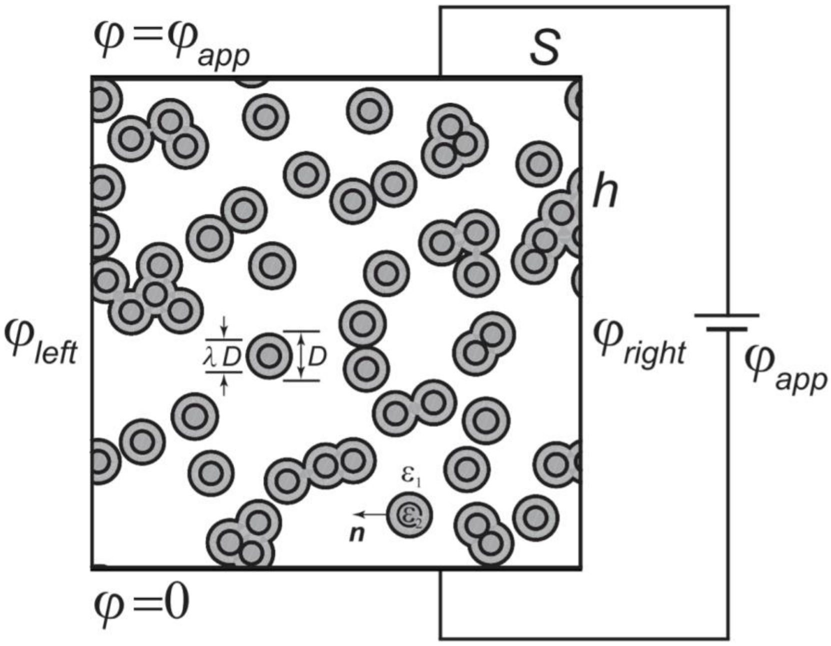

Figure 2.23 Model set -up for Myroshnychenko et al.[95] for a two-phase composite consisting of disks randomly dispersed in a medium having permittivity ε=1 and surface fraction φ1 = 1 − φ2. (reproduced with permission)

The simulations indicate that the geometrical percolation threshold significantly influences the effective permittivity and tunability of the composite, as seen in the simulations carried out by Zhou et al. previously. Below the percolation threshold, there is strong nonlinear behaviour in the field-dependent permittivity, with tunability increasing as the concentration of the dielectric phase rises. Above the threshold, however, the permittivity tends to linearise, leading to a sharp decrease in tunability. This transition explains the observed decline in tunability at intermediate dielectric concentrations in many experimental studies. In contrast, non-percolating structures without disk overlaps show increasing tunability with higher concentrations. The findings suggest that high tunability and reduced permittivity can be achieved at large concentrations, as long as the percolation transition is avoided. The simulations also reveal exceptionally high tunability for composites with impenetrable dielectric disks and even greater tunability in a 2D periodic square array of these disks. Additionally, only porous Paraelectrics and those filled with very low relative permittivity materials exhibit tunability comparable to bulk Paraelectrics.

Although the models generated by both Zhou et al. and Myroshnychenko et al. were able to model field dependence, one of the biggest drawbacks of their models was the fact that it was two-dimensional. 3D FEM models can be employed to describe materials with more complicated configurations and therefore it becomes necessary to develop such a model.

Padurariu et al.[96] developed a finite element model (FEM) that simulates a 2D grain structure. This structure is composed of nonlinear ferroelectric grain cores and paraelectric grain boundaries of varying grain sizes (Single crystal or ∞, 95, 45, and 25 cells). Local electric potentials were described using Poisson's equation, and the permittivity of the ferroelectric grain core was calculated using Johnson's equation without any modifiers. The model's data was then compared with experimental data. Their findings indicate that for single crystals, there is no difference between the local and external field. For larger grain sizes, i.e. 95, the difference between the applied and local electric field is negligible and has properties nearly equal to those of the single crystal. This was attributed to the minor contribution of grain boundaries towards the system, as seen in Figure 2.24f. However, as the grain size diminishes to 45 and 25, the local electric field in the core decreases, leading to an increase in local field inhomogeneity, as illustrated in Figure 2.24. Due to this inhomogeneity, Johnson's approximation, which uses the externally applied field, is insufficient to describe the system's behaviour. This problem can be addressed by using the local field values instead of the externally applied field to calculate the permittivity. While their method provided some valuable insights, a limitation once again is that it is a 2-dimensional model. To achieve more accurate values and a better approximation of field effects at smaller grain sizes, a 3-dimensional model needs to be developed.

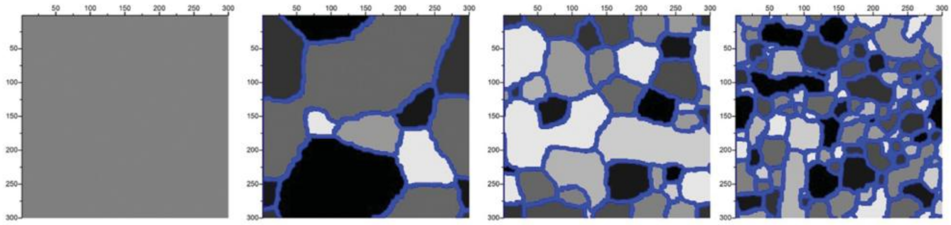

Single crystal (a) **GS = 95** (b) **GS = 45** (c) **GS = 25** (d)

Polycrystalline structures

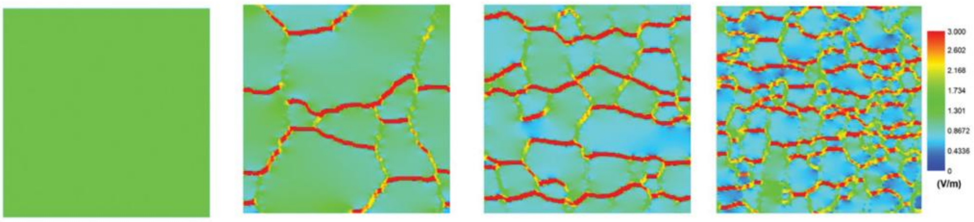

(e) (f) (g) (h)

Computed local electric field under the same applied voltage (ΔV=1.2V)

Figure 2.24: :(a)–(d) Simulated polycrystalline structures with various GS: (a) GS = ∞; single-crystal, (b) GS = 95 cells, (c) GS = 45 cells, and (d) GS = 25 cells. (e)–(h) Computed local field distributions under the same external voltage, V = 1.2V[96](reproduced with permission)

From the FEM models described above, we can see that utilising FEM enables us to use fewer variables to describe the behaviour of dielectrics in the ferroelectric state than the analytical models while still providing a detailed understanding and allow us to model the local field effects more simply. FEM is adept at handling complex geometries and non-linear behaviours, making it suitable for analysing localized electric field effects, particularly in heterogeneous materials. It also allows for dynamic, time-dependent simulations, which are often difficult to capture with analytical models and have been used previously to successfully model the field dependence in 2d. Therefore, FEM will be used to model Johnson's equation within this paper and the process used will be described in detail in the upcoming chapters.

2.9 References

1. Kerridge G, Sinclair DC, Dean JS. Resource efficient exploration of ternary phase space to develop multi-layer ceramic capacitors. Acta Mater. 2021;207:116690. doi:10.1016/j.actamat.2021.116690
2. Shimizu T, Wada K, Nakamura N. Flyback-type single-phase utility interactive inverter with power pulsation decoupling on the DC input for an AC photovoltaic module system. IEEE Trans Power Electron. 2006;21(5):1264-1272. doi:10.1109/TPEL.2006.880247
3. Rao RS, Narasimham SVL, Ramalingaraju M. Optimal capacitor placement in a radial distribution system using Plant Growth Simulation Algorithm. International Journal of Electrical Power & Energy Systems. 2011;33(5):1133-1139. doi:10.1016/J.IJEPES.2010.11.021
4. Nadjafi M, Hajivand M. Improving Reliability and Reducing Power Loss in Power Distribution Network by Determining Optimal Location and Size of Capacitor Banks. International Journal of Reliability, Risk and Safety: Theory and Application. 2018;1(1):25-33. doi:10.30699/IJRRS.1.26
5. Liu PJ, Hsu CY, Chang YH. Techniques of dual-path error amplifier and capacitor multiplier for on-chip compensation and soft-start function. IEEE Trans Power Electron. 2015;30(3):1403-1410. doi:10.1109/TPEL.2014.2320282
6. Hu H, Zhu C, Lu YF, Wu YH, Liew T, Li MF, Cho BJ, Choi WK, Yakovlev N. Physical and electrical characterization of HfO_2 metal–insulator–metal capacitors for Si analog circuit applications. J Appl Phys. 2003;94(1):551-557. doi:10.1063/1.1579550
7. Freeborn TJ, Maundy B, Elwakil AS. Fractional-order models of supercapacitors, batteries and fuel cells: A survey. Mater Renew Sustain Energy. 2015;4(3). doi:10.1007/S40243-015-0052-Y
8. Carlson J. The Kodak One-Time-Use Flash Camera. Phys Teach. 2004;42(6):375-376. doi:10.1119/1.1790348
9. Zeeff TM, Hubing TH, Van Doren TP, Pommerenke D. Analysis of Simple Two-Capacitor Low-Pass Filters. IEEE Trans Electromagn Compat. 2003;45(4):595-601. doi:10.1109/TEMC.2003.819059
10. Sierociuk D, Sarwas G, Twardy M. Resonance phenomena in circuits with ultracapacitors. 12th International Conference on Environment and Electrical Engineering, EEEIC 2013. Published online 2013:197-202. doi:10.1109/EEEIC.2013.6549616
11. Shekhar S, Dubey A, Mishra M, Gupta N. Interconnect Modeling Using the Quasi Monte Carlo Integration Technique. Advanced Computational

Techniques in Electromagnetics. 2012;2012:1-5. doi:10.5899/2012/acte-00112

12. Leng M, Zhou G, Liu X, Xu S. Dynamical effects of composite output capacitors on current-mode controlled buck converter with constant current load. IET Power Electronics. 2017;10(4):490-498. doi:10.1049/iet-pel.2016.0525
13. Hong K, Lee TH, Suh JM, Yoon SH, Jang HW. Perspectives and challenges in multilayer ceramic capacitors for next generation electronics. J Mater Chem C Mater. 2019;7(32):9782-9802. doi:10.1039/c9tc02921d
14. Pan MJ, Randall C. A brief introduction to ceramic capacitors. IEEE Electrical Insulation Magazine. 2010;26(3):44-50. doi:10.1109/MEI.2010.5482787
15. Foeller PY, Dean JS, Reaney IM, Sinclair DC. Design of a bilayer ceramic capacitor with low temperature coefficient of capacitance. Appl Phys Lett. 2016;109(8):082904. doi:10.1063/1.4961616
16. West AR. Solid State Chemistry and Its Applications.; 2012. doi:10.1351/PAC-REP-10-09-14
17. Shannon RD. Dielectric polarizabilities of ions in oxides and fluorides. J Appl Phys. 1993;73(1):348-366. doi:10.1063/1.353856
18. Arlt G, Hennings D, De With G. Dielectric properties of fine-grained barium titanate ceramics. J Appl Phys. 1985;58(4):1619-1625. doi:10.1063/1.336051
19. Moulson AJ HJ. Electroceramics: Materials, Properties, Applications. Electroceramics: Materials, Properties, Applications. Published online 2003:11. Accessed March 18, 2024. https://web-p-ebscohost-com.sheffield.idm.oclc.org/ehost/detail/detail?vid=0&sid=85f4d2e4-248a-4ba0-b2fe-c791711bc66d%40redis&bdata=JnNpdGU9ZWhvc3QtbGl2ZQ%3d%3d#db=nlebk&AN=90973
20. Eliche-Quesada D, Pérez-Villarejo L, José Sánchez-Soto P. Introductory Chapter: Ceramic Materials - Synthesis, Characterization, Applications and Recycling. In: Ceramic Materials - Synthesis, Characterization, Applications and Recycling. IntechOpen; 2019. doi:10.5772/intechopen.84710
21. Ikesue A, Aung YL. Ceramic laser materials. Nat Photonics. 2008;2(12):721-727. doi:10.1038/nphoton.2008.243
22. Park EW, Moon H, Park M soo, Hyun SH. Fabrication and characterization of Cu-Ni-YSZ SOFC anodes for direct use of methane via Cu-electroplating. Int J Hydrogen Energy. 2009;34(13):5537-5545. doi:10.1016/j.ijhydene.2009.04.060
23. Danzer R, Lube T, Supancic P, Damani R. Fracture of ceramics. Adv Eng Mater. 2008;10(4):275-298. doi:10.1002/adem.200700347
24. Li Z, Yang M, Park JS, Wei SH, Berry JJ, Zhu K. Stabilizing Perovskite Structures by Tuning Tolerance Factor: Formation of Formamidinium and Caesium Lead

Iodide Solid-State Alloys. Chemistry of Materials. 2016;28(1):284-292. doi:10.1021/ACS.CHEMMATER.5B04107/ASSET/IMAGES/LARGE/CM-2015-041079_0007.JPEG

25. Galasso F. Structure, Properties and Preparation of Perovskite Type Compounds. Structure, Properties and Preparation of Perovskite-Type Compounds. Published online 1969. doi:10.1016/C2013-0-02117-2
26. Safa Kasap and Peter Capper. Springer Handbook of Electronic and Photonic Materials.; 2007. doi:10.1007/978-0-387-29185-7
27. Pan MJ, Randall C. A brief introduction to ceramic capacitors. IEEE Electrical Insulation Magazine. 2010;26(3):44-50. doi:10.1109/MEI.2010.5482787
28. West AR. Solid State Chemistry and Its Applications.; 2012. doi:10.1351/PAC-REP-10-09-14
29. Varlioglu M, Ustundag E, Tamura N, Jones JL. Evolution of ferroelectric domain structures embedded inside polycrystalline $BaTiO_3$ during heating. In: Journal of Applied Physics. Vol 107. ; 2010. doi:10.1063/1.3311565
30. Li FX, Fang DN, Soh AK. Theoretical saturated domain-orientation states in ferroelectric ceramics. Scr Mater. 2006;54(7):1241-1246. doi:10.1016/j.scriptamat.2005.12.025
31. Acosta M, Novak N, Rojas V, Patel S, Vaish R, Koruza J, Rossetti GA, Rödel J. BaTiO3-based piezoelectrics: Fundamentals, current status, and perspectives. Appl Phys Rev. 2017;4(4):41305. doi:10.1063/1.4990046
32. Nguyen MD, Nguyen CTQ, Vu HN, Rijnders G. Experimental evidence of breakdown strength and its effect on energy-storage performance in normal and relaxor ferroelectric films. Current Applied Physics. 2019;19(9):1040-1045. doi:10.1016/J.CAP.2019.06.005
33. Introduction to Ceramic Capacitors. Accessed February 23, 2024. https://epci.eu/capacitors-introduction-to-ceramic-capacitors/
34. Cheong KY, Impellizzeri G, Fraga MA. Emerging Materials for Energy Conversion and Storage.; 2018. doi:10.1016/C2017-0-00444-5
35. Arlt G, Hennings D, De With G. Dielectric properties of fine-grained barium titanate ceramics. J Appl Phys. 1985;58(4):1619-1625. doi:10.1063/1.336051
36. Li LX, Han YM, Zhang P, Ming C, Wei X. Synthesis and characterization of BaTiO3-based X9R ceramics. J Mater Sci. 2009;44(20):5563-5568. doi:10.1007/S10853-009-3779-Y/FIGURES/6
37. Basics of capacitors [Lesson 3] How multilayer ceramic capacitors are made | Murata Manufacturing Articles. Accessed May 11, 2024. https://article.murata.com/en-global/article/basics-of-capacitors-3
38. Yue Z, Zhao J, Yang G, Li L. Electric field-dependent properties of $BaTiO_3$ -based multilayer ceramic capacitors. In: Ferroelectrics. Vol 401. ; 2010:56-60. doi:10.1080/00150191003670424

39. Zhang L, Ritter A, Nies C, Dwari S, Guo B, Priya S, Burgos R, Ngo K. Voltage-Controlled Capacitor - Feasibility Demonstration in DC-DC Converters. IEEE Trans Power Electron. 2017;32(8):5889-5892. doi:10.1109/TPEL.2017.2666478

40. Bibi I, Qayyum M, Ata S, Majid F, Kamal S, Alwadai N, Sultan M, Rehman F, Iqbal S, Iqbal M. Effect of dopant on ferroelectric, dielectric and photocatalytic properties of chromium-doped cobalt perovskite prepared via micro-emulsion route. Results Phys. 2021;20:103726. doi:10.1016/J.RINP.2020.103726

41. Liu C, Wang J. Strain engineering of ferroelectric negative capacitance in $PbZr_{(1-x)}Ti_xO_3$ thin films. Acta Mater. 2021;206:116607. doi:10.1016/J.ACTAMAT.2020.116607

42. Smith NAS, Rokosz MK, Correia TM. Experimentally validated finite element model of electrocaloric multilayer ceramic structures. J Appl Phys. 2014;116(4):44511. doi:10.1063/1.4891298/282844

43. Yang G, Yue Z, Sun T, Gou H, Li L. Effect of combined external uniaxial stress and dc bias on the dielectric property of $BaTiO_3$-based dielectrics in multilayer ceramic capacitor: thermodynamics and experiments. J Phys D Appl Phys. 2008;41(4):045307. doi:10.1088/0022-3727/41/4/045307

44. Wen H, Wang X, Chen R, Li L. Modeling of Dielectric Behaviors of Multilayer Ceramic Capacitors Under a Direct Current Bias Field. Journal of the American Ceramic Society. 2006;89(2):550-556. doi:10.1111/J.1551-2916.2005.00742.X

45. Curecheriu LP, Mitoseriu L, Ianculescu A. Nonlinear dielectric properties of $Ba_{1-x}Sr_xTiO_3$ ceramics. J Alloys Compd. 2009;482(1-2):1-4. doi:10.1016/j.jallcom.2009.04.036

46. Canedy CL, Li H, Alpay SP, Salamanca-Riba L, Roytburd AL, Ramesh R. Dielectric properties in heteroepitaxial $Ba_{0.6}Sr_{0.4}TiO_3$ thin films: Effect of internal stresses and dislocation-type defects. Volume 77, Issue 11, Pages 1695 - 1697. 2000;77(11):1695-1697. doi:10.1063/1.1308531

47. Im J, Auciello O, Baumann PK, Streiffer SK, Kaufman DY, Krauss AR. Composition-control of magnetron-sputter-deposited $(Ba_xSr_{1-x})Ti_1$ + yO_3 + z thin films for voltage tunable devices. Volume 76, Issue 5, Pages 625 - 627. 2000;76(5):625-627. doi:10.1063/1.125839

48. JAFFE H. Piezoelectric Ceramics. Journal of the American Ceramic Society. 1958;41(11):494-498. doi:10.1111/j.1151-2916.1958.tb12903.x

49. Hennings D. Barium titanate based ceramic materials for dielectric use. International Journal of High Technology Ceramics. 1987;3(2):91-111. doi:10.1016/0267-3762(87)90031-2

50. Zhang H. A theory for structural phase transitions in $BaTiO_3$ single crystal and $PbZrO_3$-$xPbTiO_3$ solid solution. AIP Adv. 2013;3(4). doi:10.1063/1.4802874

51. Gong H, Wang X, Zhang S, Wen H, Ceramic LLJ of the E, 2014 . Grain size effect on electrical and reliability characteristics of modified fine-grained $BaTiO_3$ ceramics for MLCCs. Elsevier H Gong, X Wang, S Zhang, H Wen, L Li Journal of the European Ceramic Society, 2014•Elsevier. Accessed May 20, 2024. https://www.sciencedirect.com/science/article/pii/S0955221913006018
52. Hong K, Tae ·, Lee H, Jun ·, Suh M, Park JS, Kwon HS, Choi J, Ho ·, Jang W. Direct Observation of Surface Potential Distribution in Insulation Resistance Degraded Acceptor-Doped BaTiO3 Multilayered Ceramic Capacitors. Springer K Hong, TH Lee, JM Suh, JS Park, HS Kwon, J Choi, HW Jang Electronic Materials Letters, 2018•Springer. 2018;14(5):629-635. doi:10.1007/s13391-018-0066-6
53. Buscaglia V, Society CRJ of the EC, 2020 . Size and scaling effects in barium titanate. An overview. Elsevier V Buscaglia, CA Randall Journal of the European Ceramic Society, 2020•Elsevier. Accessed May 20, 2024. https://www.sciencedirect.com/science/article/pii/S0955221920300315
54. Arlt G, Hennings D, physics GDWJ of applied, 1985 . Dielectric properties of fine-grained barium titanate ceramics. pubs.aip.org. Accessed May 20, 2024. https://pubs.aip.org/aip/jap/article-abstract/58/4/1619/172277
55. Hsiang HI, Yen FS, Huang CY. Effects of porosity on dielectric properties of batiO3 ceramics. Jpn J Appl Phys. 1995;34(4R):1922-1925. doi:10.1143/JJAP.34.1922/META
56. Yao Z, Liu H, Liu Y, Wu Z, Shen Z, ... YLMC and, 2008 . Structure and dielectric behaviour of Nd-doped BaTiO3 perovskites. Elsevier Z Yao, H Liu, Y Liu, Z Wu, Z Shen, Y Liu, M Cao Materials Chemistry and Physics, 2008•Elsevier. Accessed May 20, 2024. https://www.sciencedirect.com/science/article/pii/S0254058407007626
57. Randall C, Wang S, ... DLJ of materials, 1993 . Structure property relationships in core-shell $BaTiO_3$–LiF ceramics. cambridge.org CA Randall, SF Wang, D Laubscher, JP Dougherty, W Huebner Journal of materials research, 1993•cambridge.org. Accessed May 20, 2024. https://www.cambridge.org/core/journals/journal-of-materials-research/article/structure-property-relationships-in-coreshell-batio3lif-ceramics/79583DBD99026A08699C202600020C46
58. Liu M, Hao H, Chen W, Zhou D, Appiah M, ... BLC, 2016 . Preparation and dielectric properties of X9R core–shell $BaTiO_3$ ceramics coated by $BiAlO_3$–$BaTiO_3$. ElsevierM Liu, H Hao, W Chen, D Zhou, M Appiah, B Liu, M Cao, Z Yao, H Liu, Z Zhang Ceramics International, 2016•Elsevier. Accessed May 20, 2024. https://www.sciencedirect.com/science/article/pii/S0272884215016454

59. Yasukawa K, Nishimura M, Nishihata Y, Ichiro Mizuki J'. Core–Shell Structure Analysis of $BaTiO_3$ Ceramics by Synchrotron X-Ray Diffraction. Wiley Online Library K Yasukawa, M Nishimura, Y Nishihata, J Mizuki Journal of the American Ceramic Society, 2007•Wiley Online Library. 2007;90(4):1107-1111. doi:10.1111/j.1551-2916.2007.01537.x
60. Morrison F, Sinclair D, Physics AWJ of A, 1999 . Electrical and structural characteristics of lanthanum-doped barium titanate ceramics. pubs.aip.org. 1999;86:6355-6366. doi:10.1063/1.371698
61. Sun Y, Liu H, Hao H, ... ZSJ of the A, 2015 . Structure Property Relationship in $BaTiO_3$–$Na_{0.5}Bi_{0.5}TiO_3$–Nb_2O_5–NiO X8R System. Wiley Online Library Y Sun, H Liu, H Hao, Z Song, S Zhang Journal of the American Ceramic Society, 2015•Wiley Online Library. 2015;98(5):1574-1579. doi:10.1111/jace.13517
62. Buscaglia MT, Viviani M, Zhao Z, Buscaglia V, Nanni P. Synthesis of $BaTiO_3$ Core−Shell Particles and Fabrication of Dielectric Ceramics with Local Graded Structure. ACS Publications MT Buscaglia, M Viviani, Z Zhao, V Buscaglia, P Nanni Chemistry of materials, 2006•ACS Publications. 2006;18(17):4002-4010. doi:10.1021/cm060403j
63. Liu M, Hao H, Chen W, Zhou D, Appiah M, ... BLC, 2016 . Preparation and dielectric properties of X9R core–shell $BaTiO_3$ ceramics coated by $BiAlO_3$–$BaTiO_3$. ElsevierM Liu, H Hao, W Chen, D Zhou, M Appiah, B Liu, M Cao, Z Yao, H Liu, Z Zhang Ceramics International, 2016•Elsevier. Accessed May 20, 2024. https://www.sciencedirect.com/science/article/pii/S0272884215016454
64. Park KJ, Kim CH, Yoon YJ, Song SM, Kim YT, Hur KH. Doping behaviours of dysprosium, yttrium and holmium in $BaTiO_3$ ceramics. J Eur Ceram Soc. 2009;29(9):1735-1741. doi:10.1016/J.JEURCERAMSOC.2008.10.021
65. Kim CH, Park KJ, Yoon YJ, Hong MH, Hong JO, Hur KH. Role of yttrium and magnesium in the formation of core-shell structure of $BaTiO_3$ grains in MLCC. J Eur Ceram Soc. 2008;28(6):1213-1219. doi:10.1016/J.JEURCERAMSOC.2007.09.042
66. Kim CH, Park KJ, Yoon YJ, Sinn DS, Kim YT, Hur KH. Effects of milling condition on the formation of core–shell structure in $BaTiO_3$ grains. J Eur Ceram Soc. 2008;28(13):2589-2596. doi:10.1016/J.JEURCERAMSOC.2008.03.030
67. Gong H, Wang X, Zhang S, Li L. Synergistic effect of rare-earth elements on the dielectric properties and reliability of $BaTiO_3$ -based ceramics for multilayer ceramic capacitors. Mater Res Bull. 2016;73:233-239. doi:10.1016/j.materresbull.2015.07.010
68. Park KJ, Kim CH, Yoon YJ, Song SM, Kim YT, Hur KH. Doping behaviours of dysprosium, yttrium and holmium in $BaTiO_3$ ceramics. J Eur Ceram Soc. 2009;29(9):1735-1741. doi:10.1016/j.jeurceramsoc.2008.10.021

69. Kishi H, Kohzu N, Sugino J, Ohsato H, Iguchi Y, Okuda T. The effect of rare-earth (La, Sm, Dy, Ho and Er) and Mg on the microstructure in $BaTiO_3$. J Eur Ceram Soc. 1999;19(6-7):1043-1046. doi:10.1016/s0955-2219(98)00370-7

70. Li Y, Hao Y, Wang X, Yao X. Studies of dielectric properties of rare earth (Y, Gd, Yb) doped barium titanate sintered in pure nitrogen. In: Ferroelectrics. Vol 407. Taylor & Francis Group; 2010:134-139. doi:10.1080/00150193.2010.484757

71. Zr -x O, Thiago Martins Amaral C, Antonelli E, Alejandro Ochoa D, Eduardo Garcia J, Carlos Hernandes A. Microstructural Features and Functional Properties of Bilayered $BaTiO_3$ /$BaTi_{1-x}Zr_xO_3$ Ceramics. Wiley Online Library TM Amaral, E Antonelli, DA Ochoa, JE García, AC Hernandes Journal of the American Ceramic Society, 2015•Wiley Online Library. 2014;98(4):1169-1174. doi:10.1111/jace.13417

72. Hoshina T. Size effect of barium titanate: Fine particles and ceramics. Journal of the Ceramic Society of Japan. 2013;121(1410):156-161. doi:10.2109/jcersj2.121.156

73. Kinoshita K, Yamaji A. Grain-size effects on dielectric properties in barium titanate ceramics. J Appl Phys. 1976;47(1):371-373. doi:10.1063/1.322330

74. Padurariu L, Curecheriu L, Buscaglia V, Mitoseriu L. Field-dependent permittivity in nanostructured $BaTiO_3$ ceramics: Modeling and experimental verification. Phys Rev B Condens Matter Mater Phys. 2012;85(22):1-9. doi:10.1103/PhysRevB.85.224111

75. Yashima M, Hoshina T, Ishimura D, Kobayashi S, Nakamura W, Tsurumi T, Wada S. Size effect on the crystal structure of barium titanate nanoparticles. J Appl Phys. 2005;98(1). doi:10.1063/1.1935132

76. Hoshina T. Size effect of barium titanate: Fine particles and ceramics. Journal of the Ceramic Society of Japan. 2013;121(1410):156-161. doi:10.2109/jcersj2.121.156

77. Zhao Y, Xing H, Zhang L, Huang H, Sun D, Dong X, Shen Y, Wang J. Development of Phase-Field Modeling in Materials Science in China: A Review. Acta Metallurgica Sinica (English Letters). 2023;36(11):1749-1775. doi:10.1007/S40195-023-01593-W/FIGURES/16

78. Wang J, Shi SQ, Chen LQ, Li Y, Zhang TY. Phase-field simulations of ferroelectric/ferroelastic polarization switching. Acta Mater. 2004;52(3):749-764. doi:10.1016/J.ACTAMAT.2003.10.011

79. Wang JJ, Ma XQ, Li Q, Britson J, Chen LQ. Phase transitions and domain structures of ferroelectric nanoparticles: Phase field model incorporating strong elastic and dielectric inhomogeneity. Acta Mater. 2013;61(20):7591-7603. doi:10.1016/J.ACTAMAT.2013.08.055

80. Hu HL, Chen LQ. Three-dimensional computer simulation of ferroelectric domain formation. Journal of the American Ceramic Society. 1998;81(3):492-500. doi:10.1111/j.1151-2916.1998.tb02367.x
81. Hu HL, Chen LQ. Computer simulation of 90° ferroelectric domain formation in two-dimensions. Materials Science and Engineering: A. 1997;238(1):182-191. doi:10.1016/S0921-5093(97)00453-X
82. Yang W, Chen L -Q. Computer Simulation of the Dynamics of 180° Ferroelectric Domains. Journal of the American Ceramic Society. 1995;78(9):2554-2556. doi:10.1111/j.1151-2916.1995.tb08702.x
83. Ambati M, Gerasimov T, De Lorenzis L. Phase-field modeling of ductile fracture. Comput Mech. 2015;55(5):1017-1040. doi:10.1007/S00466-015-1151-4/FIGURES/34
84. Curecheriu L, Buscaglia MT, Buscaglia V, Zhao Z, Mitoseriu L. Grain size effect on the nonlinear dielectric properties of barium titanate ceramic. Appl Phys Lett. 2010;97:242909. doi:10.1063/1.3526375
85. Curecheriu LP, Mitoseriu L, Ianculescu A. Nonlinear dielectric properties of Ba1-xSrxTiO3 ceramics. J Alloys Compd. 2009;482(1-2):1-4. doi:10.1016/j.jallcom.2009.04.036
86. Wei X, Feng Y, Hang L, Yao X. Dielectric properties of barium stannate titanate ceramics under bias field. In: Ceramics International. Vol 30. ; 2004:1401-1404. doi:10.1016/j.ceramint.2003.12.084
87. Johnson KM. Variation of dielectric constant with voltage in ferroelectrics and its application to parametric devices. J Appl Phys. 1962;33(9):2826-2831. doi:10.1063/1.1702558
88. Liou JW, Chiou BS. Analysis of the dielectric characteristics for polycrystalline $Ba_{0.65}Sr_{0.35}TiO_3$ (II) - d.c. Field dependence with a modified bias equation. Journal of Materials Science: Materials in Electronics. 2000;11(8):645-651. doi:10.1023/A:1008949316917
89. Zhang G, Jiang S, Zeng Y, Zhang Y, Zhang Q, Yu Y. The modified model of the dielectric characteristics for porous $Ba_{0.6}Sr_{0.4}TiO_3$ ceramics. J Appl Phys. 2009;106(3):034110. doi:10.1063/1.3183921
90. Chen A, Zhi Y. Dielectric behavior of $PbZr_{0.52}Ti_{0.48}O_3$ thin films: Intrinsic and extrinsic dielectric responses. Appl Phys Lett. 2004;85(17):3821-3823. doi:10.1063/1.1808233
91. Narayanan M, Tong S, Ma B, Liu S, Balachandran U. Modified Johnson model for ferroelectric lead lanthanum zirconate titanate at very high fields and below Curie temperature. Appl Phys Lett. 2012;100(2). doi:10.1063/1.3676668/903024
92. Placeres-Jiménez R, Rino JP, Eiras JA. Modeling ferroelectric permittivity dependence on electric field and estimation of the intrinsic and extrinsic

contributions. J Phys D Appl Phys. 2015;48(3):035304. doi:10.1088/0022-3727/48/3/035304

93. Curecheriu L, Balmus SB, Buscaglia MT, Buscaglia V, Ianculescu A, Mitoseriu L. Grain size-dependent properties of dense nanocrystalline barium titanate ceramics. Journal of the American Ceramic Society. 2012;95(12):3912-3921. doi:10.1111/j.1551-2916.2012.05409.x

94. Zhou K, Boggs SA, Ramprasad R, Aindow M, Erkey C, Alpay SP. Dielectric response and tunability of a dielectric-paraelectric composite. Appl Phys Lett. 2008;93(10). doi:10.1063/1.2982086

95. Myroshnychenko V, Smirnov S, Mulavarickal Jose PM, Brosseau C, Förstner J. Nonlinear dielectric properties of random paraelectric-dielectric composites. Acta Mater. 2021;203:116432. doi:10.1016/J.ACTAMAT.2020.10.051

96. Padurariu L, Curecheriu L, Buscaglia V, Mitoseriu L. Field-dependent permittivity in nanostructured $BaTiO_3$ ceramics: Modeling and experimental verification. Phys Rev B Condens Matter Mater Phys. 2012;85(22):224111. doi:10.1103/PhysRevB.85.224111

3 Analytical Model

3.1 Overview:

In this chapter, the process used to develop an analytical two-dimensional model utilising Johnson's equation will be described. This will be used to gain a base understanding of how dielectrics behave in the presence of a DC bias and facilitate the study of field dependence characteristics of a dielectric material. Initially, material properties, specifically the Johnson's parameter, intrinsic permittivity, and applied field strength, of a simple cube will be modified while using Johnson's equation (Equation 2.23). Next, we employ the same methodology to investigate the properties of two known materials arranged in a layered structure to get a broader understanding of the field dependence of relative permittivity. The initial material properties assigned for the two materials used are those of Barium Titanate (BT), typically considered as a core material and a commonly used shell material, both of which were provided by AVX. Due to confidentiality considerations, the detailed chemical composition of the shell material was not made available.

In the layered structure, the materials will be analysed with the materials first arranged in series and then arranged in parallel. For this chapter, the parameters that will be modified are the strength of the electric field, the volume ratio of the core and shell, the conductivity of the core and shell, the thickness of the dielectric and the Johnson's parameter. The results are then analysed, and these results will be used to set the stage for the upcoming chapters. Finally, some common limitations of the analytical model will be discussed, and difficulties in modeling a core-shell model will be addressed.

As mentioned in the previous chapter, MLCCs typically use doped dielectrics that form a core-shell microstructure. This structure consists of a mixture of parallel and series zones, as seen in Figure 3.1. To start, we shall look at each of these individually, understanding the features that series and parallel configurations would lead to. These series and parallel configurations can be used as an idealised case to verify our FEM results.

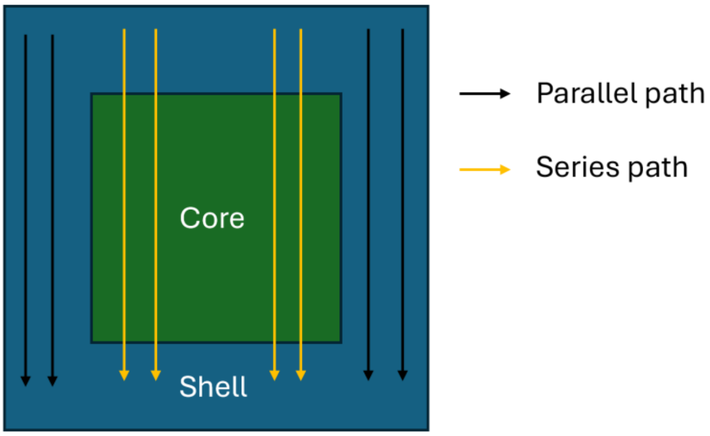

Figure 3.1 A 2d representation of a core shell model, with the core in green and the shell in blue, showing the series and parallel paths available in the model.

3.2 An analytical approach on a cube of dielectric material

Using Johnson's equation 2.23 (repeated below from the previous chapter), three main factors affect the change in relative permittivity due to the application of an external field.

$$\epsilon(E) = \frac{\epsilon(0)}{(1 + \beta(\epsilon_0 \epsilon_r)^3 E^2)^{\frac{1}{3}}}$$

Equation 2.23

These are the intrinsic permittivity, the applied electric field and its Johnson's parameter β. To gain a basic understanding of how these factors can alter the field-effected permittivity, we create an analytical model based on a simple cube of dielectric material having a side length of 10 µm, as seen in Figure 3.2. The surface area of the cube is then given as A=100 µm^2, and the distance between the electrical contacts/electrodes is 10 µm. Setting the conductivity of the cube to be 1x10^{-4} S/m, we can perform an analysis of how these three factors modify the field-effected permittivity (effective permittivity).

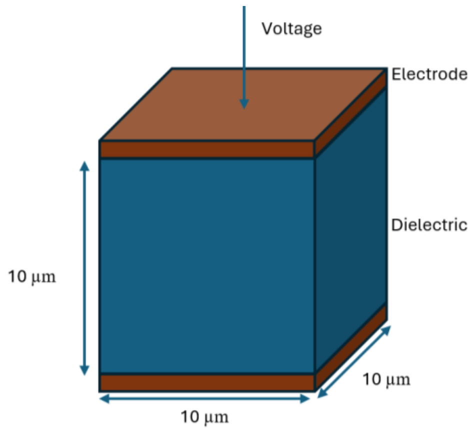

Figure 3.2: Model showing a simple cube having a side length of 10 µm and direction of applied voltage. The blue material is the dielectric, and the brown material is the electrodes.

3.2.1 Johnson's parameter β

The β value is an anharmonic coefficient known as Johnson's parameter and represents the ferroelectric non-linearity of the material. This contains information about how the domains experience the electric field and the resultant change in relative permittivity that the field generates. It can be obtained by fitting the observed relative permittivity drop with increasing voltage[1].

As mentioned in the previous chapter, the electric field in a homogeneous material can be given by $E=V/d$. We set d at 10 µm and apply a potential difference across the material, $V=10V$ equates to generating an applied field of 1MV/m. We then assign the material to have an intrinsic permittivity of $\varepsilon_r=10000$, which is around the peak value for BT at its Curie temperature. The value of Johnson's parameter is then varied from $\beta = 10^{10}\ Vm^5/C^3$ to $\beta = 10^{12}\ Vm^5/C^3$, which, as mentioned in chapter 2, falls within the known Johnson's parameter value ranges for Barium Titanate[2,3]. We then generate 1000 points to evaluate Johnson's parameter, as seen in Figure 3.3.

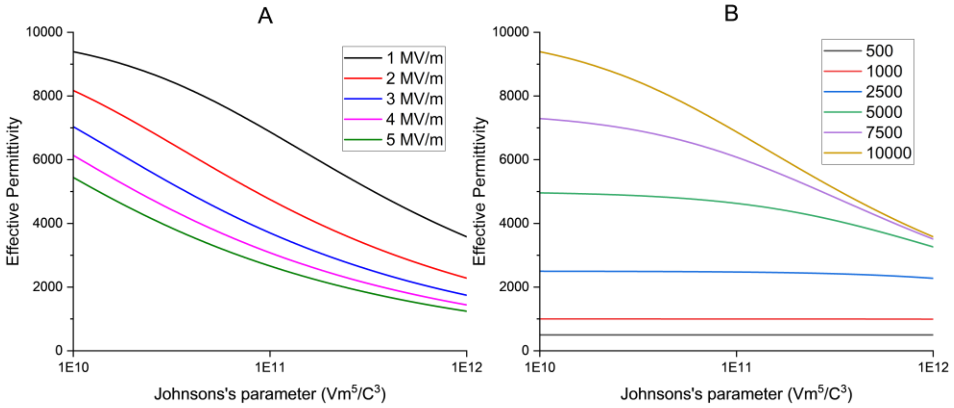

Figure 3.3: Change in relative permittivity as the Johnson's parameter is increased from 10^{10} *Vm*^{5}*/C*^{3} *to* 10^{12} *Vm*^{5}*/C*^{3} *with (A) showing the changes in effective permittivity as the applied field is increased from 1MV/m to 5 MV/m with initial relative permittivity kept constant at 10000. (B) shows the change in effective permittivity as the applied field strength is kept constant at 1MV/m and the intrinsic permittivity is increased from 500 to 10000.*

Initially, 5 studies were conducted where the Johnson's parameter and the intrinsic permittivity were set constant. The applied field strength was then varied, as seen in Figure 3.3A by changing the applied voltage from 1 MV/m to 5 MV/m. We observe a decrease in the effective permittivity across all field strengths as Johnson's parameter increases from 10^{10} Vm^5/C^3 to 10^{12} Vm^5/C^3. This inverse relationship indicates that as Johnson's parameter grows, the dielectric response of the material weakens, regardless of the applied electric field strength.

At low fields such as E=1 MV/m, the material shows a higher effective permittivity value of ε=9390 at the lower value for β and ε=3580 at the high end of β. As the electric field strength increases, the effective permittivity decreases. At E=5 MV/m, the effective permittivity is notably lower at a value of ε=5445 at β=10^{10} Vm^5/C^3 and ε=1242 for β=10^{12} Vm^5/C^3 respectively. This trend suggests that higher electric fields tend to suppress the dielectric response, resulting in lower relative permittivity values at the outset.

In Figure 3.3B, we see the change in effective permittivity as the intrinsic permittivity is increased from 500 to 10000 at an applied field strength of 1 MV/m. As Johnson's parameter increases, a decrease in the relative permittivity across all permittivities is observed. However, the rate and extent of this decline vary significantly based on the initial value set. Materials with higher intrinsic permittivity values, such as those starting at ε_r= 5000 and above, show a steep drop-off in relative permittivity as β increases. For material having an intrinsic permittivity of ε_r= 10000, this corresponds to a drop of 62% from around ε=9389 to ε=3580 when the field is increased from 1 MV/m to 5 MV/m, respectively. It indicates that high-permittivity materials are highly sensitive to changes in Johnson's parameter and that their dielectric properties decrease quicker compared to materials with a lower intrinsic permittivity.

In contrast, materials with low intrinsic permittivity, such as those starting at ε_r= 500 or ε_r= 1000, experience a much slower decrease. Their response is relatively flat compared to those of higher-permittivity materials. The material having an intrinsic permittivity of 1000 experiences a drop of just 0.7% from around ε=999 to ε=993 as the field increases from 1MV/m to 5MV/m, respectively. As Johnson's parameter approaches the higher end of the scale used here, the rate of change appears to slow down. If the maximum β is doubled to β=2 x10^{12} Vm^5/C^3 there is only an additional 10% decrease in the effective permittivity for the material having ε_r= 10000. This convergence suggests a saturation effect, where, beyond a certain threshold of Johnson's parameter, the intrinsic permittivity of the material has little impact on its effective permittivity. This highlights that for materials with lower β values, the intrinsic permittivity plays a large role in determining the effective permittivity, but at higher values, this difference becomes negligible.

3.2.2 Electric Field

The next factor that will be looked at is the effect of changing the electric field while keeping Johnson’s parameter constant. As mentioned previously, modifying the applied voltage has a direct correlation with the electric field provided the thickness remains constant. The Johnson’s parameter was assigned to be 1x10^{11} Vm^5/C^3, which falls in the average range of typical BT materials. The voltage of the material is increased from 0 V to 50 V with a step size of 0.05 V, and generates an electric field of 0 MV/m to 5 MV/m. The intrinsic permittivity was assigned five values ranging from ε_r= 500 to ε_r =10000, and the results obtained can be seen in Figure 3.4.

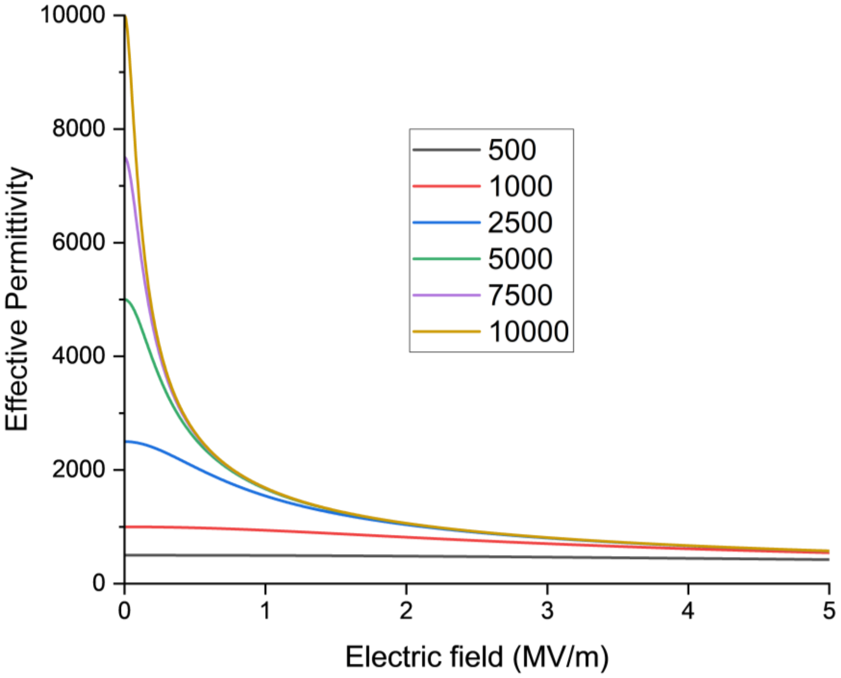

Figure 3.4: Decrease in relative permittivity as the electric field is increased to a field strength of 5 MV/m for 5 different intrinsic permittivities ranging from 500 to 10000 and a Johnson's parameter value of 10^{11} *Vm*^{5}*/C*^{3}*.*

As the electric field strength increases, all responses exhibit a decrease in relative permittivity, meaning that the material's ability to store electric energy decreases with a stronger electric field. The rate of this decrease is more pronounced for materials with higher intrinsic permittivity values. In the case of an intrinsic permittivity of ε_r=10,000, a drop in effective permittivity to about ε(E)=1650 is seen when the electric field reaches approximately 1 MV/m. This is nearly an 85% reduction in relative permittivity. By the time the electric field reaches around 5 MV/m, the relative permittivity for this intrinsic value flattens to roughly ε(E)=580.

In contrast, the results for an intrinsic permittivity of ε_r=500 exhibit a smaller decrease. At a field strength of 5 MV/m, it decreases to approximately ε(E)=420, indicating a modest decrease of just 16% compared to the higher intrinsic permittivity curves, suggesting that materials with lower intrinsic permittivity are less affected by the electric field.

All curves show a trend toward levelling off at higher electric field strengths of over 5 MV/m, where the relative permittivity becomes nearly constant, indicating that further increases in the electric field have little additional effect on relative permittivity. This behaviour again shows a saturation effect: once a certain threshold is reached, the material's relative permittivity stabilises. Overall, the graph demonstrates that materials with higher intrinsic permittivity experience a more dramatic reduction in relative permittivity as the electric field increases, while those with lower intrinsic permittivity are less sensitive to changes in the electric field.

3.2.3 Relative Permittivity

Finally, we study the effect of the intrinsic permittivity of the material while keeping both Johnson's parameter and field strength constant. We have already seen the effect of intrinsic permittivity in the previous 2 sections, but here we try to isolate the effect. Johnson's parameter is again assigned to be 10^{11} Vm^5/C^3, and the electric field is set to 1 MV/m. The relative permittivity of the model is then increased from $\varepsilon_r=0$ to $\varepsilon_r=10000$ using a step size of 10.

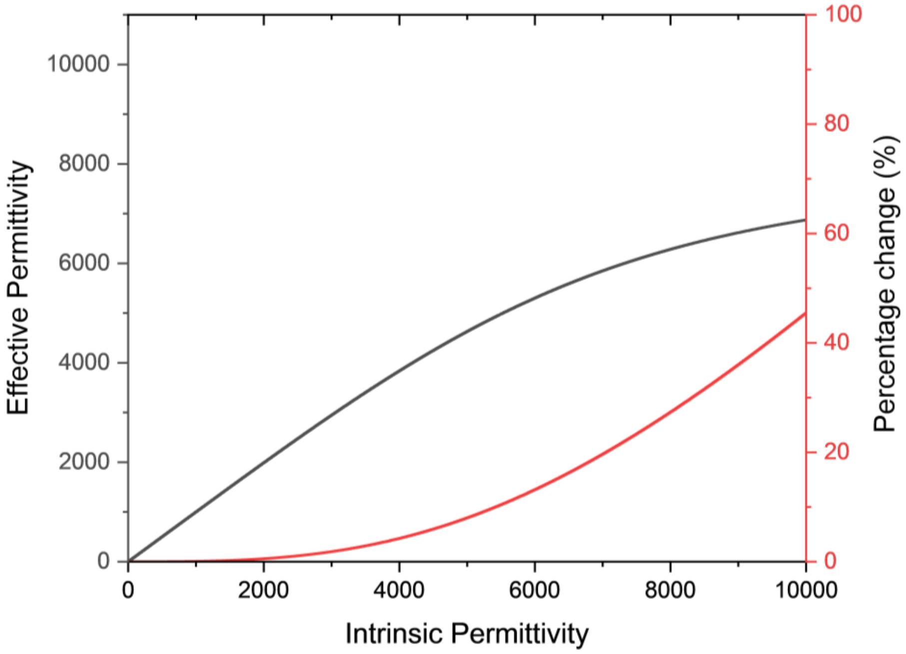

Figure 3.5: Change in effective permittivity (black) and percentage change (red) as intrinsic permittivity is increased to a value of 10000 at an applied electric field strength of 1MV/m and a Johnson's parameter value of 10^{11} Vm^5/C^3.

In Figure 3.5 we see that increasing the intrinsic permittivity from $\varepsilon_r=0$ to $\varepsilon_r=10000$ leads to a greater drop in the percentage change in relative permittivity of the material. Starting from 0%, this percentage change increases steadily as the intrinsic permittivity rises, reaching around 45% at an intrinsic permittivity of $\varepsilon_r=10{,}000$. This indicates that the higher the intrinsic permittivity, the more significant the reduction in effective permittivity. In contrast, for an intrinsic permittivity of $\varepsilon_r=5{,}000$, the percentage change is approximately 10%, suggesting that effective permittivity retains about 90% of the intrinsic value.

3.2.4 Summary

In summary, this study demonstrates that effective permittivity in materials like barium titanate is highly sensitive to Johnson's parameter (β), electric field strength, and intrinsic permittivity. As Johnson's parameter and electric field strength increase, effective permittivity decreases significantly, particularly in materials with higher intrinsic permittivity values. This decline illustrates a weakening dielectric response at elevated β values and field strengths, which is especially pronounced in high-permittivity materials, suggesting they are more sensitive to external influences. Additionally, a saturation effect becomes evident as β or field strength reaches higher thresholds, where further increases have a diminishing impact on relative permittivity. This behaviour indicates that while intrinsic permittivity plays a substantial role in determining effective permittivity at lower β values and field strengths, its influence diminishes as these parameters increase, ultimately leading to a stabilisation in relative permittivity.

3.3 Expanding the analytical model to two materials

From the previous models, we have seen that the Johnson's parameter value, applied voltage and the intrinsic permittivity of the material all play a role in the VCC of a material. We now expand the model to include two materials using experimental data of a typical 'core' like material and a typical 'shell' like material.

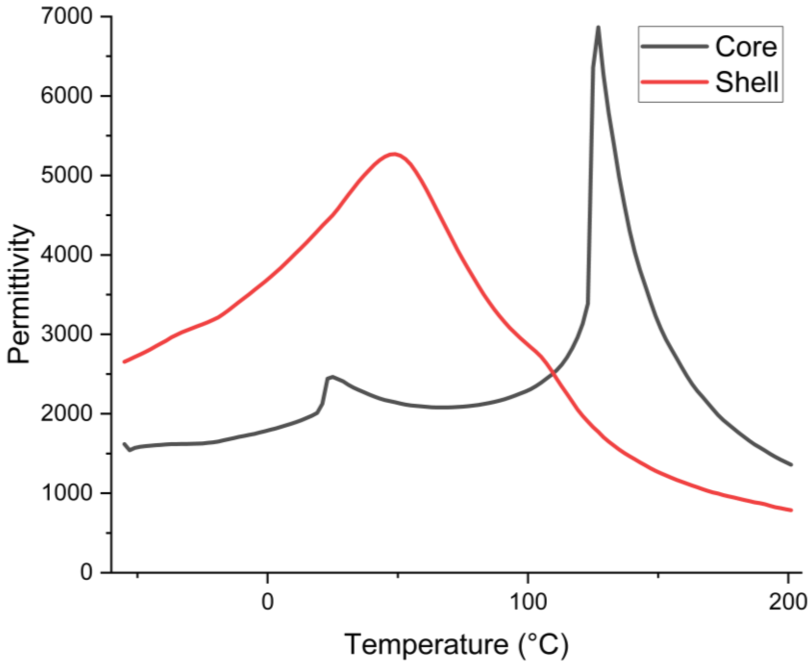

Figure 3.6: Experimental relative permittivity data over temperature for a core and shell material of an MLCC.

To generate realistic intrinsic material property data for the model, we use experimental measured conductivity and relative permittivity properties for a real MLCC core (BT), and shell material were obtained from AVX [4] as seen in Figure 3.6. Utilising these values within Excel and MATLAB[5], an analytical model was created to examine how the application of an electrical field can be used to modify the TCC of an MLCC. The relative permittivity of the two components was spline-fitted from KAVX data. To generate the conductivity values, we use measured Arrhenius plots[6], Figure 3.7, extrapolated linearly across the temperature range. To extract the values, we use the Arrhenius equation,

$$\sigma = \sigma_0 e^{\frac{E_a}{kT}}$$

Equation 3.1

where σ is the conductivity (Scm^{-1}), σ_o is the pre-exponential constant (Scm^{-1}), E_a is the activation energy (eV), k is the Boltzmann constant (8.6173324×10^{-5} eV K^{-1}), and T is the temperature (in K). Since conductivity data for the shell material was unavailable by itself, we assume the conductivity to be equal to the conductivity of BT.

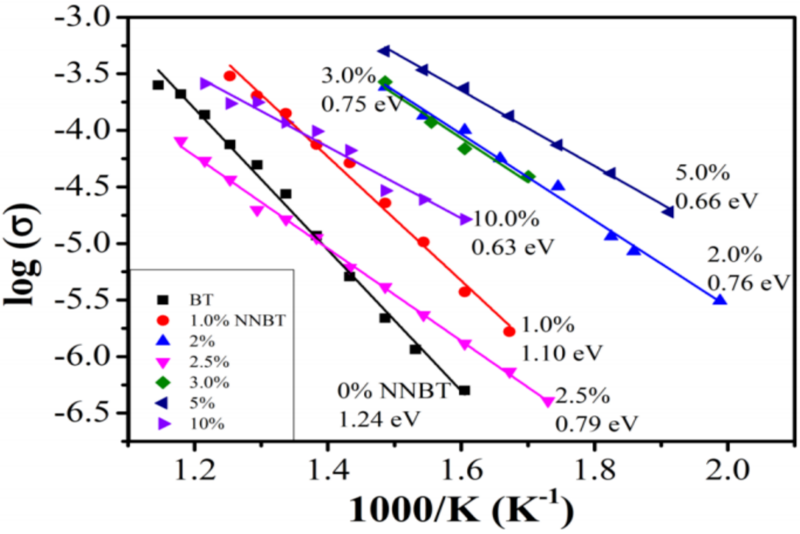

Figure 3.7: Arrhenius plot for bulk conductivity data extracted from M” spectroscopic plots for xNNBT[6]

3.3.1 Series model

We now use the input values to set up an analytical model of a two-material system, in this case, a layered model electrically connected in series. To start, we first develop the equations needed to describe the electric field in each material.

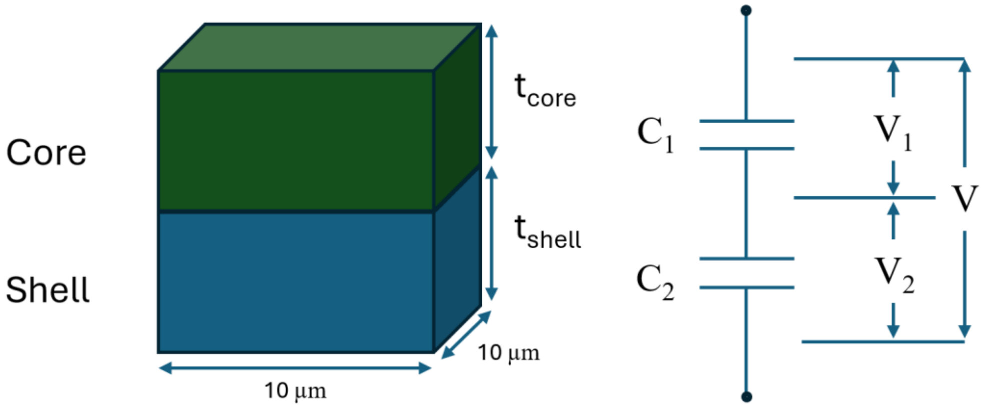

Figure 3.8: Figure(left) shows how the materials are arranged in the series analytical model. The green represents the layer which has been assigned the properties of the core material (Barium Titanate), and the blue material has been assigned the properties of the shell material. t_{core} and t_{shell} represent the thickness of the core material and the shell material, respectively. Figure (right) shows the circuit representation of the model.

For two materials arranged in series, as seen in Figure 3.8, we know that the potential drop across two materials in series can be written as,

$$V_{total} = V_{core} + V_{shell}$$

Equation 3.2

Where V_{core} is the voltage across the core material layer, and V_{shell} across the shell layer. We know that E=V/d, therefore:

$$V_{total} = E_{core}t_{core} + E_{shell}t_{shell}$$

Equation 3.3

Where E_{core} and t_{core} are the electrode field and thickness associated with the core material. According to Ohm's law, 0pwe know the current density J is related to the electric field E and conductivity σ:

$$J = \sigma E$$

Equation 3.4

and that in a series connection, the current density across both materials must be equal, i.e.

$$J_{core} = J_{shell}$$

Equation 3.5

Therefore, we can write,

$$\sigma_{core}E_{core} = \sigma_{shell}E_{shell}$$

Equation 3.6

or

$$E_{shell} = \frac{\sigma_{core}}{\sigma_{shell}}E_{core}$$

Equation 3.7

Substituting back in Equation 3.3, the electric field generated across the shell was calculated as:

$$\mathrm{E_{shell}} = \frac{\mathrm{V} * \sigma_{\mathrm{core}}}{(\mathrm{t_{core}} * \sigma_{\mathrm{shell}}) + (\mathrm{t_{shell}} * \sigma_{\mathrm{core}})}$$

Equation 3.8

Similarly, the electric field across the core can be calculated as:

$$\mathrm{E_{core}} = \frac{\mathrm{V} * \sigma_{\mathrm{shell}}}{(\mathrm{t_{core}} * \sigma_{\mathrm{shell}}) + (\mathrm{t_{shell}} * \sigma_{\mathrm{core}})}$$

Equation 3.9

Where V is the applied DC voltage, σ_{core} is the conductivity of the core, σ_{shell} is the conductivity of the shell, $\mathrm{E_{core}}$is the electric field experienced by the core, $\mathrm{E_{shell}}$ is the electric field experienced by the shell and $\mathrm{t_{core}}$ and $\mathrm{t_{shell}}$ are the thicknesses of the core and shell, respectively.

As in the previous simulations, we use $\beta = 1\mathrm{x}10^{10}\ \mathrm{C}^{-3}\mathrm{V}^{5}\mathrm{m}$ along with relative permittivity, conductivity, and electric field values in Johnson's equation.

For a capacitor in series:

$$\frac{1}{C_{total}} = \frac{1}{C_1} + \frac{1}{C_2}$$

Equation 3.10

$$C_{total} = \varepsilon_{eff}\frac{A}{d}$$

Equation 3.11

$$C_1 = \varepsilon_{\mathrm{r}}(\mathrm{core})\frac{A}{k}$$

Equation 3.12

$$C_2 = \varepsilon_r(\text{shell})\frac{A}{1-k}$$

Equation 3.13

Where C_{total} is the total capacitance, C_1 and C_2 are the capacitances of two capacitors, d=1, A is the surface area of the dielectric, k is the volume fraction of the core to the shell, in which 0 represents a pure shell material and 1 is a pure core material. $\varepsilon_r(\text{core})$is the relative permittivity of the core at the reference temperature, and $\varepsilon_r(\text{shell})$ is the relative permittivity of the shell at the reference permittivity.

Substituting these in Equation 3.10, we get

$$\frac{1}{\varepsilon_{series}} = \frac{k}{\varepsilon_r(\text{core})} + \frac{1-k}{\varepsilon_r(\text{shell})}$$

Equation 3.14

Solving for which we get Equation *3.15*.

$$\varepsilon_{\text{series}} = \frac{1}{\frac{\text{k}}{\varepsilon_r(\text{core})} + \frac{1-\text{k}}{\varepsilon_r(\text{shell})}}$$

Equation 3.15

Which is used to calculate the effective permittivity of the system of the core-shell series model.

The TCC% is then calculated as

$$\text{TCC\%} = \frac{\epsilon_\text{T} - \epsilon_{25}}{\epsilon_{25}} * 100$$

Equation 3.16

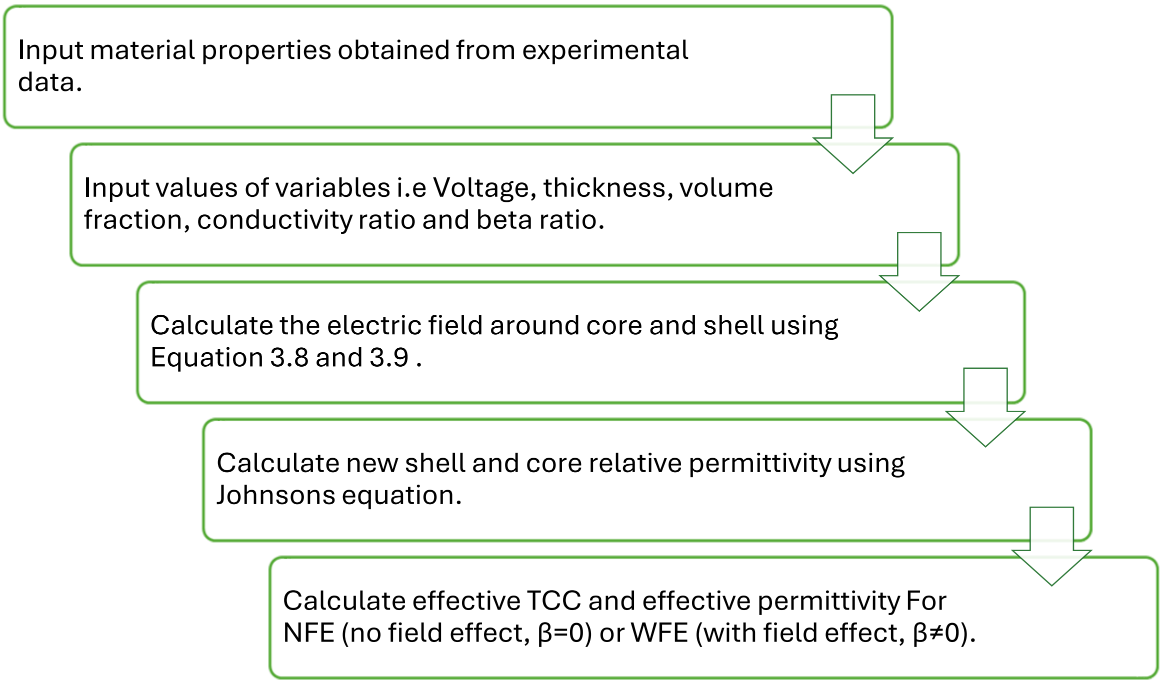

Figure 3.9: Analysis process for the analytical model.

Using the process detailed in Figure 3.9, a model is generated showing the change in TCC from the no-field effect (NFE) case and the with-field effect (WFE) case using a 10V potential difference across the system. A volume ratio of 50-50 of the two materials was considered, and the β value and conductivities assigned to both the shell and the core material were the same.

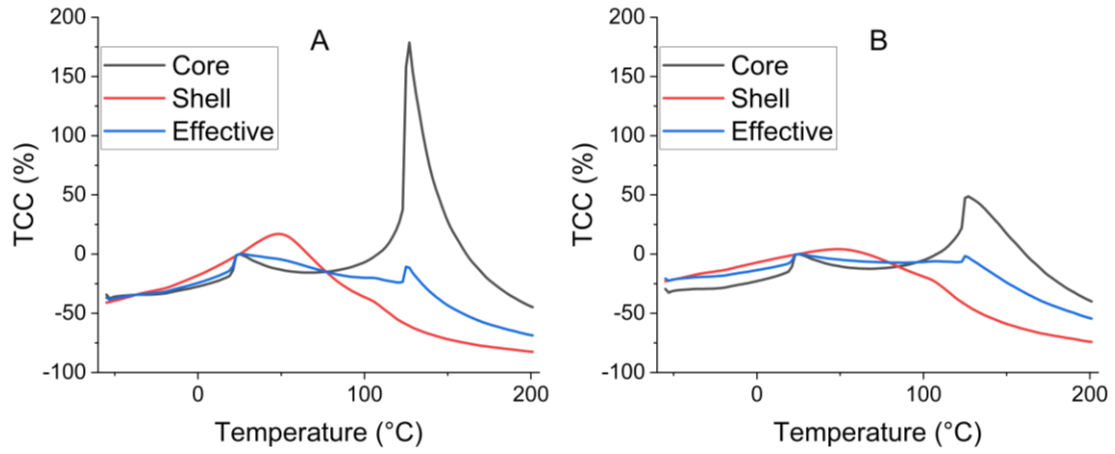

Figure 3.10: TCC (%) vs Temperature (°C) plots for (A) no field effect and (B) with field effect showing changes in the core, shell, and effective TCC at an applied field strength of 1MV/m and $\beta=1x10^{10}\ C^{-3}V^5m$ *for both materials with a volume ratio of 50-50.*

In the NFE case (Figure 3.10A), we can see that there is a change of about 50% over the temperature range. As the temperature approaches the Curie temperature (T_c), there is a sharp increase to ~180%, pushing it well outside the acceptable TCC stability range of class 2 capacitors, as mentioned in Chapter 2. This sharp spike could be reduced by doping, which leads to the generation of a shell material with properties like those seen in Figure 3.10. Solving for just the shell-like material shows a variation of TCC from +20% to -80%, which is also outside the acceptable TCC stability range for class 2 capacitors. However, when the shell and BT are combined, here in a series configuration, the TCC properties are averaged out and would possess the properties between the two materials. By tuning the volume ratio, the temperature stability can be modified. This is seen in Figure 3.10A, solving for a core-shell volume ratio of 50-50, the maximum change in TCC decreases to 68%.

In Figure 3.10B, it is quite noticeable that applying a DC bias significantly improves the temperature stability of the core and shell materials, with the core having a TCC of just 28% at the T_c. This value is further improved by making it a series structure, bringing down the TCC to just -55%. This change in the TCC is governed by several factors, including the volume ratio of the core material and shell material, their conductivities, volume fractions, relative permittivity, thicknesses, and the β value. By modifying each of these factors, the TCC can be affected in different ways, and it becomes necessary to understand the effects of modifying these properties.

3.3.1.1Results

3.3.1.1.1 Applied electric field.

The first parameter modified in solving for TCC is the strength of the electric field that the dielectric as a whole is subjected to. We solve for a model that is made up of 50% core and 50% shell-like material in a series configuration where the applied voltage is increased from 0.5 V to 2.5 V. We also study the NFE case, where voltage effects are ignored and used as a comparison.

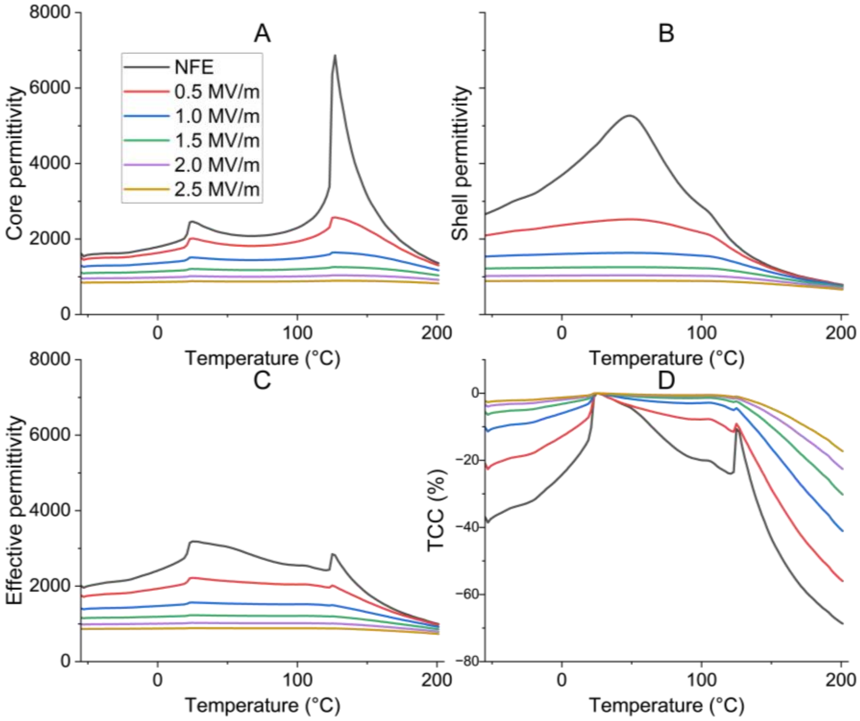

Figure 3.11: (A) *Effective* permittivity vs temperature (°C) and (B) TCC(%) vs temperature (°C) graphs showing changes in the effective TCC of a core-shell system having a volume ratio of 50-50 as the applied electric field is increased from 0.5 MV/m to 2.5 MV/m.

In Figure 3.11A, we can see that in the NFE case, there is a significant variation of the effective permittivity across the temperature range with a max effective permittivity of about ε_r=3200 and a minimum of about ε_r=1000. However, as a DC bias is applied, the TCC reduces. This stabilisation is also accompanied by a reduction in the overall effective permittivity, and therefore a drop in capacitance as well. With relative permittivity dropping to a maximum of only about 900 at the max field value of 2.5 MV/m. In Figure 3.11B, we can see that increasing the applied field improves the overall TCC while reducing the drop in TCC past the T_c. At 2.5 MV/m there is barely any variation in the TCC before the T_c with a gradual increase to about -20 at 201°C.

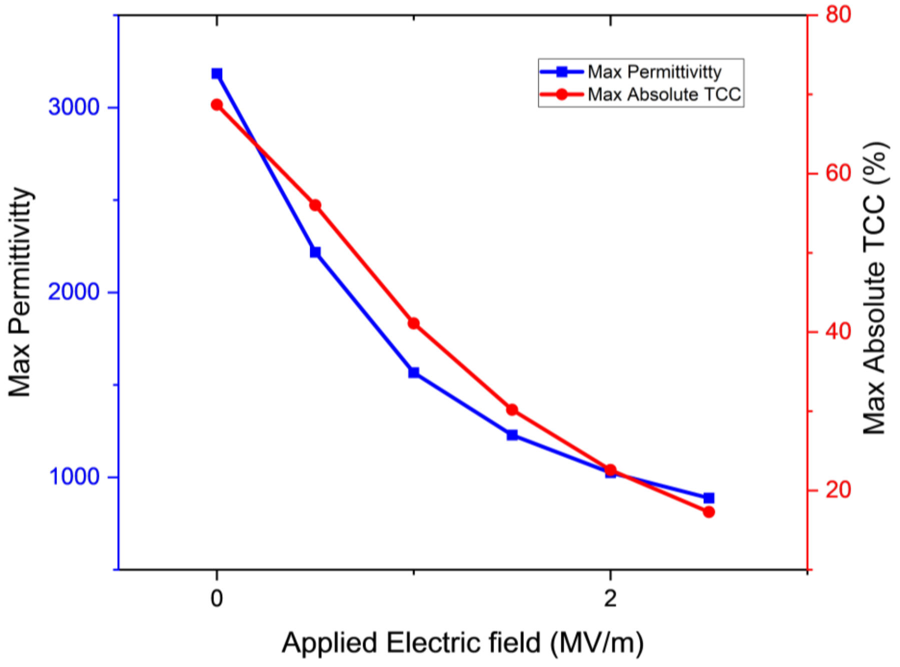

Figure 3.12: Decrease in max *effective* permittivity (blue) and max absolute TCC (red) as the electric field is increased to 2.5 MV/m. The decrease in max absolute TCC can also be referred to as an increase in stability of the TCC.

We find that increasing the applied voltage can have a significant effect on the max absolute TCC, with a 74% drop when the field strength is increased to 5 MV/m. This improvement in TCC also comes with the drawback that the effective permittivity decreases by about 72%, as seen in Figure 3.12. Although the drop in effective permittivity is high, the change in effective permittivity across the temperature range of the material is less than 5% till 125°C and less than 20% at 201°C. This brings it into the range of an X7P or an X9S for a material that is out of specification prior to applying a DC bias.

3.3.1.1.2 Volume Fraction

Next, the effects of modifying the volume fraction of the core and shell material was studied. We vary the volume fraction of the core materials such that 0.2BT denotes where a system has a core of BT that makes up 20% of the total volume of the system, with the shell material comprising the remaining 80%. Similarly, the 0.4BT, 0.60BT, 0.8BT and 1BT cases consist of 40 %, 60 %, 80 %, and 100 % of barium titanate by volume, respectively. Figure 3.13(A) and (C) show relative effective permittivity and TCC in the absence of an applied electric field, while Figure 3.13(B) and (D) show TCC and relative effective permittivity WFE applied. The core and shell materials were assigned equal conductivities and field effect fraction (β) with an applied electric field strength of 1 MV/m for the WFE case.

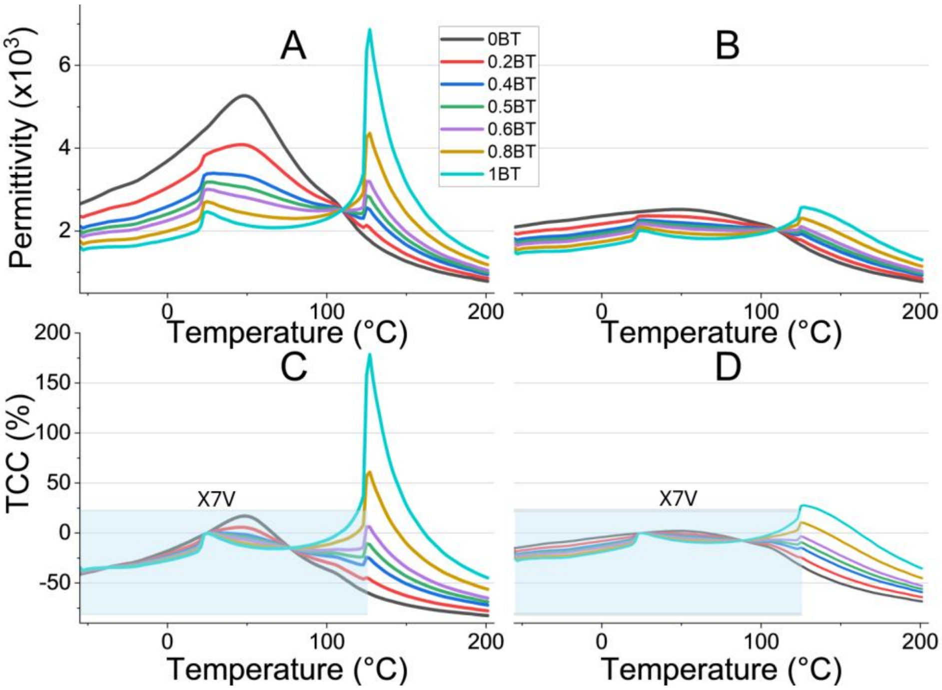

Figure 3.13: Change in relative permittivity and TCC for different core-shell volume ratios. (A) and (C) are the NFE cases, while (B) and (D) are in the presence of an electric field having a field strength of 1MV/m. The blue shaded regions show the acceptable TCC range for X7V capacitors and $\beta=1x10^{10}$ $C^{-3}V^{5}m$.

According to Figure 3.13(B), the application of an electric field reduces the overall change in TCC values. The TCC across the temperature range improves as the amount of BT present in the material increases from 0 to 80%, but a pure BT material has a wider range of TCC values than 0.8BT. The field effect also aids in mitigating the rotation observed as the quantity of shell material increases. From Figure 3.13(B), the maximum and room temperature effective permittivity values of the material are substantially diminished.

A prevalent approach to improve the TCC of BT involves the use of combining it with another material, typically through doping. The data above indicates that applying a DC bias can yield comparable effects, with a TCC improvement of approximately 400% when a 10 V voltage is applied. As mentioned previously, a crucial consideration in material selection is the variation in capacitance across its operational temperature range, with smaller variations being more desirable. This is directly related to the change in effective permittivity across the temperature range. Despite the reduction in effective permittivity due to the DC bias, the percentage change in effective permittivity across the working temperature is significantly improved. This helps improve the capacitor's stability and reliability.

In the case of a 0.8BT, the change in TCC is lowered from roughly 60% to merely 45%. This adjustment brings a material that was initially out of specification into the X9U category. Similarly, for pure BT, the maximum absolute TCC is reduced to about 35%, which comfortably falls within the range of an X7V capacitor.

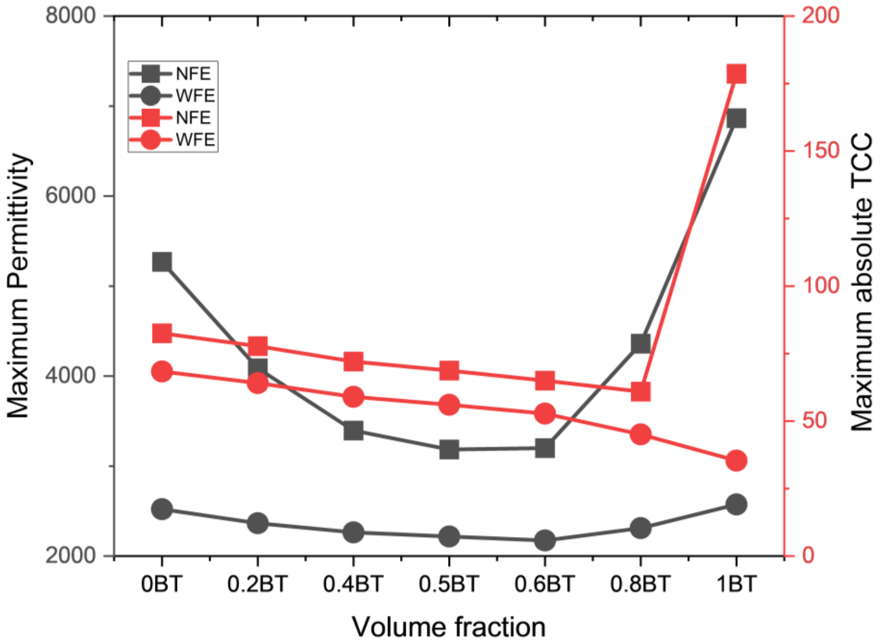

Figure 3.14: Change in max effective permittivity (black) and max absolute TCC (red) as the core-shell volume ratio is modified for the NFE and WFE cases.

From Figure 3.14, it is observed that the application of an electric field to a core-shell system with a core ratio of 0.2 (by volume) can enhance the maximum TCC to a value comparable to a core ratio of 0.6 without field effects. In a similar vein, applying a field effect to a core ratio of 0.4 boosts the maximum TCC to a value comparable to 0.8 without field effects. Additional enhancements to the TCC are noted with an increase in the core volume ratio. These advantages can be further amplified by applying a higher voltage.

3.3.1.1.3 Conductivity Ratio

Since the conductivity of the material can modify the potential difference the material experiences and, as such, the generated electric field in the material, it is important to understand how the conductivity of the different components can affect the electric field effect strength. Five cases were generated with the shell material having a conductivity of 0.5,1,1.5, and 2 times the conductivity of BT and as previously, NFE is the case where field effects are ignored. The ratio of the shell to the core is once again set to 0.5 by volume, and the applied voltage was set to be 1 V.

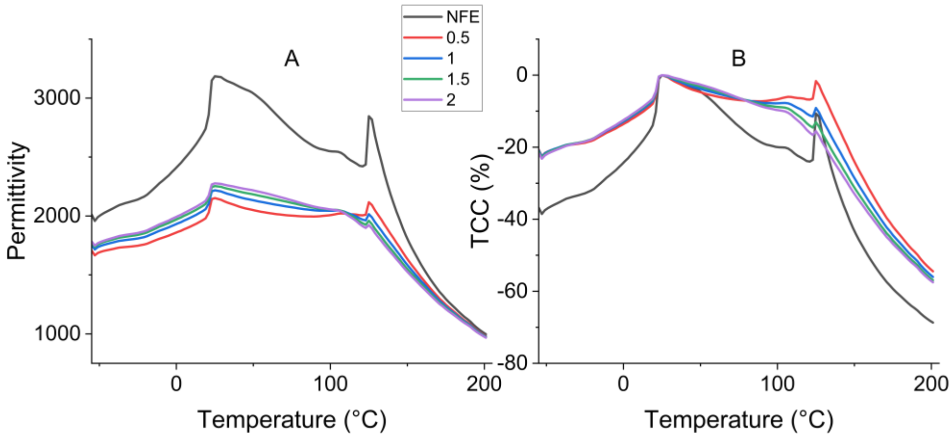

Figure 3.15: (A) TCC and (B) effective permittivity graphs showing change in values as the value of the conductivity of the shell material is modified from 0.5 times to 2 times the core conductivity *and* $\beta=1x10^{10}$ $C^{-3}V^{5}m$ *for both materials with a volume ratio of 50-50..*

From Figure 3.15(A) and (B) we see that as the shell changes from being more conductive than the core to being more resistive, there is a minor counter-clockwise rotation in the effective permittivity and the TCC of the core-shell structure, but a 'pinching' effect in relation to the room temperature value.

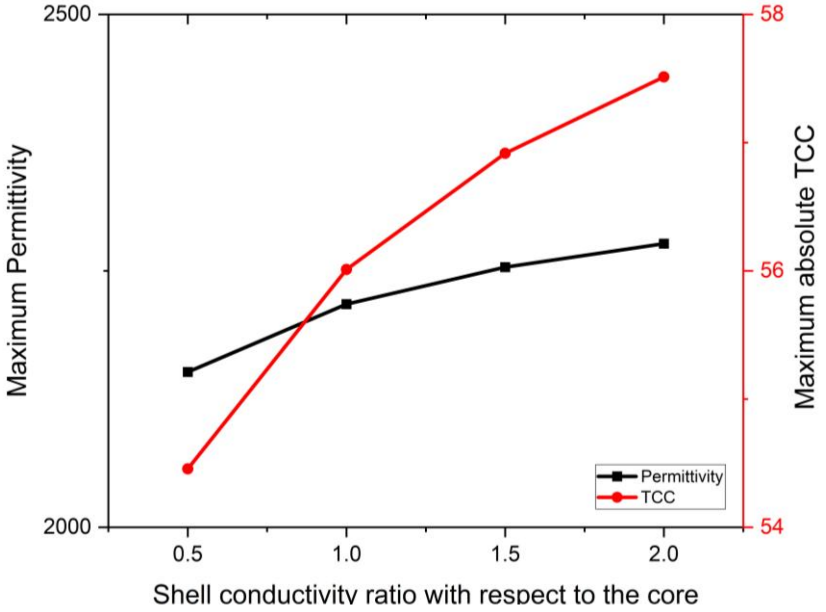

Figure 3.16: Increase in max effective permittivity (blue) and max absolute TCC (red) as the conductivity of the shell increased when compared to the core from 0.5 to 2 times the conductivity of the core.

We can see in Figure 3.16 that using a material that is more resistive than the core can provide minor benefits to the TCC. If the shell material has a 2 times higher conductivity than the core, it has a 2% higher maximum absolute TCC than when the shell has a conductivity half of that of the core. This also corresponds with a 5.7% drop in effective permittivity from approximately ε(E)=2280 to ε(E)=2150.

3.3.1.1.4 Thickness

From equation 2.2, we know that reducing the thickness of the dielectric is a common method to improve the capacitance of a capacitor. The effect of modifying the thickness of the capacitor has been modelled and described below. As in the previous model, the core-shell volume ratio was set to 0.5, and the applied voltage was set to 1V. The thickness of the model was increased from 10 µm to 30 µm.

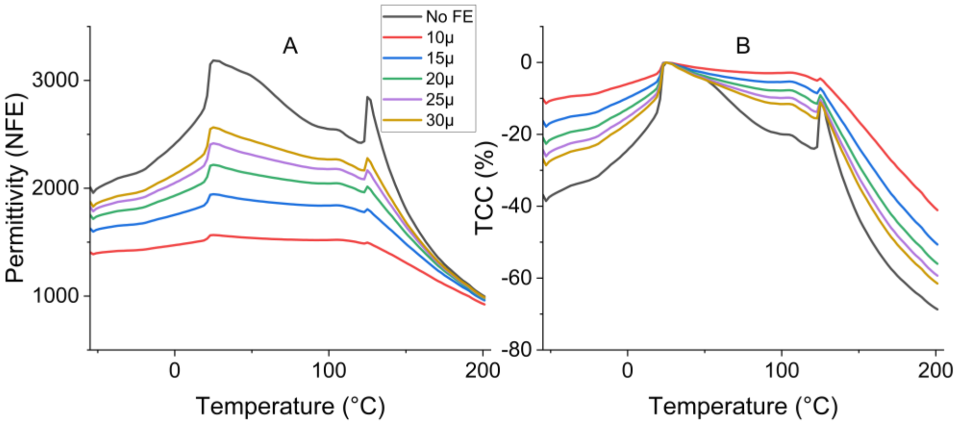

Figure 3.17: (a) TCC and (b) effective permittivity graphs showing change in values as the thickness is modified from 10µm to 30 µm and β=1x10^{10} C^{-3}V^{5}m for both materials with a volume ratio of 50-50 at an applied field of 1MV/m.

From Figure 3.17(A), we can see that reducing the thickness of the material leads to a drop in the effective permittivity of the core-shell material. The trend looks similar to the drop in effective permittivity observed in Figure 3.11(A). From equation 2.2, we know that the strength of the field is inversely proportional to the thickness, so we would expect the field strength to increase as the thickness is reduced, leading to a reduction in effective permittivity as observed. Accompanied by this reduction, a flattening of the TCC can be seen in Figure 3.17(B) as the thickness is reduced.

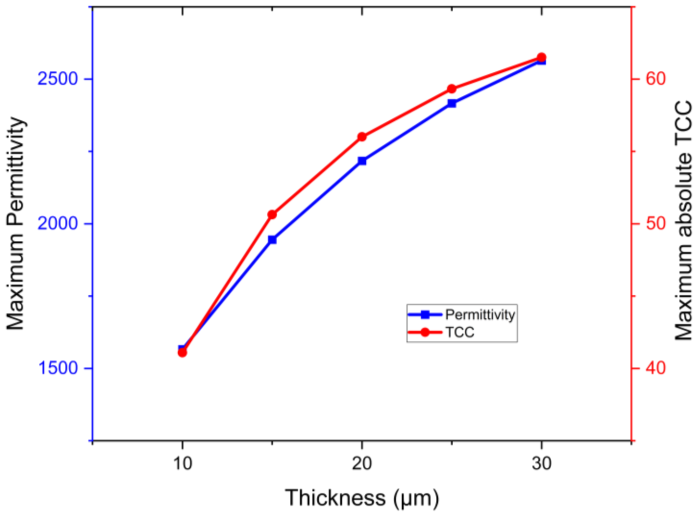

Figure 3.18: Increase in max *effective* permittivity (blue) and max absolute TCC (red) as thickness is increased from 10 µm to 30 µm

From Figure 3.18 we see that as thickness is reduced, there is a 39% drop in maximum effective permittivity from ε(E)=2564 to ε(E)=1566. However, as in the previous cases, this corresponds with an improvement of the TCC with a maximum absolute TCC reduction of nearly 20% to a value of just 42% at a thickness of ten µm.

3.3.1.1.5 Johnson's parameter β

As mentioned previously, the β value is an anharmonic coefficient, also known as Johnson's parameter and represents the ferroelectric non-linearity of the material. It can be obtained by fitting the observed effective permittivity drop with increasing voltage[1]. As stated before, BT has a range of 10^{10} and up to 10^{12} Vm^5/C^3 [7,8]. Doping BT can modify this value, so it becomes necessary to understand what happens when the core and shell have different β values. In this model, the β value for the shell was changed to 0.25, 0.5, 0.75 and 2 times that of the β value of the core.

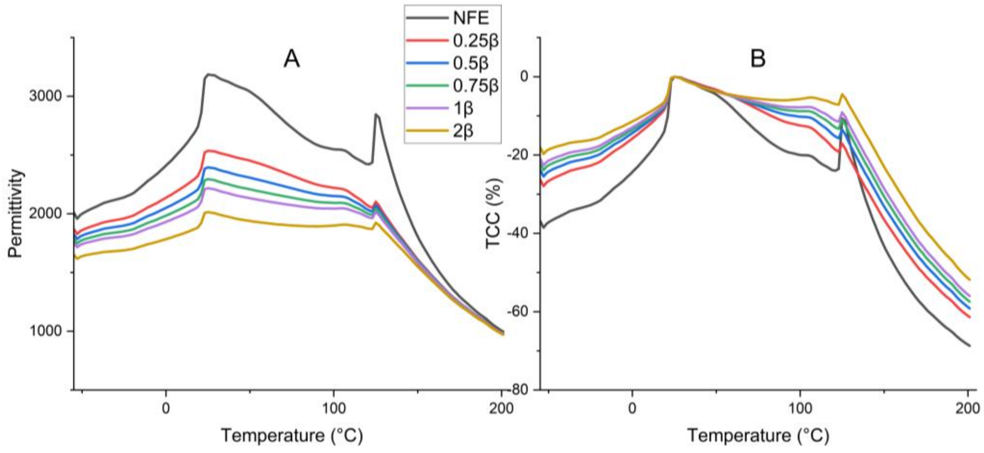

Figure 3.19: (A) TCC and (B) relative permittivity graphs showing change in values as the β of the shell is modified from 0.25 to 2 times the β of the core set to be 1x10^{10} *C*$^{-3}$*V*^{5}*m with a volume ratio of 50-50at an applied field strength of 1MV/m..*

In these cases, the modified β value has improved the max absolute TCC by about 19%. The change in effective permittivity was also improved from 59% with NFE to about 27% at 2β for the under 125° temperature range.

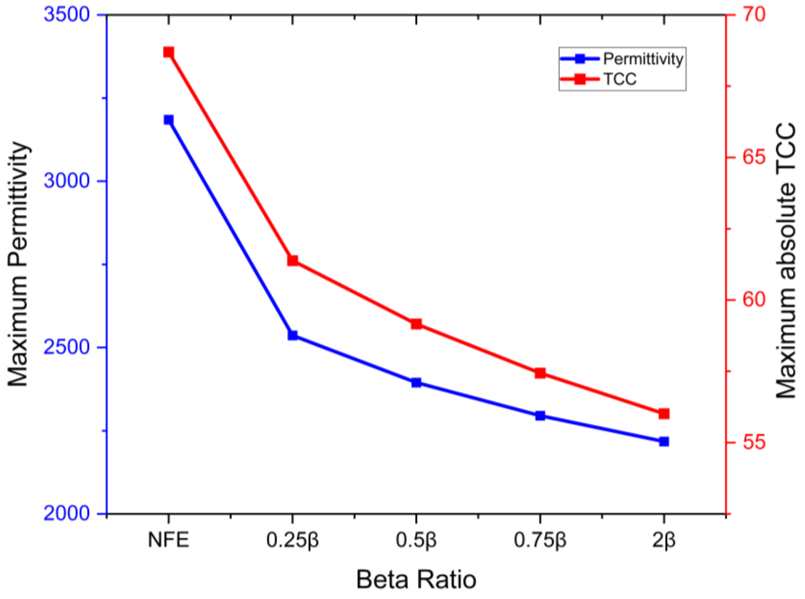

Figure 3.20: Increase in max effective permittivity (blue) and max absolute TCC (red) β value is modified.

3.3.1.1.6 Summary

In conclusion, the study highlights the significant role of various material and design factors in optimising the performance of core-shell dielectric systems. Applying an electric field greatly improves the temperature coefficient of capacitance (TCC), enhancing stability across a broad temperature range. This is coupled with a reduction in effective permittivity, which is manageable within specific tolerances. Adjusting the core-shell volume ratio, especially by increasing the proportion of barium titanate (BT) in the core, further improves TCC and brings the material into desirable specification ranges, such as X9U or X7V. The conductivity ratio between the core and shell also plays a critical role, with more resistive shell materials offering slight improvements in TCC and reduced permittivity. Reducing the thickness of the dielectric material lowers effective permittivity but enhances TCC stability, making it a key consideration in design. Finally, modifying Johnson's parameter (β) further refines the material's performance, increasing TCC stability and minimising relative permittivity variations, especially at lower temperatures. Together, these findings provide valuable insights into tailoring material properties for enhanced capacitor performance, with a focus on achieving greater stability and reliability under varying operational conditions.

3.3.2 Parallel Model

As a core and shell model has regions of a series configuration but also aspects of a parallel configuration, we now look at combining the materials electrically in parallel, as shown in Figure 3.21.

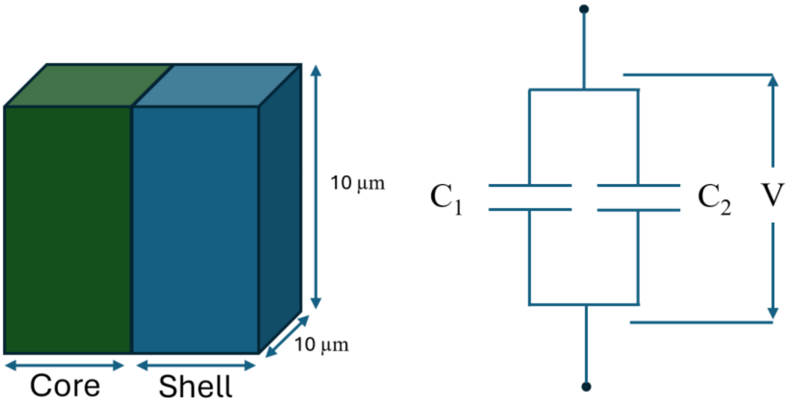

Figure 3.21: Figure (left) showing how the materials are arranged in the parallel analytical model. The green represents the layer which has been assigned the properties of the core material (Barium Titanate), and the blue material has been assigned the properties of the shell material. Figure (right) shows the circuit arrangement for the parallel model.

For two dielectrics arranged in parallel, as seen in Figure 3.21, we know that:

$$V = V_{core} = V_{shell}$$

Equation 3.17

Where V is the applied DC voltage, t is the thickness of the dielectric, $E_{core}$is the electric field experienced by the core, E_{shell} is the electric field experienced by the shell.

From Equation 2.2, we know that V=Et, therefore:

$$E_{core} = \frac{V}{t}$$

Equation 3.18

$$E_{shell} = \frac{V}{t}$$

Equation 3.19

The Johnson's parameter for both the core and shell is again set to be $\beta = 1\text{x}10^{10}$ $C^{-3}V^{5}m$. Using this alongside the effective permittivity, conductivity, and electric field values in Johnson's equation, the field-effect relative permittivity can be calculated.

For a parallel arrangement, we know that:

$$C_{total} = C_{core} + C_{shell}$$

Equation 3.20

$$C_{total} = \varepsilon_{eff} \frac{A}{d}$$

Equation 3.21

$$C_1 = \varepsilon_r(\text{core}) \frac{A_1}{d}$$

Equation 3.22

$$C_2 = \varepsilon_r(\text{shell}) \frac{A_2}{d}$$

Equation 3.23

Where, C_{total} is the total capacitance, C_1 and C_2 are the capacitances of two capacitors, d= 1, A=dxd is the surface area of the dielectric, k is the volume fraction of the core to the shell, in which 0 represents a pure shell material and 1 is a pure core material. $\varepsilon_r(\text{core})$is the relative permittivity of the core at the reference temperature, and $\varepsilon_r(\text{shell})$ is the relative permittivity of the shell at the reference permittivity.

$$A_1 = d * k$$

Equation 3.24

$$A_2 = d * (1 - k)$$

Equation 3.25

Substituting these in $\varepsilon_{eff} = \varepsilon_r(\text{core})k + \varepsilon_r(\text{shell})(1 - k)$

Equation *3.27* Equation 3.20 we get:

$$\varepsilon_{eff} = \varepsilon_r(\text{core})\frac{d * k}{d} + \varepsilon_r(\text{shell})\frac{d * (1 - k)}{d}$$

Equation 3.26

Solving for which gives us the effective permittivity of the core-shell series model.

$$\varepsilon_{eff} = \varepsilon_r(\text{core})k + \varepsilon_r(\text{shell})(1 - k)$$

Equation 3.27

Where k is the volume fraction of the core to the shell, in which 0 represents a pure shell material and 1 represents a pure core material. $\varepsilon_r(\text{core})$is the relative permittivity of the core at the reference temperature, and $\varepsilon_r(\text{shell})$ is the relative permittivity of the shell at the reference permittivity.

3.3.2.1 Results

3.3.2.1.1 Applied electric field.

As in the series case, the first parameter modified is the strength of the electric field the dielectric is subjected. Using a core-shell volume ratio of 50-50 as used previously and discussed in section 3.3.2. The applied voltage is again increased from 1 to 5 V, which leads to an applied field strength of 1 to 5 MV/m, and the NFE case is where there are no voltage effects on permittivity.

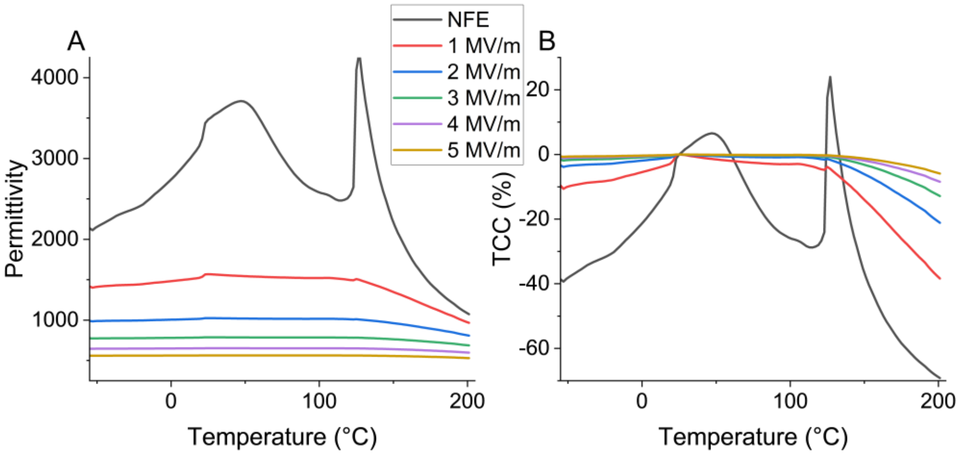

Figure 3.22: (A) Effective Permittivity vs Temperature (°C) and (B) TCC(%) vs Temperature (°C) graphs showing changes in the effective TCC of a parallel system having a core shell volume ratio of 50-50 as the applied electric field is increased from 1 MV/m to 5 MV/m and $\beta=1x10^{10}$ $C^{-3}V^{5}m$ *for both materials with a volume ratio of 50-50..*

In Figure 3.22(A), we can see that in the NFE case, there is a significant variation of the effective permittivity across the temperature range with a max effective permittivity of ε(E)=4319 and a minimum of about ε(E)=1073. As in the series case, applying a DC bias stabilises the TCC over the temperature range, with the stability increasing with increased DC bias. However, this stabilisation is also accompanied by a reduction in the overall effective permittivity, and therefore a drop in capacitance as well, dropping to a maximum effective permittivity of only about 563 at the max field value of 5 MV/m. In Figure 3.22(B) we can see that increasing the applied voltage improves the overall TCC while reducing the drop in TCC past the T_c. At 5 MV/m, there is barely any variation in the TCC before the T_c, with a gradual increase to about -6% at 201°C.

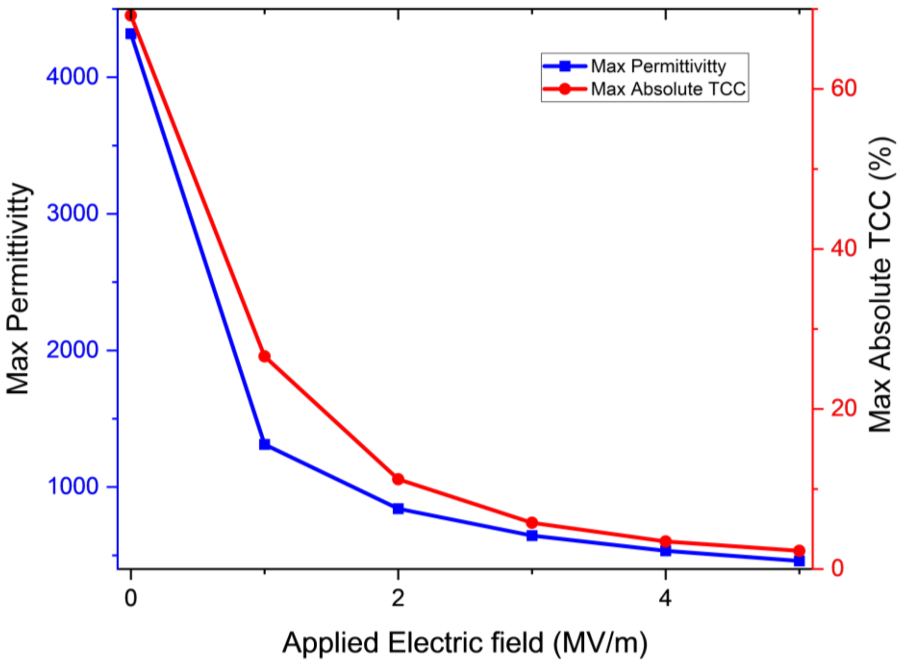

Figure 3.23: Decrease in max effective permittivity (blue) and max absolute TCC (red) as the electric field is increased to 5mv/m. The decrease in max absolute TCC can also be referred to as an increase in stability of the TCC.

We find that increasing the applied voltage can have a significant effect on the max absolute TCC, with a 91.5% drop when the field strength is increased to 5 MV/m. This improvement in TCC also comes with the drawback that the effective permittivity decreases by about 87%, as seen in Figure 3.23. Although the drop in effective permittivity is high, the change in effective permittivity across the temperature range of the material is less than 5% at 201°C. Just as in the series model, this brings it into the range of an X9S for a material that is out of specification prior to applying a DC bias

3.3.2.1.2 Volume Fraction

Next, the effects of modifying the volume fraction of the core and shell material was studied just as for the series model. Similarly, we study the ratios of 0.2BT, 0.4BT, 0.60BT, 0.8BT and 1BT cases. Figure 3.24(A) and (C) show relative effective permittivity and TCC in the absence of an applied electric field, while Figure 3.24(B) and (D) show TCC and relative effective permittivity WFE applied. The core and shell materials were assigned equal conductivities and equal Johnson's parameter with an applied electric field strength of 1 MV/m for the WFE case.

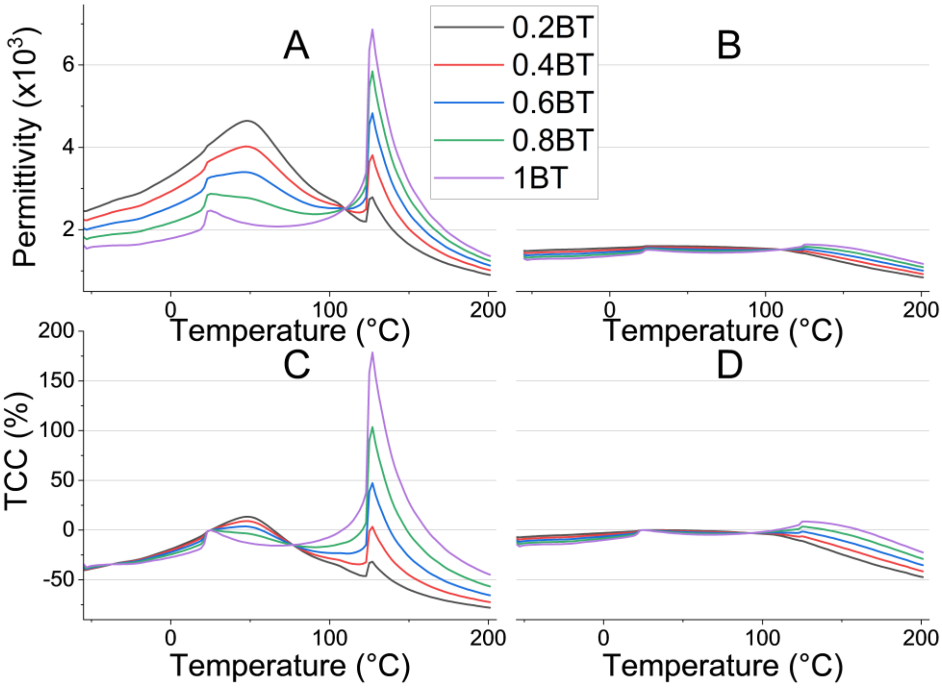

Figure 3.24: Change in effective permittivity and TCC for different core-shell volume ratios. (A) and (C) are the NFE cases, while (B) and (D) are in the presence of an electric field having a field strength of 1MV/m and $\beta=1x10^{10}$ $C^{-3}V^5m$ *for both materials.*

As shown in Figure 3.24(C) and (D), applying an electric field leads to improved TCC values, i.e. less variation over the temperature range studied. This improvement becomes more pronounced as the volume fraction of barium titanate increases, with the maximum TCC shifting from -47% up to a peak value of 22.5%. In Figure 3.24(C) the TCC appears to rotate clockwise as the amount of shell material is increased. This effect is greatly diminished when field effects are taken into account. Finally, from Figure 3.24(A) and (B), it is evident that the maximum and room temperature effective permittivity values of the material are substantially diminished, with pure BT having a 76% reduction in max effective permittivity to 1643.

As discussed previously, combining core and shell-like materials is used to improve the TCC of dielectrics. The data above indicates that applying a DC bias can yield comparable effects, with a TCC improvement from a maximum TCC of 178% down to 22.5% for the 1BT case. As mentioned previously, a crucial consideration in capacitor selection is the variation in capacitance across its operational temperature range, with smaller variations being more desirable. This is directly related to the change in effective permittivity across the temperature range. Despite the reduction in effective permittivity due to the DC bias, the percentage change in effective permittivity across the working temperature is significantly improved. This helps improve the capacitor's stability and reliability.

In the case of a 0.8BT ratio, the change in capacitance is lowered from roughly 104% to merely 29%. This adjustment brings a material that was initially out of specification into the X9U category. Similarly, for pure barium titanate, the change in capacitance is reduced to about 70%, which comfortably falls within the range of an X7V capacitor.

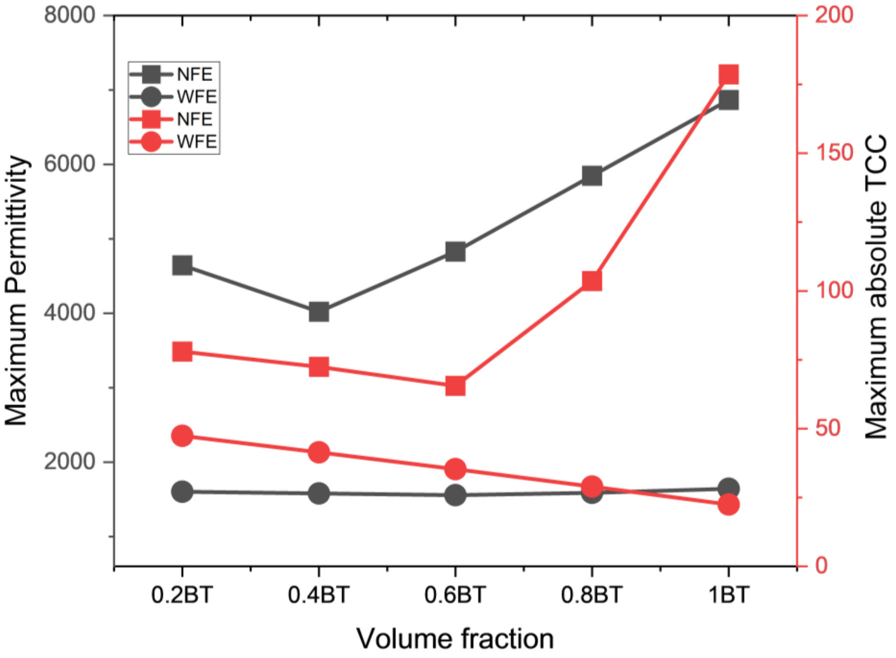

Figure 3.25: Change in max effective permittivity (black) and max absolute TCC (red) as the core-shell volume ratio is modified for the NFE and WFE cases.

From Figure 3.25 for the parallel model, the TCC for the WFE case is better than the NFE case across the board. Implying that there is no combination of shield and core of materials with these properties that is comparable to the TCC of the WFE case. These advantages can be further amplified by applying a higher voltage as well. Additionally, the maximum effective permittivity stays nearly the same as the amount of shell material present is changed.

3.3.2.1.3 Thickness

As in the series model, the core-shell volume ratio was set to 0.5, and the applied field strength was set to be 1MV/m. The thickness of the model was increased from 10μm to 30μm with a step size of 5 μm.

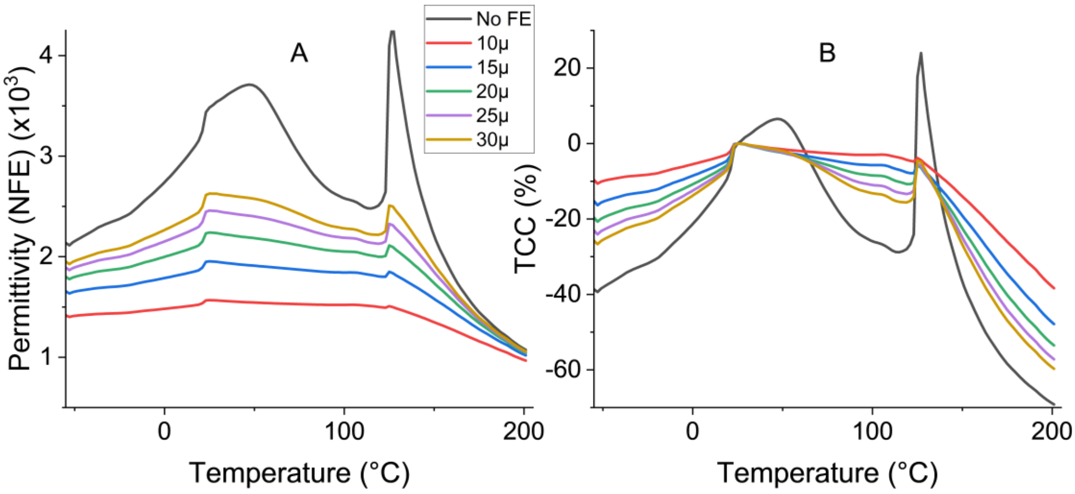

Figure 3.26: (A) TCC and (B) relative permittivity graphs showing change in values as the thickness is increased from 10µm to 30µm and $\beta=1x10^{10}$ $C^{-3}V^5m$ for both materials with a volume ratio of 50-50 at an applied electric field strength of 1MV/m.

From Figure 3.26(A), we can see that reducing the thickness of the material leads to a drop in the relative permittivity of the core-shell material. The trend once again matches the drop in relative permittivity observed in Figure 3.26(A). From equation 2.2, we know that the strength of the field is inversely proportional to the thickness, so we would expect the field strength to increase as the thickness is reduced, leading to a reduction in relative permittivity as observed. Accompanied by this reduction, a flattening of the TCC can be seen in Figure 3.26(B) as the thickness is reduced.

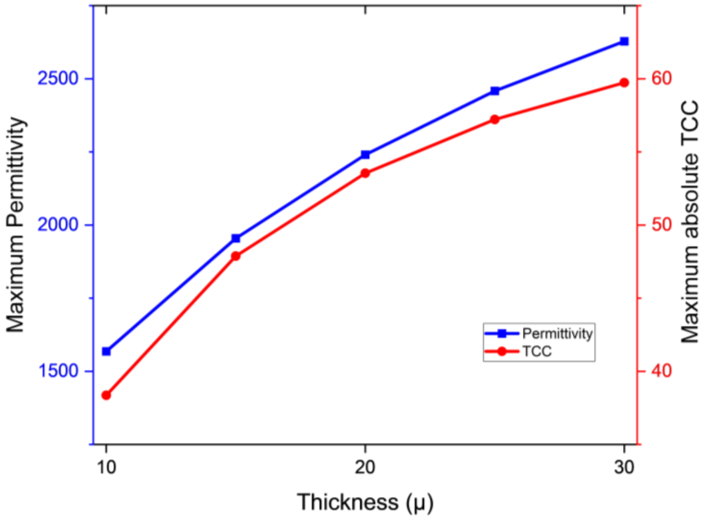

Figure 3.27: Increase in max effective permittivity (blue) and max absolute TCC (red) as thickness is increased from 10 µm to 30 µm

From Figure 3.27, we see that as the thickness is reduced to 10µm, there is a 39% drop in maximum effective permittivity from ε(E)=2628 to ε(E)=1568. However, as in the previous cases, this corresponds with an improvement of the TCC with a maximum absolute TCC reduction of nearly 20% to a value of just 39% at a thickness of 10µm.

3.3.2.1.4 Johnson's parameter, β

Similar to the Series model, we once again change the Johnson's parameter β of the shell to 0.25, 0.5, 0.75 and 2 times that of the core. The 0β case is the case where the shell material is not susceptible to field effects.

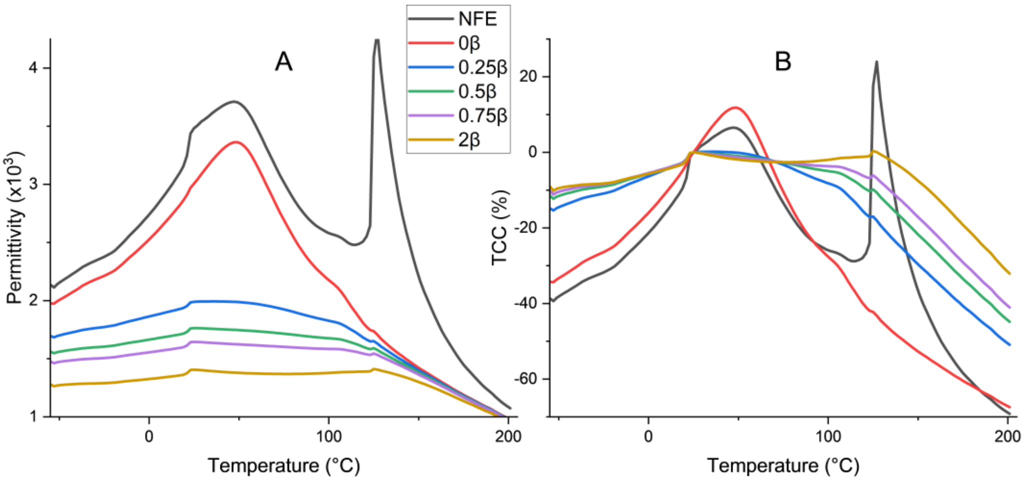

Figure 3.28: (A) TCC and (B) effective permittivity graphs showing change in values as the β of the shell material is modified from 0.25 to 2 times the β of the core set to be 1x10^{10} *C*$^{-3}$*V*^{5}*m with a volume ratio of 50-50 at an applied field strength of 1MV/m.*

In Figure 3.28(B) as the β of the shell material increases from 0 to 2β , the Maximum TCC is reduced from 67% to 32%. Simultaneously, the maximum effective permittivity of the model is reduced from ε(E)=4319 for the NFE case to about ε(E)=1411 at 2β.

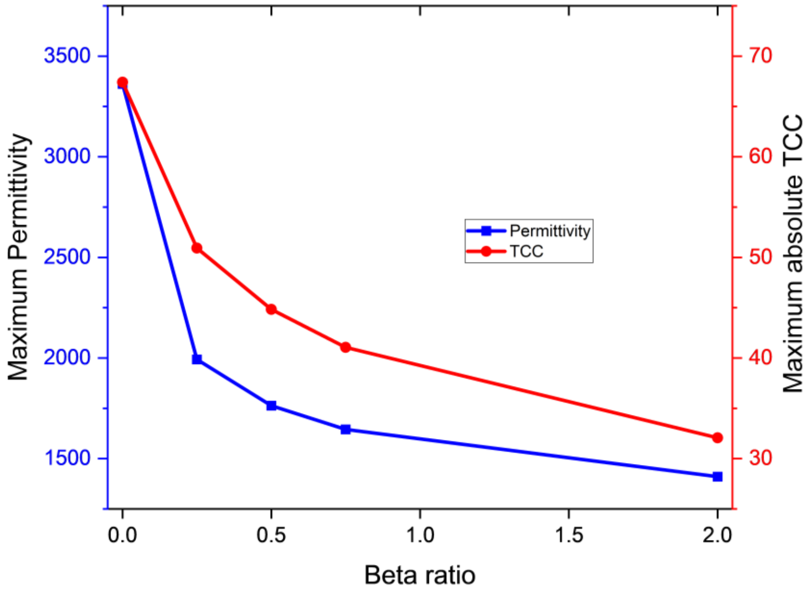

Figure 3.29: Increase in max effective permittivity (blue) and max absolute TCC (red) as the Johnson's parameter of the shell material is modified with respect to the β of the core material.

3.3.2.1.5 Summary

From the analytical models of the parallel system, we see that volume fraction, thickness and the β value of the material can all affect the final TCC of a material when accounting for field effects.

In conclusion, the parallel model of the core-shell dielectric system offers several key insights into optimising the performance of capacitors. Increasing the applied electric field results in a significant reduction in effective permittivity, but it also leads to a marked improvement in temperature coefficient of capacitance (TCC), enhancing the stability of the material across a broad temperature range. While the effective permittivity can drop by as much as 87%, the stability of the TCC improves, making the material more suitable for applications requiring reliable performance despite temperature fluctuations. The volume fraction of the core material, particularly when composed of barium titanate, significantly influences the TCC, with higher core fractions enhancing TCC stability while reducing effective permittivity. Furthermore, adjusting the thickness of the dielectric material results in a trade-off between relative permittivity and TCC stability, with thinner materials leading to lower relative permittivity but improved TCC. Additionally, manipulating Johnson's parameter (β) for the shell material reveals that increasing the β value reduces both TCC and relative permittivity, emphasising the importance of carefully selecting material properties for optimal performance.

Table 3.1: Summary of key changes observed for the series and parallel models.

Property	Series Model	Parallel Model
Permittivity drop (1→5 MV/m)	72% ↓	87% ↓
Max TCC improvement(0.8BT)	60% → 45%	103% → 29%
Permittivity drop (30μm→10μm)	39% ↓	38%↓
Max TCC improvement (0.25β→2β)	59% → 27%	67%→32%

Just as in the series model cases, the strongest effect is the thickness of the material and the applied field strength, with the rest only leading to minor changes in the effective permittivity. As the electric field is inversely related to the thickness, we can focus on the effects of just the applied field strength to better understand how materials react to field effects. As doped BT forms a core and shell structure, the electric field would no longer be uniform across the entire material region. To determine the electric field at each point in the model, a finite element model of a three-dimensional system needs to be solved, and this is the focus of the next chapter.

The experimental work conducted by Yoon et al.[9] provides some insights into the field-dependent capacitance loss in $BaTiO_3$ (BT)-based ceramics. In their study, the researchers evaluated how the particle size of BT powders used in the fabrication process influences the permittivity loss under applied electric fields. Their results demonstrated that finer powder sizes, which typically exhibit higher surface-area-to-volume ratios, led to more pronounced interfacial effects and polarisation losses. Specifically, for an applied field strength of 5 MV/m, the observed capacitance loss ranged significantly from 20% to 60%, depending on the initial powder morphology and processing conditions. This wide variability underscores the importance of microstructure control in mitigating dielectric losses. Notably, their experimental data show strong qualitative agreement with our analytical model predictions, confirming that increasing the applied electric field increases permittivity loss. However, quantitative comparisons reveal some discrepancies. At the same field strength, our series model predicts a 72% reduction in effective permittivity, while the parallel model shows an 87% reduction, both values being higher than the experimental measurements. These differences may be attributed to several factors, including variations in core-shell volume fractions, interfacial defects, or material-specific properties like conductivity that were not fully accounted for in our models.

As their models have a core-shell microstructure, it would utilise both series and parallel pathways thereby leading to further discrepancies. Additionally, experimental factors such as broader particle size distributions or imperfect interfacial bonding could contribute to the smaller observed permittivity changes compared to our simulations. Despite these quantitative variations, the consistent trend of increasing permittivity loss with higher electric fields in both models and experiments provides meaningful validation of our theoretical approach. The agreement in field-dependent behaviour supports the fundamental assumptions of our framework.

Further corroboration comes from the work of Gong et al.[10], who investigated the grain-size dependence of permittivity loss in BT ceramics. Their experiments revealed that coarse-grained samples (grain sizes > 1 µm) exhibited relatively modest capacitance reductions (8–15%) at 3 MV/m, attributed to reduced domain-wall density and weaker interfacial effects. In contrast, fine-grained ceramics (grain sizes < 0.5 µm) showed more severe degradation (25–35%) under the same field, consistent with the heightened role of grain boundaries in charge trapping and field screening. While these experimental values show significant variation compared to our earlier model predictions (72% reduction for the series configuration and 87% for the parallel configuration), these differences can be explained by the same factors we identified previously. This consistent pattern of deviation, despite differences in magnitude, further highlights how microstructure and material homogeneity critically influence field-dependent permittivity loss behaviour not only reinforce the trends observed in our analytical model but also highlight the universal trade-offs between grain size, dielectric nonlinearity, and field stability. Collectively, these independent studies provide a foundation for optimising material design to minimise field-induced losses in high-power applications and highlight the need for a more detailed model to account for these discrepancies.

3.4 Conclusions

When comparing the series and parallel models for core-shell dielectrics, differences emerge in terms of their response to applied electric fields, temperature stability, and relative permittivity. In the series model, increasing the applied electric field from 1 MV/m to 5 MV/m results in an 87% decrease in effective permittivity, while the maximum absolute TCC improves by 91.5%, from a high instability to a more stable value around -6% at 201°C. In contrast, the parallel model exhibits a 75% reduction in the effective permittivity from 1 MV/m to 5 MV/m. However, the TCC in the parallel model shows a marked improvement, stabilising at nearly -6% at 201°C as well, with much less fluctuation compared to the series model. Notably, the maximum TCC in the parallel system improves from -47% (without an electric field) to a maximum of 22.5% as the core material's volume fraction increases. For a pure Barium Titanate (1BT) case, the reduction in TCC and the more stable relative permittivity bring it closer to the X9U specification, reducing the variation in capacitance from 104% to 29%. In the series model, similar effects are observed, but the improvement in stability is more pronounced in the parallel model, which maintains a consistent performance despite varying core-shell volume ratios or applied electric field strengths. The influence of Johnson's parameter (β) in the parallel model also stands out, as increasing β leads to a reduction in both TCC (from 67% to 32%) and relative permittivity (from 4319 to approximately 1411).

The above models account for the global electric field applied to the series and parallel systems, but it does not consider the local field effects within the dielectric materials themselves. Local field effects, as seen in Chapter 2, are influenced by the heterogeneity and interactions between the core and shell materials. These can significantly impact the dielectric behaviour at a microscopic level, leading to variations in the relative permittivity and capacitance across different regions of the material. As the model currently stands, it overlooks these complexities, treating the materials as though they respond uniformly to the global field. To address this limitation and accurately incorporate field dependence for dielectrics, a more advanced model must be developed that integrates the effects of the local electric field variations. Such a model would offer a more comprehensive understanding of the material's performance.

3.5 References

1. Curecheriu LP, Tufesclt FM, Ianculescu A, Ciomaga CE, Mitoseriu L, Stancu A. Tunability characteristics of $BaTiO_3$ -based ceramics: Modeling and experimental study. In: *Journal of Optoelectronics and Advanced Materials*. Vol 10. National Institute of Optoelectronics; 2008:1792-1795. doi:https://doi.org/10.2298/PAC0702023C

2. Placeres Jiménez R, Pedro Rino J, Marino Gonçalves A, Antonio Eiras J. Nonlinear dielectric response and transient current: An effective potential for ferroelectric domain wall displacement. *Appl Phys Lett*. 2013;103(11):112901. doi:10.1063/1.4820589/130034

3. Curecheriu LP, Mitoseriu L, Ianculescu A. Nonlinear dielectric properties of $Ba_{1-x}Sr_xTiO_3$ ceramics. *J Alloys Compd*. 2009;482(1-2):1-4. doi:10.1016/j.jallcom.2009.04.036

4. Graham Dale. *Principal Engineer, KYOCERA AVX Components*.

5. Hahn Brian, Valentine DT. *Essential MATLAB for Engineers and Scientists*. Elsevier; 2019. doi:10.1016/C2018-0-02192-1

6. Foeller P. Novel materials and routes for rare-earth-free $BaTiO_3$-based ceramics for MLCC applications. 2017;(September).

7. Curecheriu L, Buscaglia MT, Buscaglia V, Zhao Z, Mitoseriu L. Grain size effect on the nonlinear dielectric properties of barium titanate ceramics. *Appl Phys Lett*. 2010;97(24). doi:10.1063/1.3526375

8. Myroshnychenko V, Smirnov S, Mulavarickal Jose PM, Brosseau C, Förstner J. Nonlinear dielectric properties of random paraelectric-dielectric composites. *Acta Mater*. 2021;203:116432. doi:10.1016/j.actamat.2020.10.051

9. Yoon JR, Kim MK. Electrical Characteristics of Multilayered Ceramic Capacitors Depending on $BaTiO_3$ Particle Size. *Journal of Electrical Engineering and Technology*. 2020;15(6):2685-2690. doi:10.1007/S42835-020-00505-7

10. Gong H, Wang X, Zhang S, Wen H, Li L. Grain size effect on electrical and reliability characteristics of modified fine-grained $BaTiO_3$ ceramics for MLCCs. *J Eur Ceram Soc*. 2014;34(7):1733-1739. doi:10.1016/J.JEURCERAMSOC.2013.12.028

4 Finite element modeling

4.1 Overview

In this chapter a detailed discussion on finite element modeling (FEM) will be provided. First an introduction to FEM will be provided, emphasizing how it works on a fundamental level.

Next, the role of software to accomplish these fundamental steps will be discussed, along with the process of generating models, focusing on creating accurate geometric representations of the problem domain. The section on boundary conditions discusses how constraints and external factors, such as applied forces, are incorporated into the models to simulate real-world scenarios effectively.

The techniques and information provided will then be applied to describe the generation of a simple layered model. The methodology segment outlines the systematic approach for constructing such models, while the model setup explains the initialisation, including assigning material properties to each layer and defining their interactions. The simulation section details how computational analyses are performed to predict layer-specific behaviours under various conditions.

The discussion on series and parallel models provides insight into two different configurations of layered systems. The series model explores scenarios where layers are interconnected sequentially, influencing each other directly. In contrast, the parallel model examines configurations where layers act independently, contributing separately to the system's overall performance. By comparing these two models with their comparative analytical models, we can test the accuracy of our simulations, thereby testing the accuracy of our future, more complex models.

4.2 Finite element modeling

FEM is a computational technique used to approximate solutions to complex problems in several fields including but not limited to engineering and physical sciences. It has been used to solve complex engineering and physical problems that involve structures, fluids and heat. It is particularly good for simulating physical phenomena in systems where the analytical solutions are difficult or impossible to derive. In all cases, however, it provides an approximation to the solution. To achieve this, it uses governing equations, derived from the mathematical representation of the physical phenomena (heat flow, electrical flow), typically in the form of partial differential equations. These equations can represent equilibrium and the balance of forces or energy in the system, or through constitutive equations relating two physical quantities, such as stress and strain relationships for structural analysis or the heat conduction equation for thermal analysis[1]. By breaking the complex problem down into smaller, simpler parts called finite elements, these governing equations can then be assigned to each of the elements.

These elements are then interconnected at points known as nodes, and by solving the response of the system of elements, the collective behaviour of these elements approximates the behaviour of the entire system. The last main set of equations that are used in this process are known as boundary conditions and play a crucial role in this process. These define how the model interacts with the environment and applied forces. They are critical for ensuring a realistic and solvable model that accurately represents physical behaviour.

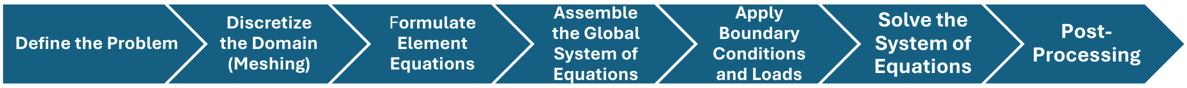

Figure 4.1: Schematic representation of the FEM process.

The process of the FEM is shown in the flowchart in Figure 4.1. It begins with defining the problem by specifying the geometry of the structure. This includes defining the material properties such as relative permittivity and conductivity, identifying external forces or loads applied to the structure and setting appropriate boundary conditions.

Once the problem has been initialised, the domain is discretised through meshing as seen in Figure 4.2, where a cube is divided into 5 smaller simple elements (tetrahedra). The selection of an appropriate choice of element type is based on the problem requirements (e.g., linear or quadratic elements). Tetrahedrons are commonly used as an element shape in FEM for several important reasons, particularly when modeling 3D problems with complex geometries. The tetrahedral element (a pyramid-like 3D shape with four triangular faces) offers flexibility, computational efficiency, and ease of use, especially for unstructured meshes. One potential issue, however, is that tetrahedral elements can sometimes become severely distorted if the mesh is poorly generated, leading to inaccuracies or numerical instability. This can be mitigated with proper mesh refinement and element quality control when setting up the meshing process. In figure 4.2, each ‘node’ has been labelled with a value from 1 to 8. This allows us to define the 5 tetrahedra, known as elements, using 4 nodes each, such as (1235), (3578), (2483), (2856) and (2853).

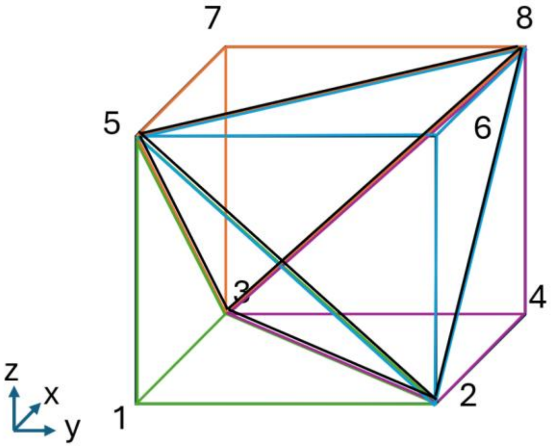

Figure 4.2: Discretised model, showing a cube split into 5 smaller tetrahedra with each tetrahedra given a distinct colour.

The next step is to select the functions that describe how the field variable varies within each element. The element equations are formulated by deriving the governing equations for each element, which involves calculating matrices like the stiffness matrix and force vector based on the shape functions and material properties.

The stiffness matrix K is a square matrix that links the nodal stimuli (forces, voltage, applied at each node) to the nodal response (displacements, current, etc).

In its simplest form, for a linear system, the relationship between nodal forces F and nodal displacements U

$$F = K \times u$$

Equation 4.1

Where F is a vector of applied forces (external loads) at the nodes, u is the vector of unknown displacements at the nodes, and K is the global stiffness matrix that relates the forces to the displacements. Each element, possessing its assigned material property, is therefore assigned its own local stiffness matrix. This could be based on the conductivity or relative permittivity of that material. These local element equations are then assembled into a global system that represents the entire domain. Boundary conditions and loads are applied next, modifying specific nodes in the global system. This could be to incorporate fixed nodes, constraints, and external forces, ensuring that it reflects the problem's physical requirements. Once completed, the matrix of forces, displacements and the stiffness matrix represent a set of simultaneous equations which can be solved.

The system of equations can be solved using numerical methods such as Gaussian elimination; however, in most cases, more specialised algorithms are required, such as iterative solvers to obtain unknown nodal values like displacements or temperatures or in our case, field-dependent permittivities. Results are then visualised to interpret the system's response.

In this chapter, we talk specifically about the setup of the electrical model and how we verified it using an initial, simpler layered model. We then discuss how this was used to model a more complicated core-shell structure.

4.2.1 Software

To conduct a finite element analysis, a governing set of equations needs to be set for each element and then utilised to solve the global set of equations. The electrical properties of the materials in the models in this study were analysed utilising an in-house impedance software, ElCer[2–4]. This method employs a time domain finite element method (TDFEM) to address Maxwell's equations in both space and time. One of the key advantages of this technique is that it allows for the computation of the electronic response based on a mix of material properties (such as conductivity and relative permittivity) and the ceramic system's microstructure, which includes elements like grain boundaries, grain cores, and grain shells of varying shapes and sizes.

The system is meshed using a blend of tetrahedra (4 nodes) and prisms (6 nodes), then solved and examined for its electrical response. Each electrically active area, like a grain or grain boundary phase, can be assigned its own distinct time constant (i.e., conductivity and relative permittivity), enabling the creation of both microstructural and electrical heterogeneity within ceramics.

This model can then be resolved for the electrical response, and the impedance data can be simulated using ElCer, eliminating the need for an equivalent circuit composed of a combination of resistors, capacitors, and/or constant phase elements. A more detailed explanation of this software can be found in Dean et al. [5]

The simulations in this paper were run by submitting bash jobs to the high-performance computing (HPC) clusters at the University of Sheffield. The bash jobs consisted of a mix of Python and MATLAB[6] codes which worked in tandem to simulate the models.

4.2.2 Model generation

As mentioned above, the first step in FEM is model generation. In this thesis, this is done utilising a Python code. The code first requires the user to enter how many grains are designed. We then use a Voronoi process to generate a subdivision of the space into polyhedral (3D) cells. This is achieved by the code generating seed points in space. These can be made regular (for cubic grains) or moved slightly from their ideal position to create more realistic shapes. We then use Voro++[7] to generate the structure, whether it is a simple cube (1 seed point) or a collection of 3x3x3 grains (27 seed points). Once the tessellation is completed, we now have defined a simple structure which we can discretise. This is achieved utilising a well-known meshing software known as Gmsh[8]. A file is generated where each of the nodes is assigned a numerical value. Next, their coordinate values in a 3-dimensional x, y, z coordinate system are assigned. Finally, each of the elements is numbered, assigned a material ID and the nodes making up each element are listed.

For the simple cube seen in Figure 4.2 having a side length of 1 unit and having node 1 located at (0,0,0), the input data provided is the side length of 1, no subdivisions in the x, y and z axes and no mesh. The model data generated by the code is as follows:

Table 4.1: Representive data showing how a cube is divided into 5 tetrahedra as seen in Figure 4.2 is shown in the code. Green indicates the number of nodes and elements within the structure. Blue are the node locations, and pink is the element data.

<table>
<tr><td>Nodes</td><td>Elements</td></tr>
<tr><td>8</td><td>5</td></tr>
<tr><td>Node Number</td><td>x-coordinate</td><td>y-coordinate</td><td colspan="4">z-coordinate</td></tr>
<tr><td>1</td><td>0</td><td>0</td><td colspan="4">0</td></tr>
<tr><td>2</td><td>0</td><td>1</td><td colspan="4">0</td></tr>
<tr><td>3</td><td>1</td><td>0</td><td colspan="4">0</td></tr>
<tr><td>4</td><td>1</td><td>1</td><td colspan="4">0</td></tr>
<tr><td>5</td><td>0</td><td>0</td><td colspan="4">1</td></tr>
<tr><td>6</td><td>0</td><td>1</td><td colspan="4">1</td></tr>
<tr><td>7</td><td>1</td><td>0</td><td colspan="4">1</td></tr>
<tr><td>8</td><td>1</td><td>1</td><td colspan="4">1</td></tr>
<tr><td>Element number</td><td>Material id</td><td>Element shape</td><td colspan="4">Node numbers</td></tr>
<tr><td>1</td><td>1</td><td>Tet</td><td>1</td><td>2</td><td>3</td><td>5</td></tr>
<tr><td>2</td><td>1</td><td>Tet</td><td>3</td><td>5</td><td>7</td><td>8</td></tr>
</table>

3	1	Tet	2	4	8	3
4	2	Tet	2	8	5	6
5	2	Tet	2	8	5	3

Row 1 (green) indicates the number of nodes and elements within the structure. Rows 2-9 (blue) are the node locations, and the last 5 rows (pink) are the element data. In the last 5 rows, column 2 indicates the material ID number and column 3 the shape of the element and how many nodes to expect to connect the shape, in this case 4. In this case, tetrahedra 1 to 3 have been assigned the material id 1, and 4 and 5 have been assigned the material id 2. By assigning different material IDs, they can be assigned different material properties. The material ID number is utilised to assign material properties to the element using a secondary file, which assigns different properties to each ID. For this thesis, the secondary file consists of 3 columns: material id, conductivity and relative permittivity and an example file can be seen in Table 4.2. Using these two files allows us to locate all the elements present in the model and perform the necessary calculations individually.

Table 4.2: Table showing the material data for a model containing two materials. Column one contains the element number, column 2 the conductivity and column 3 the relative permittivity.

Material id	Conductivity	Relative permittivity
1	1e-7	1000
2	1e-4	2000

4.2.3 Boundary conditions

An important part of setting up an FEM problem is defining the boundary conditions. Boundary conditions specify how the system interacts with its environment at the domain boundaries and are critical because they help determine the stability and accuracy of the solution. They can be seen as constraints applied to the problem that influence the behaviour of the field variables (such as displacement, temperature, pressure, or velocity). Correctly defining and applying boundary conditions ensures that the model's behaviour matches real-world interactions. The most common types of boundary conditions used in FEM are Dirichlet, Neumann, and Robin boundary conditions. Each of these represents a different type of constraint, either specifying the value of the field variable or its derivative at the boundary. These boundary conditions are applied to the problem to reflect physical realities like fixed displacements, temperature distributions, or external forces.

The Dirichlet boundary condition occurs when the value of the field variable is known at the boundary of the domain. This can be written as

$$u(x) = g(x)$$

Equation 4.2

Where u(x) is the unknown function, such as temperature and pressure, and g(x) is the known function that defines the value on the boundary. As such, this means that the function u(x) is constrained to take the specific value of g(x) on the boundary of the domain.

For example, in mechanical analysis, Dirichlet conditions are often used to fix the displacement of a structure at certain points (e.g. u(x)=0), such as holding one end of a beam in place. Mathematically, a Dirichlet boundary condition is expressed by setting the field variable equal to a known function on the boundary of the domain. This type of condition can represent situations such as a fixed displacement in structural mechanics or a specified temperature at the surface of an object in thermal analysis. In thermal analysis, a Dirichlet condition might specify that the temperature at the boundary of a solid object is constant.

In contrast, the Neumann boundary condition is often referred to as the natural boundary condition. Neumann conditions are applied when the derivative of the field variable, rather than its value, is specified at the boundary.

This can be written as

$$\frac{\delta u}{\delta n} = g(x)$$

Equation 4.3

Where $\frac{\delta u}{\delta n}$ is known as the normal derivation of the boundary, usually normal to the surface. As such, this type of boundary condition is used when the rate of change of the field variable, such as flux, stress, or heat flow, is known, as it defines a rate of change. This condition is important in problems where external forces or energy flows are applied to the system. For example, in a thermal analysis, a Neumann condition might specify the heat flux at the surface of an object, which is the rate of heat transfer per unit area. These boundary conditions are essential in problems where the system's interaction with its environment is expressed in terms of fluxes or gradients, such as the flow of heat, fluid, or other physical quantities.

The Robin boundary condition, also known as the mixed boundary condition, is a combination of the Dirichlet and Neumann boundary conditions. It can be written as

$$au(x) + \ b\frac{\delta u}{\delta n} = g(x)$$

Equation 4.4

Where a and b represent constants or functions that weight the contributions of the Dirichlet and Neumann components, respectively. It is used when a linear combination of the field variable and its normal derivative is specified at the boundary. This type of boundary condition appears frequently in heat transfer problems, where both the temperature at the boundary and the heat flux are known, such as in convection heat transfer. The Robin condition is particularly useful in modeling situations involving coupled effects, such as thermal conduction and convection or fluid dynamics, where both the value of the field variable and its rate of change at the boundary are important for accurately simulating the system.

The correct application of boundary conditions is critical for ensuring the accuracy of the solution. Applying the wrong type of boundary condition or incorrectly defining the parameters in a boundary condition can lead to erroneous results. For example, if a Neumann condition is mistakenly applied where a Dirichlet condition should be used, the solution for displacement or temperature may not reflect the real physical behaviour of the system. Similarly, applying the wrong flux or pressure conditions in a fluid flow or structural problem can lead to inaccurate predictions of stress distributions or fluid velocities.

In FEM, the boundary conditions are typically applied at the nodes or edges of the mesh that discretizes the domain. The system of algebraic equations that result from the discretisation of the governing differential equations must be adjusted to incorporate the boundary conditions. In the case of Dirichlet conditions, the global system of equations is modified to enforce the known values at the boundary. For Neumann or Robin conditions, the flux or derivative values are incorporated into the system. These modifications ensure that the boundary conditions are satisfied at all relevant points in the domain.

4.3 Layered model

In the previous section, a brief description of how the equations are assigned to the elements of the models is given and how the models are generated. Now we need to look at how these steps are applied to actual models that will be tested. Prior to trying to solve a more complicated core-shell model, which involves a mix of series and parallel sections of materials, a series of test models were constructed to test the accuracy of our simulation. This was done by generating models representing two materials arranged in series and parallel, similar to the previous chapter. These materials were then solved for and compared with an analytical solution to determine the accuracy of our model.

4.3.1 Methodology

To analyse the effect of Johnson's approximation on a material's electrical response under an applied electric field, two types of three-dimensional layered models were constructed: one with materials arranged in series and the other in parallel. These models represent extruded versions of the two-dimensional configurations discussed in the previous chapter, enabling a direct comparison of results to validate the FEM code's functionality. Firstly, a description of how the model is generated and discretised, and finally assigned material properties, will be provided.

4.3.1.1Model set up

The first step is to generate a shape having the overall dimensions of our model. For this discussion, we will be using a cube with a side length of 10 µm represented in 2d in Figure 4.3 (A). This cube has then been divided into several smaller tetrahedra, represented by triangles in Figure 4.3(B), We shall refer from now on to these tetrahedra as elements and each of the vertices that make them up as nodes. Finally, an electrode layer is attached to the top of the model to simulate the applied voltage, which will be applied in a direction from the top to the bottom of the model.

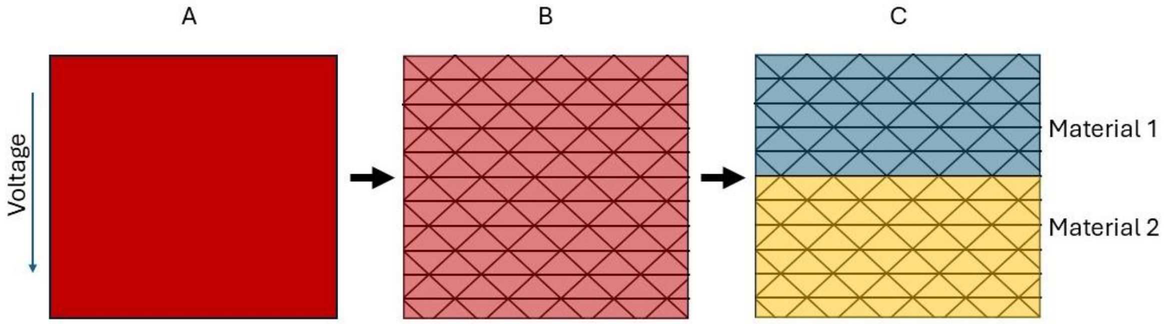

Figure 4.3: Schematic showing the first three steps in the FEM process where (A) is the creation of the model, (B) is discretisation and (C) is the initialisation of material properties for material 1 (blue) and material 2 (yellow)

The first model tested was a series model consisting of two materials stacked one on top of the other. To model this, we assign material properties to each of the elements. This step is referred to as initialisation and is once more done utilising an in-house Python code. Three properties are assigned to each element: the conductivity, relative permittivity and a Johnson's coefficient. Figure 4.3(C) shows what the model looks like after initialisation, where the elements in blue have been assigned the properties of material 1 and the elements in yellow have been assigned the properties of material 2. This method for model set-up can be used for both the series and the parallel models.

4.3.1.2Simulation

To reliably simulate the effects of an electric field on a material utilising Johnson's equation, a program was developed within MATLAB that modelled the changes in the local electric field. Initially, ElCer was used to read the material properties from the secondary file (specifically the conductivity and relative permittivity) and generate an electric field across the material for a given applied voltage, as seen in Figure 4.4(A). Dirichlet boundary conditions at the electrode-air interface to set the electric potential were applied during this process. Additionally, we assume zero displacement currents across the material's free surface by using Neumann boundary conditions in those areas. Although the model could undergo other thermal and electromechanical effects like thermoelectricity and piezoelectricity, we exclude these from our model for simplicity, but could be investigated in future studies.

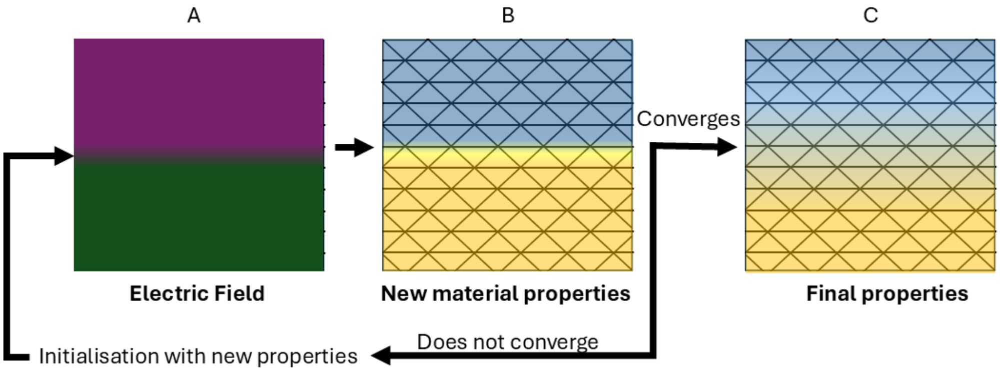

Figure 4.4: Image showing the steps for simulating the field effect. (A) shows the generation of the electric field across the model, (B) shows the new material properties generated after the application of Johnson's equation and (C) shows the final properties of the model once the relative permittivity has converged.

The first step is to run ElCer to determine the electric field profile across the entire model. The output of the model allows us to identify the electric field associated with each of the nodes, where each node contains both the magnitude and the direction of the field. Noting that the material properties are assigned to each element, as such we need to calculate the information of the electric field value from each of the nodes that make up the element to a single value that affects the material property of the element. As such, the local electric field values at each node were used to calculate the electric field at the centroid of each of the elements. The Electric field at each element was calculated by averaging the field at the centroid of each element. The electric field at the centroid $E_{field,Cent}$(x,y,z) of the tetrahedrons was calculated as follows for a tetrahedron having 4 vertices A, B, C, and D, having electric fields of A(x_1,y_1,z_1), B(x_2,y_2,z_2), C(x_3,y_3,z_3), and D(x_4,y_4,z_4) as seen in Figure 4.5.

$$x = \frac{x_1 + x_2 + x_3 + x_4}{4}$$

Equation 4.5

$$y = \frac{y_1 + y_2 + y_3 + y_4}{4}$$

Equation 4.6

$$z = \frac{z_1 + z_2 + z_3 + z_4}{4}$$

Equation 4.7

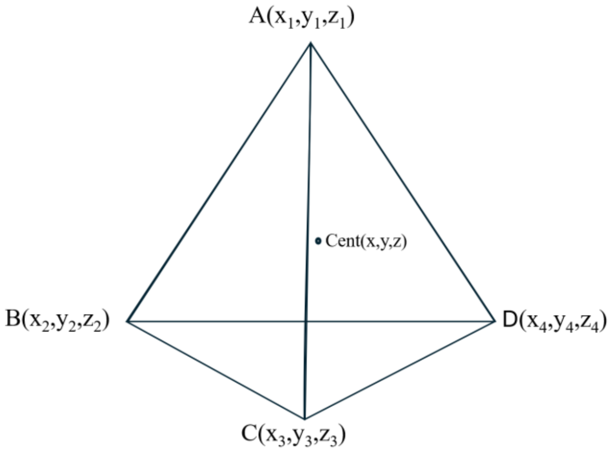

Figure 4.5: A tetrahedron with its 4 nodes A, B, C and D marked with their x,y and z coordinates and the centroid Cent.

The effective electric field at the centroid was also calculated using the same method. Utilising Johnson's equation, the original relative permittivity, the effective electric field and the Johnson's coefficient, we then calculated the new field-effect permittivity for each of the elements as seen in Figure 4.4(B). These calculations were done utilising a program developed in MATLAB. We then initialised the models once more, utilising the new relative permittivity data for the elements. These steps were then repeated until the values converged to less than 0.1% difference in relative permittivity of an element between successive runs. And took these properties to be our final properties as seen in Figure 4.4(C). Once converged, a final model is generated, and an impedance analysis is then conducted.

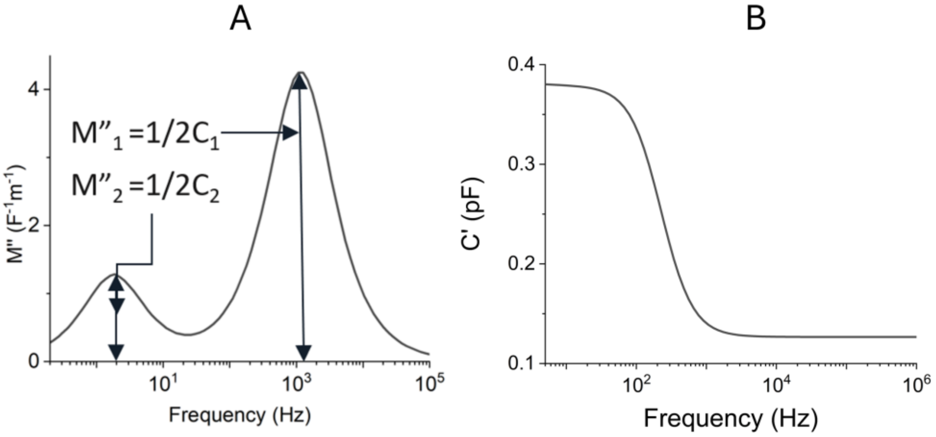

Figure 4.6: Figure showing an example impedance spectrum where (A) M" impedance spectrum having two peaks M"$_1$ and M"$_2$ and how their respective capacitances can be extracted and (B) showing the C' spectrum of a core-shell structured material with the low frequency value representing the shell material and the high frequency the core.

The impedance analysis was conducted by applying an alternating current (AC) voltage across simulated electrodes, and the program computes the resulting distribution of electric potential and current density throughout the microstructure. By systematically varying the frequency of the applied voltage, ElCer calculates the complex impedance at each frequency by dividing the applied voltage by the resulting current. This process yields a frequency-dependent impedance spectrum, which can be directly compared to experimental impedance spectroscopy data, typically presented as Nyquist or Bode plots.

The simulation of the impedance spectra provides us with a method of identifying the individual response of the constituent materials[9]. Here, we focus on the analysis of the M" spectra as seen in Figure 4.6(A), as these are typically dominated by electroactive regions with small capacitances (typically grain-type responses). Conventionally, each Debye-like peak in the M" spectroscopic plots can be considered (in the first instance) to be a parallel Resistor-Capacitor (RC) element. The peak can then be related to the effective capacitance of the model by the formula:

$$M'' = \frac{1}{2C}$$

Equation 4.8

Where M" refers to the peak height and C is the capacitance. In the case of a multi-response (such as when two materials with a time constant which differ by at least two orders of magnitude are present), the assignment of materials is performed based on ω_{max} and the frequency at which M" is the maximum (f_{max}). These are calculated using the following formulae:

$$\tau = \frac{\epsilon_0 \epsilon_r}{\sigma}$$

Equation 4.9

$$\omega_{\max} = \frac{1}{\tau}$$

Equation 4.10

$$\omega_{\max} = 2\pi f_{max}$$

Equation 4.11

Where τ is the time constant, and ω is the angular frequency.

By utilising the electric fields for each element, we effectively simulate the local electric field rather than using the global field. This allows us to simulate the change in electric field over smaller areas of the material to generate a more realistic response from the material by accounting for local field interactions.

4.3.2 Series model

Using the methodology detailed above, we generated models in two different configurations. One in which the materials were aligned in series and one in parallel to test the program and locate any errors in coding.

In the series model generated, the materials were assigned the same conductivities of 10^{-4} S/m. The relative permittivity of material 1 was set to be ε_r =5000 and material 2 to be ε_r =10000. These were then tested across various applied voltages from 1V to 15V and then compared with an equivalent analytical model. The model was arranged as seen in Figure 4.7 with material 1 and material 2 arranged in series, with an electrode layer connected on top of the model.

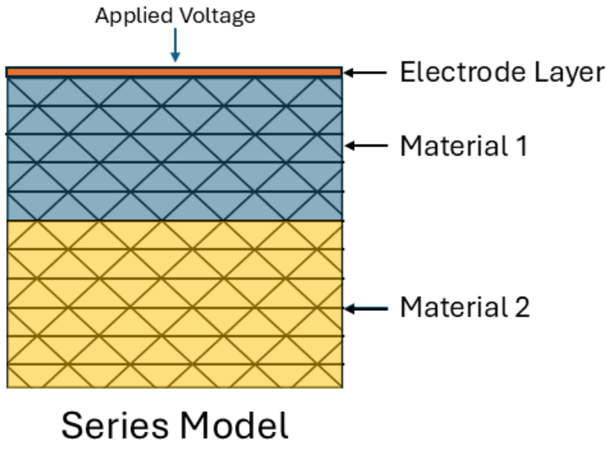

Figure 4.7: Series model showing materials 1 and 2 arranged in series with an attached electrode layer.

To calculate the value of the effective permittivity in the analytical model, the electric field of material 1 (E_1) was calculated using the formula:

$$E_1 = \frac{V * \sigma_1}{(t_1 * \sigma_1) + (t_2 * \sigma_2)}$$

Equation 4.12

Similarly, the electric field across the second material was calculated as:

$$E_2 = \frac{V * \sigma_2}{(t_1 * \sigma_1) + (t_2 * \sigma_2)}$$

Equation 4.13

Where V is the applied DC voltage, σ_1 is the conductivity of material 1, σ_2 is the conductivity of material 2, $E_1$is the electric field experienced by material 1, E_2 is the electric field experienced by material 2 and t_1 and t_2 are the thicknesses of material 1 and 2, respectively. The β value for both materials was assigned to be $1x10^{12}$ $C^{-3}V^5m$, and the thickness of each material was set to be 5µm. These values were then plugged into Equation 2.9, and the effective permittivity for each material was then calculated. Finally, as the materials were arranged in series, the effective permittivity ε_{eff} was calculated using the formula:

$$\frac{1}{\varepsilon_{eff}} = \frac{f_1}{\varepsilon_1} + \frac{f_2}{\varepsilon_2}$$

Equation 4.14

Where $\varepsilon_1$is the relative permittivity of material 1 and ε_2 is the relative permittivity of material 2, and f_1 and f_2 are the volume fractions of material 1 and material 2, respectively.

4.3.2.1Results

For the simulated model, the Johnson's parameter value for both materials was assigned to be $1\text{x}10^{12}$ $C^{-3}V^5m$ and the width of each material was set to be 10 µm and a height of 5 µm and was discretised into approximately 10^5 elements. The materials were assigned the same conductivities of 10^{-4} S/m. The relative permittivity of material 1 was set to be ε_r =5000 and material 2 to be ε_r =10000. For the simulated model, first let us look at the electric field distribution of the layered model as the voltage is increased, as seen in Figure 4.8. One of the key factors that can be seen is that despite the strength of the applied voltage changing, without any changes to the material properties, the electric field distribution remains the same. However, the strength of the field present in materials one and two increases with increasing applied voltage. At an applied voltage of 1 V, the maximum electric field strength is only 0.1 MV/m. This increases to a value of nearly 1.5 MV/m as the applied voltage is increased to 15V.

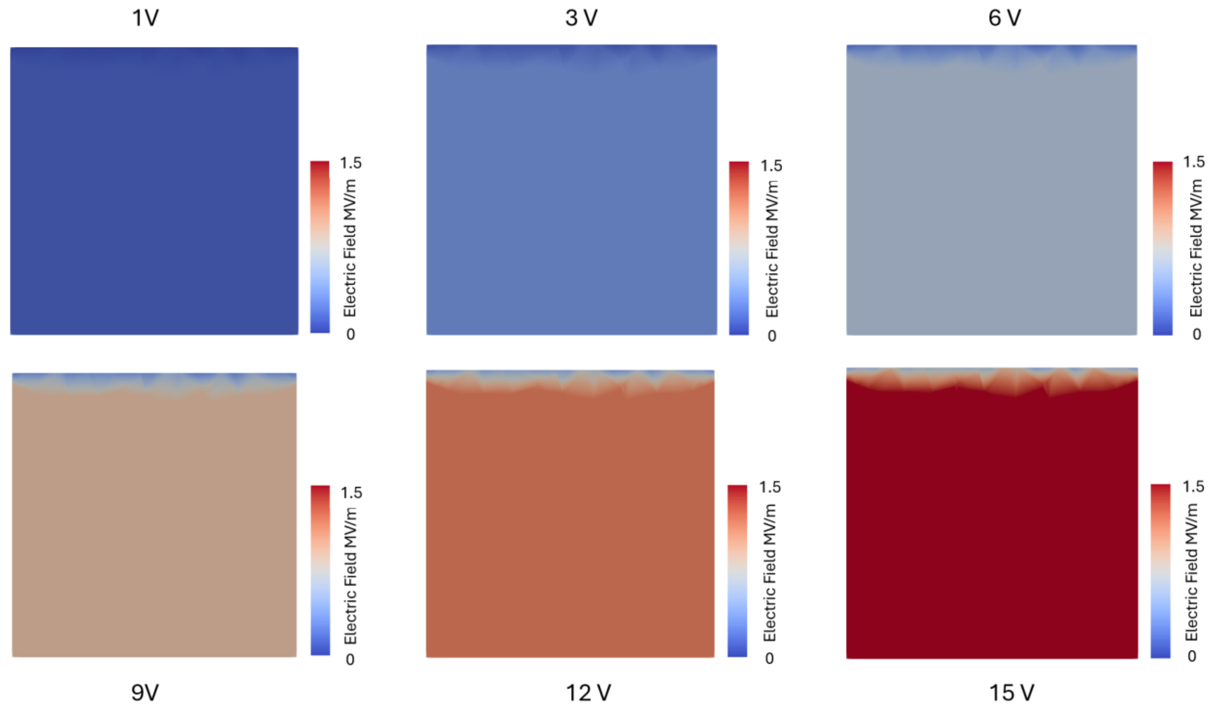

Figure 4.8: Electric field distribution for the series layered model as the applied voltage is increased from 1V to 15V showing the field distribution remaining constant across material 1 (ε_r =5000) and material 2 (ε_r =10000) with the strength of the field increasing as applied voltage increases, The β of both materials was set to be $1\text{x}10^{10}$ $C^{-3}V^5m$ with a volume ratio of 50-50..

Taking a look at the relative permittivity of the simulated models in Figure 4.9, we can see something interesting. For an applied voltage of 1V, we can still observe two distinct materials/layers having distinct relative permittivities of about ε=3750 for material 1 and ε=3000 for material 2. However, as the field strength in increased past this point, the materials start looking more like a single material than a layered structure consisting of two materials with a difference of less than 0.01 between the relative permittivities of material 1 and material 2 and an applied voltage of 15 V. Additionally, similar to the analytical model, there is an 94% reduction in the maximum relative permittivity of the material as the voltage is increased from an expected maximum value of 10000, down to just 600 in the 15 V model.

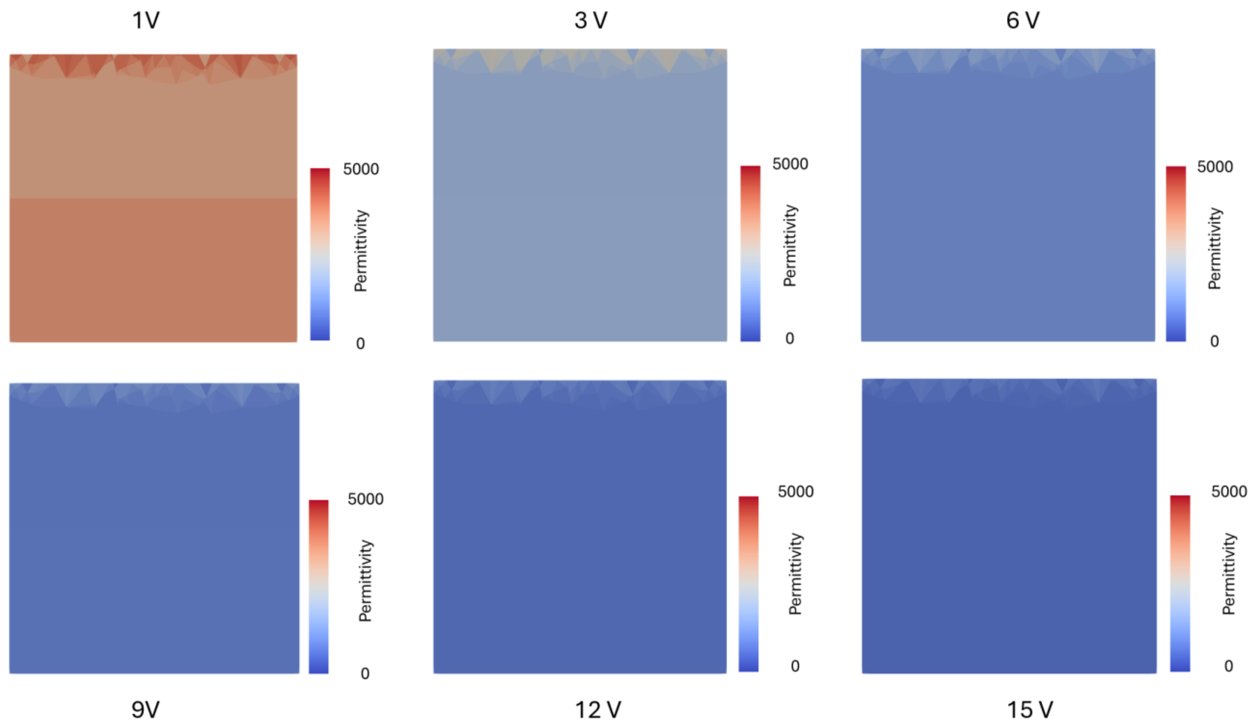

Figure 4.9: Relative permittivity distribution for the series layered model as the applied voltage is increased from 1V to 15V, showing the relative permittivity across materials 1 and 2, with the strength of the field increasing as the applied voltage increases.

Next, an impedance analysis was conducted on the data, which provided us with the effective capacitance of the structure. The relative permittivity was then calculated using the capacitance data and Equation 2.7, as seen in Figure 4.9.,

For the analytical model, the expected permittivity can be seen in Figure 4.10. From these results, we can see that as the voltage increases, the effective permittivity of the model decreases. For our model, this leads to a percentage decrease of around 90% when a voltage of 15 V is applied when compared to the expected value in the absence of field effects. This demonstrates how strong the field effects can be on the capacitance of a material, depending on its Johnson’s parameter value.

For the analytical model, the expected permittivity can be seen in Figure 4.10. From these results, we can see that as the voltage increases, the effective permittivity of the model decreases. For our model, this leads to a percentage decrease of around 90% when a voltage of

15 V is applied when compared to the expected value in the absence of field effects. This demonstrates how strong the field effects can be on the capacitance of a material, depending on its Johnson's parameter value.

The simulated model can be seen to follow a similar trend as the analytical model, with the relative permittivity decreasing with increasing voltage. The decrease from the no field effect case to the 15 V case was also about 90% in the simulated model.

For the analytical model, the expected permittivity can be seen in Figure 4.10. From these results, we can see that as the voltage increases, the effective permittivity of the model decreases. For our model, this leads to a percentage decrease of around 90% when a voltage of 15 V is applied when compared to the expected value in the absence of field effects. This demonstrates how strong the field effects can be on the capacitance of a material, depending on its Johnson's parameter value.

In Figure 4.10 it can be seen that the analytical model and the simulated have a strong correlation, with a less than 1.5% difference between the two models. The difference between the two models can be accounted for by the noise seen at the top of the models in Figure 4.8 and Figure 4.9. This error occurs due to the contact boundary between the electrode layer and the model, and can't be completely removed. However, this can be reduced by using a finer mesh at the contact layer, and so in the core shell models, a finer mesh has been used in the contact layer to reduce the impact from this error source.

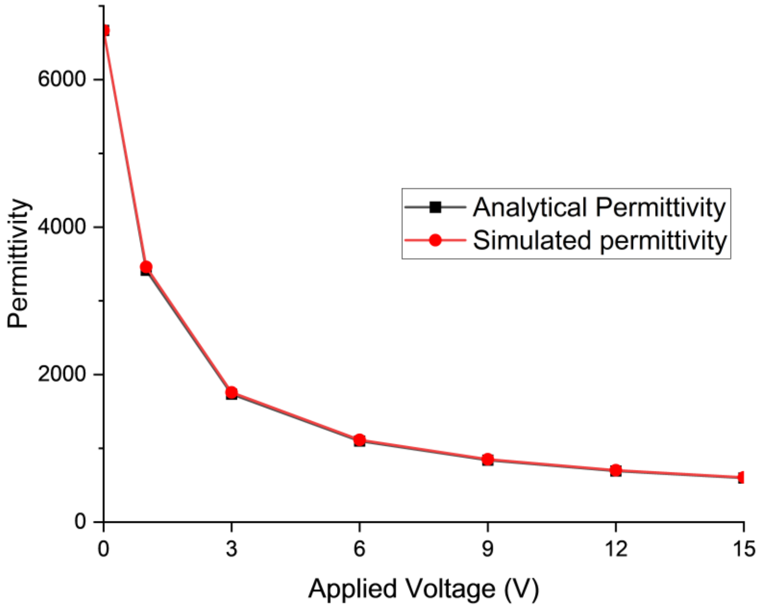

Figure 4.10: Comparison between the analytical and simulated results for the series model shows negligible differences between the models.

From the comparison in Figure 4.10, we can see that the program that has been developed can successfully simulate the field effects on relative permittivity using Johnson's equations for two materials in series with minimal errors. Next, we will simulate two materials arranged in parallel as a further test of our model to ensure its validity.

4.3.3 Parallel model

In the parallel model generated, the materials were assigned the same conductivities of 10^{-4} S/m. The relative permittivity of material 1 was set to be ε_r=10000 and material 2 to be ε_r=5000 once again. These were then tested across the same applied voltages as the series case, ranging from 1V to 15V and then compared with an equivalent analytical model. The model was arranged as seen in Figure 4.11 with material 1 and material 2 arranged in parallel, with an electrode layer connected on top of the model.

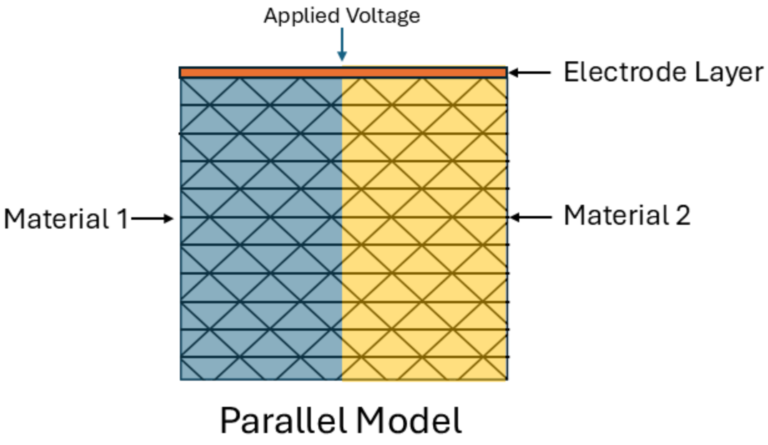

Figure 4.11: Parallel model showing materials 1 and 2 arranged in parallel with an attached electrode layer.

For the analytical model, E_1 and E_2 were once more calculated using Equation 4.1 and Equation 4.2. The β value for both materials was once again assigned to be $1\text{x}10^{12}$ $C^{-3}V^5m$, and the width of each material was set to be 5 µm and a height of 10 µm. These values were then plugged into Equation 2.9, and the effective permittivity for each material was then calculated. Finally, as the materials were arranged in parallel, the effective permittivity ε_{eff} was calculated using the formula:

$$\varepsilon_{eff} = f_1\varepsilon_1 + f_2\varepsilon_2$$

Equation 4.15

Where $\varepsilon_1$is the relative permittivity of material 1 and ε_2 is the relative permittivity of material 2, and f_1 and f_2 are the volume fractions of material 1 and material 2, respectively.

For the simulated model, the materials properties were once again assigned the same properties as the analytical parallel model, and the model was once again discretised into approximately 10^5 elements.

4.3.3.1Results

For the simulated parallel model, first let us look at the electric field distribution of the layered model as the voltage is increased, as seen in Figure 4.12. One of the key differences between this model and the series model is that the electrical field across the material is constant. However, the strength of the field present in materials one and two increases with increasing applied voltage. At an applied voltage of 1 V, the maximum electric field strength is only 0.1 MV/m. This increases to a value of nearly 1.5 MV/m as the applied voltage is increased to 15V, which is in line with the field strength expected by the equation E=V/d.

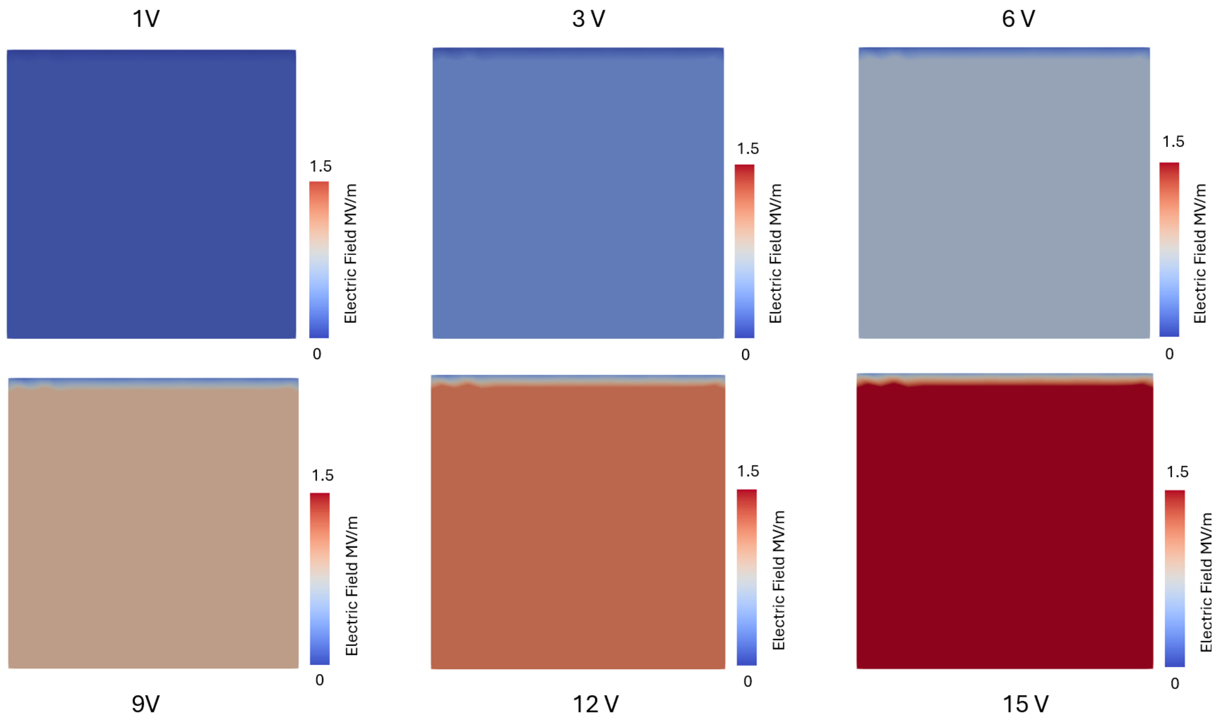

Figure 4.12: : Electric field distribution (magnitude) for the parallel layered model having a β of 1x10^{12} C^{-3}V^{5}m as the applied voltage is increased from 1V to 15V, showing the field distribution remaining constant across materials 1 and 2 with the strength of the field increasing as applied voltage increases. The β of both materials was set to be 1x10^{10} C^{-3}V^{5}m with a volume ratio of 50-50.

Looking at the relative permittivity of the simulated models in Figure 4.13, we can see something similar to the series model. For an applied voltage of 1V, we can still observe two distinct materials/layers having distinct relative permittivities of about ε=3580 for material 1 and ε=3260 for material 2. However, as the field strength increases past this point, the materials begin looking more like a single material than a layered structure consisting of two materials. Additionally, as seen in the analytical model, there is an 89% reduction in the maximum permittivity of the material as the voltage is increased from an expected maximum value of 10000, down to just 597 in the 15 V model.

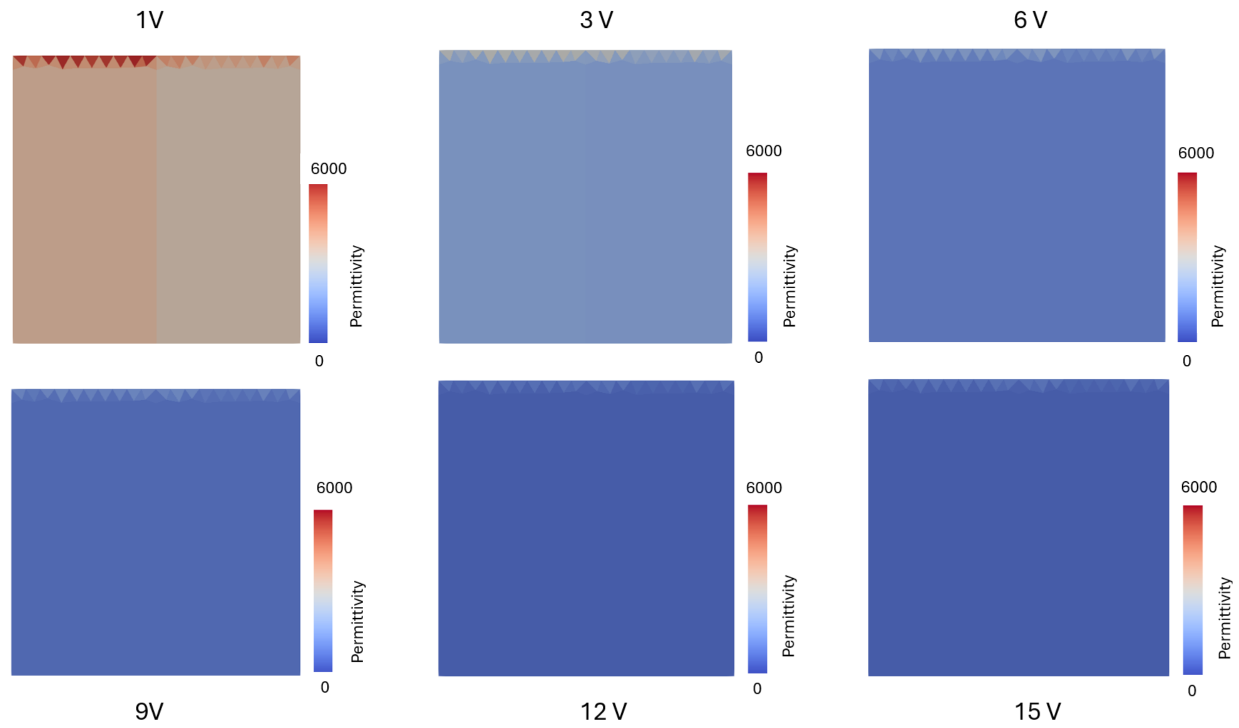

Figure 4.13: Relative permittivity distribution for the series layered model as the applied voltage is increased from 1V to 15V, showing the relative permittivity across materials 1 and 2, with the strength of the field increasing as the applied voltage increases.

Next, an impedance analysis was conducted on the data, which provided us with the effective capacitance of the structure. The relative permittivity was then calculated using the capacitance data and Equation 2.7.

For the analytical model, the expected permittivity can be seen in Figure 4.10. From these results, we can see that as the voltage increases, the effective permittivity of the model decreases. For our model, this leads to a percentage decrease of around 90% when a voltage of 15 V is applied when compared to the expected value in the absence of field effects. This demonstrates how strong the field effects can be on the capacitance of a material, depending on its Johnson's parameter value.

The simulated model can be seen to follow a similar trend as the analytical model, with the relative permittivity decreasing with increasing voltage. The decrease from the no field effect case to the 15 V case was also about 90% in the simulated model.

For the analytical model for a capacitor with the plates arranged in parallel, the expected permittivity can be seen in Figure 4.14. From these results, we can see that as the voltage increases, the effective permittivity of the model decreases. For our model, this leads to a percentage decrease of around 92% when a voltage of 15 V is applied when compared to the expected value in the absence of field effects. This demonstrates how strong the field effects can be on the capacitance of a material, depending on its Johnson's parameter value.

In Figure 4.14 it can be seen that the analytical model and the simulated once more have a strong correlation, with a less than 0.7% difference between the two models. The difference between the two models can once again be accounted for by the noise seen at the top of the models in Figure 4.12 and Figure 4.13. As mentioned previously, this error occurs due to the contact boundary between the electrode layer and the model and can't be completely removed. However, this can be reduced by using a finer mesh at the contact layer, and so in the core shell models, a finer mesh has been used in the contact layer to reduce the impact from this error source.

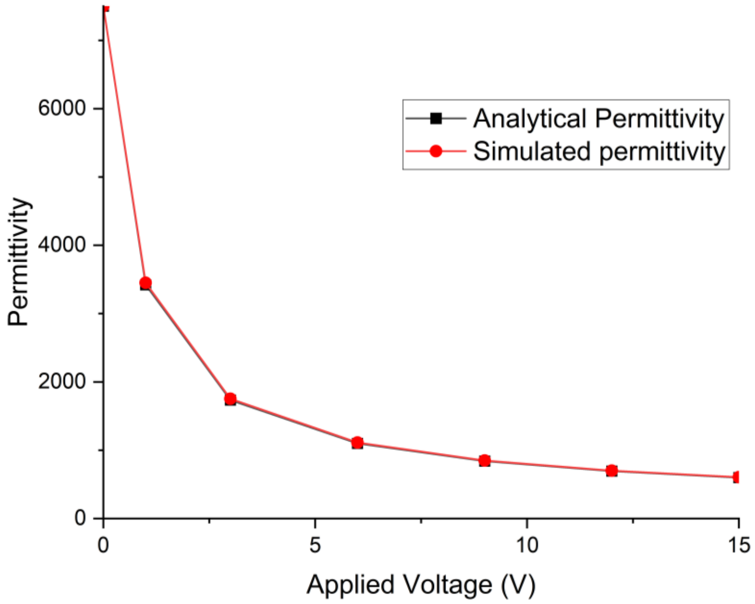

Figure 4.14: Comparison between the analytical and simulated results for the parallel model shows negligible differences between the two models.

4.4 Conclusion

In this chapter we have seen that FEM can be used to solve complex engineering and physical problems by approximating solutions through discretization. The FEM process involves defining the problem, discretizing the domain using mesh generation, selecting element types, and applying material properties. The local element equations are assembled into a global system and solved using numerical methods to obtain unknown values. The chapter shows how ElCer software can be used to simulate electronic responses based on material properties and microstructures.

The chapter focuses on testing a simulation methodology using the Finite Element Method (FEM) to model electric responses in layered materials. Initial tests were conducted with two materials arranged in a series and parallel configuration, with material properties such as conductivity, relative permittivity, and Johnson's coefficient assigned to each element. The models were subjected to varying voltages to compare simulated results with analytical solutions.

In the series model, materials with different relative permittivities were tested, and the results showed a significant reduction in relative permittivity as the applied voltage increased, aligning closely with the analytical model. Similarly, in the parallel model, relative permittivity decreased with voltage, also following the expected trend.

Impedance analysis was performed to determine the effective capacitance, confirming that the simulated model accurately predicted the relative permittivity behaviour, with minimal discrepancies from the analytical results. The study demonstrates the validity of the simulation method, with further refinement suggested for boundary layer errors, which were minimised using finer meshes in more complex models.

To accurately capture the field-dependent dielectric response described by Johnson's equation, it is necessary to construct a three-dimensional (3D) model of the dielectric microstructure. While analytical approaches based on idealised geometries, such as a single cube or simplified series and parallel models, can provide initial insight into the influence of Johnson's parameter β and the overall permittivity response, these models inherently assume uniform electric field distributions and neglect the spatial complexity present in real materials. In practice, dielectric microstructures-particularly those found in advanced ceramics and composites-exhibit significant local variations in electric field and permittivity due to interfaces, grain boundaries, and heterogeneity at multiple length scales[10,11].

As mentioned previously, by implementing Johnson's approximation within a finite element framework, we can simulate the local electric field distribution and the resulting spatially resolved permittivity. This approach reveals how microstructural features, such as core–shell architectures or layered composites, lead to non-uniform field profiles and graded permittivity responses that cannot be predicted using one-dimensional or two-dimensional analytical models. Thus, a 3D model is essential for bridging the gap between analytical predictions and experimental measurements, providing a robust platform for understanding and optimising the voltage dependence of advanced dielectric materials.

4.5 References

1. Baccouch, M. A Brief Summary of the Finite Element Method for Differential Equations. In: Baccouch M, ed. *Finite Element Methods and Their Applications*. IntechOpen; 2021. doi:10.5772/intechopen.95423

2. Dean JS, Harding JH, Sinclair DC. Simulation of impedance spectra for a full three-dimensional ceramic microstructure using a finite element model. *Journal of the American Ceramic Society*. 2014;97(3):885-891. doi:10.1111/JACE.12750

3. Kerridge G, Sinclair DC, Dean JS. Resource-efficient exploration of ternary phase space to develop multi-layer ceramic capacitors. *Acta Mater*. 2021;207:116690. doi:10.1016/j.actamat.2021.116690

4. Heath JP, Harding JH, Sinclair DC, Dean JS. The Analysis of Impedance Spectra for Core–Shell Microstructures: Why a Multiformalism Approach is Essential. *Adv Funct Mater*. 2019;29(38):1904036. doi:10.1002/adfm.201904036

5. Heath JP, Dean JS, Harding JH, Sinclair DCJ. Simulation of impedance spectra for core-shell grain structures using finite element modeling. *Journal of the American Ceramic Society*. 2015;98(6):1925-1931. doi:10.1111/JACE.13533

6. The MathWorks Inc. MATLAB. Published online in 2021. http://www.mathworks.com/

7. Rycroft CH. VORO++: A three-dimensional Voronoi cell library in C++. *Chaos*. 2009;19(4). doi:10.1063/1.3215722/135670

8. Geuzaine, Christophe and Remacle JF. Gmsh. Published online in 2022. http://gmsh.info/

9. Heath JP, Harding JH, Sinclair DC, Dean JS. The Analysis of Impedance Spectra for Core–Shell Microstructures: Why a Multiformalism Approach is Essential. *Adv Funct Mater*. 2019;29(38):1904036. doi:10.1002/adfm.201904036

10. Padurariu L, Brunengo E, Canu G, Curecheriu LP, Conzatti L, Buscaglia MT, Stagnaro P, Mitoseriu L, Buscaglia V. Role of Microstructures in the Dielectric Properties of PVDF-Based Nanocomposites Containing High-Permittivity Fillers for Energy Storage. *ACS Appl Mater Interfaces*. 2023;15(10):13535-13544. doi:10.1021/ACSAMI.2C23013/SUPPL_FILE/AM2C23013_SI_001.PDF

11. Myroshnychenko V, Smirnov S, Mulavarickal Jose PM, Brosseau C, Förstner J. Nonlinear dielectric properties of random paraelectric-dielectric composites. *Acta Mater*. 2021;203:116432. doi:10.1016/J.ACTAMAT.2020.10.051

5 Core-shell Model.

5.1 Introduction

In this chapter, we build on the techniques and principles of finite element modeling (FEM) developed in the previous chapter to create and analyse a core-shell model. Chapter 4 provided a comprehensive discussion of FEM, beginning with its fundamental principles and moving through practical aspects such as model generation, boundary conditions, and computational simulations. It also explored the construction and simulation of simple layered models, with detailed comparisons of series and parallel configurations, verifying the accuracy of these simulations through comparison with analytical models. These methods provided a foundation for developing more advanced and realistic models.

Using the methodologies established earlier, we now focus on a core-shell model that has been published in a peer-reviewed journal and reproduced in this chapter. The core-shell structure represents a significant step forward in complexity and application, leveraging FEM to simulate intricate interactions within a multi-layered system. The insights gained from this chapter further validate the robustness of FEM in handling real-world engineering problems and pave the way for future studies on advanced composite materials and systems.

5.2 Peer-Reviewed Publication

5.2.1 Publication Information

Application of Johnson's approximation in finite element modeling for electric field-dependent materials

Rassell C. D'Silva Green, Graham Dale, Garry McLaughlin, Maureen Strawhorne, Derek C. Sinclair, Julian S. Dean

https://doi.org/10.1111/ijac.14824

5.2.2 Abstract

Johnson's approximation is implemented in a finite element code to simulate the electric field dependence of a core–shell microstructure material. We show how the microstructure, based here on a 50:50 volume fraction, influences the measured effective permittivity as a function of applied voltage. Using a Johnson's parameter of $\beta = 1.0 \times 10^{10}$ Vm^5/C^3, verified from commercial BaTiO$_3$-based multilayer ceramic capacitors (MLCC), we show how the microstructure and the difference in core and shell conductivities alter the local fields generated

and how this influences the voltage dependence of the effective permittivity. Systems that comprise a conductive core-like material surrounded by a resistive shell experience little or modest voltage dependence due to the shell material providing shielding to large electric fields within the cores. Conversely, if the core material is more resistive than the shell material, substantial voltage dependence occurs, with simulations showing over a 50% decrease in the effective permittivity. These simulations give an improved understanding of voltage dependence and provide a method to help guide the design of future materials for MLCCs with improved performance.

5.2.3 Introduction

Multilayer ceramic capacitors (MLCCs) are among the most mass-produced devices, with over 3.5 trillion units being manufactured per year[1], with the value of the MLCC global market expected to reach over 14 billion USD by 2024[1]. They are used in small- and large-scale applications varying from smartphones and automobiles to uses in wireless communication[2,3]. With the rapid growth of 5G and electric vehicles, capacitors need to evolve toward higher frequencies (>MHz), higher voltages (>1 kV), higher breakdown strengths (>100 kV/cm), and higher temperatures (>400°C for some space exploration applications)[4]. In automotive applications, due to their use in under-the-hood applications, the materials are required to operate at temperature ranges of −55 to 150°C, and voltages over 240 V while maintaining their small size and high thermally stable capacitance. A capacitor which meets these requirements is classified as an X8R ±15%.

MLCCs consist of several layers of a ceramic material sandwiched between two metal electrodes, where the capacitance of an MLCC is calculated by:

$$C = \frac{\epsilon_r \epsilon_0 A}{d} \times (n)$$

Equation 5.1

Here, capacitance C is typically measured in pF or µF, ϵ_r is its relative permittivity, and ϵ_0 is the permittivity of free space (8.8542×10^{-12} F/m). The geometry is defined as the surface area of the electrode given by A, d is the distance between the electrodes, and n is the number of active ceramic layers between electrodes, which can be several hundred in typical commercial MLCCs.

The three variables in Equation 5.1 provide possible ways to improve the capacitance of an MLCC. The first is to increase the relative permittivity of the ceramic, the second is to reduce the distance between the electrodes, and the third is to increase the surface area of the plates. Each of these methods has its benefits and implications. Although increasing the surface area of the electrode is possible, this would increase the footprint of the device. Since MLCCs are usually size-limited due to space available on circuit boards, this is not a viable solution.

Although the relative permittivity of the material could be improved, there are limitations on which materials could achieve this. Ferroelectric barium titanate ($BaTiO_3$) is the base ceramic material of choice as it possesses a high intrinsic room temperature permittivity (1000–7000[5]) and is compatible with current manufacturing techniques[6]. However, the relative permittivity is highly dependent on the temperature and needs modification to meet current requirements[7]. A measurement of the temperature dependence of ferroelectrics is via the temperature coefficient of capacitance (TCC), which is calculated by the formula:

$$TCC\% = \frac{\epsilon_T - \epsilon_{25}}{\epsilon_{25}} \text{x } 100$$

Equation 5.2

where ϵ_{25} is the relative permittivity at room temperature and ϵ_T Is the relative permittivity at the reference temperature. One way to increase temperature stability is via chemical doping of $BaTiO_3$ to form a core–shell microstructure [8]. Undoped $BaTiO_3$ has a sharp peak in relative permittivity at its Curie temperature as it undergoes a phase transition from a tetragonal to a cubic crystal structure. Through chemical modifications via different dopants[9,10], a dopant-rich shell can be formed, which typically has a much broader transition range at lower temperatures than the Curie temperature of undoped $BaTiO_3$. The combination of the core and shell microstructure extends the temperature range over which a capacitor can operate, allowing it to meet the required specification that undoped $BaTiO_3$ could not achieve. In addition, other properties such as processing conditions[11], layer thicknesses[12], and grain size[13] allow the TCC to be controlled to meet industrial specifications. Determining the optimal volume ratio for the application, however, can involve a time-consuming iterative process to arrive at the appropriate formulation and processing conditions [14].

An efficient method to increase capacitance is to reduce the distance between the electrodes. This provides two benefits: it gives the possibility of smaller devices and increased capacitance; however, the electric field is increased as the dielectric thickness is decreased, given by:

$$E_G = \frac{V}{d}$$

Equation 5.3

where V is the applied voltage across the electrodes and d is the distance between the electrodes. As Equation 5.3 only considers the global properties of the system, we shall refer to this value as the global electric field E_G to distinguish it from the variations of the local electric fields produced inside the material. As d is reduced to a few µm, the strength of the global electric field can increase to over 1 MV/m for an applied voltage of 1 V. At room temperature, the breakdown voltage of $BaTiO_3$ is around 3 MV/m [15]. The lifetime of these components can therefore be compromised in higher voltage applications.

There has been extensive research into improving TCC; however, an often-overlooked aspect in optimising these materials is the voltage coefficient of capacitance (VCC). For some materials, the application of high electric fields can create a reduction in the relative permittivity along with a shift of the Curie peak toward a higher temperature[16]. The macroscopic tunability of the capacitance can be attributed to several bias field-induced modifications at various length scales from the unit cell polarisation (intrinsic), polar nanoregions, domain relaxation, grain boundaries, and interphases[17,18]. These occur at length scales from nano- to micrometres and can depend on temperature, frequency, crystal symmetry, and ceramic microstructure. One method of approximating the macroscopic tunability is to use the empirical Johnson's approximation[19,20]. This is based on the Landau–Devonshire phenomenological theory[18], which has been used successfully to fit the tunability of various materials[19]. Although the Johnson's approximation is limited in explaining the hysteretic behaviour of the relative permittivity below the Curie temperature, it has been shown to work well in predicting the voltage dependence of $BaTiO_3$-based materials[19, 21,22]. Furthermore, it has also been shown that the weak field approximation model, based on the Gibbs free energy, also provides good agreement with Johnson's equation[22].

The nonlinear field dependence of the relative permittivity can be described by Johnson's equation, which has been used successfully to fit the variation of relative permittivity with electric field data for $BaTiO_3$ [19,21,22]

$$\epsilon_r(E) = \frac{\epsilon_r(0)}{\left(1 + 3\beta\left(\epsilon_0\epsilon_r(0)\right)^3 E^2\right)^{\frac{1}{3}}}$$

Equation 5.4

Here, $\epsilon_r(E)$ is the modified relative permittivity measured when an electric field strength E (V/m) is generated in the material. The relative permittivity in the absence of an electric field is given by $\epsilon_r(0)$ and the variable β is an anharmonic coefficient, also known as

Johnson's parameter and represents the ferroelectric nonlinearity of the material. This can be estimated by fitting the observed relative permittivity drop with increasing voltage[23] as shown in Figure 5.1. By fitting experimental data using this equation, depending on the composition, the value of β can be temperature dependent and vary by an order of magnitude[19].

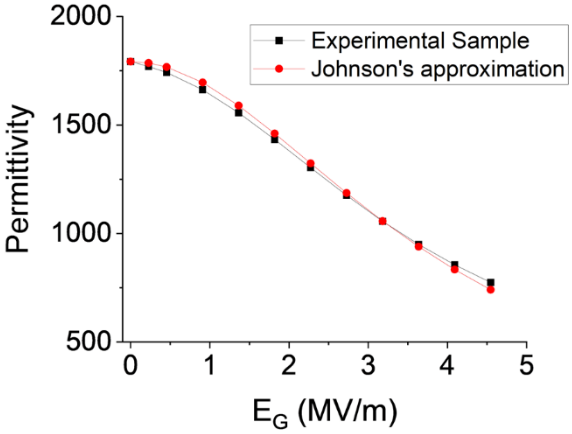

Figure 5.1 VCC data for a commercial $BaTiO_3$-based MLCC measured at 25 °C (black) at a frequency of 100 kHz and fitted with equation 5.2 (in red) to extract the Johnson parameter β. In this case, the value extracted is $\beta=6.7x10^9$ Vm^5/C^3.

In Figure 5.1, experimental data from a commercial $BaTiO_3$-based MLCC are measured as a function of E_G. In this case, the data were generated by changing the applied voltage on the same thickness of dielectric (i.e., changing V, but maintaining d), however, using Equation 5.3, as the relative permittivity change is generated by the applied E_G (i.e., the ratio of V/d) this could also give insight into what can happen if the applied voltage is maintained but the dielectric thickness, d is reduced. Fitting Figure 5.1 with Equation 5.4, Johnson's parameter can be extracted, in this case, $\beta = .67 \times 10^{10}$ Vm^5/C^3 at a temperature of 25°C. Within the literature, β values are reported in the order of 10^{10} and up to 10^{12} Vm^5/C^3 [24,25], matching well with our results here. There are limitations to the accuracy of Johnson's approximation. For example, when the grain size is reduced to nanometers, there is a known decrease in the relative permittivity of $BaTiO_3$. This has been attributed to increasing electrical inhomogeneity as the grain size is reduced [14]. Some approaches to tackle this issue involve using a material-dependent exponent[26] or utilising a coefficient dependent on the microstructure[27]. Typically, VCC data are not measured for nanostructured ceramics as it requires measuring relative permittivity at low thicknesses, which leads to the generation of extremely high electric fields[14, 28].

There has been work on studying this effect through modeling. Padurariu et al[14] developed a finite element model (FEM) to mimic a two-dimensional grain structure consisting of nonlinear ferroelectric grain cores with paraelectric grain boundaries. The model consisted of multiple grains of varying sizes. For large grain sizes, they showed there is a negligible difference between the global and local electric fields. With decreasing grain size, there is a reduction in the local electric field in the core, leading to an increase in the local field inhomogeneity. Due to the presence of this inhomogeneity, Johnson's approximation applied globally to the system would not be sufficient to describe the behaviour of this system, as it uses the global field. This can be resolved by using the local field values generated to determine the local changes in relative permittivity. Although their method was able to describe the effective field permittivity using the local field evolution and local relative permittivity, a limitation of their method is that it is confined to a two-dimensional model.

In this article, we implement Johnson's approximation into our in-house impedance software, ElCer[29]. This provides the ability to simulate the local electric fields arising from the microstructure and variation in core and shell material properties, which we can represent in a full three-dimensional model. This can be used to help understand how microstructural features can influence the field-dependent response of materials used in MLCCs.

5.2.4 Methodology

To simulate how Johnson's approximation influences the material's electric response under an applied electric field, we first create the desired microstructure. Figure 5.2 highlights the procedure on a simple series layered model, Figure 5.2(a), noting that this procedure is the same for any microstructure, such as a core–shell or a collection of grains. The model is drawn, in this case as a 10 µm cube encompassing two layers, and discretised into elements using Gmsh[30], where each element is individually assigned the material relative permittivity, conductivity, and Johnson's parameter. Materials which are field dependent are set to Johnson's parameter of $\beta = 1.0 \times 10^{10}$ Vm^5/C^3, chosen as it falls within the accepted known range for $BaTiO_3$ [19, 20] and close to our experimentally extracted value. For materials which experience non-field dependence (NFD), we set $\beta = 0$. We finally apply a voltage of 110 V across the model as explained in Figure 5.2(b), which, using Equation 5.3, generates an E_G of 11 MV/m over the model.

Using our in-house impedance software, ElCer [24], we first simulate the local electric field distribution within the microstructure as shown in Figure 5.2(c). We assume the material properties to be isotropic and linear and that any inductive effects are negligible when compared with the capacitive behaviour. ElCer uses a time-domain finite element method

(TDFEM) based on Maxwell's equations to calculate the electric potential as a function of space and time. This permits the current density to be calculated by integrating over the whole sample, and thus, in turn, allows simulation of the electrical response of the electroceramic. We use Dirichlet boundary conditions at the electrode–air interface to fix the electric potential. Furthermore, we assume that the displacement currents across the free surface of the material are zero by implementing a Neumann boundary condition at those regions. We note that although other thermal and electromechanical effects, such as thermoelectricity or piezoelectricity, are present in $BaTiO_3$, for simplicity we do not consider these in the model, but they could be explored in the future.

Depending on the microstructure and material properties, this could be significantly higher or lower than the global electric field. These local values are then weighted onto the centroid of each element and converted to a change of local relative permittivity using Johnson's equation (Equation 5.4) as shown in Figure 5.2(d). The process is repeated until convergence is achieved, which we set at a value of less than 0.1% difference between subsequent runs, Figure 5.2(e). At convergence, a final model is generated (Figure 5.2(f)), and an impedance spectrum is generated for analysis via ElCer as shown in Figure 5.2(g). This entire process can be repeated for higher voltages to understand how the materials respond at different electric field strengths. Although we have controlled the voltage to generate large electric field strengths across the materials, from Equation 5.3, the larger electric fields can also be used to represent a change in the multilayer thickness with a constant voltage.

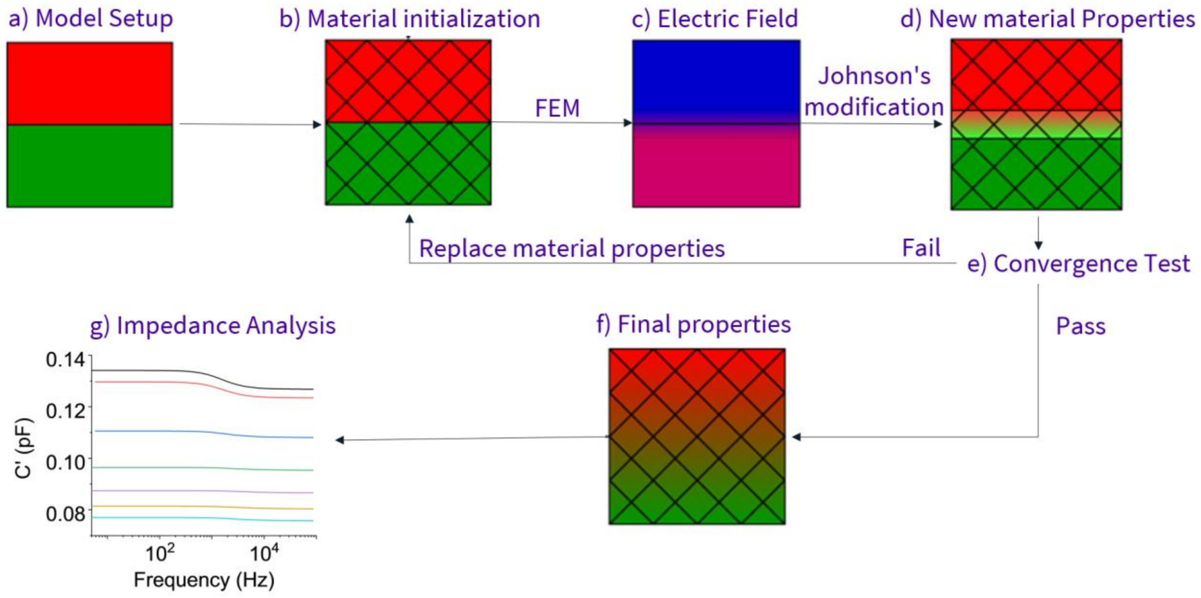

Figure 5.2 Schematic showing the coding process using a simple layered model as an example. The initial model (a) and the materials initialised (b). We use ElCer to simulate the electric field (c) and then use Johnson's equation to modify the material properties as shown in (d). Once converged, we can simulate the impedance response of the final properties (f) and analyse the capacitance formalism C' to extract capacitance at fixed frequencies.

The simulation of the impedance spectra provides a method of identifying the response of the constituent materials[31]. Here, we focus on the analysis of the *C*' spectra (real part of capacitance vs. frequency), Figure 5.2(g), where the effective capacitance at various fixed frequencies can be extracted and converted to relative permittivity using a geometric factor.

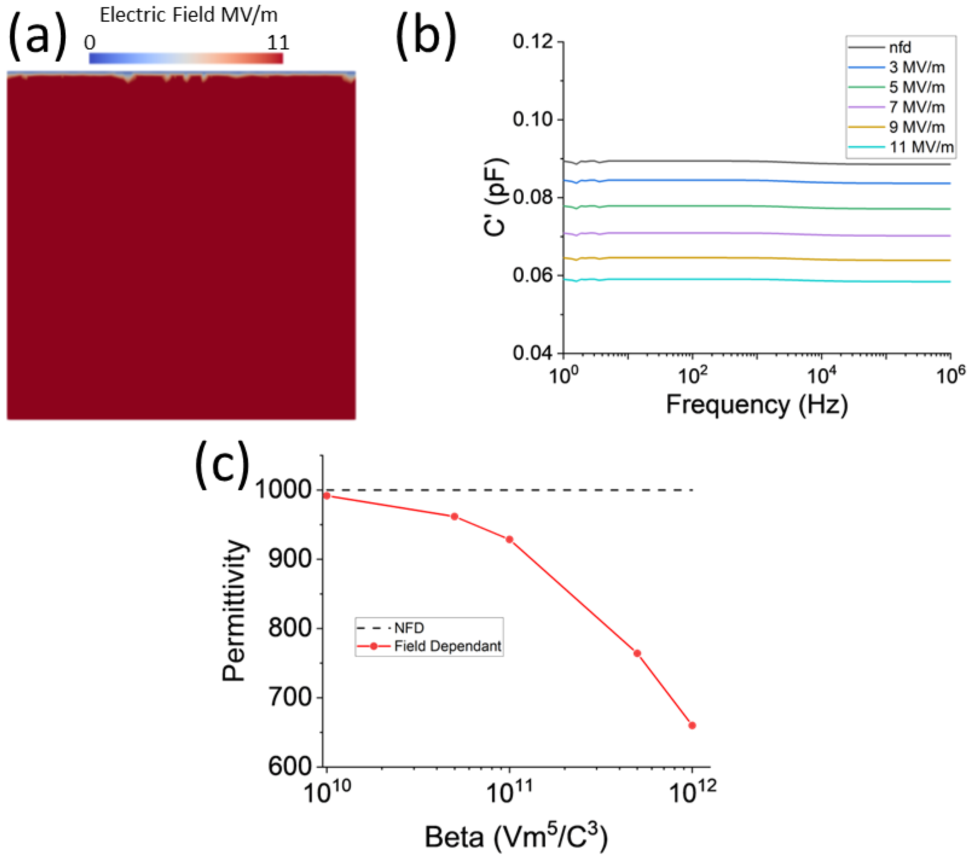

Figure 5.3 A simple uniform material under a potential difference of 110 V a) The electric field distribution within the material, b) C' spectroscopic plots for the simple cubic model with increasing electric field, and c) the change in relative permittivity as the Johnson's parameter, β, is increased for the simple cubic model. The dashed line indicates the non-field dependence (NFD) model.

To verify this method, we simulate the impedance response of a simple, electrically homogenous cube as shown in Figure 5.3. The model consists of a cube with a side length of 10 µm, the initial relative permittivity of ε_r=1000 and conductivity of σ = 100 µS/m. This cube is discretised into ~165k tetrahedral elements, and the local electric field distribution is simulated. As the cube is made from a single material, a homogeneous response is generated, as shown in Figure 5.3(a). The resulting *C*' spectra of this system are shown in Figure 5.3(b).

As applying zero voltage across the material is equivalent to the material being assigned $\beta = 0$ Vm^5/C^3, for clarity, we refer to these simulations throughout the article as the non-field dependent (NFD) case. Solving and plotting spectra in the *C*' formalism generates a single plateau with the capacitance of 0.089 pF. As the voltage is increased, the *C*' plateau decreases uniformly, as seen in Figure 5.3(b). This continues up to the maximum applied global field of 11 MV/m, where the capacitance decreases to 0.059 pF. As Johnson's parameter β range can be a few orders of magnitude, we simulate various values within the literature range as shown in Figure 5.3(c) and by converting the capacitance, *C*', to relative permittivity using the geometrical factor. As shown, the drop in relative permittivity from the NFD of ε_r=1000 to below 700 for global fields of 11 MV/m when $\beta = 1 \times 10^{10}$ Vm^5/C^3 is used. It should be noted that all solved values here are consistent with Equation 5.4 as the global and local fields are equivalent.

To increase realism in the physical microstructure, we now create a core and shell structure which can arise in doped $BaTiO_3$ materials and commercial MLCCs[7, 32]. We set the core–shell volume ratio as a 50–50 ratio and the total side length of the system as 10 µm, as shown in Figure 5.4(a). To ensure the results are not influenced by surface effects, we use 27 identical core–shell cubes set in a 3 × 3 × 3 array and extract the results from only the central grain. In this first study, the core and shell were both assigned a relative permittivity of ε_r=1000 and a conductivity σ = 100 µS/m. Typical shell materials have a significantly lower sensitivity to field effects[33,34], and so we set the core to have Johnson's parameter of $\beta = 1 \times 10^{10}$ Vm^5/C^3 but assign the shell to be NFD (i.e., $\beta = 0$ Vm^5/C^3).

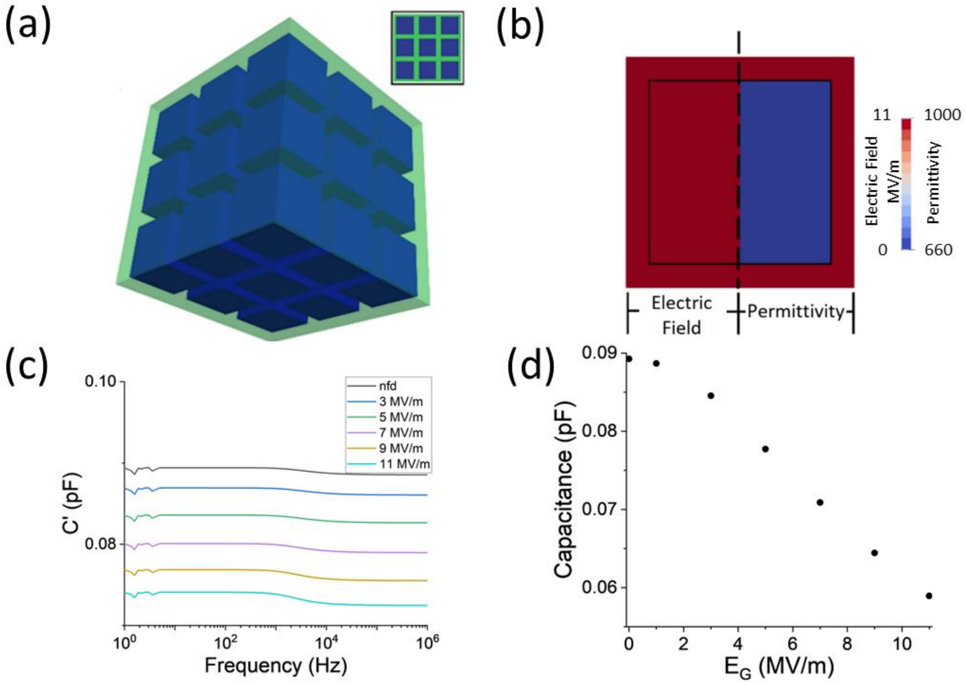

Figure 5.4 a) Core-shell model used with the green shell region encapsulating the blue core region. Inset: A front-facing cut in half view of the respective model. b) A combined view of the electric field (left) and final relative permittivity (right) for the centre cube in the middle row for an E_G of 11 MV/m. The resulting electrical response in C' spectra is shown in c), with the measured extracted capacitance (at 100 kHz) with increasing E_G shown in d).

Figure 5.4(b) shows a combined image of the electric field and relative permittivity distribution after convergence. The left side of Figure 5.4(b) highlights the electric field distribution in the core–shell model (left). As both core and shell have the same conductivity, as in the previous simple cube case, the response at NFD is a homogeneous field response of 11 MV/m through both materials. However, as the core experiences the electric field, its relative permittivity is reduced as shown in Figure 5.4(b) (right). This generates a 33.7% drop in the capacitance of the material from ~.089 pF to .059 pF when a global field of 11 MV/m is applied, Figure 5.4(c). The simulated *C*’ spectra begin to display two distinct plateaus at higher fields, highlighting a significant change in the core material, whereas the shell remains unchanged. This drop becomes linear as shown in Figure 5.4(d), and the trend reproduces that observed experimentally in Figure 5.1.

5.2.5 Results and discussion

In the above methodology, the core and shell materials were set to have the same properties, but this is unlikely and unrealistic due to known compositional changes of the core and shell materials in $BaTiO_3$-based MLCCs. We therefore extend our study to six different configurations, as shown in Table 5.1. In each study, the core and shell properties are varied so regions have either a relative permittivity of $\varepsilon_r = 1000$ or 2000 and a conductivity of either $\sigma = 100$ or 0.1 µS/m. In Cases I–III, we simulate a field-dependent core, with a shell that is independent of the electric field, whereas in Cases IV–VI, we simulate conditions where both the core and shell are field dependent.

Table 5.1 The assigned material properties used for Cases I–VI for the core–shell models. C and S refer to the core and shell, respectively. H refers to the higher values of relative permittivity and conductivity of 2000 and 100 µS/m, respectively, and L refers to the lower values of relative permittivity and conductivity of 1000 and 0.1 µS/m, respectively.

Case	**Core/shell**	**Permittivity**	**Conductivity (µS/m)**
I/IV/CHH-SLH	Core	2000	100
	Shell	1000	100
II/V/CHL-SLH	Core	2000	0.1
	Shell	1000	100
III/VI/CHH-SLL	Core	2000	100
	Shell	1000	0.1

In Case I (CHH-SLH), we simulate a grain where the core and shell have the same conductivity of $\sigma = 100$ µS/m, but the core has a higher relative permittivity of $\varepsilon_r = 2000$ compared to the shell with an initial value of $\varepsilon_r = 1000$. The core is only field dependent (i.e., $\beta = 1 \times 10^{10}$ Vm^5/C^3), whereas the shell is set with $\beta = 0$ Vm^5/C^3, making it field independent. As both the core and shell have the same conductivity, an E_G of 11 MV/m is generated throughout the core and shell material as shown in Figure 5.5(a) (left).

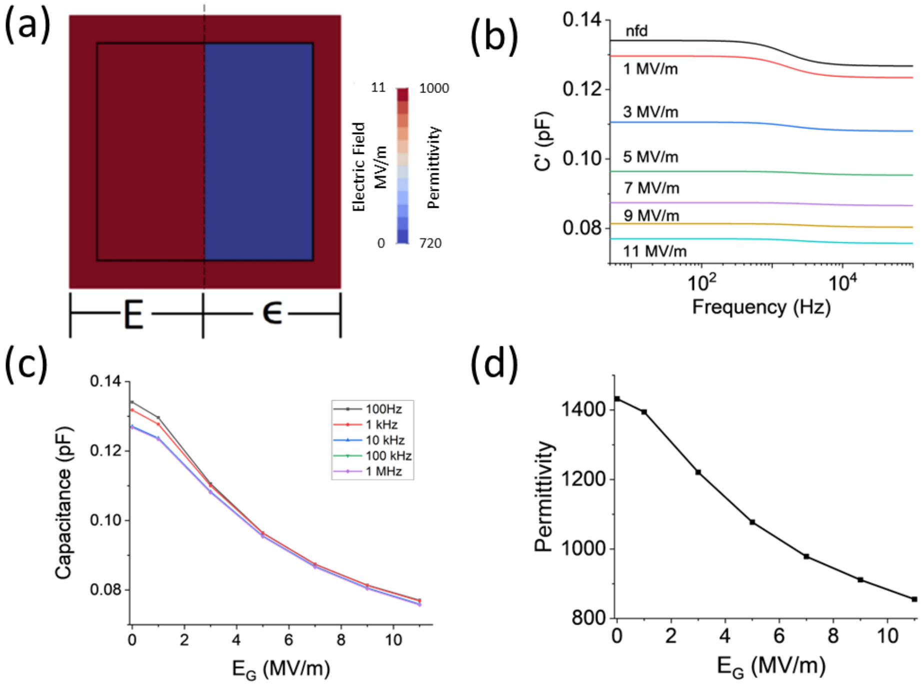

Figure 5.5 Case I (CHH-SLH), where both core and shell materials have the same conductivity. a) Combined cross-section view of the electric field (left) and final relative permittivity (right) for the centre cube in the middle row for an E_G of 11 MV/m. b) Change in C' spectra as a function of global field, with extracted capacitance at various frequencies. c) The change in capacitance as a function of E_G. A minimal change is observed with the curves overlapping at frequencies greater than 10 kHz. d) Extracted relative permittivity (at 100 kHz) versus E_G.

The electric field gives rise to a uniform drop in the core relative permittivity from its initial value of $\varepsilon_r = 2000$ to a value of 720, Figure 5.5(a) (right), when E_G reaches 11 MV/m. This results in the core relative permittivity dropping below that of the shell value of $\varepsilon_r = 1000$. In the C' spectra, Figure 5.5(b) for NFD, we initially observe two distinct plateaus at low electric fields of 0.134 pF (100 Hz) and 0.127 pF (100 kHz) representing the dominating components of the core and shell, respectively. As E_G is increased to 11 MV/m, the response becomes close to a single plateau with a measured capacitance of 0.077 pF, Figure 5.5(c). This is a 40% drop from the NFD case and results in the relative permittivity at 100 kHz decreasing from an initial value of 1430 to 850, as shown in Figure 5.5(d).

In Case II(CHL-SLH), we maintain the properties of the shell but reduce the core conductivity to $\sigma = 0.1$ µS/m. This now results in a model where the core is more resistive than the shell. The initial relative permittivity of the core is retained at $\varepsilon_r = 2000$, but as this region possesses lower conductivity, the electric field generated is now elevated compared to the shell, as shown in Figure 5.6(a) (left). Again, note that the core is the only field-dependent material.

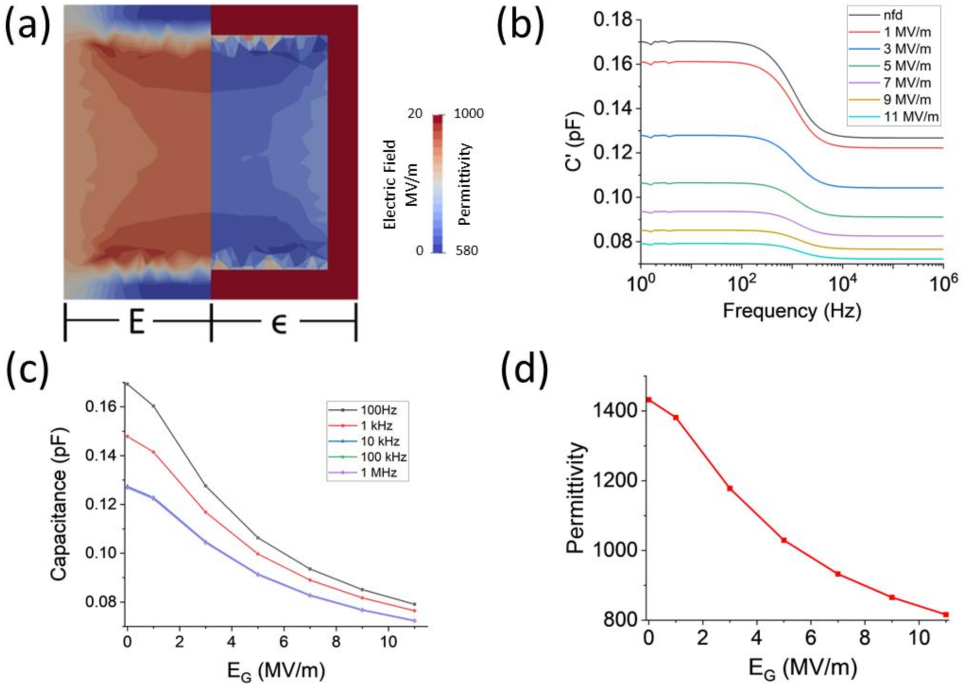

Figure 5.6 ***Case II****(CHL-SLH),* *where the core material is more resistive than the shell material. a) Combined cross-section view of the electric field (left) and final relative permittivity (right) for the centre cube in the middle row for an E_G of 11 MV/m. b) Change in C' spectra as a function of global field, with extracted capacitance at various frequencies. c) The change in capacitance as a function of E_G. A minimal change is observed with the curves overlapping at frequencies greater than 10 kHz. d) Extracted relative permittivity (at 100 kHz) versus E_G.*

The field in the core is now no longer electrically homogeneous due to the more resistive core and this increased strength in the electric field in the core forms an "hourglass" shape leading to a greater drop in the relative permittivity of the core than in Case I(CHH-SLH), as shown in Figure 5.6(a) (right). The local electric field at the top and bottom regions of the core rises to 16 MV/m, dropping to a value of 14 MV/m nearer the centre of the core. It should be noted that both these local values are higher than the applied E_G calculated by Equation 5.3 and highlight the importance of considering local electric fields.

Near the external regions of the core, the local field falls close to the global value of 11 MV/m due to the proximity of the conductive shell region and falls below the average within the top and bottom areas of the shell material. As the relative permittivity change follows the electric field, the core, which starts with a single relative permittivity of $\varepsilon_r = 2000$, now becomes graded as it experiences a stronger reduction in the central regions than the edges. This leads to over half the core's volume, which consists of the top, bottom, and central regions, dropping to a relative permittivity value of $500 < \varepsilon_r < 650$, whereas the remainder of the core volume reduces to $650 < \varepsilon_r < 950$. As a consequence, the resulting *C*’ spectra and relative permittivity, Figure 5.6(c), (d), show a strong change as a function of the field. For the NFD case, there are two distinct plateaus in *C*’ of 0.170 and 0.127 pF, Figure 5.6(c). As the global field strength is increased to 11 MV/m, the capacitance response for the shell- and core-dominated regions both drops to values of 0.078 and 0.071 pF, respectively. Additionally, the difference in capacitance between the shell and the core decreases from 0.043 pF for the NFD case, to a difference of just 0.005 pF for an E_G of 11 MV/m. The effective permittivity at 100 kHz also decreases to nearly half, with the high field case $\varepsilon_r = 800$ compared to the NFD simulation of $\varepsilon_r = 1430$. As the electric field is increased, the relative permittivity of the core is also reduced below that of the shell, bringing plateaus in *C*’ spectra closer together.

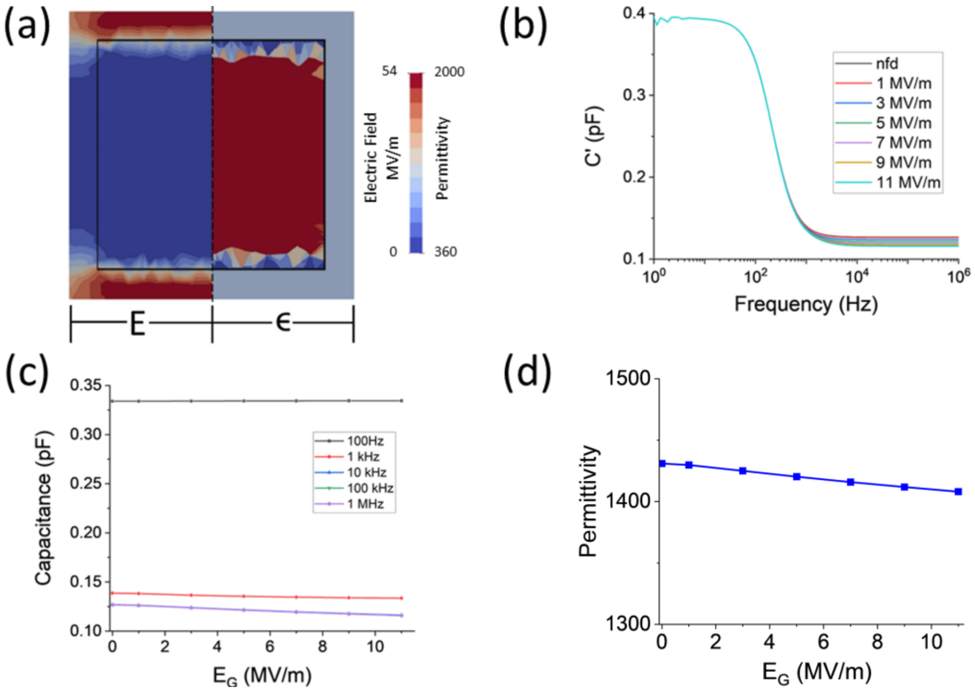

Figure 5.7 ***Case III*****(CHH-SLL),** *where the core material is more conductive than the shell material. A combined cross-section view of the electric field (left) and final relative permittivity (right) for the centre cube in the middle row for an E_G of 11 MV/m. b) Change in C’ spectra as a function of global field, with extracted capacitance at various frequencies. c) The change in capacitance as a function of E_G. A minimal change is observed with the curves overlapping at frequencies greater than 10 kHz. d) Extracted relative permittivity (at 100 kHz) versus E_G.*

In case III(CHH-SLL), we reverse the conductivity of Case II(CHL-SLH), thereby making the core more conductive than the shell. Consequently, the electric field experienced in the core falls below the global field value of 11 MV/m, as shown in Figure 5.7(a) (left). The shell regions above and below the core region account for ~10% of the grain volume and experience an extremely high field of ~54 MV/m, but this decreases sharply to 0.80 MV/m in the regions to the side of the core. This reduction in the electric field leaves a large amount of the core, over 80%, relatively unchanged from the initial value of ε_r = 2000. This illustrates that the shell, while under an enhanced electric field, provides a shielding effect to the core and therefore reduces the electric field that it experiences.

As shown in Figure 5.7(b), the high-frequency plateau arising predominantly from the core response experiences a low field-dependent change. At NFD, *C'* is .138 pF at 100 kHz, and when a global field of 11 MV/m is applied, the high-frequency *C'* plateau falls by only 8% to 0.127 pF. The low-frequency plateau, associated predominantly with the shell, remains unchanged at 0.397 pF as shown in Figure 5.7(b). As a consequence, the relative permittivity decreases from its initial value of ε_r = 1430 to 1408, Figure 5.7(d). Unlike the previous cases, Case III(CHH-SLL) still exhibits a clear core–shell response even after a field is applied.

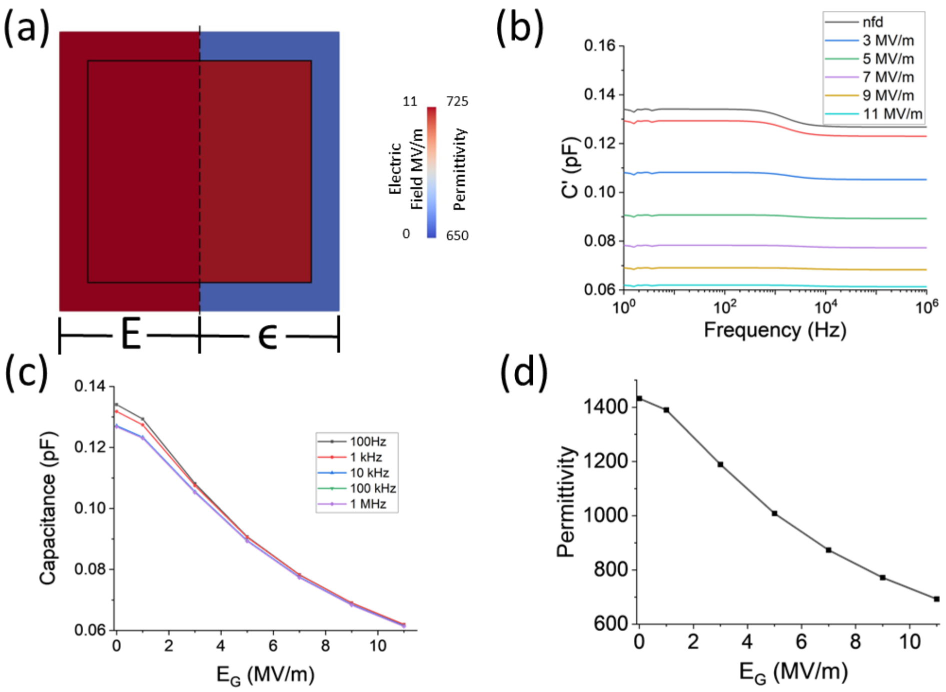

Figure 5.8 ***Case IV(CHH-SLH),*** *where both core and shell material have the same conductivity. a) Combined cross-section view of the electric field (left) and final relative permittivity (right) for the centre cube in the middle row for an E_G of 11 MV/m. b) Change in C' spectra as a function of global field, with extracted capacitance at various frequencies. c) The change in capacitance as a function of E_G. A minimal change is observed with the curves overlapping at frequencies greater than 10 kHz. d) Extracted relative permittivity (at 100 kHz) versus E_G.*

We now move on to cases where both materials are ferroelectric and exhibit field dependence. Here, we use the material configurations of Cases I, II(CHL-SLH), and III(CHH-SLL) but assign both the core and shell $\beta = 1.0 \times 10^{10}$ Vm^5/C^3.

In Case IV(CHH-SLH), as in Case I, the core and shell are assigned a conductivity of $\sigma = 100$ µS/m. The core is assigned a higher relative permittivity of $\varepsilon_r = 2000$ compared to the shell with an initial value of $\varepsilon_r = 1000$. Due to the core and shell having the same conductivity, we once again observe an E_G of 11 MV/m generated throughout the core and shell materials as shown in Figure 5.8(a) (left). This electric field leads to a uniform drop in the core from an initial value of ε_r from 2000 to 720, Figure 5.8(a) (right), similar to that of Case I. However, the shell now also experiences a drop in ε_r from 1000 to 650, and as a consequence, the core relative permittivity remains higher than that of the shell as E_G is increased.

In the *C*' spectra, Figure 5.8(b) for NFD, we initially observe two distinct plateaus at low electric fields of 0.134 pF (100 Hz) and 0.127 pF (100 kHz) representing the dominating components of the core and shell, respectively. As E_G is increased to 11 MV/m, the response becomes close to a single plateau with a measured capacitance of 0.062 pF, Figure 5.8(c). This results in a 52% drop from the NFD case and relative permittivity at 100 kHz decreasing from an initial value of 1430 to 700, as shown in Figure 5.8(d).

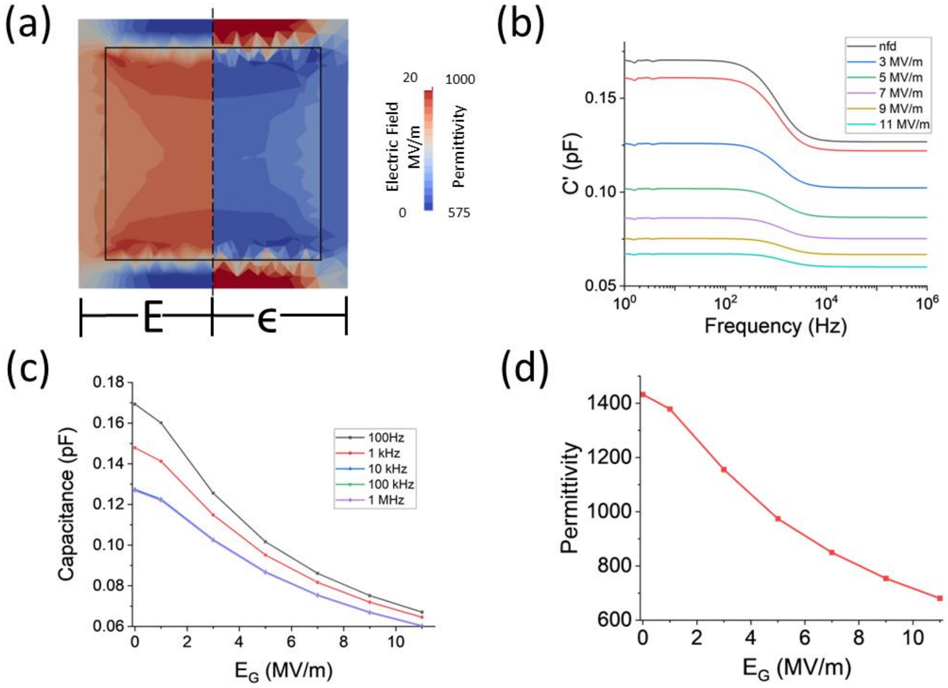

Figure 5.9 ***Case V(CHL-SLH),*** *where the core material is more resistive than the shell material. a) Combined cross-section view of the electric field (left) and final relative permittivity (right) for the centre cube in the middle row for an* E_G *of 11 MV/m. b) Change in C' spectra as a function of global field, with extracted capacitance at various frequencies. c) The change in capacitance as a function of* E_G*. A minimal change is observed with the curves overlapping at frequencies greater than 10 kHz. d) Extracted relative permittivity (at 100 kHz) versus* E_G*.*

As in Case II(CHL-SLH), in Case V(CHL-SLH), the core conductivity is set as $\sigma = 0.1$ µS/m, lower than that of the shell with $\sigma = 100$ µS/m, resulting in a resistive shell model. Again, note that in this case, both materials are field dependent. As in Case II(CHL-SLH), the electric field in the core is no longer electrically homogeneous, Figure 5.9(a) (left) and forms an "hourglass" shape. This leads to a greater drop in the relative permittivity of the core than in Case II(CHL-SLH), as shown in Figure 5.9(a) (right). The local electric field at the top and bottom regions of the core rises to 16 MV/m, dropping to a value of 14 MV/m nearer the centre of the core, now higher than the value of the global field. Toward the core–shell interface, the local field is close to the global value of 11 MV/m and then falls below the average within the top and bottom areas of the shell material. The relative permittivity of the core once again becomes graded, with over half the core's volume dropping to a relative permittivity value of $500 < \varepsilon_r < 650$, whereas the rest of the core volume reduces to $650 < \varepsilon_r < 950$. In the shell region, as the local electric field at the top and bottom of the core is low, a negligible drop in the relative permittivity of the shell in this area is generated. However, in the regions surrounding the side of the core, the field is elevated to 12 MV/m, leading to a relative permittivity drop in the shell to a value of approximately $\varepsilon_r = 650$.

This response results in *C*’ spectra and relative permittivity, Figure 5.9(c), (d), showing a stronger change as a function of field than in Case II. For the NFD case, there are two distinct plateaus in *C*’ of 0.170 and 0.127 pF, Figure 5.6(c). As E_G is increased to 11 MV/m, the capacitance response for the shell- and core-dominated regions both decreases to values of .067 and .060 pF, respectively. Additionally, the difference in capacitance between the shell and the core decreases from .043 pF for the NFD case, to a difference of just 0.007 pF for an E_G of 11 MV/m. The effective permittivity at 100 kHz also decreases to over half, with the high field case $\varepsilon_r = 680$ compared to the NFD simulation of $\varepsilon_r = 1430$. As the electric field is increased, the low-frequency response decreases more rapidly than that of the high-frequency response, bringing the plateaus in *C*’ spectra closer together.

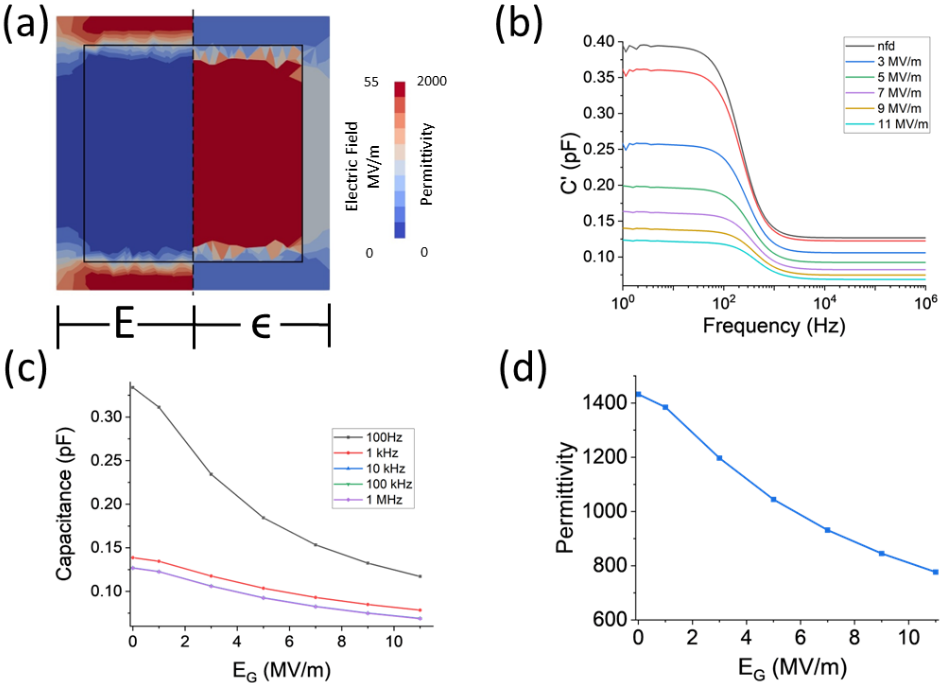

Figure 5.10 In case VI(CHH-SLL) where the core material is more conductive than the shell material. A combined cross-section view of the electric field (left) and final relative permittivity (right) for the centre cube in the middle row for an E_G of 11 MV/m. b) Change in C’ spectra as a function of global field. c) Capacitance extracted at various fixed frequencies versus E_G. There is minimal change in capacitance, and the curves overlap at frequencies greater than 10 kHz. d) Extracted relative permittivity (at 100 kHz) versus E_G.

In case VI(CHH-SLL), we reverse the conductivity of Case V(CHL-SLH), and the core is now more conductive than the shell. Consequently, just as in Case III(CHH-SLL), the electric field experienced in the core falls below the global field value of 11 MV/m, Figure 5.10(a) (left). The shell regions above and below the core experience an extremely high field of ~54 MV/m, dropping sharply to 0.90 MV/m in the regions surrounding the side of the core. As simulated in Case III(CHH-SLL), it leaves over 80% of the core unchanged from its initial value of $\varepsilon_r = 2000$. Crucially, however, as the shell is now field dependent, due to the high field in the top and bottom regions of the shell, the relative permittivity in these regions decreases dramatically from the initial value of $\varepsilon_r = 2000$ to below 400, leading to a greater significant change overall.

As shown in Figure 5.10(b), at NFD, *C*' is 0.127 pF at 100 kHz, and when a global field of 11 MV/m is applied, the high-frequency *C*' plateau falls by only 45.8% to 0.0688 pF. The low-frequency plateau, associated predominantly with the shell, decreases by 65% from 0.334 pF to 0.117 pF as shown in Figure 5.10(c). This leads to a drop in relative permittivity from its initial value of $\varepsilon_r = 1430$ to 780, Figure 5.10(d). Unlike Cases IV(CHH-SLH) and V(CHL-SLH), Case VI(CHH-SLL) still exhibits a clear core–shell response even after a field is applied.

Comparing all relative permittivity decreases at 100 kHz, in Figure 5.11(b), we see that all cases, except for Case III(CHH-SLL), follow a trend similar to that shown in Figure 5.1. Both experimental and model data experience a decrease in relative permittivity of about 40%–50% at an E_G of ~10 MV/m. However, this resemblance to experimental data could be coincidental, though the overall trend aligns. This is due to the variations in the core/shell volume fraction are expected to influence the outcomes, and since it is improbable that the true core volume fraction of the experimental capacitor would be 0.5. Additionally, since this involves a 7µm-layer MLCC, the grain size is probably between 10 – 20% of that thickness, all of which differ from the properties used in the models.

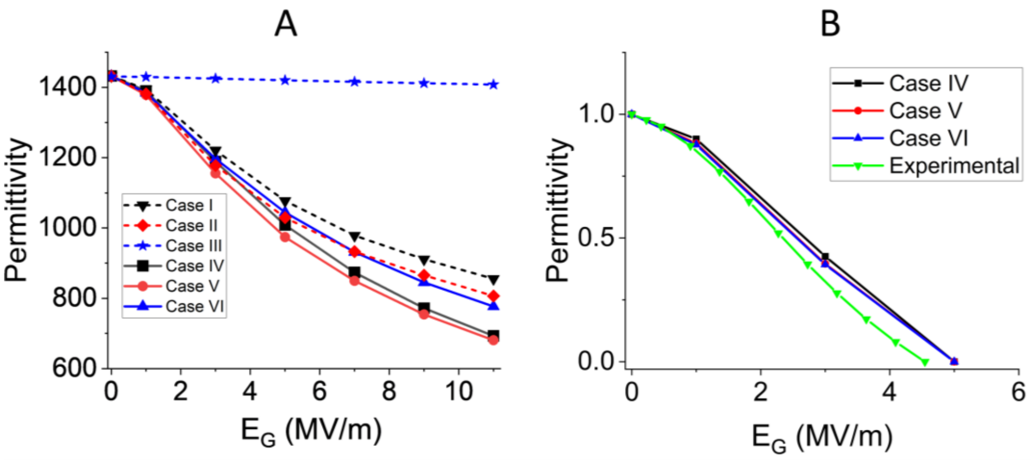

Figure 5.11 a) The overall decrease in relative permittivity for each case versus E_G*. Data sets with the same colour have the same material properties except for the field dependency of the shell. Cases I and II are highly field-dependent, whereas it is much less pronounced in case III. Cases IV, V and VI all experience a higher field dependency than cases I, II and III. B) Normalised relative permittivity vs field plot comparing the experimental data for a capacitor material having a thickness of 7 µm provided by AVX to cases IV, V and VI.*

These studies show that a key parameter in determining the core material change is the surrounding material's conductivity. As shown in Figure 5.11(a), Cases I(CHH-SLH) and II(CHL-SLH) show significant sensitivity to the global electric field if the core material is lower or equal in conductivity to that of the shell. In Case I, the conductivity of the materials is identical and as such, the electric field set up in both materials is the same (Figure 5.5(a)). This leads to the system responding with a relative permittivity change in the core due to the applied global field. In Case II(CHL-SLH), as the conductivity of the core is lower than the shell, an enhanced current density is generated in the core region (Figure 5.6(a)), consistent with work shown by Heath [35]. This leads to an enhanced electric field in the core and, as such, greater VCC sensitivity. In these configurations, it offers the ability to tune the capacitance and, as such, TCC through the control of dielectric layer thickness. This could be detrimental, however, as the increased local electric field could raise the likelihood of the core material failing and the possibility of dielectric breakdown. While Cases IV and V(CHL-SLH) have the same material properties as Cases I(CHH-SLH) and II(CHL-SLH), although the shell is now field sensitive, they still behave similarly. In Case IV(CHH-SLH), where the materials have the same conductivity, the shell VCC response now causes the overall relative permittivity to drop, which can be seen in Figure 5.11(a). This is also true of Case II(CHL-SLH), but with a reduced amount due to the current mostly acting through the core and avoiding, if possible, the more resistive parallel shell regions, lowering the electric field in those regions (Figure 5.6(a)).

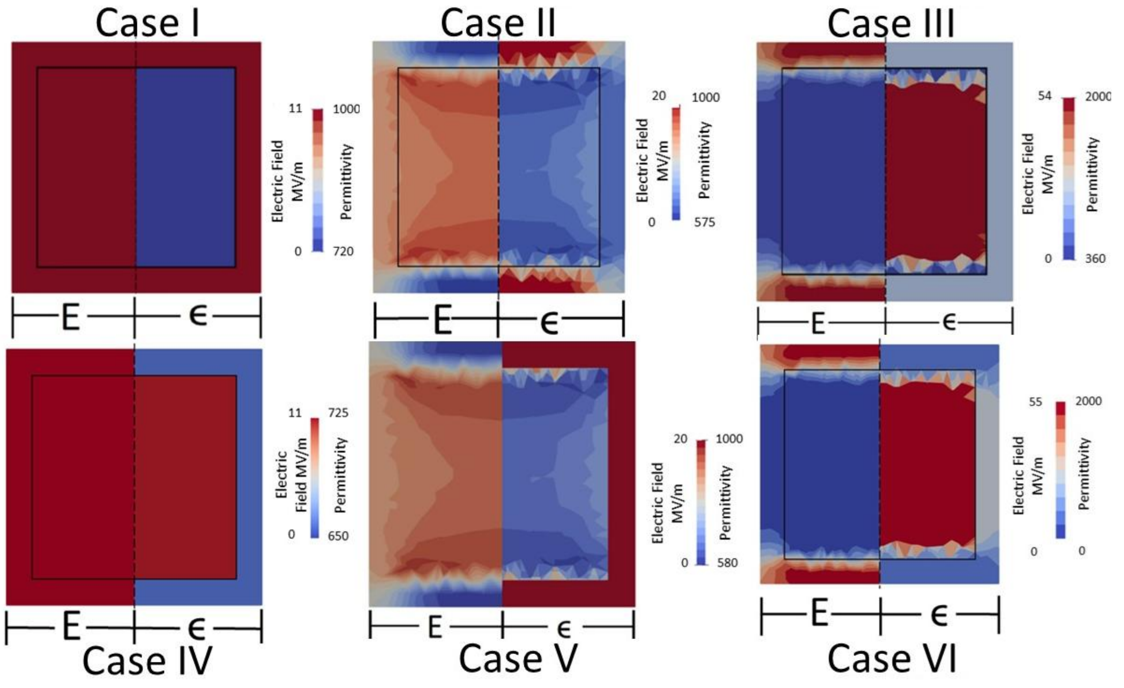

Figure 5.12: Figure showing the electric field and permittivity of Cases I-VI, showing the cross section of the centre cube in the middle row for an E_G of 11 MV/m.

If the core is surrounded by a lower conductive material, such as Case III(CHH-SLL), the current primarily wants to find the path of least resistance through the core. This generates a higher electric field in the shell material, primarily in the top and bottom layers, as seen in Figure 5.10(a). This effectively “screens” the core from high local electric fields, causing the system to exhibit almost little or no NFD. Only a small region of the model, primarily the top and bottom surfaces of the core, experiences a high local field, whereas the rest of the core material remains unchanged. This leads to the capacitance remaining relatively constant when increasing the global electric field and therefore reducing the system's apparent sensitivity to field effects. If the shell material is assigned field dependence as in Case VI(CHH-SLL), while the shielding effect to the core is still present, the shell material now experiences a drop in relative permittivity instead. Although this drop in Case VI(CHH-SLL) is much stronger than in Case III(CHH-SLL), it is still less than that experienced by Cases IV(CHH-SLH) and V(CHL-SLH). In Figure 5.11(b), it can be seen that after normalising the plot for relative permittivity, all plots, regardless of their VCC strength, experience the same general trend. It also shows that the experimental data follow a similar rate of drop in relative permittivity as the model data for Cases IV(CHH-SLH), V(CHL-SLH), and VI(CHH-SLL) as the voltage is increased to 5 MV/m.

The studies shown here investigate how large changes in relative permittivity and conductivity of those regions affect the response; however, small changes (~10% variation) in either the core or shell conductivity caused less than a 5% change in the overall field dependence response. It is only when the values start to become comparable (less than two orders of magnitude) that the current paths through the system are altered and then begin to affect the observed field dependence. We note, however, that the changes to the β value do influence the response more significantly, mainly as it is a scaling component of Equation 5.4, but the trend of the models, irrespective of the value used, remains the same.

Comparing our findings to the work of Zhang et al[38], in which the DC-bias electric field dependence of the dielectric constant was studied for BaTiO3-based ceramics and MLCCs. They confirmed that the permittivity decreases with increasing DC electric field, displaying dielectric nonlinearity. They further established that for ceramics, the DC-bias stability improves with a lower shell ratio and higher effective doping concentration in the shell, as these factors dilute the dielectric nonlinearity of the ferroelectric core. Among the ceramics selected, BT-3Dy7Y showed the least reduction in relative permittivity. From their data, this structure possessed the least initial relative permittivity. This matches the previous findings where having a higher initial relative permittivity leads to larger reductions in permittivity at the same applied field.

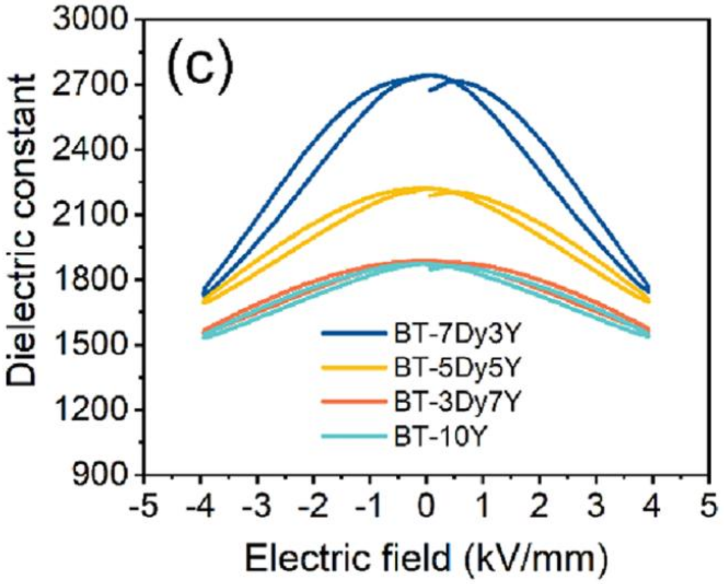

Figure 5.13: Dielectric constant vs Electric field for dielectrics with different dopant concentrations at different applied field strengths[38]*.*

This was attributed to the fact that by responding more linearly to the DC-bias electric field, the highly doped shell enhances the DC-bias stability of the ceramics and reduces the dielectric nonlinearity of the ferroelectric core. While their experiments revealed that the lowest-resistivity material exhibited the greatest permittivity reduction with applied field, it also had the highest initial relative permittivity and the largest shell fraction in the core-shell structure. Both factors contribute to permittivity loss and could account for the difference in our findings.

Through the models presented here, we have assigned a 50:50 volume ratio for the core and shell materials. The measured strength of the VCC dependence of the system will be modified by the core–shell volume ratio due to changes in the current and field profiles previously shown by Heath et al.[34] For example, if the volume fraction of core material were made larger and more conductive, a greater flow of current through the core would be expected, thereby raising the electric field. This would lead to a lower shielding effect and a greater field dependence to be exhibited. Other effects present in MLCC materials, such as grain shape, roughness,[35] or porosity,[36] have been shown to increase local electric fields and, along with volume fraction, are the focus of ongoing and future studies.

In conclusion, we have developed a finite element modeling approach that can aid the understanding of how VCC is affected by the electric microstructure of a system. Typically, MLCC materials are formed from a $BaTiO_3$ material with a doped shell, giving rise to a core that has higher conductivity than the surrounding shell. The findings in this article indicate in this case, over 80% of the core volume experiences a field that is lower than the global value applied, and as such, the core response is relatively unchanged. If the shell has little or NFD, then the apparent VCC change is negligible (Figure 5.11(a), blue stars); however, if the shell does possess some field dependence, although the field which the core experiences is still reduced, a VCC reduction is observed (Figure 5.11(a), blue triangles) and attributed to the change in the properties of the shell. Therefore, through a selection of the core and shell properties, the VCC effects can be enhanced or suppressed as desired while still shielding the core from the high electric fields and improving the apparent breakdown strength of the system. These simulations provide an improved understanding of voltage dependence and help guide the design of future materials for MLCCs with improved performance.

5.3 Additional Information

5.3.1 Additional Model

To further analyse the effect of the conductivity of the material, an additional configuration was analysed in which we maintain the more conductive core with a conductivity of 100 μS/m and the more resistive shell with a conductivity of 0.1 μS/m, but assign the core and shell the same relative permittivity of ε_r =1000. For this model, only the core was field dependent, as in cases I-III

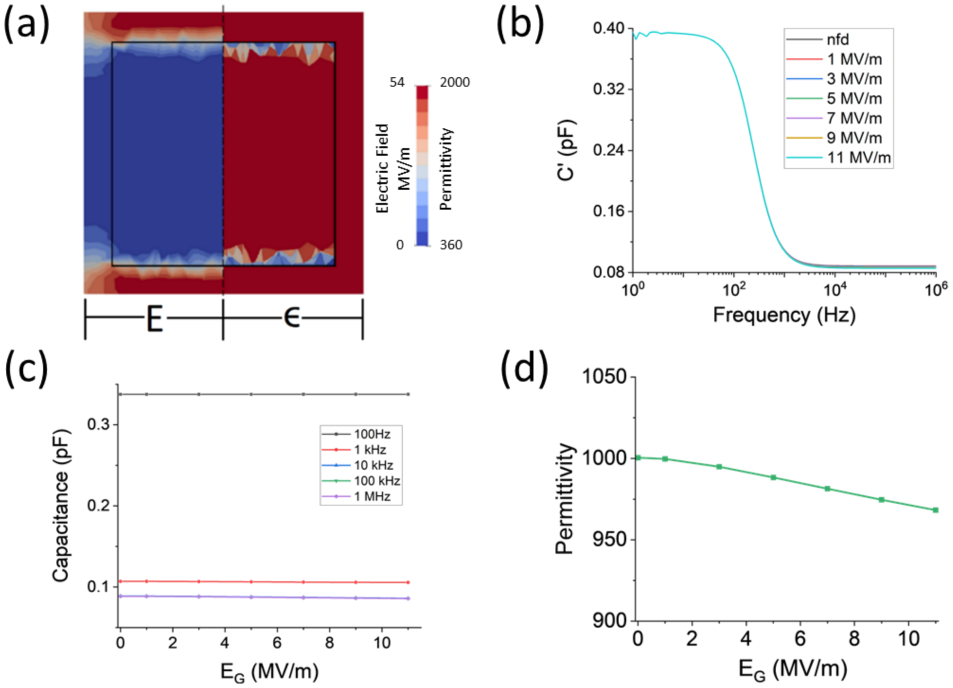

Figure 5.14 The additional case, where the core material is more conductive than the shell material. a) Combined view of the electric field (left) and final relative permittivity (right) when an E_G of 11 MV/m is applied. b) Change in C' as a function of global field, with capacitance (c) extracted at various fixed frequencies. Part c) shows extracted relative permittivity taken at 100 kHz.

In the final configuration, seen in Figure 5.12, we observe a similar shielding effect as seen in study III. Like study III, the top and bottom of the core experience a high field of around 1.6 MV/m and the centre experiences a small field of 7kV/m. The penetration depth of the high electric field is smaller than in the previous case, with only ~5% of its volume experiencing this, and over 85% of the core relative permittivity left unchanged. Similarly, the C' spectra also show a much smaller drop of 3% from 0.089 pF to 0.086 pF in the core, with the shell once again remaining unchanged for a field strength of 11MV/m, less than half the drop of 7% seen in study III and significantly lower than studies I and II.

From these results, it highlights that the ratio of the conductivity between the core and shell plays an important role in determining the strength of the field effect of the material. If the core is surrounded by a lower conductive material, this generates a much larger electric field in the shell material, which in turn effectively screens the core from high local electric fields, causing the system to exhibit almost NFD. Only a small region of the model, primarily the top and bottom surfaces of the core, experiences a high local field while the rest of the core material remains unchanged. This leads to the capacitance remaining relatively constant when increasing the global electric field, which can also be thought of as reducing layer thicknesses.

5.3.2 Overall view

In the above section, while 27 cores and shells were simulated, only the behaviour of the centre core shell structure was analysed and visualised. This was to negate any surface or edge effects that in a real model would be negligible, however, some interesting features can be observed. In Figure 5.15 we see a cross-section of the relative permittivity of 9 core-shells for cases II, III(CHH-SLL), V, and VI(CHH-SLL) at an applied field strength of 11 MV/m. Firstly, looking at case V, where both the core and shell exhibit field dependence and the core is more resistive than the shell, it can be seen that the model appears less like a core-shell model, and more like a layered structure having 7 layers. In case VI, which has the same properties as case V except that the core is more conductive than the shell, a similar layered structure can also be observed; however, this effect is less pronounced as most of the core remains effectively unchanged, as discussed previously. In cases II and III, where the shell material was not field dependent, we still clearly observe a distinct core-shell microstructure. By utilising this information, we can simplify prediction methodologies for certain configurations, thereby aiding in the guidance of the development of future materials to be used in MLCCs.

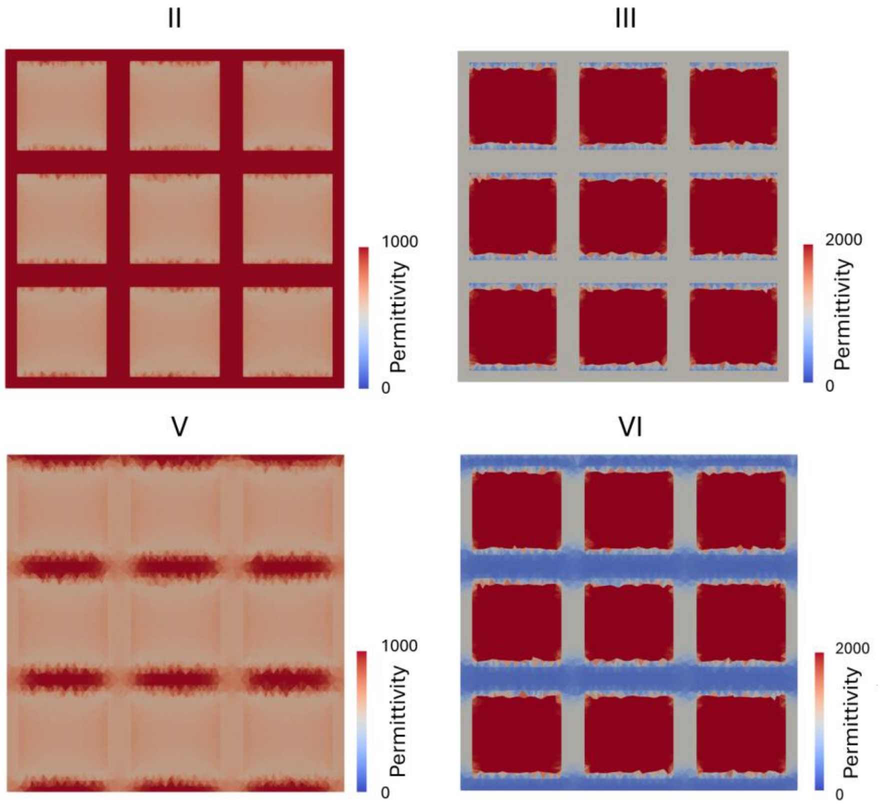

Figure 5.15 Cross-sectional view of 9 core-shells of the 3x3x3 core-shell microstructure showing the relative permittivity when an E_G *of 11 MV/m is applied for cases II, III, V AND VI.*

5.3.3 Single core-shell models

For the models discussed previously in this chapter, the region where two different material properties connect (e.g. where the core meets the shell) could be a possible source of error due to how the code averages the field across the nodes of the quadrilaterals, as seen in chapter 4. In order to check on this, a single core shell model was developed, but with a highly reduced mesh size (1/10 of the normal model) at the interface where the core and shell connect.

This could not be performed for the 3x3x3 models due to the effect this had on the model size. A finer mesh size can increase accuracy but also lead to much larger file sizes and significantly longer processing times. The 3x3x3 models mentioned in this chapter have a file size of about 20 megabytes (mb) per model, and this model has a file size of 180mb with a single core-shell and an increase in processing time from 8 hours to around 96 hours. As an estimate, if the 3x3x3 were modelled in the same way, this would have created a file size of 520mb and an estimated run time of over 80 days.

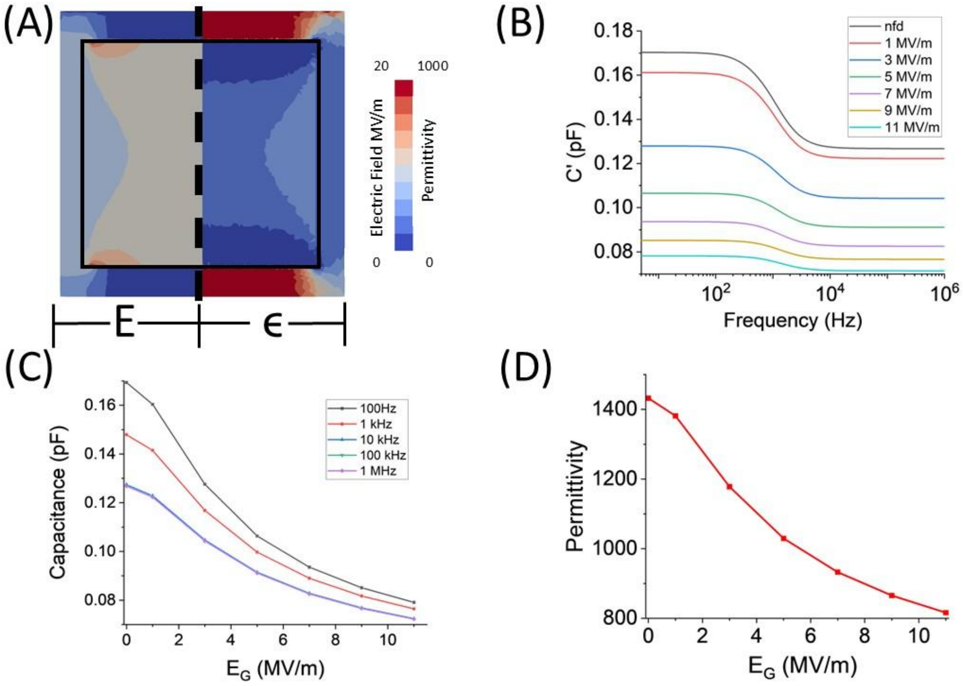

Figure 5.16 ***Case V****(CHL-SLH) with fine mesh****,*** *where the core material is more resistive than the shell material. a) Combined view of the electric field (left) and final relative permittivity (right) for an E_G of 11 MV/m. b) Change in C' spectra as a function of global field, with extracted capacitance at various frequencies. c) The change in capacitance as a function of E_G. A minimal change is observed with the curves overlapping at frequencies greater than 10 kHz. d) Extracted relative permittivity (at 100 kHz) versus E_G.*

We used this finely meshed model for the most complex model, case V, where the core conductivity is set as σ=0.1 μSm^{-1}, lower than that of the shell with σ=100 μSm$^{-1,}$ resulting in a resistive shell model, and both materials are field dependent. As in the previous case V, the electric field in the core is no longer electrically homogeneous. Figure 5.16(a)(left) and forms an 'hourglass' shape. The local electric field at the top and bottom regions of the core once again rises to 16 MV/m, dropping to a value of 14 MV/m nearer the centre of the core. However, unlike previously, an increase in the field to a value of about 17 MV/m can be seen at the corners. Like the previous case V, the relative permittivity of the core once again becomes graded, with over half the core's volume dropping to a relative permittivity value $500 < \varepsilon_r < 650$, whereas the rest of the core volume reduces to $650 < \varepsilon_r < 950$. In the shell region, as the local electric field at the top and bottom of the core is low, a negligible drop in the relative permittivity of the shell in this area is generated. In the regions surrounding the side of the core, the field is once again elevated to 12 MV/m, leading to a relative permittivity drop in the shell of approximately $\varepsilon_r = 650$.

Once again, in the C' spectra and relative permittivity Figure 5.16(c) and Figure 5.16(d) for the NFD case, there are two distinct plateaus in C' of 0.170 and 0.127 pF. As E_G is increased to

11MV/m the capacitance response for the core and shell dominated regions once again drops to values of 0.067 and 0.060 pF, respectively. The effective relative permittivity at 100 kHz once again decreases, with the high field case ε_r=678 compared to the NFD simulation of ε_r=1430.

When comparing the results obtained from the standard mesh and the fine mesh models, the difference in relative permittivity was found to be less than 0.3%. This small variation indicates that the finer mesh does not introduce significant changes to the relative permittivity calculations, suggesting that the errors associated with the mesh size are effectively minimised. Therefore, we can be confident that the choice of mesh has little impact on the accuracy of the results, ensuring that the model's behaviour is not overly influenced by the resolution of the discretisation. This confirms that the numerical results are stable and reliable, regardless of mesh refinement.

5.4 Conclusions

The published paper outlines the development of a finite element modeling approach to understand how VCC is influenced by the electric microstructure of a system. The study shows that the properties of the shell can significantly impact the VCC, with field dependence in the shell leading to noticeable VCC reductions. By carefully selecting core and shell properties, VCC effects can be controlled to improve the performance of MLCCs, providing insights for designing future materials with enhanced performance. Furthermore, it was confirmed that errors due to mesh size are minimised, ensuring reliable results.

In addition to this, we have observed that having a lower initial relative permittivity leads to a lower penetration depth of the field and to lower changes in the field-affected relative permittivity of the dielectric. Finally, we have determined that in multiple core-shell configurations, distinct core-shell microstructures are observed in cases when the shell is not field-dependent. In cases with field-dependent shells, the structure appears more layered, aiding in the simplification of prediction methodologies. Overall, the study highlights the importance of core and shell properties in controlling the voltage dependence and performance of MLCC materials, providing valuable insights for the design of future materials with improved stability and reliability.

5.5 References

1. Analysis of Global Multi-Layer Ceramic Capacitor (MLCC) Markets, 2019-2024. ResearchAndMarkets.com. Published 2019. Accessed June 7, 2023. https://www.businesswire.com/news/home/20191209005389/en/Analysis-of-Global-Multi-Layer-Ceramic-Capacitor-MLCC-Markets-2019-2024---ResearchAndMarkets.com

2. Sun Y, Wu S, Zhang J, Hwang C, Yang Z. Measurement Methodologies for Acoustic Noise Induced by Multilayer Ceramic Capacitors of Power Distribution Network in Mobile Systems. *IEEE Trans Electromagn Compat*. 2020;62(4):1515-1523. doi:10.1109/TEMC.2020.2993850

3. Abebe R, Vakil G, Calzo G Lo, Cox T, Lambert S, Johnson M, Gerada C, Mecrow B. Integrated motor drives: State of the art and future trends. *IET Electr Power Appl*. 2016;10(8):757-771. doi:10.1049/iet-epa.2015.0506

4. Kerridge G, Sinclair DC, Dean JS. Resource-efficient exploration of ternary phase space to develop multi-layer ceramic capacitors. *Acta Mater*. 2021;207:116690. doi:10.1016/j.actamat.2021.116690

5. Hoshina T, Takizawa K, Li J, Kasama T, Kakemoto H, Tsurumi T. Domain size effect on dielectric properties of barium titanate ceramics. *Jpn J Appl Phys*. 2008;47(9 PART 2):7607-7611. doi:10.1143/JJAP.47.7607

6. Hong K, Lee TH, Suh JM, Yoon SH, Jang HW. Perspectives and challenges in multilayer ceramic capacitors for next-generation electronics. *J Mater Chem C Mater*. 2019;7(32):9782-9802. doi:10.1039/c9tc02921d

7. Pan MJ, Randall C. A brief introduction to ceramic capacitors. *IEEE Electrical Insulation Magazine*. 2010;26(3):44-50. doi:10.1109/MEI.2010.5482787

8. Jeon SC, Yoon BK, Kim KH, Kang SJL. Effects of core/shell volumetric ratio on the dielectric-temperature behaviour of $BaTiO_3$. *Journal of Advanced Ceramics*. 2014(1):76-82. doi:10.1007/s40145-014-0096-y

9. Gong H, Wang X, Zhang S, Li L. Synergistic effect of rare-earth elements on the dielectric properties and reliability of $BaTiO_3$-based ceramics for multilayer ceramic capacitors. *Mater Res Bull*. 2016;73:233-239. doi:10.1016/j.materresbull.2015.07.010

10. Park KJ, Kim CH, Yoon YJ, Song SM, Kim YT, Hur KH. Doping behaviours of dysprosium, yttrium and holmium in $BaTiO_3$ ceramics. *J Eur Ceram Soc*. 2009;29(9):1735-1741. doi:10.1016/j.jeurceramsoc.2008.10.021

11. Benlahrache MT, Benhamla N, Achour S. Dielectric properties of $BaTiO_3$-$NaNbO_3$ composites. *J Eur Ceram Soc*. 2004;24(6):1493-1496. doi:10.1016/S0955-2219(03)00577-6

12. Wang SF, Dayton GO. Dielectric properties of fine-grained barium titanate-based X7R materials. *Journal of the American Ceramic Society*. 1999;82(10):2677-2682. doi:10.1111/j.1151-2916.1999.tb02141.x

13. Arlt G, Hennings D, De With G. Dielectric properties of fine-grained barium titanate ceramics. *J Appl Phys*. 1985;58(4):1619-1625. doi:10.1063/1.336051

14. Kerridge G, Sinclair DC, Dean JS. Resource-efficient exploration of ternary phase space to develop multi-layer ceramic capacitors. *Acta Mater*. 2021;207:116690. doi:10.1016/j.actamat.2021.116690

15. Padurariu L, Curecheriu L, Buscaglia V, Mitoseriu L. Field-dependent permittivity in nanostructured $BaTiO_3$ ceramics: Modeling and experimental verification. *Phys Rev B Condens Matter Mater Phys*. 2012;85(22):1-9. doi:10.1103/PhysRevB.85.224111

16. Yue Z, Zhao J, Yang G, Li L. Electric field-dependent properties of $BaTiO_3$-based multilayer ceramic capacitors. In: *Ferroelectrics*. Vol 401. ; 2010:56-60. doi:10.1080/00150191003670424

17. Wei X, Yao X. Analysis on dielectric response of polar nanoregions in paraelectric phase of relaxor ferroelectrics. *J Appl Phys*. 2006;100(6):64319. doi:10.1063/1.2337408/370305

18. Deluca M, Stoleriu L, Curecheriu LP, Horchidan N, Ianculescu AC, Galassi C, Mitoseriu L. High-field dielectric properties and Raman spectroscopic investigation of the ferroelectric-to-relaxor crossover in $BaSn_xTi_{1-x}O_3$ ceramics. *J Appl Phys*. 2012;111(8):84102. doi:10.1063/1.3703672

19. Johnson KM. Variation of Dielectric Constant with Voltage in Ferroelectrics and Its Application to Parametric Devices. *J Appl Phys*. 1962;33(9):2826-2831. doi:10.1063/1.1702558

20. Placeres Jiménez R, Pedro Rino J, Marino Gonçalves A, Antonio Eiras J. Nonlinear dielectric response and transient current: An effective potential for ferroelectric domain wall displacement. *Appl Phys Lett*. 2013;103(11):112901. doi:10.1063/1.4820589/130034

21. Curecheriu LP, Mitoseriu L, Ianculescu A. Nonlinear dielectric properties of $Ba_{1-x}Sr_xTiO_3$ ceramics. *J Alloys Compd*. 2009;482(1-2):1-4. doi:10.1016/j.jallcom.2009.04.036

22. Wei X, Feng Y, Hang L, Yao X. Dielectric properties of barium stannate titanate ceramics under bias field. In: *Ceramics International*. Vol 30. ; 2004:1401-1404. doi:10.1016/j.ceramint.2003.12.084

23. Curecheriu LP, Tufesclt FM, Ianculescu A, Ciomaga CE, Mitoseriu L, Stancu A. Tunability characteristics of $BaTiO_3$ - Based ceramics: Modeling and experimental study. In: *Journal of Optoelectronics and Advanced Materials*. Vol 10. National Institute of Optoelectronics; 2008:1792-1795. doi:https://doi.org/10.2298/PAC0702023C

24. Curecheriu L, Buscaglia MT, Buscaglia V, Zhao Z, Mitoseriu L. Grain size effect on the nonlinear dielectric properties of barium titanate ceramics. *Appl Phys Lett*. 2010;97(24). doi:10.1063/1.3526375

25. Myroshnychenko V, Smirnov S, Mulavarickal Jose PM, Brosseau C, Förstner J. Nonlinear dielectric properties of random paraelectric-dielectric composites. *Acta Mater*. 2021;203:116432. doi:10.1016/j.actamat.2020.10.051

26. Liou JW, Chiou BS. Analysis of the dielectric characteristics for polycrystalline $Ba_{0.65}Sr_{0.35}TiO_3$ (II) - d.c. Field dependence with a modified bias equation. *Journal of Materials Science: Materials in Electronics*. 2000;11(8):645-651. doi:10.1023/A:1008949316917

27. Zhang G, Jiang S, Zeng Y, Zhang Y, Zhang Q, Yu Y. The modified model of the dielectric characteristics for porous $Ba_{0.6}Sr_{0.4}TiO_3$ ceramics. *J Appl Phys*. 2009;106(3):034110. doi:10.1063/1.3183921

28. Zhao Z, Buscaglia V, Viviani M, Buscaglia MT, Mitoseriu L, Testino A, Nygren M, Johnsson M, Nanni P. Grain-size effects on the ferroelectric behaviour of dense nanocrystalline $BaTiO_3$ ceramics. *Phys Rev B Condens Matter Mater Phys*. 2004;70(2):024107. doi:10.1103/PhysRevB.70.024107

29. Dean JS, Harding JH, Sinclair DC. Simulation of impedance spectra for a full three-dimensional ceramic microstructure using a finite element model. Tanaka I, ed. *Journal of the American Ceramic Society*. 2014;97(3):885-891. doi:10.1111/jace.12750

30. Geuzaine, Christophe and Remacle JF. Gmsh. Published online in 2022.

31. Heath JP, Harding JH, Sinclair DC, Dean JS. The Analysis of Impedance Spectra for Core-Shell Microstructures: Why a Multiformalism Approach is Essential. *Adv Funct Mater*. 2019;29(38):1904036. doi:10.1002/adfm.201904036

32. HENNINGS D, ROSENSTEIN G. Temperature-Stable Dielectrics Based on Chemically Inhomogeneous $BaTiO_3$. *Journal of the American Ceramic Society*. 1984;67(4):249-254. doi:10.1111/J.1151-2916.1984.TB18841.X

33. Zhao C, Zhang H, Yang L, Wang Y, Ding Y. Dual laser beam revising the separation path technology of laser-induced thermal-crack propagation for asymmetric linear cutting glass. *Int J Mach Tools Manuf*. 2016;106:43-55. doi:10.1016/j.ijmachtools.2016.04.005

34. Buscaglia MT, Viviani M, Buscaglia V, Mitoseriu L, Testino A, Nanni P, Zhao Z, Nygren M, Harnagea C, Piazza D, Galassi C. High dielectric constant and frozen macroscopic polarisation in dense nanocrystalline $BaTiO_3$ ceramics. *Phys Rev B Condens Matter Mater Phys*. 2006;73(6):064114. doi:10.1103/PHYSREVB.73.064114/FIGURES/6/MEDIUM

35. Heath JP, Dean JS, Harding JH, Sinclair DCJ. Simulation of impedance spectra for core-shell grain structures using finite element modeling. *Journal of the American Ceramic Society*. 2015;98(6):1925-1931. doi:10.1111/JACE.13533

36. Heath JP, Dean JS, Harding JH, Sinclair DCJ. Electric field enhancement in ceramic capacitors due to interface amplitude roughness. *Journal of the American Ceramic Society*. 2019;39(4):1170-1177. doi:10.1016/j.jeurceramsoc.2018.10.033

37. Dale G, Strawhorne M, Sinclair DCJ, Dean JS. Finite element modeling on the effect of intra-granular porosity on the dielectric properties of $BaTiO_3$ MLCCs. *Journal of the American Ceramic Society*. 2017;101(3):1211-1220. doi.org/10.1111/jace.15261

38. Zhang W, Jiang Y, Xiao M, Zhen Y, Zhu C, Zhao P, Hui K, Guo L, Cheng X, Fu Z, Cao X, Wang X. High DC-Bias Stability and Reliability in BaTiO3-Based Multilayer Ceramic Capacitors: The Role of the Core-Shell Structure and the Electrode. *ACS Appl Mater Interfaces*. 2024;16(1):1158-1169. doi:10.1021/ACSAMI.3C16740,

6 Temperature coefficient of capacitance

6.1 Experimental

In chapters 3, 4 and 5, TCC and VCC and extracting Johnson's parameter values from material data were discussed. In this chapter, these will be expanded upon. Initially, experimental VCC data of two materials provided by AVX will be analysed. This will help describe how temperature changes can affect the voltage dependency for dielectrics. This data will then be used to generate TCC plots, which will then be used to understand how the temperature stability changes with increasing applied voltages. Next, the process to extract Johnson's parameter will be described by using the experimental data for both materials.

Finally, in order to demonstrate the utility of the code described in chapters 4 and 5, it will be used to generate TCC data using the experimental material data seen in chapter 3 for two different configurations.

6.1.1 Study one

Two commercial materials which has been designed and supplied by KAVX[1] along with experimental data for us to use in our simulations. Due to confidentiality, their names cannot be provided and will be hereby referred to as material 1 and material 2. The relative permittivity of the material has been measured for a temperature range from -55°C to 125°C for applied voltages varying from 0 (the NFD case) to 50 V. Each of these materials were tested at two different thicknesses. As seen in the data below, the relative permittivity once again exhibits significant variations depending on both the temperature and the applied voltage. Study one will study Material 1 having two different thicknesses of 7 µm and 11 µm.

6.1.1.1 7µm thickness

Figure 6.1 illustrates the relative permittivity vs temperature graph for the material having a thickness of 7 µm, ranging from approximately -50°C to 150°C, under applied voltage conditions varying from 0V to 50V. At lower temperatures, below 20°C, the relative permittivity remains relatively stable for all applied voltages. The values for 0V start around 1500, gradually decreasing with increasing voltage. At this stage, the material exhibits minimal sensitivity to temperature changes, and the relative permittivity remains nearly constant across the range, although there is a slight downward shift as the applied voltage increases.

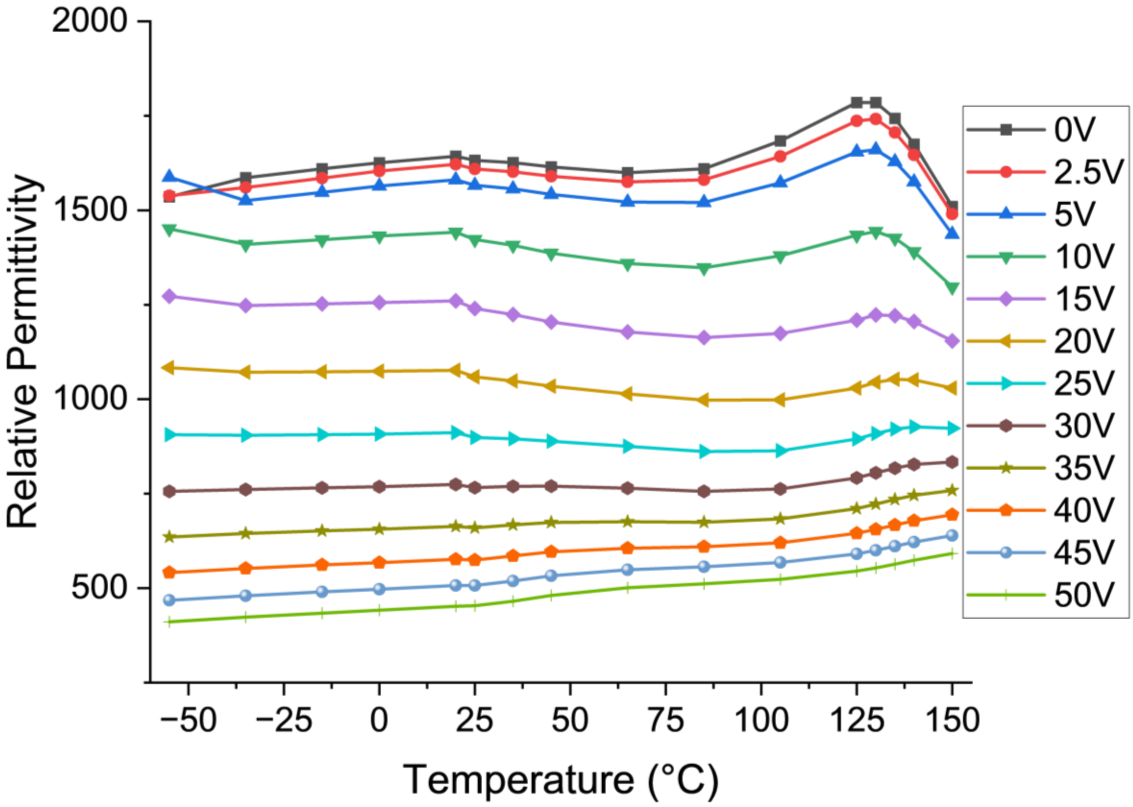

Figure 6.1: Variation of relative permittivity with temperature under different applied voltages ranging from 0V to 50V for material 1 having a thickness of 7µm, showing a consistent decrease in permittivity as voltage increases across the entire temperature range.

As the temperature rises, between 20°C and 120°C, the relative permittivity increases, reaching a peak around 125°C. This peak is prominent for all voltages, but the magnitude of the relative permittivity varies significantly and starts shifting towards 135°C as the applied voltage increases. For 0V, the relative permittivity reaches its highest value at about 1700, while at 50V, the peak value is substantially lower, just over 900. This indicates a strong suppressive effect of the electric field on the relative permittivity, with higher voltages leading to reduced dielectric responses.

As the voltage increases, the percentage drop in the relative permittivity as higher voltages are applied begins to decrease, suggesting a threshold limit on the voltage dependence. Additionally, the relative permittivity under 0V shows a prominent peak, indicating strong dielectric performance, whereas higher voltages not only reduce the peak value but also flatten the response, showing a muted dependence on temperature. This data highlights what we have seen in previous chapters, that voltages cause a notable suppression of the relative permittivity, and that increasing voltage leads to an increased reduction.

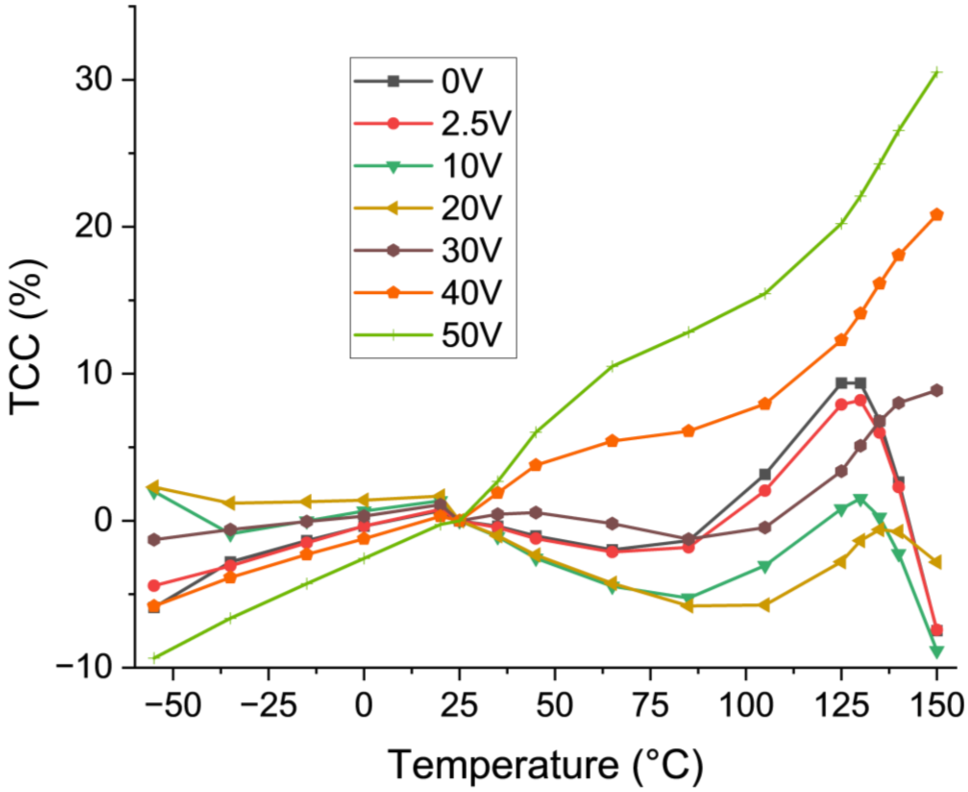

Figure 6.2: Graph illustrating the Temperature Coefficient of Capacitance (TCC) as a function of temperature for different applied voltages (0V to 50V), highlighting the shift in TCC behaviour with increasing voltage, particularly the decreased stability at higher voltages.

Figure 6.2 shows the TCC values vs temperature under varying applied voltages from 0V to 50V. Some of the data from Figure 6.1 has been removed to increase the legibility of the graph. At 0V, the TCC values fluctuate noticeably, ranging from -7.5% to 9.5%. This shows a significant variation, suggesting that the dielectric material experiences considerable changes in capacitance due to temperature, even in the absence of an applied electric field.

Moving to 10V, there is further tightening of TCC values toward zero, especially in the middle temperature ranges. The TCC values now range between -9% and 6%, showing improved stability. However, there are still significant deviations, particularly at more extreme temperature points.

At 20V, the dielectric material shows improved stability in mid-temperature ranges with less extreme TCC values, but variation is still present. The TCC values -3% to 6% at 20V. These indicate moderate improvement, particularly in terms of reduced spread in certain regions.

At applied voltages above 20 V, readings start to change. Below this point, the TCC appeared to be undergoing a clockwise rotation. However, at higher voltages, it starts rotating back in the counterclockwise direction. Additionally, the TCC begins to increase past the peak temperature of 125-135°C rather than decreasing as seen at lower applied voltages.

Finally, at 30V to 50V, the values show strong positive shifts, with 50V having a TCC of -9.5% to 30%. This demonstrates significant instability, showing higher temperature dependence under high applied voltages.

In conclusion, the mid-range voltages around 20V to 30V show the best performance in terms of stability, with the least deviation from zero and minimal variation. In contrast, lower and higher voltages exhibit greater instability, with significant fluctuations and larger deviations from zero.

6.1.1.2 11μm thickness

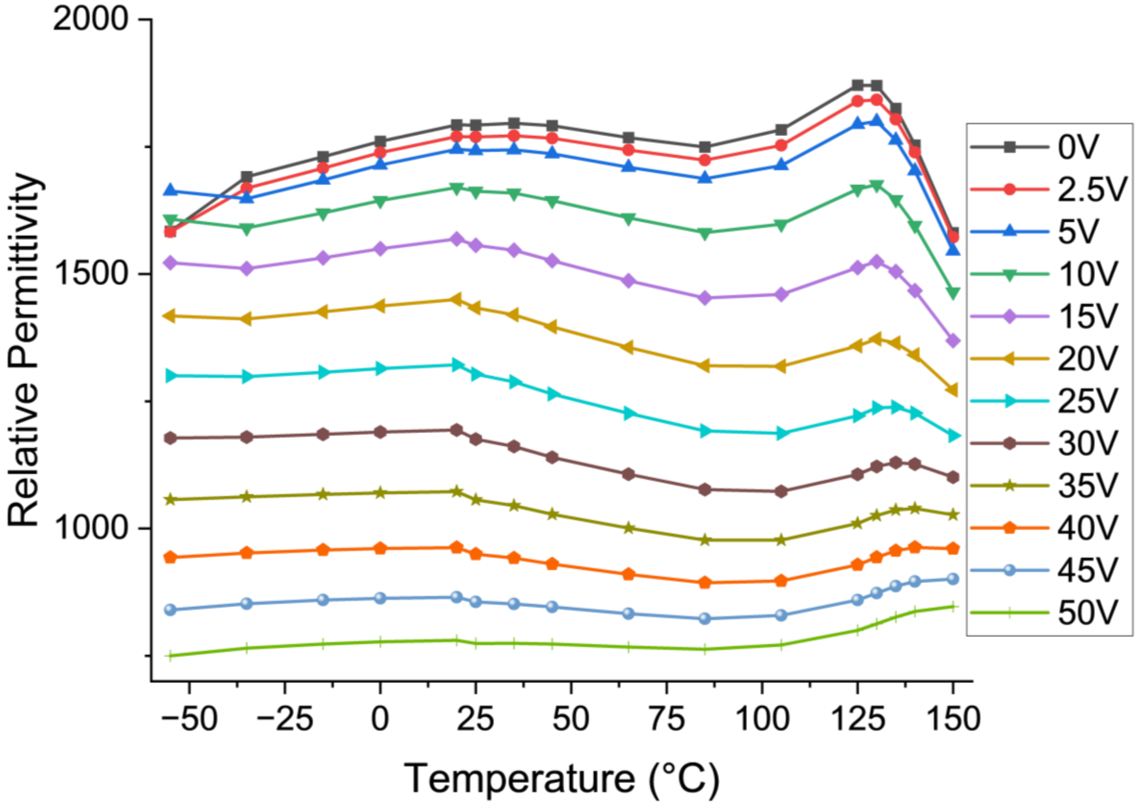

Figure 6.3: Variation of relative permittivity with temperature under different applied voltages ranging from 0V to 50V for material 1 having a thickness of 11μm, showing a consistent decrease in relative permittivity as voltage increases across the entire temperature range.

Figure 6.3 shows the relative permittivity of a material at different temperatures ranging from -55°C to 150°C, under various applied voltages from 0V to 50V for the same material but having a thickness of 11 µm. This follows a similar trend as the 7 µm thickness model with a few key differences. Firstly, the NFD relative permittivity at 0V across all temperatures is consistently higher in the thicker model. For example, at 0°C, the 7µm material has a relative permittivity value of 1625.8, whereas the 11µm material starts at 1760.5. This indicates that the thicker dielectric in the 11µm material exhibits a greater inherent polarizability, possibly due to a higher density of dipoles or a different structural arrangement.

The effect of voltage on relative permittivity also differs significantly between the datasets. The 7µm material shows a sharper decline in relative permittivity as the voltage increases. At 0°C, the relative permittivity in the 7µm material decreases from 1625 at 0V to 450 at 50V, reflecting a substantial reduction. In contrast, the 11µm material experiences a more gradual decline, dropping from 1760 to 780 under the same conditions. The maximum percentage drop in relative permittivity between 0V and 50V is another critical aspect. In 7µm material, the drop at 0°C is approximately 72.8%, whereas in 11µm material, the drop is about 55.8%. This suggests that the thinner dielectric in the 7µm material is more sensitive to the applied electric field, likely due to the greater electric field intensity affecting the alignment of dipoles more drastically, as discussed in previous chapters.

Regarding temperature dependence, both datasets show a general trend of decreasing relative permittivity with increasing temperature, particularly at higher voltages.

At low temperatures, such as -55°C, the relative permittivity starts high across all voltages, peaking at 1583.9 for 0V and gradually decreasing as voltage increases, reaching 749.9 at 50V. This trend shows that the relative permittivity diminishes significantly with higher applied voltages at low temperatures, indicating strong voltage dependence.

As the temperature increases to -35°C, the relative permittivity remains high but slightly lower than at -55°C for most voltages, again showing a decrease with increasing voltage. At this temperature, 0V shows a relative permittivity of 1691.0, while at 50V, it is reduced to 765.0, reflecting a similar pattern of voltage-dependent decline.

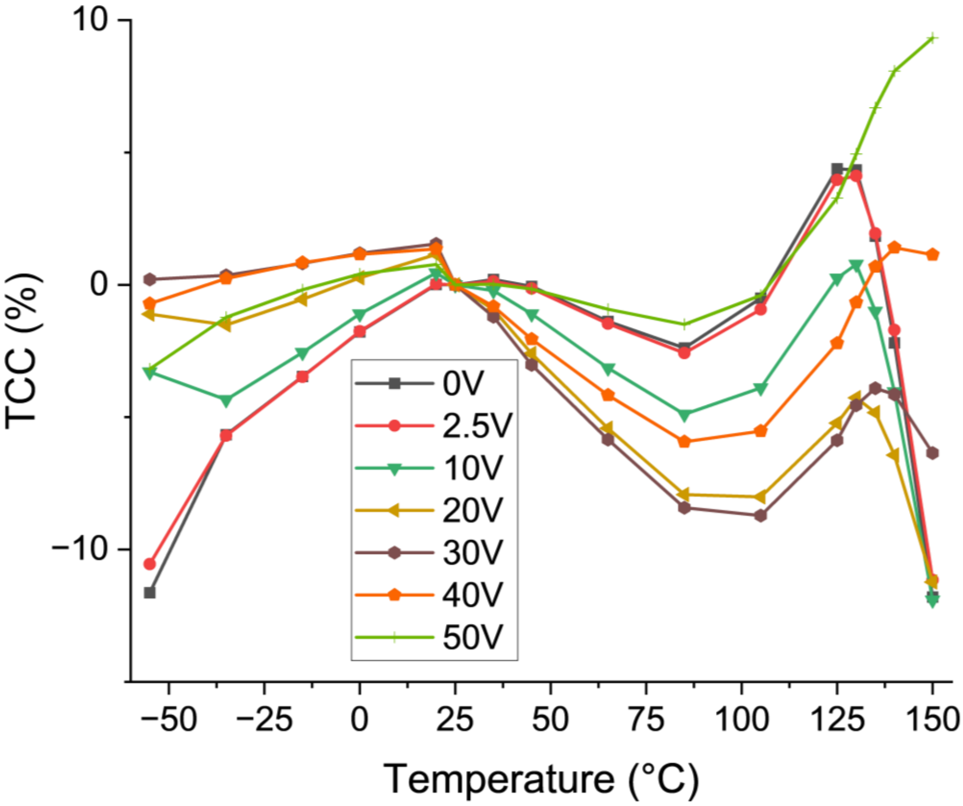

Figure 6.4: Graph illustrating the Temperature Coefficient of Capacitance (TCC) as a function of temperature for different applied voltages (0V to 50V), highlighting the shift in TCC behaviour with increasing voltage, particularly the decreased stability at higher voltages.

When comparing the TCC versus temperature datasets for the two thicknesses, several distinct differences and similarities can be observed.

The 11µm thick material as seen in Figure 6.4, generally exhibits more negative TCC values across the temperature and voltage range compared to the 7µm material. For instance, at 0V and -55°C, the TCC in the 11µm material is -11.5%, while in the 7µm material it is -6%. This indicates that the thicker dielectric is more temperature dependent.

As voltage increases, the sensitivity of TCC in the 7µm material appears to be greater, particularly at higher voltages. For example, at 50V and 150°C, the 7µm material reaches a TCC of 30.5%, whereas the 11µm material shows a TCC of only 9%. This once again suggests that the thinner dielectric in the 7µm material is more responsive to voltage changes, especially under higher voltage conditions.

Despite these differences, both datasets demonstrate similar trends in how TCC changes with temperature. Both show a reduction in the negative TCC values as temperature increases, and a shift towards more positive or less negative values at higher temperatures. Additionally, both datasets exhibit a decrease in TCC as voltage increases from 0V to 50V, but the rate and magnitude of this decrease differ between the two thicknesses.

Overall, the major difference lies in the baseline TCC values and their sensitivity to voltage changes, with the 11µm material showing more negative TCC values and less sensitivity to voltage compared to the 7µm material. Both datasets, however, follow a consistent trend of TCC change with temperature and voltage.

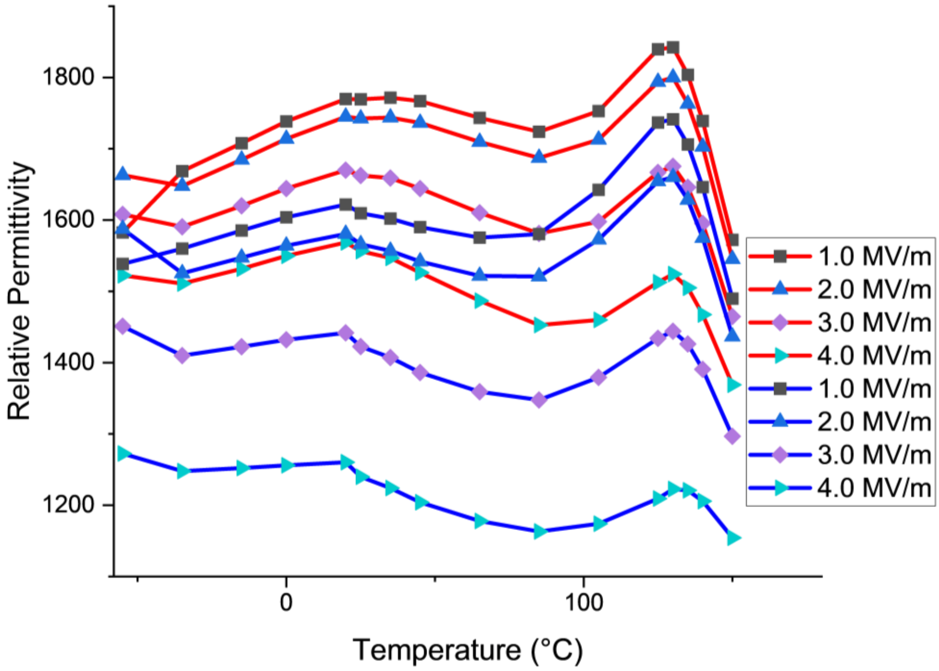

Figure 6.5:Graph comparing the 7µm (blue) and 11µm(red) thick materials when the applied electric field is equalised, showing the difference in the permittivities.

From Figure 6.5, we see that the 11 µm samples consistently demonstrate higher permittivity values than the 7 µm samples at low electric fields (below 2 MV/m). However, this difference becomes less pronounced as the electric field strength increases. The 7 µm samples show a more rapid decline in permittivity at higher fields (above 3 MV/m), indicating a stronger suppression of polarisation under increased electric field stress. Both thicknesses exhibit peak permittivity values in the moderate temperature range of 0–20°C, with significant reductions at temperature extremes (e.g., -55°C and 150°C). Notably, the 11 µm samples maintain higher permittivity values at elevated temperatures. For example, at 150°C and 1 MV/m, the 11 µm sample records a permittivity of 1572.1, compared to 1489.9 for the 7 µm sample. The 7 µm samples undergo a substantial reduction in permittivity of approximately 40 to 50% when the electric field increases from 1 MV/m to 4 MV/m. For instance, at 25°C, the permittivity drops from 1609.5 to 1240.0. In contrast, the 11 µm samples experience a less severe decline of 30 to 40% over the same field range (from 1769.4 to 1556.3), suggesting greater stability under high-field conditions. All of this highlights the fact that at smaller thicknesses, similar applied electric fields can lead to stronger sensitivity to the applied field.

6.1.2 Study two

Study two will cover material 2, which was tested at two different thicknesses of 3.9 µm and 4.9 µm for voltages ranging from 0 V to 50 V at a temperature range of -55°C to 130°C.

6.1.2.1 3.9 µm Thickness

Figure 6.6 shows the relationship between relative permittivity and temperature across a range of applied voltages, from 0V to 50V for a thickness of 3.9 µm. At 0V, the relative permittivity starts at around 2700 at the lowest temperature of -55°C, reaching a peak of approximately 3000 near 20°C, and then gradually declines to about 2500 at the highest temperature of 125°C. As voltage increases, the relative permittivity values uniformly decrease across the temperature range. At 2.5V, the initial permittivity is lower than at 0V, starting near 2500, peaking around 2650, and then descending to roughly 2400. This represents approximately a 7.4% reduction at -55°C, increasing to 10.3% at 40°C, and decreasing to about 4.5% at the highest temperature of 125°C.

By the time the voltage reaches 50V, the relative permittivity decreases significantly, beginning at about 320 at -55°C, peaking just below 500, and maintaining a relatively flat curve. The percentage drop between the 0V and 50V cases is much more significant. At -55°C, the relative permittivity experiences approximately an 88% decrease. At the highest temperature of 125°C, it experiences an 80% reduction.

Overall, this analysis once again highlights the dramatic impact of increasing voltage on relative permittivity across the temperature spectrum, with more substantial decreases occurring at higher voltages. The consistent downward shift of the curves with increasing voltage indicates a significant suppression of relative permittivity as electric field strength rises. However, as applied voltage increases, the reduction effect begins to get weaker.

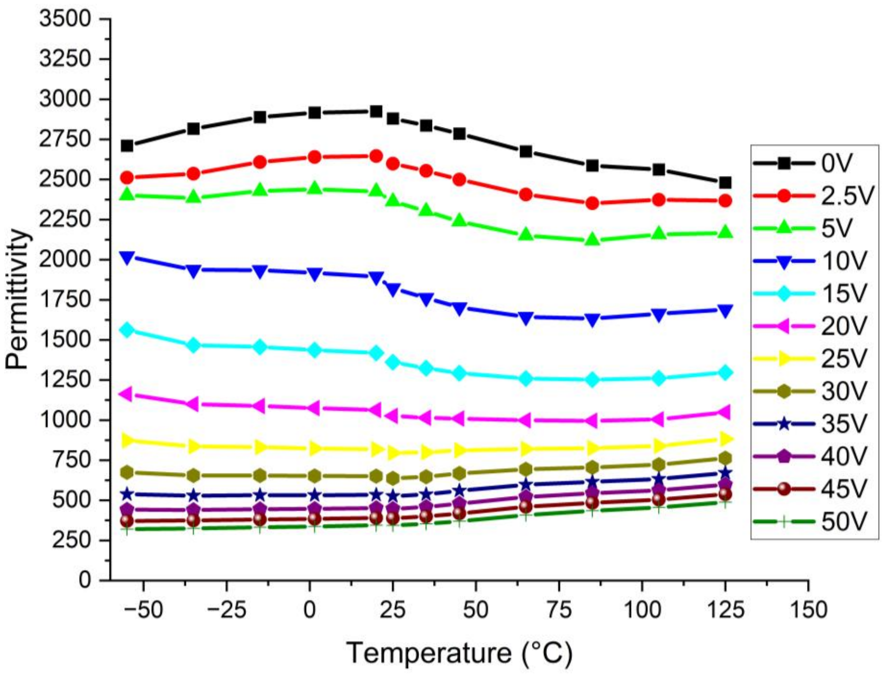

Figure 6.6 Variation of relative permittivity with temperature under different applied voltages ranging from 0V to 50V for material 2 with a thickness of 3.9 µm, showing a consistent decrease in relative permittivity as voltage increases across the entire temperature range.

Figure 6.7 shows the variation in the TCC as a function of temperature for different applied voltages, ranging from 0 V to 50 V, with a temperature range from -55°C to 125°C for material 1. Some of the data from Figure 6.6 has been removed to increase the legibility of the graph.

At 0 V, the TCC curve starts near -6% at -55°C, with a slight decrease to about 2% near 20°C, followed by a steady return toward -14% at 125°C. This line demonstrates relatively stable behaviour, with only minor deviations throughout the temperature range. The curve for 2.5 V closely follows the 0 V case, with the curve flattening slightly at -55°C and after 85°C.

As the applied voltage increases to 10 V, the curve varies significantly from the 0V case. The TCC starts off at close to 11% at lower temperatures but begins to dip further below -10% around 65°C before curving upwards at higher temperatures. At 20 V, the curve exhibits a similar pattern but with a more pronounced flattening effect at temperatures higher than 25°C.

For 30 V and higher voltages, the curves exhibit a dramatic shift. The 30 V starts out at around 6% at lower temperatures and rises steeply past 25°C, reaching 20% at 125°C. The curves for 40 V and 50 V amplify this trend, with even steeper slopes past 25°C. At 50 V, the TCC reaches nearly -7% at the lowest temperatures and climbs above 40% at 125°C. This indicates significant instability under higher applied voltages, with the TCC becoming more sensitive to temperature changes.

The general trend reveals that as the applied voltage increases, the TCC curves initially flatten but then rotate counterclockwise and exhibit increasingly greater deviations from the baseline (0 V). The curves for higher voltages not only become more divergent but also display pronounced non-linear behaviour. Stability diminishes significantly as voltage increases, with the 50 V curve being the least stable across the entire temperature range. Conversely, the 2.5 V curve is the most stable, maintaining proximity to 0% TCC with minimal fluctuation.

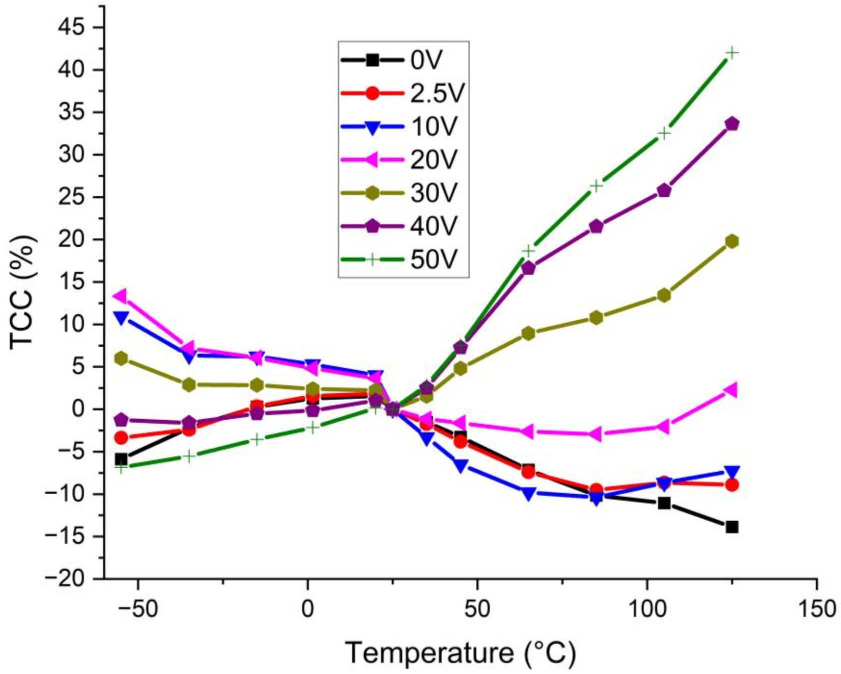

Figure 6.7: Graph illustrating the Temperature Coefficient of Capacitance (TCC) as a function of temperature for different applied voltages (0V to 50V), highlighting the shift in TCC behaviour with increasing voltage, particularly the decreased stability at higher voltages.

6.1.2.2 4.9 μm Thickness

The same material was used by KAVX, but this time using a 4.9µm thickness of dielectric between the electrodes. Again, the relative permittivity has been measured for a temperature range from -55°C to 125°C for applied voltages varying from 0 (the NFD case) to 16 V. As seen in Figure 6.8, the relative permittivity once again exhibits significant variations depending on both the temperature and the applied voltage.

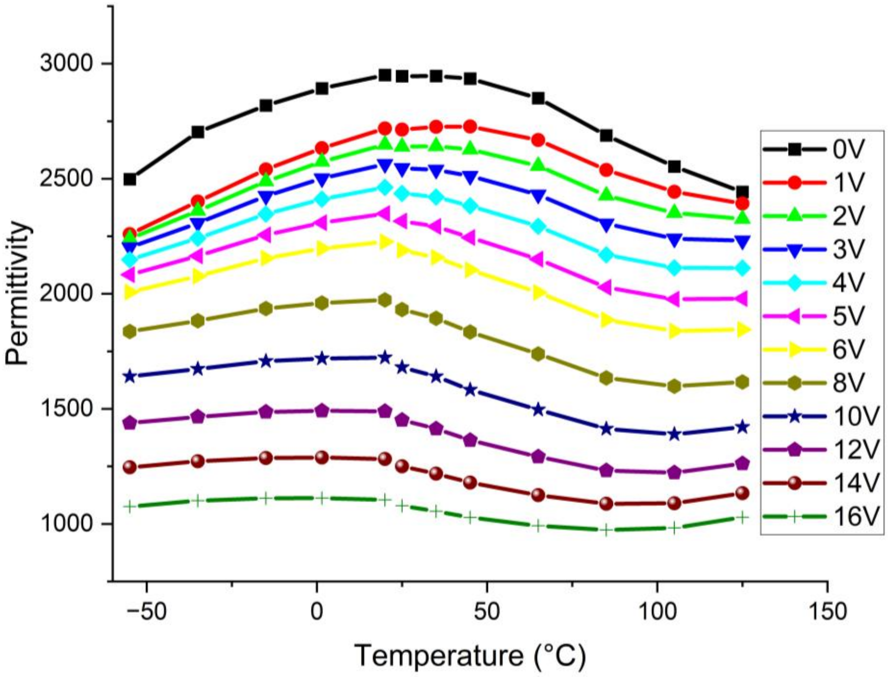

Figure 6.8: Graph depicting the variation of relative permittivity with temperature across different applied voltages (0V to 16V), showing the significant decrease in relative permittivity as voltage increases for material 2 with a thickness of 4.9 µm..

At 0V, the relative permittivity once again starts around 2500 at low temperatures, gradually increases to a peak near 3000 around 50°C, and then slowly declines as the temperature continues to rise, eventually dropping below 2500 by 150°C. This curve represents the baseline behaviour of the material without an applied electric field, showing a typical increase in relative permittivity with temperature up to a maximum, followed by a decrease as the material reaches higher temperatures. The 0V to 1V transition shows a relatively small drop in relative permittivity, ranging from 3.33% at peak to 9.5% at -55°C and 2% at 125°C.

As voltage increases to 16V, there is a substantial drop in relative permittivity with a decrease of nearly 58 % at -55°C and 125°C, and 50% at the peak temperature. This highlights the strong suppressive effect of higher voltages on the material's relative permittivity. There is a noticeable decrease in the overall relative permittivity at all temperatures, like material 1.

At 16 V, the graph also indicates a systematic shift in the curves as voltage increases, with each curve showing less variation between the peak and low-temperature relative permittivity. This suggests that higher voltages dampen the temperature sensitivity of the relative permittivity, leading to a more uniform response across the temperature range. The overall trend is that increasing voltage results in a lower peak relative permittivity and a more linear decline with temperature.

In summary, the graph once again supports our finding that applying an electric field systematically reduces relative permittivity across the entire temperature range, with higher voltages causing a more significant reduction in relative permittivity and diminishing the temperature-dependent variation typically seen in the 0V case. This behaviour highlights the impact of the electric field on the dielectric properties of the material, emphasising both the suppression of relative permittivity and the reduction of thermal sensitivity as voltage increases.

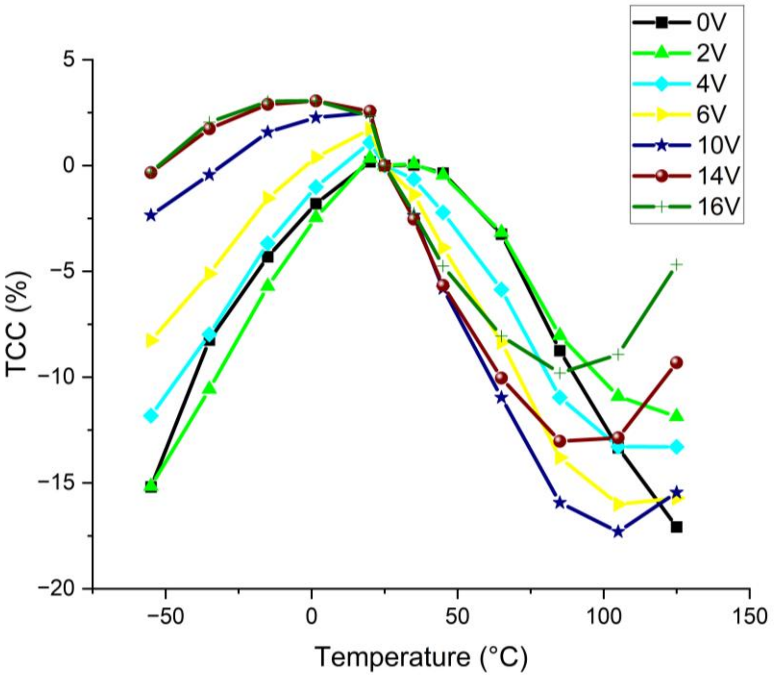

Figure 6.9: Graph illustrating the Temperature Coefficient of Capacitance (TCC) as a function of temperature for different applied voltages (0V to 16V), highlighting the shift in TCC behaviour with increasing voltage, particularly the clockwise rotation and increased stability at higher voltages.

Figure 6.9 shows the Temperature Coefficient of Capacitance (TCC) as a function of temperature for different applied voltages, ranging from 0V to 16V for material 2. Some voltages are not shown to ease our understanding of the graph. Using the 0V curve as the NFD case, the influence of increasing applied voltage on TCC is evident through shifts and rotations in the graph.

At 0V, the TCC starts near -15% at temperatures of -55°C, gradually increases, peaking at 0% at 25°C, and then declines, falling below -15% by 125°C. This behaviour shows a typical thermal response where capacitance improves with temperature up to a certain point before degrading.

As voltage increases to 2V, 4V, and 6V, the overall shape of the curves remains consistent with the 0V case, but the peaks shift slightly higher in temperature and are positioned closer to 0% peaking at nearly 2.5% at 6V. This pattern continues up to 10V, where the peak is more pronounced, suggesting an initial stabilisation effect of the applied voltage on capacitance.

As the voltage is increased past 6V to 10V, 14V, and 16V, the curves exhibit a more complex behaviour. For temperatures up to around 25°C, the initial TCC is much higher; for example, 14V has an initial TCC at -55°C of less than 0.5%, which then peaks at 3%. From temperatures of 25°C to 65°C, they follow a similar declining trend as the lower voltages. However, as the temperature increases further, the curve begins to flatten out and then begins to increase past 105°C, indicating a reversal or reduced rate of decline in TCC. This might suggest that at very high voltages, the system begins to stabilise or respond differently to temperature increases, possibly due to saturation or nonlinear dielectric effects.

Overall, as voltage increases up to 10V, the graph exhibits a clockwise rotation with the peaks shifting towards higher temperatures and becoming less negative or slightly positive, except for 2V, which exhibits a slight counterclockwise rotation. This indicates that increasing voltage initially counteracts the thermal effects on capacitance. However, beyond 10V, the curves start to rotate back in an anticlockwise direction, particularly visible in the 16V curve where the high-temperature region rises, and the TCC shows less degradation.

In summary, as voltage increases, the TCC curves show a clockwise rotation initially, indicating stabilisation of capacitance at lower temperatures. However, at higher voltages like 14V and 16V, there is an anticlockwise rotation in the high-temperature region, reflecting a complex interaction between applied voltage and temperature effects on capacitance, which leads to a slight improvement of the TCC at higher temperatures.

6.1.3 Conclusions

The study of Materials 1 and 2 describes the impact of temperature and applied voltage on relative permittivity and the TCC. For Material 1, relative permittivity decreases significantly with increasing voltage, with reductions ranging from 7.4% at lower voltages to over 88% at the highest voltage of 50V. The temperature dependency is also evident, as relative permittivity peaks around 20°C and declines at both lower and higher temperatures. Higher voltages further suppress relative permittivity and reduce its temperature sensitivity.

Similarly, Material 2 exhibits a consistent decrease in relative permittivity with rising voltage, reaching a nearly 58% reduction at 16V. The trend demonstrates a dampened temperature sensitivity as voltage increases, leading to more uniform relative permittivity across the temperature range.

In terms of TCC, both materials show initial stabilisation of capacitance with increasing voltage, followed by more complex behaviours at higher voltages. For Material 1, the TCC curves shift and rotate counterclockwise, indicating significant instability at higher voltages, with the most pronounced changes at 50V. In contrast, Material 2 exhibits an initial clockwise rotation, suggesting stabilisation at lower temperatures, but at voltages beyond 10V, the TCC curves display an anticlockwise rotation at higher temperatures, reflecting nonlinear dielectric effects.

Overall, the study highlights the critical influence of applied voltage on both relative permittivity and TCC, with higher voltages causing more pronounced suppression of relative permittivity and complex TCC behaviour, demonstrating the relationship between electric fields and thermal effects in dielectric materials.

6.1.4 Johnson's parameter

In the previous chapter, the extraction of Johnson's parameter from material data was discussed. However, the method to do this was not described. Johnson's parameter can be determined by using the least mean squares method (LMS) to fit the graphs, and this will be shown by using the data from Materials 1 and 2. This technique fits a model to a dataset by minimising the error between the observed data and the model's predictions. It operates iteratively to adjust the model parameters and tries to reduce the mean square error (MSE) over the dataset. This approach is particularly useful in scenarios where the relationship between input features and output is dynamic or not well understood, and the model needs to adapt continuously. It is to be noted that Johnson's parameter obtained by this method corresponds to the material as a whole and not to the individual core and shell parameters.

Table 6.1 Table showing the data used in calculating Johnson's parameter for relative permittivity values calculated at two voltages at a single temperature.

Applied Voltage	**Measured Permittivity**	**Field over core (MV/m)**	**Calculated Permittivity**	**Error**	**Error Squared**
0	2480	0.00E+00	2.48E+03	0.00E+00	0.00E+00
2.5	2367	6.41E+05	2.41E+03	-4.61E+01	2.13E+03

To apply LMS, you start with an initial guess for the model parameters, which could be set to zero or small random values. In our model, Johnson's parameter will be fitted. We input the experimental data (seen in the measured relative permittivity column in Table 6.1 The method then processes the data points one at a time. For each data point, it predicts the calculated relative permittivity, which is calculated using Johnson's equation (Equation 2.23) using the current model parameters and computes the error, which is the difference between the measured value and the calculated value. It then squares the error and adds the error of all data points.

The core of the LMS method lies in its parameter update rule. After calculating the error for a given data point, the method updates the model parameters in the direction that reduces the total error. This update is proportional to both the error and the input values of the current data point. A crucial part of this process is the step-size parameter, which controls how much the parameters are adjusted at each step. A small step size results in slow but stable convergence, while a larger step size accelerates the process but risks overshooting the optimal parameters or causing instability. In our case, the iterative calculation was carried out using the Solver add-on in Excel[2].

The LMS method continues this process iteratively, refining the model parameters as it cycles through the dataset multiple times till the parameters converge to values that minimise the mean square error, thereby fitting the model to the data. Figure 6.10 demonstrates the relative permittivity vs applied voltage graph for material 1, showing the difference between the experimental data vs the data generated by using Johnson's parameter by the LMS method at a temperature of 25°C. We can see that for both thicknesses, the fit value follows the observed value closely, indicating that the LMS method provides a reliable prediction of the relative permittivity behaviour under varying applied voltages. This suggests that the model is well-suited to capturing the material's response to changes in voltage, with minimal deviation between the experimental and predicted data across the voltage range. The consistency of the fit across both thicknesses further supports the robustness of the model in representing the material's dielectric properties at this specific temperature.

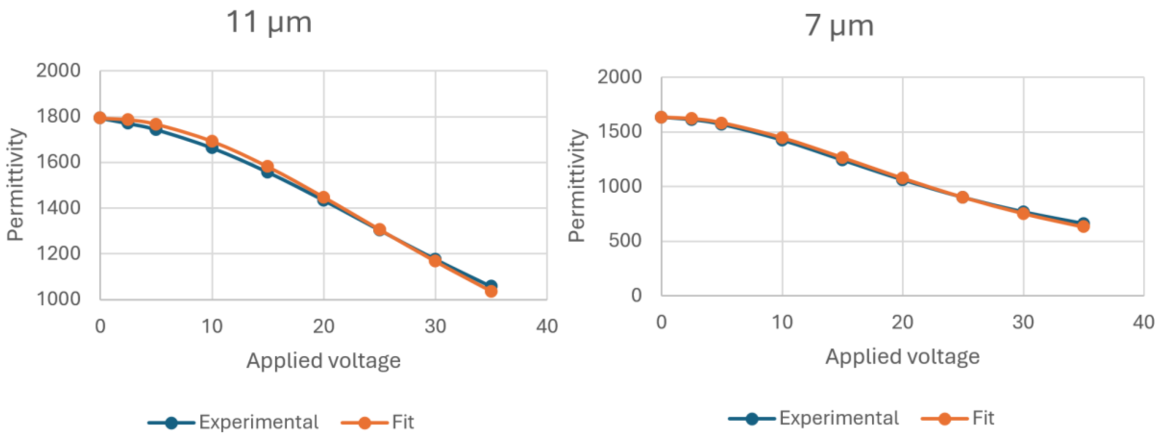

Figure 6.10: Figure showing the relative permittivity vs applied voltage graph for material 1, showing the difference between the experimental data vs the data generated by using Johnson's parameter by the LMS method at a temperature of 25°, at a thickness of 11 µm and 7 µm.

This method is particularly advantageous for its simplicity and computational efficiency, making it suitable for real-time applications or situations where data arrives sequentially. Additionally, because it continuously updates the model, LMS is well-suited for environments where the underlying data patterns may change over time.

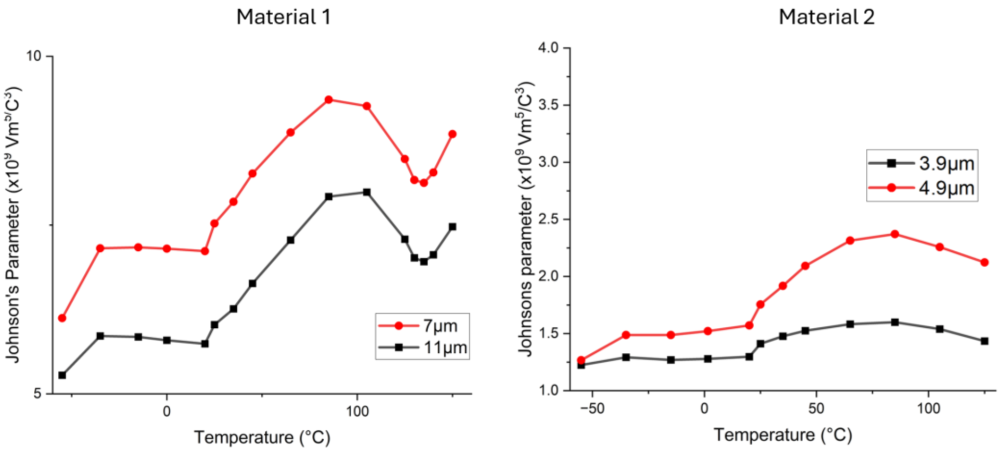

Figure 6.11: Change in Johnson's parameter as temperature is increased. Material 1 was fit over a range of voltages from 0V to 50V. Material 2, having a thickness of 3.9µm, was fit for voltages from 0V to 15V, and the 4.9µm was fit from 0V to 16V, to have an equal comparison.

In Figure 6.11, Johnson's parameter is shown against temperature for four materials with different thicknesses. In material 1, having thicknesses of 11 μm and 7 μm, we observe a similar trend in both datasets across the temperature range from -55°C to 150°C. For the 11 μm thick material, the Johnson's parameter starts at 5.28x10^9 Vm^5/C^3 at -55°C and slightly decreases as the temperature rises, reaching 7.48 x10^9 Vm^5/C^3 at 150°C. In contrast, the 7 μm thick material begins with a higher value of 6.12 x10^9 Vm^5/C^3 at -55°C, decreasing over the same temperature range to 8.85 x10^9 Vm^5/C^3 at 150°C. The Johnson's parameter for the 7 μm thick material consistently shows a higher value compared to the 11 μm thick material at each temperature point, though both materials exhibit a decrease in the parameter as temperature increases.

Next, when comparing material 2 having thicknesses of 3.9 μm and 4.9 μm, the trend shows that both materials follow a similar pattern, with the Johnson's parameter increasing as the temperature rises, though at different rates. For the 3.9 μm thick material, the Johnson's parameter starts at 2.62 x10^9 Vm^5/C^3 at -55°C and gradually increases to 3.68 x10^9 Vm^5/C^3 at 125°C. For the 4.9 μm thick material, it begins at a slightly lower value of 1.22 x10^9 Vm^5/C^3 at -55°C, and increases to 1.43 x10^9 Vm^5/C^3 at 125°C. While the overall trend is similar—both materials show an increase in Johnson's parameter with temperature—the 3.9 μm thick material has a higher initial value and a greater overall increase in Johnson's parameter compared to the 4.9 μm thick material.

When comparing material 1 to material 2, we can see that the material with a smaller thickness consistently shows a higher Johnson's parameter across the temperature range. For both materials 1 and 2, the thinner material exhibits higher values for the Johnson's parameter.

6.2 Modeling TCC

In chapter 3, we utilised experimental data supplied by AVX for a typical shell material and BT to determine the TCC analytically for a layered material arranged in series and parallel. Utilising this same material data and the FEA model developed in chapter 5, we will now determine the TCC of these two materials in different configurations. In Figure 6.12(A) we see the relative permittivity of the core and shell material once again over a range of 12 temperatures, ranging from -55°C to 155°C. In Figure 6.12(B) we see the conductivity of BT also taken from experimental data. The conductivity of the shell material was generated by separating it from the core conductivity at all temperatures by 3 orders of magnitude.

Twelve 3x3x3 models, one for each temperature being analysed, were generated having a side length of 10 μm and using the material properties seen in Figure 6.12(A) at each of the temperatures ranging from a minimum of -55°C to a maximum of -155°C, β =0 Vm^5/C^3 for the core and the shell for all temperatures to generate the NFD case. The effective permittivity values for each of the models were calculated by utilising the methods described in chapter 4, and then plotted and can be seen in Figure 6.13(A).

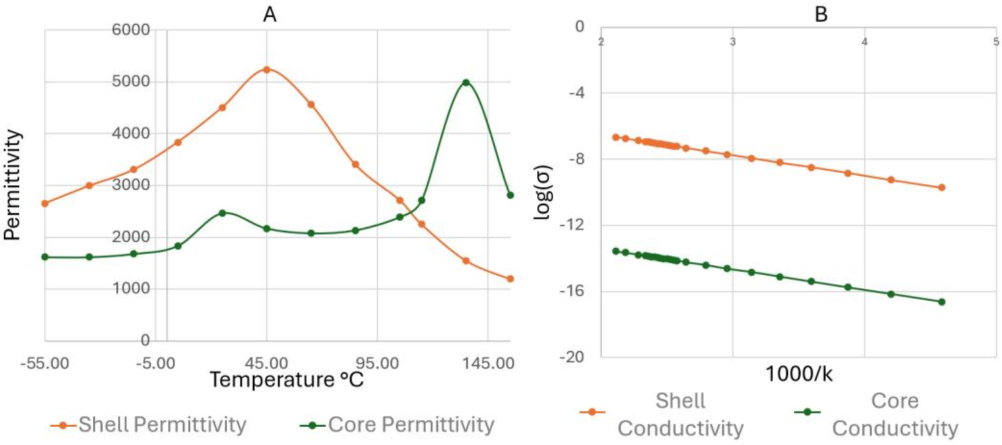

Figure 6.12 (A) relative permittivity properties of BT (green), representing the core material, and a typical shell material (orange) and (B) conductivity of the core and shell material, where the shell material is 3 orders of magnitude more conductive than the core at all temperatures.

6.2.1 More resistive core

6.2.1.1 NFD Case

For the core-shell model, which contains a combination of parallel and series layers, the effective permittivity and temperature coefficient of capacitance (TCC) properties are expected to fall between the values for the series and parallel models. This is because the core-shell microstructure is a blend of series and parallel pathways, each contributing differently to the overall behaviour.

In a series arrangement, as discussed in Chapter 4, the overall relative permittivity is generally lower because the layers' electric fields add up, but their capacitances add reciprocally. On the other hand, in a parallel arrangement, layers are connected side-by-side, resulting in a higher overall relative permittivity since the capacitances add directly. As we have already determined these series and parallel values for a layered model previously, these can serve as a benchmark for comparison.

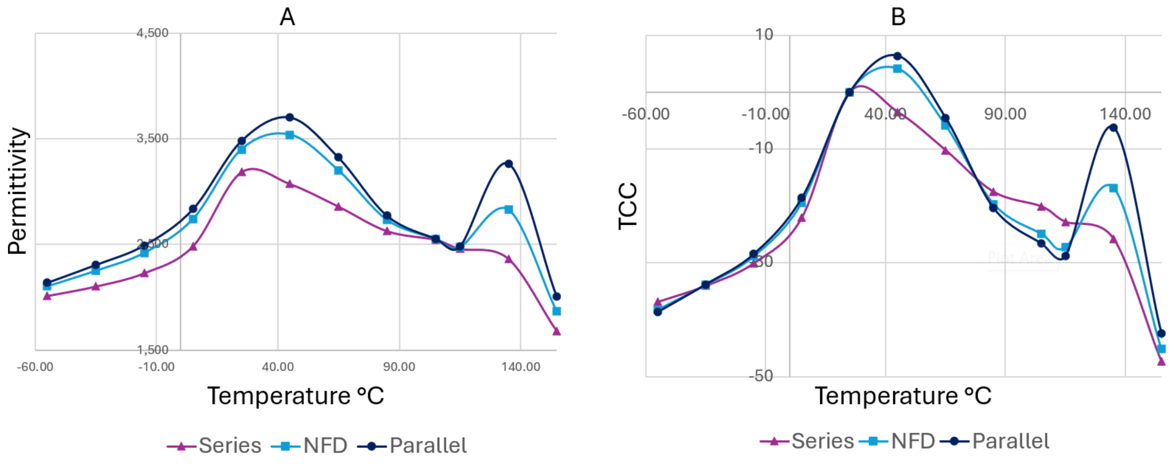

Figure 6.13: (A) relative permittivity properties of the NFD case for a 3x3x3 core-shell model compared to a layered series and parallel model with one layer having the same material properties as the shell and the other layer having the same material properties as the core displaying that the core-shell model will have properties between the series and parallel models. (B) TCC properties for the core-shell, layered series and layered parallel models demonstrating their differences.

In Figure 6.13, we see that both the effective permittivity and TCC values in the NFD case lie between the series and parallel values, confirming the expected behaviour. The observed values can be seen to be closer to the parallel model at all temperatures. This suggests that the parallel pathways have a more significant influence on the core-shell structure. Therefore, despite the presence of series pathways, the parallel arrangements are more dominant, leading to higher relative permittivity and TCC values.

6.2.1.2 Relative permittivity

Utilising the NFD models generated above, we now generated 12 more models ranging from of -55°C to 155°C in which the core is assigned a value of $\beta = 10^{12}$ Vm^5/C^3, the shell $\beta = 0$ Vm^5/C^3 and the applied field voltage was set to be 11 V similar to cases I, II and III in chapter 5.

To represent the configuration of the field-dependent core+shell case, models were generated in which both the core and shell are assigned a value of $\beta = 10^{12}$ Vm^5/C^3 and the applied field voltage was set to be 11 V, similar to cases IV, V and VI in chapter 5.

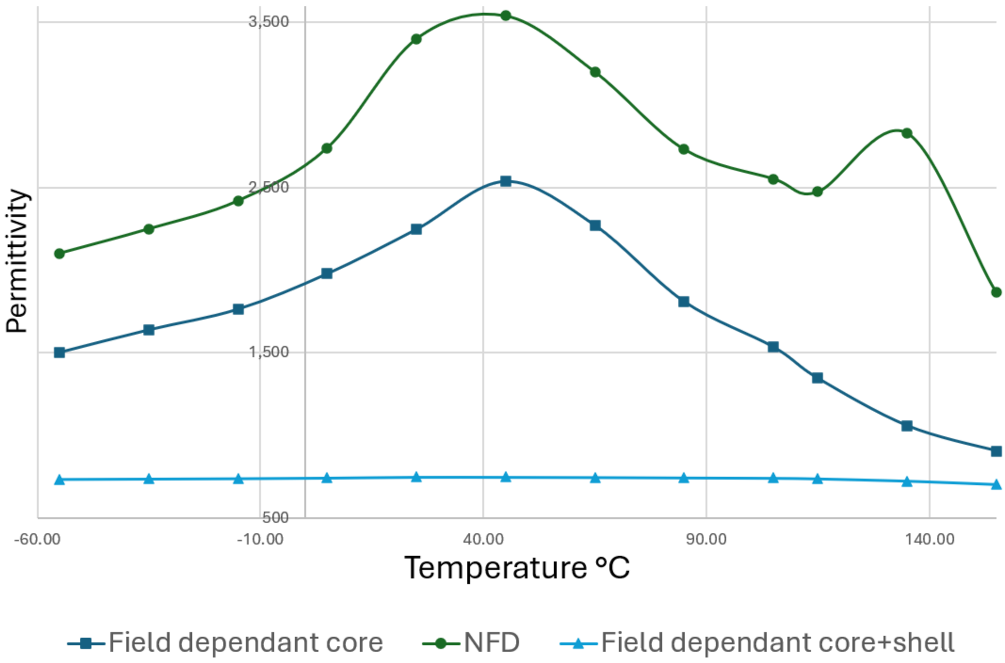

Figure 6.14: Relative permittivity vs. temperature for NFD, Field dependent core and field dependent core+shell configurations. The graph shows the relative permittivity behaviour across a temperature range from -55°C to 155°C. The NFD configuration demonstrates a peak in relative permittivity around 40°C, while the field-dependent core exhibits a similar trend but with a lower peak. The field-dependent core + shell case shows minimal temperature dependence, maintaining a stable relative permittivity throughout.

Figure 6.14 demonstrates the relative permittivity behaviour across a temperature range for the three different configurations, with the NFD case serving as the baseline. The NFD curve exhibits a significant increase in relative permittivity, starting around 2100 at -55°C, peaking at 3500 near 40°C, and then declining with a secondary peak around 135°C. This behaviour shows a strong temperature-dependent dielectric response influenced by intrinsic material properties and structural changes at specific temperatures discussed in chapter 2.

When comparing the Field dependent core case to the NFD case, we observe that the core configuration starts with lower relative permittivity at around 1500 at -55°C and follows a similar trend of increasing relative permittivity with temperature, peaking near 45°C. However, the peak is lower than that of NFD, reaching about 2500. The decline in relative permittivity beyond this peak is more gradual. Across the temperature range, there is a decrease of around 20-30 % in the effective permittivity. However, at a temperature of 135 degrees, this decrease increases to about 55% from 2800 down to about 1050.

In contrast, the field-dependent core+shell case shows remarkably different behaviour. Its relative permittivity remains nearly constant, starting around 735 and only slightly increasing to about 750 and finally dropping to about 700 throughout the temperature range, which corresponds to a significantly higher decrease of around 65-80%. Unlike the NFD case and the field-dependent core case, this configuration demonstrates minimal sensitivity to temperature changes. The core + shell modification appears to stabilise the dielectric properties, preventing the significant fluctuations observed in the NFD baseline

6.2.1.3 TCC

In Figure 6.15, The NFD curve shows a TCC that starts around -40% at -55°C, increases steadily with temperature, peaking just above 4% near 40°C, and then decreases again, dipping below -45% by 155°C. In comparison, the field-dependent core case starts similarly but exhibits a slightly higher initial TCC of around -30% at -55°C. This curve also increases with temperature but peaks at a slightly higher TCC value of about 10% near 40°C. After this peak, the TCC declines more sharply than the NFD, falling below -60% by 140°C. Overall, a clockwise rotation of the TCC can be observed when compared to the NFD case. This leads to an overall decrease in the temperature stability as it goes from having the highest TCC value of -45% to a value of nearly -60% at 155 °C, leading to a configuration that has worse temperature stability than the NFD case.

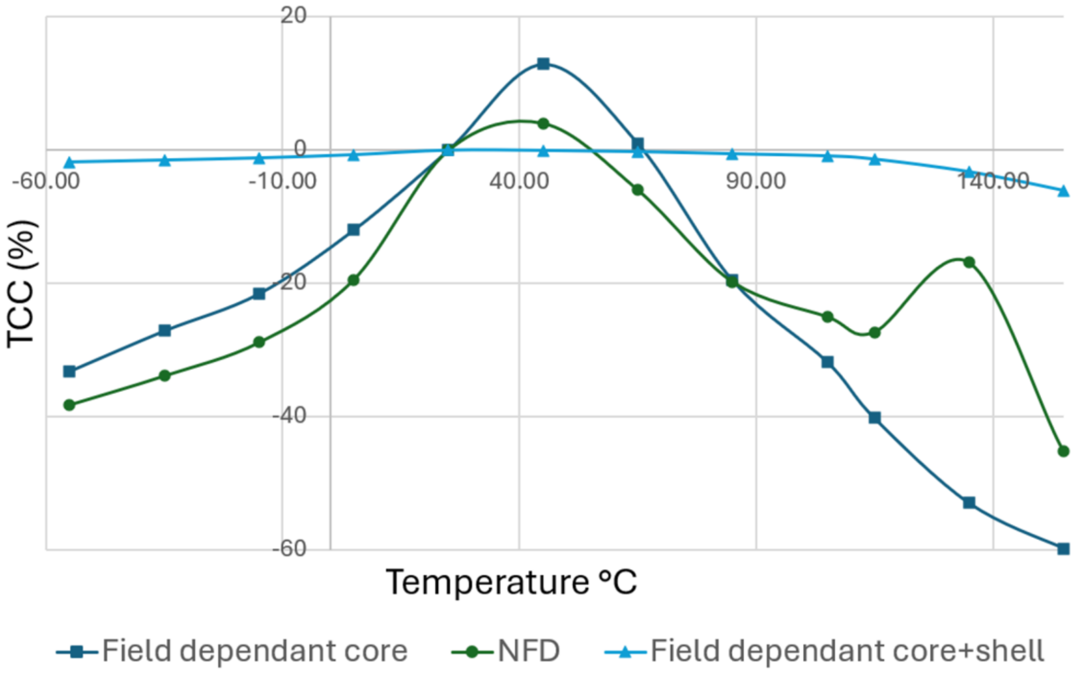

Figure 6.15: Temperature Coefficient of Capacitance (TCC) vs. Temperature for NFD, Field dependent core and field dependent core+shell. The NFD and Field dependent core configurations exhibit significant temperature-dependent changes, with peaks around 40°C. In contrast, the field-dependent core + shell configuration maintains a remarkably stable TCC across the entire temperature range, indicating consistent capacitance behaviour.

The "Field dependent core + shell" configuration, however, demonstrates a distinctively stable TCC across the temperature range. Starting close to -2% at -55°C, it maintains a nearly flat trajectory, with minimal variation, slightly increasing towards 0% around 40°C and then gradually declining back towards -6% by 155°C. This stability contrasts sharply with the NFD baseline, indicating that the core + shell modification effectively neutralises the temperature sensitivity, resulting in a consistent TCC which falls well within the X8F category. However, this is coupled with the massive loss in relative permittivity of nearly 75% seen previously.

6.2.2 More resistive shell

6.2.2.1 *Relative permittivity*

Now that we have seen how TCC changes due to the core being more resistive than the shell, we will study what happens when the shell is more resistive. Once again models are generated over a range of temperatures ranging from of -55°C to 155°C in which the core is assigned a value of $\beta = 10^{12}$ Vm^5/C^3 and the shell Johnson's parameter value is $\beta = 0$ Vm^5/C^3 and the applied field voltage was set to be 11 V for the core dependent case and $\beta = 10^{12}$ Vm^5/C^3 and the shell Johnson's parameter value is $\beta = 0$ Vm^5/C^3 for the core+shell dependent case. The core and shell relative permittivity properties will once again be assigned the same as in the previous case, however, the conductivity properties of the core and shell will be swapped.

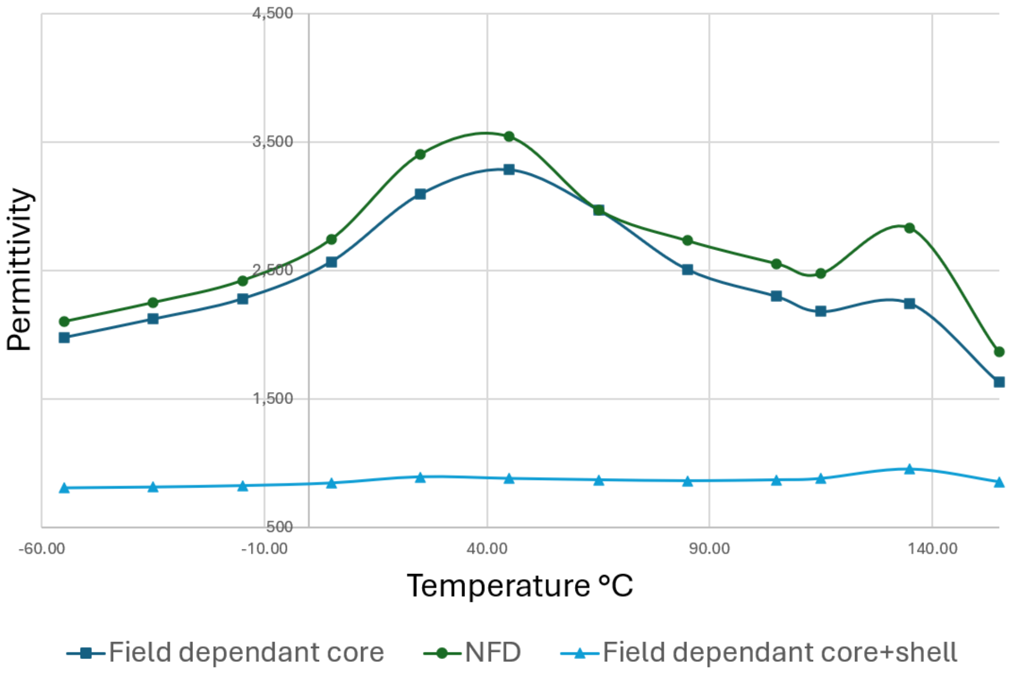

Figure 6.16: relative permittivity vs. Temperature for NFD, Field dependent core and field dependent core+shell cases for a more resistive shell. The Field dependent core follows a similar trend as the NFD with slightly lower values. The field-

dependent core + shell exhibits minimal variation, maintaining a stable relative permittivity throughout the temperature range, indicating enhanced stability in dielectric properties.

In Figure 6.16, we once again observe the relative permittivity as a function of temperature for three configurations: NFD, Field dependent core, and Field dependent core + shell. The Field dependent core case starts with a slightly lower relative permittivity at around 2000 compared to the 2100 of the NFD case at -55°C. It follows a similar trend of increasing relative permittivity, reaching a peak close to 3250 near 40°C. After this peak, the relative permittivity decreases more steadily and consistently than in the NFD case. This suggests that the core modification somewhat reduces the relative permittivity's sensitivity to temperature, especially in the higher temperature range, but still retains a significant response around the peak temperature. Overall, we can see that across the temperature range, there is a decrease of around 5-10 % in the effective permittivity. However, the decreased relative permittivity at a temperature of 135 degrees is once again the greatest, decreasing from a value of 2830 to about 2240.

The field-dependent core + shell case, however, once again shows a distinctively stable relative permittivity across the entire temperature range. Starting around 800 and fluctuating minimally to a max of about 950, this configuration displays an almost flat response to temperature changes. This corresponds to a significantly higher decrease between 55% and 70% across the temperature range.

Unlike the NFD and field-dependent core-only configurations, the core + shell dependence appears to suppress the temperature-dependent variations in relative permittivity entirely at an applied voltage of 11V, ensuring that the dielectric properties remain constant regardless of the thermal environment.

6.2.2.2 TCC

In Figure 6.17, the Field dependent core case starts similarly to the NFD case but exhibits a slightly higher initial TCC of around -36% at -55°C. This curve also increases with temperature but peaks at a slightly higher TCC value of about 6% near 40°C. After this peak, the TCC declines more sharply than the NFD, falling below -50% by 155°C. Overall, a clockwise rotation of the TCC can be observed when compared to the NFD case. This leads to an overall decrease in the temperature stability as it goes from having the highest TCC value of -45% to a value of nearly -60% at 155 °C, leading to a configuration that has worse temperature stability than the NFD case. However, for temperatures below room temperature, it exhibits minor improvements to the TCC.

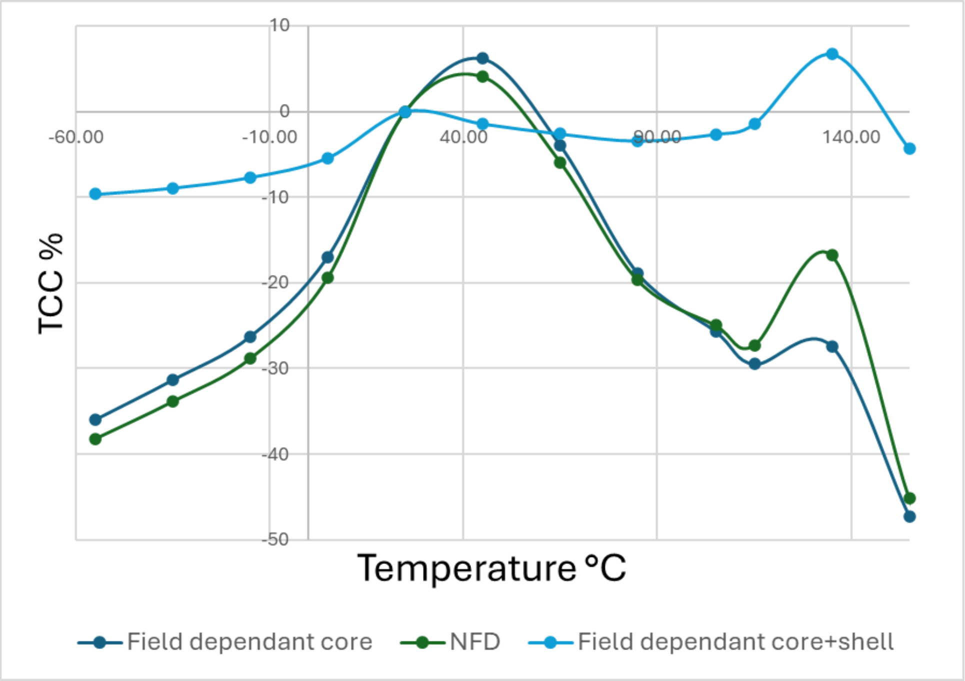

Figure 6.17 Temperature Coefficient of Capacitance (TCC) vs. Temperature for NFD, Field dependent core and field dependent core+shell. The NFD and field-dependent core configurations exhibit significant temperature-dependent changes, with peaks around 40°C. In contrast, the field-dependent core + shell configuration maintains a relatively stable TCC across the entire temperature range, indicating consistent capacitance behaviour.

The field-dependent core + shell configuration, however, once again demonstrates a distinctively stable TCC across the temperature range. Starting close to -10% at -55°C, it maintains a relatively flat trajectory, with minimal variation, slightly increasing towards -1% around 40°C and then gradually declining back towards -4% by 155°C. There is a slight peak at around 140°C where it increases to 7%. This peak takes it out of the X8P category and brings it to an X8F. However, compared to the more resistive case, this configuration allows for around 10% higher relative permittivity values.

6.2.3 Conclusions

The analysis of the core-shell models under varying configurations and temperature ranges reveals distinct differences in relative permittivity and temperature coefficient of capacitance (TCC) behaviours. The NFD case demonstrated a temperature-dependent increase in relative permittivity, peaking near 40°C, and a corresponding rise and fall in TCC values. The Field dependent core case exhibited similar trends with slightly reduced relative permittivity and a sharper decline in TCC at higher temperatures, indicating reduced temperature stability compared to the NFD baseline.

In contrast, the field-dependent core+shell configuration maintained a remarkably stable relative permittivity and TCC across the entire temperature range, highlighting the effectiveness of this setup in minimising temperature sensitivity. This stability comes at the cost of a significant reduction in overall relative permittivity, suggesting a trade-off between temperature stability and dielectric performance.

Additionally, when the shell was made more resistive, the field-dependent core+shell configuration continued to demonstrate minimal variation in relative permittivity and TCC, further confirming its role in stabilising dielectric properties under thermal stress. This consistent behaviour across different scenarios demonstrates the field-dependent core+shell configuration's potential for applications requiring stable dielectric properties over a wide temperature range.

6.3 References

1. Graham Dale. *Principal Engineer, KYOCERA AVX Components*.
2. Solver. Accessed January 16, 2025. https://appsource.microsoft.com/en-us/product/office/wa104100404?tab=overview

7 Conclusions and future work.

7.1 Future Work

The current implementation of the code to calculate the field dependency of dielectrics using Johnson's equation and a core-shell 3x3x3 cube arrangement serves as a strong foundation for exploring various aspects of dielectric behaviour. Multiple avenues for future work can build upon this model to enhance our understanding of dielectric materials, particularly by investigating additional features such as changes in volume fraction, pores, surface roughness, and more complex geometries.

7.1.1 Pores in Dielectric Materials

One of the most promising extensions of this work is the incorporation of pores within the dielectric materials. Porosity plays a significant role in the electrical and mechanical properties of dielectrics. The presence of pores can affect the relative permittivity, breakdown strength, and overall dielectric performance. By modifying the existing code to introduce different pore sizes, shapes, and distributions within the 3x3x3 cube model, we can simulate and study their impact on voltage dependency. A simple model has been generated below to show how this can be done utilising the Johnson's equation code developed.

A simple model of a pore having a radius of 0.3 μm in a cube of material having a side length of 10 μm, a ε_r=1000 and conductivity of $\sigma = 100$ μS/m. This cube is discretised into ~267k tetrahedral elements, and the local electric field distribution is simulated and can be seen in Figure 7.1 A showing the electric field and relative permittivity for the NFD case. From this, we can easily see that in the regions surrounding the pore, there is a significant variation in the electric field around the pore. The base field strength across the material is 11MV/m, however, the regions to the side of the pore experience a field strength of 17MV/m. This field strength decreases to nearly zero at locations above and below the pore. When comparing this to the relative permittivity data, we see that the relative permittivity decreases to about 655 in a majority of the model. In the regions around the sides of the pore, the relative permittivity decreases further to a value of about 550. The regions above and below the pore, however, experience negligible change in the relative permittivity values.

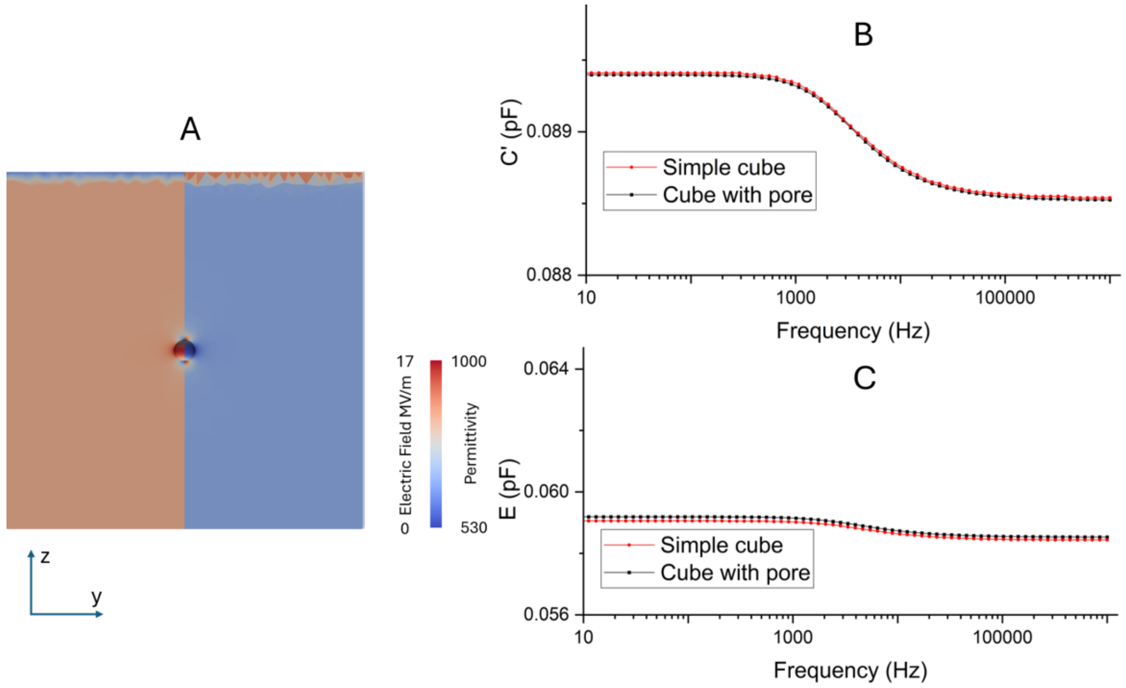

Figure 7.1: A) A combined view of the electric field (left) and relative permittivity (right) for the simple cube with a pore model having an EG of 11 MV/m. The resulting electrical response in C' spectra is shown in B) and C) with comparisons to the simple cube model.

In Figure 7.1(B) we see the NFD cases for the simple cube model (from chapter 5) and the cube with a single pore model. Both models exhibit capacitance values in the range of approximately 0.0885 pF to 0.0894 pF, with the pore model having a minor decrease in relative permittivity due to the structural difference. The overall percentage difference of adding a single pore in the model is just 0.012%, which is negligible.

Looking at Figure 7.1(C), we see the case where an applied field voltage of 11 MV/m has been applied to the simple cube, and the cube with single pore models and $\beta = 1 \times 10^{10}$ Vm^5/C^3. Comparing the two models, we see very similar trends. In both datasets, the capacitance remains largely consistent across frequencies, with only slight differences observed.

For the simple cube model, the capacitance values fluctuate minimally around 0.0591 pF. In contrast, for the cube with a pore model, the capacitance values are similarly clustered around 0.0591 pF but tend to be slightly higher on average, particularly for higher frequencies. This difference is generally on the order of 0.0001 pF, reflecting a small but consistent increase in capacitance when the pore is added to the model.

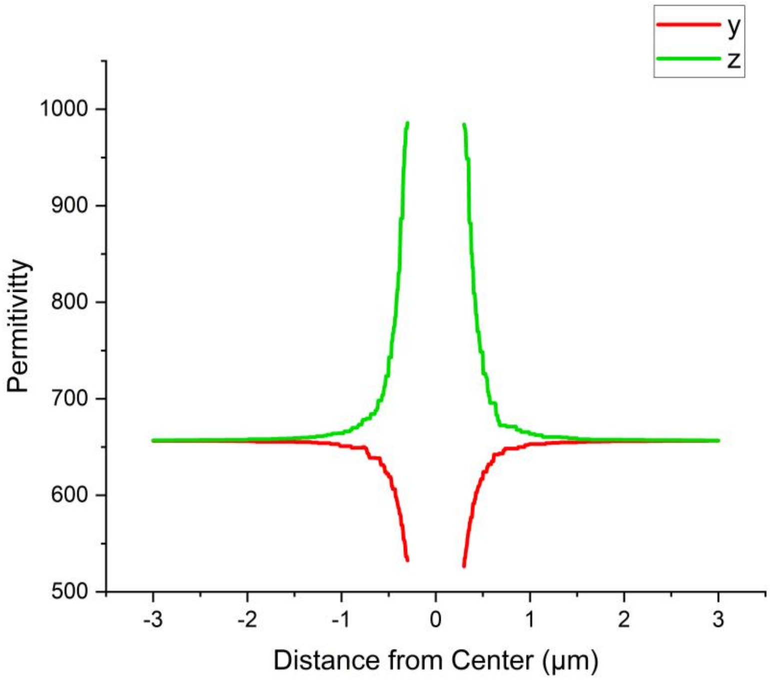

Figure 7.2: Relative permittivity variation as a function of distance from the pore centre along the y-axis (red) and z-axis (green), showing anisotropic behaviour with a sharp increase in relative permittivity along the z-axis and a decrease along the y-axis near the pore centre.

In Figure 7.2 we see the variation of relative permittivity along the y and z axes as a function of distance from the centre of the pore. As the distance decreases along the z-axis (green line), the relative permittivity increases sharply as it approaches the pore, peaking at a value of about 985. In contrast, along the y-axis (red line), the relative permittivity decreases sharply as it approaches the pore, reaching a minimum just below 530. Away from the pore, the relative permittivity stabilises for both axes, with the values converging at about 1.5µm from the surface of the pore.

In summary, while the capacitance in both models is largely consistent across the frequency range, the cube with a pore model generally shows marginally higher capacitance values compared to the simple cube model in the presence of an electric field. However, the overall differences between the two datasets are small, indicating that the pore has a minimal impact on the capacitance within the frequency range presented.

The future code can be enhanced to allow for the simulation of varying pore sizes, from nanometre-scale to micrometre-scale, and different distributions (random, uniform, or clustered). This will enable us to analyse how pore characteristics influence the electric field distribution, polarisation, and relative permittivity under varying voltages. By applying Johnson's equation in these new scenarios, we can derive insights into optimising dielectric materials for specific applications.

Porous structures are known to lower the dielectric breakdown strength of materials. Future simulations can focus on quantifying this effect by correlating the density and size of pores with the voltage at which breakdown occurs. This will provide valuable data for designing more resilient dielectric materials, especially for high-voltage applications.

7.1.2 Surface Roughness

Surface roughness is another critical factor that influences the electrical properties of dielectric materials. The current smooth core-shell model can be extended to include surface irregularities, which are often present in real-world materials due to fabrication processes.

The code can be modified to introduce surface roughness by applying random or patterned perturbations to the shell surface of the cubes. By simulating various degrees of roughness, we can study how these irregularities impact the local electric field distribution and overall dielectric performance.

Surface roughness can lead to localised enhancements of the electric field, which may result in increased polarisation and, consequently, altered relative permittivity. Future work can involve a detailed analysis of these effects using the enhanced code. The results will be particularly relevant for applications in thin-film dielectrics, where surface effects become increasingly significant.

7.2 Final Conclusions

This thesis explored the complex relationships between various material properties and their response to electric fields, specifically focusing on effective permittivity, dielectric response, and voltage-dependent capacitance. The findings underscore the critical role of parameters such as Johnson’s parameter, applied electric field strength, material thickness, and intrinsic permittivity in determining the behaviour of materials under field effects.

A code that replicates the voltage dependency of dielectric materials using Johnson's equation was successfully developed. This code accurately models the nonlinear relationship between voltage and relative permittivity, capturing the complex behaviour of dielectrics under varying electric fields. To ensure the validity of the simulation, the results were verified by comparing them with established models and experimental data. The output from the code closely matched the expected trends, confirming its reliability in predicting the voltage-dependent properties of dielectrics. This verification process demonstrated that the code is an effective tool for simulating dielectric behaviour under different electrical conditions.

This code was then used to analyse several different configurations of dielectrics. The analysis reveals that effective permittivity is highly sensitive to changes in Johnson’s parameter and electric field strength, with a noticeable decline as these parameters increase, particularly in high-permittivity materials like barium titanate. This decline is indicative of a weakening dielectric response, which is more pronounced in materials with higher intrinsic permittivity values. A saturation effect is also observed at higher Johnson’s parameter values and field strengths, suggesting that the influence of intrinsic permittivity diminishes beyond a certain threshold. Notably, the thickness of the material has the strongest effect on the final temperature coefficient of capacitance (TCC), with other factors such as volume fraction and conductivity ratio leading to only minor changes.

When comparing analytical and simulated models, the thesis demonstrates that simulated models provide accurate and reliable results, with minimal deviations from the analytical solutions. The maximum difference between the analytical and simulated models in both series and parallel configurations is less than 2%, confirming the validity of the simulations for modeling complex material systems.

Furthermore, the development of a finite element modeling approach aids in understanding the voltage-dependent behaviour of multilayer ceramic capacitors (MLCCs). By simulating the effects of the electric microstructure, the study highlights how the core-shell structure of $BaTiO_3$ materials influences VCC. The results show that a well-designed core-shell structure can reduce or enhance VCC effects while shielding the core from high electric fields. This knowledge can guide the design of future MLCC materials with improved performance and breakdown strength.

In conclusion, this research provides significant insights into the factors influencing the dielectric response of materials, validating the accuracy of simulation models, and offering new strategies for the design of advanced MLCCs with tailored voltage dependence and enhanced breakdown strength.